

Mechanism and kinetics of mineral weathering under acid conditions

C. Anbeek

Ontvangen

24 FEB. 1994

UB-CARDEK

CENTRALE LANDBOUWCATALOGUS



0000 0575 8392

60951

Promotor: Dr. ir. N. van Breemen
hoogleraar in de bodemvorming
en ecopedologie

Co-promotor: Dr. L. van der Plas
hoogleraar in de bodemmineralogie

NN08201, 1736

Mechanism and kinetics of mineral weathering under acid conditions

C. Anbeek

Proefschrift

ter verkrijging van de graad van doctor
in de landbouw- en milieuwetenschappen,
op gezag van de rector magnificus,
Dr. C.M. Karssen,
in het openbaar te verdedigen op
woensdag 16 februari 1994
des namiddags te vier uur in de Aula
van de Landbouwuniversiteit te Wageningen.

157 590114

Cover: The scanning electron microscope image (right) shows a polished surface of adularia feldspar after 10 minutes immersion in a 2 % HF solution. Etch pits have developed at crystallographically controlled surface sites. The 3-D matrix surface shows the result of a Monte Carlo simulation of etch pit development at a crystal defect.

**BIBLIOTHEEK
LANDBOUWUNIVERSITEIT
WAGENINGEN**



CIP-DATA KONINKLIJKE BIBLIOTHEEK, DEN HAAG

Anbeek, C.

Mechanism and kinetics of mineral weathering under acid conditions / C. Anbeek. - [S.l. : s.n.]. - III.

Thesis Wageningen. - With ref. - With summary in Dutch.
ISBN 90-5485-215-1

Subject headings: mineral weathering / feldspar / quartz.

Stellingen

1. Earth is the cradle of mankind, but one should not live in the cradle forever.
K. Tsiolkovsky (1920) Beyond the Planet Earth
2. Alle aandacht is gericht op het kappen van het tropisch regenwoud, maar ook in China, Siberië, Canada en de Verenigde Staten maakt men korte metten met de oerbossen.
Wagenings Universiteitsblad, 16 jan. 1992
3. De vermeende Cambrische explosie van levensvormen na 2½ miljard jaar blauwwieren duidt veeleer op natuurlijke selectie en steeds grotere soortenrijkdom in een periode waarin uiteindelijk de eerste harde skeletdelen werden ontwikkeld.
4. Het belangrijkste doel van de geldverslindende "Postbus 51" campagnes is het wekken van de schijn dat de Rijksoverheid beleid voert.
5. De nauwkeurige afstemming van vele fysische grootheden op een heelal vol diversiteit en met ontwikkelingsmogelijkheden voor organisch leven bewijst het bestaan van een Hogere Macht, óf het bestaan van talloze afzonderlijke heelals - inclusief een aantal met planeten van pizzadeeg - waaruit wij per definitie een "winnend lot" hebben getrokken.
6. Een tweemaal zo sterke *Unterseebootdienst* aan het begin van de oorlog zou, zowel voor *Der Kaiser* als voor *Der Führer*, het pleit binnen twee jaar in hun voordeel hebben beslecht.
7. Alle bestaande literatuur inzake de oplossingskinetiek van "vers" gemalen minerale monsters dient opnieuw te worden geïnterpreteerd.
Dit proefschrift
8. Voor het onderling vergelijken van verwerkingssnelheden is normalisatie naar het geometrisch oppervlak leerzamer en eenvoudiger te realiseren dan normalisatie naar het BET oppervlak.
Dit proefschrift
9. De verwerkingssnelheid van vers gemalen veldspaat, genormaliseerd naar het geometrisch of naar het BET oppervlak, is evenredig met de korrelgrootte.
Dit proefschrift
10. Door natuurlijke verwerking vormt zich een uiterst poreuze oppervlaktelaag op veldspaatkorrels. De vorming van deze laag bij veldspaat - en het achterwege blijven ervan bij kwarts - kan worden beschreven met behulp van een thermodynamische theorie voor kristalfouten in deze mineralen.
Dit proefschrift

11. De lage verwerkingssnelheid van veldspaat in de natuur, vergeleken met die van vers gemalen veldspaat in gangbare laboratorium-experimenten, wordt gedeeltelijk verklaard doordat het oppervlak van de poriën in verweerde veldspaat niet-reaktief is.
Dit proefschrift
12. For feldspar at low pH, the presence of a Si-rich surface layer and the increasing plagioclase dissolution rate with increasing anorthite content imply that, under acid conditions, Al is the destabilizing component in the tetrahedral framework.
Alex E. Blum (in press) In: Feldspars and Their Reactions.
13. Het feit dat de verwerkingssnelheid van natuurlijk verweerde veldspaat, genormaliseerd naar BET oppervlak, onafhankelijk is van de korrelgrootte bewijst nog niet dat het aantal reaktieve plaatsen per eenheid van geometrisch oppervlak onafhankelijk is van de korrelgrootte.
Dit proefschrift
14. De verzadigingsgraad van de bulk-oplossing is een slechte schatter van de verzadigingsgraad waarbij de verwerking van veldspaat daadwerkelijk plaatsvindt.
Dit proefschrift
15. Helaas is voor het reizen Sneller Dan Licht meer nodig dan de vermakelijke, quasi-wetenschappelijke praatjes van SF-auteurs over graviton-interactie, hyperruimte en illiniumstaven in een krachtveld van vrije mesonen.
W.F. Temple (1968) The Fleshpots of Sansato.
J. Blish (1970) Cities in Flight.
J.P. Hogan (1978) The Gentle Giants of Ganymede.
16. Mijn vrouw noemt mij een model-echtgenoot: thuiskomend van het modelleren van bodemverweringsprocessen ga ik verder met het modelleren van Amerikaanse spoorwegen.

Stellingen behorend bij het proefschrift "Mechanism and kinetics of mineral weathering under acid conditions". Chris Anbeek, Wageningen, 16 februari 1994.

De burgemeester keek versuft naar de deur, die zich achter de wetenschapsman sloot. "Wat wilde hij?" vroeg hij zich af. "Hij is tenslotte een geleerde en men kan zijn woorden niet verwaarlozen. Als men ze maar begreep."

M. Toonder (1978) *De geweldige wiswassen*

Aan mijn ouders
Aan Gerrie

zonder jullie steun zou dit proefschrift niet zijn verschenen

Abstract

Anbeek, C. (1994) Mechanism and kinetics of mineral weathering under acid conditions. Doctoral thesis, Agricultural University of Wageningen, The Netherlands.

This study deals with the relationships between crystal structure, grain diameter, surface morphology and dissolution kinetics for feldspar and quartz under acid conditions.

Intensively ground samples from large, naturally weathered mineral fragments are frequently used in dissolution studies. The surface area of such samples, estimated from their gas adsorption isotherm (BET method), is normally implied to be all freshly created by grinding. This study revealed that: (1) during natural weathering, micropores (diameters ≈ 2 nm) develop in feldspar but not in quartz grains; (2) the micropores account for virtually all BET surface area of naturally weathered feldspar grains; and (3) due to the micropores, grinding of large, naturally weathered feldspar fragments is highly ineffective in creating samples with only freshly ground BET surface area.

By assuming all BET surface area of ground feldspar samples to be freshly created, experimental dissolution data have been explained from dissolution rates essentially independent of the grain diameter. For ground feldspar samples this study revealed that: (1) the dissolution rate of the freshly created BET surfaces is essentially proportional to the grain diameter; and (2) the dissolution rate of the naturally weathered BET surfaces, still present after grinding, is most likely independent of the grain diameter. Moreover, the dissolution rate, normalized to BET surface area, of unfractured, naturally weathered feldspar grains was essentially independent of the grain diameter. These findings can be explained if: (1) the average density of dissolution sites on freshly created feldspar surfaces is approximately proportional to the grain diameter; (2) micropores develop at dissolution sites during natural weathering; and (3) the BET surface area of the micropore "walls" (i.e. the area perpendicular to the grain surface) is essentially non-reactive.

Thermodynamical considerations and Monte Carlo simulations showed that: (1) the formation of micropores in feldspar but not in quartz grains during natural weathering can be explained from enhanced dissolution at crystal defects; and (2) the BET surface area of micropore "walls" from enhanced dissolution at crystal defects is essentially non-reactive. A kinetic model is developed, showing for feldspar that the non-reactivity of the micropore "walls" helps to explain the discrepancy, reported in the literature, between laboratory and field dissolution rates.

Keywords: mineral weathering, feldspar, quartz, BET surface area, geometric surface area, surface roughness, crystal defects, etch pits, micropores.

Voorwoord

Na zelf ook weer vier en een half jaar verder verweerd te zijn, is thans mijn proefschrift over mineraalverwerking afgerond. Dat dit mogelijk werd dank ik allereerst aan mijn ouders, die mij altijd stimuleerden en in staat stelden om de opleiding van mijn keuze te volgen. Ik ben blij dat zij dit moment kunnen meebeleven. En ik weet zeker dat zij hetzelfde voelen, al zou met name mijn vader liever een Nederlandstalige versie in handen hebben gehad.

Naast de bijzondere rol van mijn ouders hierin dankt dit proefschrift zijn bestaan bovenal aan de inspanningen en interesse van mijn promotor Nico van Breemen. Nico, bedankt voor het in mij gestelde vertrouwen en voor het kernachtig herformuleren van mijn soms amorfe gedachtenspinsels. Verder wil ik hier speciaal noemen de steun en hulp die ik ontving van mijn co-promotor en voormalig professor in de bodemmineralogie Leendert van der Plas, en van mijn collega Ed Meijer. Leendert, bedankt voor het met raad en daad terzijde staan tijdens momenten waarop met name mijn onvoldoende ervaring op optisch-mineralogisch gebied mij parten speelde. Ed, naast alle dingen die je voor me hebt gedaan dank ik je speciaal voor de vele lessen logisch redeneren die je me - wellicht onbewust - hebt gegeven tijdens onze discussies.

Enorm veel werk is mij uit handen genomen door Leo Begheyn en Barend van Lagen, die samen alle nat-chemische analyses hebben verzorgd zoals die plaatsvonden in het kader van dit onderzoek. Veel dubbel werk is mij bespaard gebleven dankzij Marcel Lubbers, die mijn soms rebellerende computer immer in het gareel terug wist te dwingen. Van de overige collega's van de vakgroep Bodemkunde en Geologie dank ik verder met name Andrea Broesder, Joke Cobben, Jan van Doesburg, Toine Jongmans, Bram Kuijper en Igor Staritsky voor de onvoorwaardelijke hulp en collegialiteit die ik van hen mocht ontvangen.

Een belangrijk deel van de bevindingen in dit proefschrift is gebaseerd op metingen van mineraaloppervlaktes met behulp van de gasadsorptie-methode. Zonder hulp van diverse collega's en vakgenoten zouden mijn eigen metingen op dit gebied zijn mislukt. Derhalve ben ik veel dank verschuldigd: aan Daniel Tessier en René Prost van het Institut National de la Recherche Agronomique, Versailles, Frankrijk, voor het helpen ontwikkelen van de te volgen meetstrategie; aan Anton Korteweg van de vakgroep Fysische- en Kolloïdchemie van de Landbouwniversiteit te Wageningen, voor het beschikbaar stellen van meetapparatuur; aan Paul van Ekeren en Aad van Genderen van het Centrum voor Chemische Thermodynamica van de Rijksuniversiteit te Utrecht, voor het beschikbaar stellen van hoogwaardige vacuüm-systemen en werkruimte voor mijn meetopstelling, en aan Phillip Bennett, Department of Geology, University of Texas, Austin, U.S.A., en prof. Lars I. Staffansson, Department of Theoretical Metallurgy, Royal Institute of Technology, Stockholm, Zweden, voor het uitvoeren van ijk-metingen aan referentiemonsters. Voor hulp ten aanzien van overige onderdelen van mijn onderzoek dank ik verder: Joop Harmsen, voor het beschikbaar stellen van de Grafiet-

oven Autoanalyzer van het ICW te Wageningen; Arie "Canadabalsem" van Dijk, voor het vervaardigen van onvervaardigbare slijpplaten, en Bram Boekestein en Anke Clerckx, voor het beschikbaar stellen van, en behulpzaam zijn bij, de electronen-microscopische faciliteiten op het TFDL te Wageningen. Een gedeelte van mijn onderzoek werd gesteund door de Stichting Aardwetenschappelijk Onderzoek (AWON) met een subsidie van de Nederlandse Organisatie voor Wetenschappelijk Onderzoek (NWO).

Met name de volgende doctoraalstudenten hebben aanzienlijke bijdragen geleverd aan de totstandkoming van mijn proefschrift: Luis Francisco de Moraes Faria da Costa Lopes, die de BET- en geometrische oppervlaktemetingen heeft uitgevoerd en geanalyseerd voor de hoofdstukken 3 en 4 en gedeeltelijk voor hoofdstuk 5; Paul Flapper, die veel werk heeft verricht in het kader van het onderzoek als beschreven in hoofdstuk 5, en Paul Verburg, die als mede-auteur van hoofdstuk 7 nauw betrokken is geweest bij de voorbereiding en uitvoering van de aldaar beschreven Monte Carlo simulaties.

Het is vrijwel ondoenlijk om iedereen die op enigerlei wijze betrokken is geweest bij de totstandkoming van dit proefschrift persoonlijk te bedanken. Neemt u het mij dus niet kwalijk als uw naam hier niet uitdrukkelijk staat vermeld; uw hulp werd zeer op prijs gesteld. Wel wil ik nog gaarne persoonlijk bedanken: Alex E. Blum, U.S. Geological Survey, Menlo Park, California, U.S.A., voor het beschikbaar stellen van het computerprogramma SCSV.FOR, en George R. Holdren, Jr., ManTech Environmental Technology Inc., Corvallis, Oregon, U.S.A., voor het beschikbaar stellen van Crystal Bay Bytownite en Grass Valley Anorthite monstermateriaal. Voor de uitvoering van diverse veldexperimenten in de aanloopfase van mijn onderzoek mocht ik vertrouwen op de hulp en deskundigheid van: Rien van der Maas, Proefstation voor de Fruitteelt, Wilhelminadorp; André Nieuwenhuysse, Centro Agronomico Tropical, Guápiles, Costa Rica; prof. Charles T. Driscoll, Department of Civil Engineering, Syracuse University, New York, U.S.A.; Lennart Rasmussen en Per Gundersen, Laboratory of Environmental Sciences and Ecology, Technical University, Lyngby, Denemarken, en prof. Hans M. Seip, Department of Chemistry, University of Oslo, Blindern, Noorwegen.

Gedurende de momenten waarop experimentele waarnemingen mijn theoretische modellen en nachtrust verstoorden was daar altijd mijn lieve vrouw, Gerrie. Naast het opbrengen van veel geduld voor mijn verstrooide en afwezige buien heeft zij mij, op de haar bekende praktische wijze, veel werk uit handen genomen door vrijwel al het typewerk voor deze uitgave te verzorgen. Verdere steun uit de huiselijke kring mocht ik in de laatste paar maanden ontvangen van onze pasgeboren zoon Daan. Zijn luidruchtige aanwezigheid bleek zeer motiverend te werken op de wil mijn proefschrift nu definitief af te ronden.

Een laatste woord van dank ben ik verschuldigd aan vergelijking (42) uit Helgeson *et al.* (1984). Meer dan wie of wat ook heeft deze mij aan het denken gezet omtrent de samenhang tussen kristalstructuur, oppervlakteruwheid, fractie vers oppervlak en de verweringskinetiek van mineraalkorrels.

Contents

Abstract	5
Voorwoord	6
Glossary of symbols	10
1. General introduction	15
1.1. Acid atmospheric deposition	16
1.2. Soil processes upon acid deposition	17
1.3. Aim of this thesis	19
1.4. Outline of this thesis	20
Part A: The dissolution of ground feldspar samples in the laboratory	
2. Surface roughness of minerals and implications for dissolution studies	23
2.1. Introduction	24
2.2. Theoretical considerations	26
2.3. Application to actual data	31
2.4. Conclusions	40
3. The effect of grain diameter after grinding	43
3.1. Introduction	44
3.2. Model description	48
3.3. Materials and methods	51
3.4. Results	54
3.5. Discussion	68
3.6. Conclusions	71
4. The effect of grain diameter in the starting material	73
4.1. Introduction	74
4.2. Theoretical considerations	76
4.3. Sample preparation and characterization	78
4.4. Dissolution experiments	82

4.5. Results	84
4.6. Discussion	87
4.7. Conclusions	94

Part B: The dissolution of naturally weathered feldspar and quartz

5. Results from surface roughness data	97
5.1. Introduction	98
5.2. Materials and methods	100
5.3. Results and discussion	105
5.4. Conclusions	114
6. Results from dissolution data	117
6.1. Introduction	118
6.2. Materials and methods	119
6.3. Results	121
6.4. Discussion	124
6.5. Conclusions	135
7. Crystal defects, micropores, and the reactivity of mineral surfaces; a theoretical study	137
7.1. Introduction	138
7.2. Thermodynamic considerations	140
7.3. Monte Carlo simulations	151
7.4. A kinetic model	165
7.5. Conclusions	170
References	172
Appendices	187
Summary	202
Samenvatting	206
Curriculum Vitae	210

Glossary of symbols

Numbers between parentheses refer to the equation where the symbol is defined or introduced. If no number is indicated, the symbol is referred to in the text only. Similarly denoted algebraic operations are printed *italic*.

a	activity (mol.l^{-1} ; 7.2)
a_{av}	average activity inside a dissolution hole (mol.l^{-1} ; A5.2)
a_b	activity in the bulk solution, i.e. outside a dissolution hole (mol.l^{-1} ; A5.1)
a_m	activity at the bottom of a dissolution hole (mol.l^{-1} ; A5.2)
B	energy of a chemical bond (kJ; 7.14)
b	magnitude of the Burgers vector (i.e. the "distortion" vector) of a crystal line defect (nm; 7.3)
$C_1, C_2 \dots$	constants in various equations
c	concentration (mol.l^{-1} ; 7.11)
D	diffusion coefficient ($\text{cm}^2.\text{s}^{-1}$; A5.4)
d	average equivalent spherical grain diameter (μm ; 2.2)
d_a, d_b	average equivalent spherical grain diameter after and before sample (pre)treatment (μm ; 5.7)
d_c	thickness of a secondary coating on primary grains (μm ; 5.4)
d_g	average equivalent spherical grain diameter of ground material (μm ; 2.13)
$d_{i,j}$	average equivalent spherical grain diameter of mineral i in sample j (μm ; A4.8)
d_p, d_q	smaller and larger sieve opening of a size fraction (μm ; 2.26)
d_r	reference grain diameter (μm ; 3.23)
d_t	"transition" grain diameter in Fig. 2.1
d_w	average equivalent spherical grain diameter of weathered material (μm ; 2.13)
d'_w	grain diameter d_w , normalized to the average grain diameter over a number of samples (-; 6.1)
e	edge length of the basic unit of dissolution (i.e. a cube) in the Monte Carlo simulations (nm; 7.14)
F_f	ratio of fresh BET to BET surface area (-; 2.3)
\bar{F}_f	ratio of fresh reactive BET to reactive BET surface area (-; 3.14)
F_m	ratio of BET surface area of micropore walls to BET surface area (-; 7.17)
F_r	F_f at a reference grain diameter d_r (-)
f_f	ratio of fresh geometric to geometric surface area (-; 2.4)
G	free energy (kJ; 7.1)

ΔG	molar free energy change of the dissolution reaction of unstrained mineral bulk ($\text{kJ}\cdot\text{mol}^{-1}$; 7.2)
ΔG_{pit}	total change in free energy, normalized to unit depth, upon creating one mole of cylindrical dissolution holes of radius r at crystal line defects ($\text{kJ}\cdot\text{mol}^{-1}\cdot\text{nm}^{-1}$; 7.7)
g	sample mass (g; A3.1)
g_g	sample mass of ground material (g; 2.22)
$g_{g,i}$	sample mass of the i^{th} ground size fraction (g; 2.16)
$g_{i,j}$	mass of mineral i in sample j (g; A4.8)
g_w	sample mass of weathered material (g; 2.16)
ΔH_m	enthalpy of melting ($\text{kJ}\cdot\text{mol}^{-1}$; 7.12)
h	Planck's constant ($6.626\cdot 10^{-37}$ kJ.s)
i, j	subscripts indicating the i^{th} (or j^{th}) chemical reaction, mineral species, etc.
J	diffusion flux ($\text{mol}\cdot\text{cm}^{-2}\cdot\text{s}^{-1}$; A5.4)
K_{eq}	equilibrium constant for the dissolution of unstrained mineral bulk (unit depends on the chemical reaction; 7.2)
K'_{eq}	equilibrium constant for the dissolution of strained mineral bulk (unit depends on the chemical reaction; A5.16)
$K_{M,\text{eq}}$	equilibrium constant for the dissolution of strained mineral bulk according to the Monte Carlo method (unit depends on the chemical reaction)
k	Boltzmann's constant ($1.381\cdot 10^{-26}$ kJ.K $^{-1}$; 7.14)
L	depth inside a pore of length L_m (μm ; 7.1)
L_m	maximum depth inside a pore, i.e. the pore length (μm ; 5.9)
M	molar weight ($\text{g}\cdot\text{mol}^{-1}$)
N_{av}	Avogadro's constant ($6.023\cdot 10^{23}$ mol $^{-1}$; 7.7)
n	number of moles (mol; 3.5)
P_f	ratio of fresh reactive BET to fresh BET surface area (-; 3.9)
$P_f^{\#}$	actual value, as opposed to model assumption, of P_f (-)
P_w	ratio of weathered reactive BET to weathered BET surface area (-; 3.10)
$P_w^{\#}$	actual value, as opposed to model assumption, of P_w (-)
p	Poisson's ratio (-; 7.4)
q	stoichiometric reaction coefficient (-; 7.2)
q_b	stoichiometric reaction coefficient in the bulk solution, i.e. outside a dissolution hole (-; A5.13)
q_m	stoichiometric reaction coefficient at the bottom of a dissolution hole (-; A5.9)
\mathcal{R}	gas constant ($8.314\cdot 10^{-3}$ kJ.K $^{-1}\cdot\text{mol}^{-1}$; 7.2)
R	apparent dissolution rate ($\text{mol}\cdot\text{cm}^{-2}$ of BET surface.s $^{-1}$; 3.5)
\bar{R}	effective dissolution rate ($\text{mol}\cdot\text{cm}^{-2}$ of reactive BET surface.s $^{-1}$; 3.8)

R^*	bulk dissolution rate ($\text{mol.g}^{-1}.\text{s}^{-1}$; A3.1)
R_f	apparent dissolution rate of fresh material (mol.cm^{-2} of fresh BET surface. s^{-1} ; 3.6)
\bar{R}_f	effective dissolution rate of fresh material (mol.cm^{-2} of fresh reactive BET surface. s^{-1} ; 3.11)
$\bar{R}_f^\#$	actual value, as opposed to model assumption, of \bar{R}_f (mol.cm^{-2} of fresh reactive BET surface. s^{-1})
R_g	apparent dissolution rate of ground material (mol.cm^{-2} of BET surface. s^{-1} ; 3.6)
\bar{R}_g	effective dissolution rate of ground material (mol.cm^{-2} of reactive BET surface. s^{-1} ; 3.15)
R_g^*	bulk dissolution rate of ground material ($\text{mol.g}^{-1}.\text{s}^{-1}$; A3.2)
$R_{j,b}$	Monte Carlo dissolution rate of a mineral j in contact with a solution of bulk composition (mol.cm^{-2} of Monte Carlo surface. s^{-1} ; A5.15)
$R_{j,m}$	Monte Carlo dissolution rate of a mineral j in contact with the solution at the bottom of a dissolution hole (mol.cm^{-2} of Monte Carlo surface. s^{-1} ; A5.15)
R_m	apparent dissolution rate of surfaces of micropore walls (mol.cm^{-2} of micropore wall BET surface. s^{-1} ; 7.21)
R_p	apparent dissolution rate of surfaces other than micropore walls (mol.cm^{-2} of non-micropore wall BET surface. s^{-1} ; 7.21)
R_r	R_g at a reference grain diameter d_r (mol.cm^{-2} of BET surface. s^{-1})
R_r^*	R_g^* at a reference grain diameter d_r ($\text{mol.g}^{-1}.\text{s}^{-1}$; A3.6)
R_w	apparent dissolution rate of weathered material (mol.cm^{-2} of weathered BET surface. s^{-1} ; 3.6)
R_w^*	bulk dissolution rate of weathered material ($\text{mol.g}^{-1}.\text{s}^{-1}$)
R_w'	apparent dissolution rate R_w , normalized to the average apparent dissolution rate over a number of samples (-; 6.2)
\bar{R}_w	effective dissolution rate of weathered material (mol.cm^{-2} of weathered reactive BET surface. s^{-1} ; 3.12)
$\bar{R}_w^\#$	actual value, as opposed to model assumption, of \bar{R}_w (mol.cm^{-2} of weathered reactive BET surface. s^{-1})
r_w	apparent dissolution rate of weathered material (mol.cm^{-2} of geometric surface. s^{-1} ; 6.3)
r_w'	apparent dissolution rate r_w , normalized to the average apparent dissolution rate over a number of samples (-; 6.3)
r	radial distance from a crystal line defect, i.e. the radius of a cylindrical dissolution hole (nm; 5.6)
r_c	critical radius of two-dimensional nucleation (nm; 7.8)

r_f	Frank's radius, i.e. the radius of a cylindrical dissolution hole at equilibrium conditions for unstrained mineral bulk, in the case where $r_h = 0$ (nm; 7.6)
r_h	Hooke's radius, i.e. the radial distance r from a crystal line defect where the strain energy density u_r has dropped to 50 % of its (maximum) value at $r = 0$ (nm; 7.5)
S	BET surface area; also referred to as actual surface area (cm^2 ; 2.1)
\overline{S}	reactive BET surface area (cm^2 ; 3.8)
S_c	BET surface area of secondary coating material (cm^2 ; 5.3)
S_f	fresh BET surface area of ground material (cm^2 ; 2.3)
\overline{S}_f	fresh reactive BET surface area of ground material (cm^2 ; 3.9)
$S_{f,i}$	fresh BET surface area of the i^{th} ground size fraction (cm^2 ; 2.17)
S_g	BET surface area of ground material (cm^2 ; 2.3)
\overline{S}_g	reactive BET surface area of ground material (cm^2 ; 3.10)
S_g^*	specific BET surface area of ground material ($\text{cm}^2 \cdot \text{g}^{-1}$; A3.2)
$S_{g,i}$	BET surface area of the i^{th} ground size fraction (cm^2 ; 2.15)
$S_{i,j}$	BET surface area of mineral i in sample j (cm^2 ; A4.1)
S_m	BET surface area of micropore walls (cm^2 ; 7.17)
S_w	BET surface area of weathered material (cm^2 ; 2.10)
s	geometric surface area (cm^2 ; 2.1)
s^*	specific geometric surface area ($\text{cm}^2 \cdot \text{g}^{-1}$; 2.2)
s_a^*, s_b^*	specific geometric surface area after and before sample (pre)treatment ($\text{cm}^2 \cdot \text{g}^{-1}$; 5.7)
s_f	fresh geometric surface area of ground material (cm^2 ; 2.4)
s_g	geometric surface area of ground material (cm^2 ; 2.4)
s_g^*	specific geometric surface area of ground material ($\text{cm}^2 \cdot \text{g}^{-1}$)
$s_{g,i}$	geometric surface area of the i^{th} ground size fraction (cm^2 ; 2.15)
$s_{i,j}$	geometric surface area of mineral i in sample j (cm^2 ; A4.1)
s_w	geometric surface area of weathered material (cm^2 ; 2.11)
T	temperature (K; 7.2)
t	time (s)
u_r	strain energy density u as a function of radius r ($\text{kJ} \cdot \text{nm}^{-3}$; 7.1)
u_0	maximal strain energy density (i.e. at $r = 0$) ($\text{kJ} \cdot \text{nm}^{-3}$; 7.5)
V	molar volume ($\text{cm}^3 \cdot \text{mol}^{-1}$; 7.1)
V_c	volume of secondary coating material (cm^3 ; 5.3)
$v_{i,j}, v_{i,w}$	volume fraction of mineral i in sample j (-; A4.9) or sample w (-; 5.11)
v_p	volume fraction of pores (-; 5.6)
α, β	parameters describing the linear trend of surface roughness with grain diameter (α : μm^{-1} ; β : -; 2.18)

γ, δ	parameters describing the non-linear trend of surface roughness with grain diameter (γ and δ : -; 2.18)
η	viscosity (kJ.s.cm^{-3} ; A5.14)
Θ	concentration gradient ($\text{mol.l}^{-1}.\text{cm}^{-1}$; A5.1)
λ	surface roughness factor (-; 2.1)
λ_a, λ_b	surface roughness factor after and before sample (pre)treatment (-; 5.8)
λ_f	roughness factor of fresh surfaces (-; 2.6)
λ_g	surface roughness factor of ground material (-; 2.5)
λ_g^o	linear estimate of λ_g (-; 2.20)
$\lambda_{i,j}$	surface roughness factor of mineral i in sample j (-; A4.1)
λ_r	λ_g at a reference grain diameter d_r (-; A3.5)
λ_w	roughness factor of weathered surfaces (-; 2.7)
μ	shear modulus (kJ.nm^{-3} ; 7.3)
ν	frequency factor (s^{-1})
Ξ_p	production term, due to mineral dissolution, in the diffusion model (mol.l^{-1} ; A5.3)
Ξ_r	removal term, due to the diffusion flux, in the diffusion model (mol.l^{-1} ; A5.3)
$\xi_{i,j}$	the proportion of the geometric surface area of sample j which is geometric surface area of mineral i (-; A4.4)
ρ	density (g.cm^{-3} ; 2.2)
$\rho_{i,j}$	density of mineral i in sample j (g.cm^{-3} ; A4.8)
β	pore density (cm^{-2} of geometric surface area; 5.9)
σ	surface free energy (kJ.nm^{-2} ; 7.1)
τ	dimensionless time in the Monte Carlo simulations (-)
Ψ	angle between a crystal line defect and its Burgers vector ($^\circ$; 7.4)
Ω_g	concentration factor of weathered surface area in ground material (-; 2.21)
$\Omega_{g,i}$	concentration factor of weathered surface area in the i^{th} ground size fraction (-; 2.23)
\mathfrak{D}	geometry factor related to the average shape of mineral grains (-; 2.2)
$\mathfrak{D}_a, \mathfrak{D}_b$	geometry factor related to the average shape of mineral grains, after and before sample (pre)treatment (-; 5.7)
$\mathfrak{D}_{i,j}$	geometry factor related to the average shape of mineral grains i in sample j (-; A4.8)
\aleph	geometry factor related to the type of crystal line defect (-; 7.4)

Chapter 1. General introduction

1.1. Acid atmospheric deposition

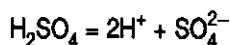
Since its beginning in the previous century, industrialization has been accompanied by a considerable emission and atmospheric deposition of potentially acid chemicals. In many industrialized areas, present-day emissions from anthropogenic sources (for instance, the burning of fossil fuel for energy supply) outweigh those from natural sources (for instance, volcanic eruptions and the volatilization of biogenic substances). In highly industrialized areas, such as the central and north-western parts of Europe and the north-eastern part of the USA, increases have been observed by a factor 10 for some individual chemicals (OECD, 1977). The acidic chemicals, such as SO_x , NO_x , and their derivatives, may be dissolved in precipitation water ("wet deposition") or may alternatively be deposited in a "dry" form, particularly in forest areas (Ulrich *et al.*, 1979). Although formally restricted to wet deposition, the expression "acid rain" is generally used for the total of wet and dry deposition of acidifying substances. A source of acidification of particular importance in The Netherlands is atmospheric deposition and nitrification of NH_3 , emitted mainly from intensive animal husbandry (Van Breemen *et al.*, 1982). Besides short-distance effects from acid deposition, long-distance transport has led to enhanced deposition in remote, non-industrialized areas, causing acidification of lakes and streams, for instance, in Canada and northern Scandinavia, and affecting forest production and the functioning of ecosystems over vast stretches of land. The quality of groundwater can also be negatively affected, and concentrations of, for instance, NO_3^- , SO_4^{2-} and Al^{3+} may exceed drinking water standards, both in private wells and in pumping stations for public drinkwater production.

Increased deposition of acidic chemicals results in increased soil acidification and soil degradation. Typical acidification phenomena in surface waters, groundwaters and soils are: a decrease in pH and in alkalinity, an increase in Al concentrations, a decrease in concentrations of base cations like Ca, Mg and K, and a depletion of the acid buffering capacity (Van Grinsven, 1988). Theoretically, these phenomena are reversible by the addition of lime or fertilizers. In practical situations, however, such additions are feasible only in agriculture and in small areas of special interest, being almost impossible and hardly affordable in vast, poorly accessible forest regions. Although the nature and magnitude of the chemical changes in surface waters, groundwaters and soils are reasonably well understood, there is yet no consensus about toxic levels and the extent of damage caused by acid atmospheric deposition on the biota in terrestrial and aquatic ecosystems. As long as the effects of chemical changes in water and soil on biota are uncertain, the long-term fate of these ecosystems is an additional matter of great concern.

1.2. Soil processes upon acid deposition

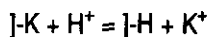
Soil acidification refers to the decrease of the acid neutralization capacity, being the potential of a soil to consume protons above a certain pH, for instance, pH 3 (Van Breemen *et al.*, 1983, 1984). Soil acidification is a natural process which may be caused by carbonic acid from atmospheric CO₂, organic acids, and the deposition of volcanic substances. Particularly in the last decades, however, soil acidification has been greatly enhanced by acid atmospheric deposition from anthropogenic sources. Depending on the composition of the soil solids, the effect of acidification can manifest itself in different ways. The soil solids generally consist of a large bulk of relatively inert quartz, combined with varying amounts of primary minerals, secondary minerals and organic matter (e.g. see Dixon and Weed, 1977). Most primary minerals are aluminosilicates containing large amounts of base cations relative to secondary minerals. Secondary minerals are residues of incomplete dissolution of primary minerals, or newly formed minerals from the reaction products of dissolution of primary minerals. The two main groups of secondary minerals are the clay minerals and the (hydr)oxides of aluminum and iron. Clay minerals and organic matter have predominantly negatively charged surfaces, which are neutralized by exchangeable cations.

If none of the solid soil constituents reacts with protons (acids) entering the soil, acidification causes a decrease in soil pH, for instance, according to:

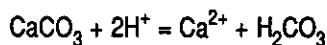


Usually, however, protons are largely consumed by: (1) cation exchange, due to the presence of negatively charged clay minerals and/or organic matter; and (2) dissolution reactions of primary and secondary minerals (normally referred to as mineral weathering).

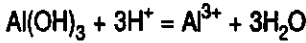
The positively charged protons can exchange against base cations like Na, K, Ca and Mg, bound to clay minerals and organic matter, for instance, according to:



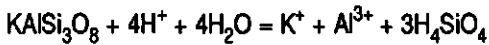
where J represents a negatively charged surface site on the clay or organic matter. Proton consumption by mineral weathering may be seen, for instance, from the dissolution reaction of calcite (CaCO₃):



In this particular example, the consumption of protons is accompanied by the production of a base cation. Aluminum, which is toxic already in μmol to mmol concentrations to many biota (Baker and Schofield, 1980; Vogelman, 1982; Wright *et al.*, 1987), is another reaction product in many mineral weathering processes (Cronan and Schofield, 1979). For instance, soils generally contain several % of amorphous aluminum (hydr)oxides which dissolve readily after input of protons (Mulder, 1988):



Proton consumption and combined production of base cations, aluminum and silicic acid results from the complete (congruent) dissolution of a wide variety of minerals, for instance, for microcline (KAlSi_3O_8) according to:



The process of mineral weathering can be quantified by: (1) the reaction stoichiometry, which determines the nature and the relative amounts of the reactants and products; and (2) the rate of dissolution, normally expressed as the number of moles dissolved per unit of time and per unit of mineral or landscape surface area. If a relatively reactive mineral is present, such as calcite, acids entering the soil will be neutralized almost instantaneously, and the pH will remain near-neutral as long as the mineral is still present. However, if minerals such as calcite are absent, a pH increase due to proton consumption by weathering will be noticeable only at long residence times of the percolating soil solution.

The exchange complex of clay minerals and organic matter may be considered as the readily available pool of cationic plant nutrients. In the case of buffering of acid deposition, the composition of the pool changes, getting poorer in base cations and richer in protons and aluminum from mineral weathering. In typical dutch forest soils, cation exchange reactions are largely limited to the topsoil, due to the absence of clay throughout the soil profile and of organic substances at greater depths. For a root zone of approximately 0.5 m, typical values of the exchange capacity (and thus, of the maximum readily available proton buffering capacity) of dutch forest soils range from 200 to 500 $\text{kmol}\cdot\text{ha}^{-1}$ (Van Grinsven, 1988). At the current deposition rate of approximately 2 to 8 $\text{kmol}\cdot\text{ha}^{-1}\cdot\text{yr}^{-1}$ (Van Breemen *et al.*, 1984), the exchange complex in typical dutch forest root zones would be depleted in base cations within the order of one century. However, the release of base cations from the weathering of primary minerals may slow down, or keep pace with, the depletion of base cations from the exchange complex. The capacity of weathering of primary minerals to consume protons is

normally much larger than that of the cation exchange complex. For an average soil with some 20 % of primary minerals and a root zone of 0.5 m., the buffering capacity from mineral weathering is approximately $20,000 \text{ kmol}\cdot\text{ha}^{-1}$ (Van Grinsven, 1988). However, the dissolution rates of the constituent minerals in the soil are often of more concern than the total buffering capacity. Once readily available pools such as the exchange complex and reactive minerals such as calcite and amorphous aluminum (hydr)oxides are depleted, the low dissolution rates of less reactive minerals will determine the rate of proton consumption in the soil. In most dutch forest soils, calcite is absent and depletion of readily available aluminum (hydr)oxides is expected to occur within the next few decades (Mulder, 1988).

1.3. Aim of this thesis

From the preceding, the dissolution rates of base cation-bearing minerals (calcite, feldspar, pyroxene, amphibole, etc.) are important parameters for the study of acid consumption rates in soils. However, the reaction mechanism and dissolution kinetics of these minerals are not yet sufficiently understood to accurately predict their dissolution rate under varying conditions.

Early dissolution studies suggested that leached layers, depleted in cations, develop at the surface of dissolving mineral grains. This led to the hypothesis that diffusion of reaction products through the leached layers is the rate-limiting step in the dissolution reaction (e.g. Tamm, 1930; Correns, 1963; Wollast, 1967; Busenberg and Clemency, 1976). Holdren and Berner (1979) showed that this concept is probably based on experimental artifacts, and that dissolution rates are more likely controlled by chemical reactions at the mineral-water interface. This led to the hypothesis that the formation of highly reactive intermediate complexes at the mineral surface is the rate-limiting step (e.g. Lasaga, 1981a,b; Schindler, 1981; Aagaard and Helgeson, 1982; Chou and Wollast, 1985; Schindler and Stumm, 1987; Stumm and Furrer, 1987; Wehrl, 1989a,b). However, new evidence has been provided that chemical alterations in weathered mineral surface layers may extend as deep as 100 nm or more (Petit *et al.*, 1987a,b, 1989; Schott and Petit, 1987; Nesbitt and Muir, 1988; Mogk and Locke, 1988; Althaus and Tirtadinata, 1989; Casey *et al.*, 1989a; Goossens *et al.*, 1989; Hellmann *et al.*, 1990). This observation has reopened the question of a diffusion- versus a surface-controlled reaction mechanism.

Crystal defects have been proposed as localized sites of enhanced mineral dissolution, leading to the formation of etch pits (Cabrera *et al.*, 1954; Berner and Holdren, 1979; Eggleton and Buseck, 1980; Lasaga and Blum, 1986; see also the cover of this thesis).

Although it has indeed been observed that naturally weathered mineral grains can be rough and deeply etched (e.g. Grandstaff, 1978; Berner, 1978; Berner and Holdren, 1979), the exact role of crystal defects on the magnitude of dissolution rates is not yet clear.

Dissolution rates from laboratory studies are normally expressed per unit of mineral surface area, e.g. $\text{mol.cm}^{-2}.\text{s}^{-1}$, while rates from watershed budget studies are normally expressed per unit of landscape surface area, e.g. $\text{kmol.ha}^{-1}.\text{yr}^{-1}$. Best estimates of feldspar dissolution rates from watershed budget studies are up to several orders of magnitude lower than those in many laboratory experiments (Pačes, 1983; Velbel, 1985; Schnoor, 1990; Swoboda-Colberg and Drever, 1993). However, little is known about the dissolution reactive mineral surface area in $\text{cm}^2.\text{ha}^{-1}$, needed to compare field- and laboratory derived dissolution rates.

It is the aim of this thesis to contribute to these discussions on mineral weathering. The theoretical considerations in the following chapters apply to a large variety of minerals, both in laboratory experiments and in natural situations. Experimental emphasis is on quartz and feldspar. Quartz was chosen because it is abundant, and because its dissolution behaviour differs distinctly from that of feldspar. Feldspar was chosen because, due to its abundance and relatively high content of base cations, this mineral is of primary interest in the prediction of the acid consumption rate of our (still) remaining natural soils.

1.4. Outline of this thesis

This thesis forms the reflection of four and a half years of research at the Department of Soil Science and Geology, Agricultural University of Wageningen, The Netherlands. The underlying studies were carried out in the context of the VF program #8925 (Environmental Research). The thesis is a collection of publications and submitted manuscripts, some of which multi-authored, on the following subjects:

In chapter 2, the morphology is discussed of mineral surfaces in artificially ground samples derived from large, naturally weathered starting fragments. Such samples are frequently used in laboratory dissolution studies, and their surface area, estimated from the gas adsorption technique (BET method), is normally assumed to be all freshly created by grinding. It is shown that: (1) by far most BET surface area of naturally weathered feldspar grains is present as "internal" surface area; and (2) artificially ground mineral samples can still contain large proportions of naturally weathered BET surface area.

In chapter 3, a kinetic model is presented that incorporates the findings from chapter 2. In the model, experimental dissolution data from artificially ground samples are explained from the simultaneous presence of freshly created and naturally weathered mineral surfaces. It is shown that, contrary to literature assumptions, feldspar dissolution rates normalized to the freshly created BET surface area in ground samples are essentially proportional to the grain diameter after grinding.

In chapter 4, the kinetic model from chapter 3 is applied to the dissolution of ground samples derived from a naturally weathered assemblage of feldspar and quartz. It is shown that the results from chapters 2, 3 and 4 help to explain the discrepancy, observed in the literature, between field- and laboratory derived feldspar dissolution rates.

In chapter 5, the morphology of the "internal" BET surface area is discussed for a naturally weathered assemblage of feldspar and quartz. It is shown that: (1) during natural weathering, micropores (diameters \approx 2 nm) develop in surficial layers of feldspar grains; (2) during natural weathering, micropores do not develop in quartz grains; (3) for feldspar, the micropore density (cm^{-2} of geometric surface area) is approximately proportional to the grain diameter; and (4) the micropores explain by far most BET surface area of naturally weathered feldspar grains.

In chapter 6, the reactivity of naturally weathered BET surfaces is discussed for the same assemblage used in chapter 5. It is shown that the experimental dissolution data can be explained only if: (1) dissolution occurs primarily from the micropores; (2) the pore area perpendicular to the mineral surface (i.e. the micropore "walls") is non-reactive; and (3) the pore area parallel to the mineral surface (i.e. the micropore "bottoms") is highly reactive.

In chapter 7, the results from the earlier chapters are discussed in terms of thermodynamic principles and Monte Carlo simulations. It is shown that micropore formation in feldspar but not in quartz during natural weathering can be explained from enhanced dissolution at dislocations (= crystal line defects). It is also shown that, if the solution composition is constant with time, micropore "walls" at dislocations are non-reactive. A kinetic model is presented to account for the non-reactivity of micropore "walls" in naturally weathered feldspar. It is shown that dissolution rates of naturally weathered feldspar grains, corrected this way, are approximately similar to those of equally sized fresh-surface grains. This means that the formation of non-reactive micropore "walls" at dislocations is probably the most essential change in surface area character during the natural weathering of feldspar.

Part A

The dissolution of ground feldspar samples
in the laboratory

Chapter 2. Surface roughness of minerals and
implications for dissolution studies

Abstract

Large, naturally weathered mineral fragments are often ground and sieved to obtain samples for dissolution studies in the laboratory. If the fragments are ground to much smaller dimensions, the samples are normally assumed to contain only freshly created surface area. A model has been developed to test the validity of this assumption. The model describes the surface roughness factor of ground mineral material as a function of grain diameter and can be used to: (1) estimate the roughness factors of the freshly created and the naturally weathered surfaces; (2) estimate the ratio of freshly created to measured (freshly created plus naturally weathered) surface area in the ground samples, both for geometric and for gas adsorbed (BET) surfaces; and (3) test the internal consistency of surface area measurements. Literature data were evaluated for intensively ground size fractions, derived from nine different naturally weathered feldspars. Roughness factors of the freshly created surfaces ranged from 2.5 to 11. Roughness factors of the naturally weathered surfaces ranged from 130 to 2600, which is much higher than is generally recognized for feldspar. Comparison with surface roughness estimates from scanning electron microscopy strongly suggests that etch pit formation plays a minor role in the increase in BET surface area during natural weathering. Instead, virtually all increase in BET surface area must be attributed to the formation of internal surface structures such as micropores. The model also showed that for these samples, the assumption that all surface area is freshly created by grinding is approximately correct for the geometric surfaces. For the BET surfaces, ratios of freshly created to measured surface area varied over almost the entire range from 0 to 1. This demonstrates that, even after intensive grinding, samples from large naturally weathered mineral fragments can still contain substantial proportions of naturally weathered BET surface area. Thus, previous dissolution studies assuming all BET surface area to be freshly created may need reinterpretation.

2.1. Introduction

Over the past several decades many authors have reported on the kinetics of mineral dissolution, both in the laboratory and in the field. Laboratory experiments frequently involve the use of large, naturally weathered mineral fragments as starting material (e.g. Luce *et al.*, 1972; Berner, 1976; Plummer and Wigley, 1976; Grandstaff, 1977; Schott *et al.*, 1981; Chou and Wollast, 1984; Knauss and Wolery, 1986; McKibben and Barnes, 1986; Casey *et al.*, 1988a). Normally, these are ground to much smaller dimensions to create large amounts of fresh surface area. Sieving of the ground material is also commonly applied to restrict the range of grain diameters. To evaluate experimental dissolution data from such samples, a number of kinetic models is available from the literature (e.g. Aagaard and Helgeson, 1982; Helgeson *et al.*, 1984; Wintsch and Dunning, 1985; Chou and Wollast, 1985; Lasaga and Blum, 1986; Murphy and Helgeson, 1987; Wieland *et al.*, 1988). Virtually all kinetic models yield dissolution rates per unit of mineral surface area. Therefore, authors frequently include

data on the specific surface area of their samples (e.g. Lagache, 1965; Busenberg and Clemency, 1976; Chou and Wollast, 1984; Helgeson *et al.*, 1984; Holdren and Speyer, 1985, 1987; Knauss and Wolery, 1986; Casey *et al.*, 1988a). No distinction is made, however, between the actual types of surface morphology that may be present. So, dissolution rates in the literature are normally expressed per unit of "average" surface area. For intensively ground material from large naturally weathered starting fragments, it is generally implied that the "average" type of surface morphology closely resembles that of the freshly created surfaces. This assumes the amount of freshly created surface area by grinding to be much larger than the initial amount of naturally weathered surface area. In this chapter, the purpose is to demonstrate that this assumption is fundamentally incorrect. Its validity will be shown to depend primarily on the surface area measurement technique being used.

The morphology of mineral surfaces can be characterized by the surface roughness factor (λ). λ is defined as the ratio of the actual surface area (S ; cm^2) to the geometric surface area (s ; cm^2), which is the area of a hypothetical smooth surface enveloping the actual surface (Jaycock and Parfitt, 1981):

$$\lambda \equiv S/s \tag{2.1}$$

Both the actual and the geometric surface area are in fact scale dependent, and vary with the amount of detail observed by a specific measurement technique. Thus, λ can be quantified from surface area measurements at different levels of surface detail. Surface details associated with weathering, such as etch pits, may not be observed by a specific measurement technique. Weathered and unweathered mineral grains will then give similar surface area estimates if all other parameters of size and shape are equal. Such estimates are referred to hereafter as geometric surface areas. Estimates from techniques that, partly or totally, account for surface details from weathering processes are referred to hereafter as actual surface areas.

Estimates of the geometric surface area (s) can be obtained, for instance, from size fractionation by sieving or settling, photon correlation spectroscopy (Cummins and Staples, 1987), small-angle neutron scattering (Hall *et al.*, 1985), and optical methods using (dissecting) microscopes, image analyzers and/or particle counters. From particle size and shape distribution parameters, s can be estimated by various geometric models. The specific geometric surface area (s^* ; $\text{cm}^2 \cdot \text{g}^{-1}$) may, for instance, be found from (Cartwright, 1962):

$$s^* = \frac{3}{2} \rho / (\rho d) \tag{2.2}$$

where \mathcal{V} is a geometry factor related to the average shape of the grains (\mathcal{V} equals 6 for ideal spheres if d is in cm), ρ is the density ($\text{g}\cdot\text{cm}^{-3}$), and d is the average grain diameter.

Techniques to estimate the actual surface area (S) include adsorption of organic molecules (Heilman *et al.*, 1965), infrared internal reflectance spectroscopy (Mulla *et al.*, 1985), scanning electron microscopy (SEM), and determination of the gas adsorption isotherm (BET method). The BET method is dealt with elsewhere (Brunauer *et al.*, 1938; Gregg and Sing, 1982), but a few remarks in the light of this study are in order.

The internal surface area from (micro)pores, both in naturally weathered and in ground feldspar samples may be far larger than is generally recognized (see hereafter). This may affect BET measurements in several ways, depending, for instance, on the range of pore diameters (Gregg and Sing, 1982).

The use of different adsorbate gases and associated analytical techniques may cause different results from BET measurements. For anhydrous cement samples, Vidick (1987) found very similar specific surface areas from N_2 , Ar and Kr measurements. For hydrated cement samples, the specific surface area from N_2 adsorption led to erroneous results and was four to five times higher than that from Ar or Kr. Chow and Grant (1988) analyzed a number of α -alumina standards and recrystallized griseofulvin samples. They found higher surface areas from N_2 than from Kr in the large specific area range ($> 5 \text{ m}^2\cdot\text{g}^{-1}$). In the small specific area range, Kr gave higher and more accurate results than N_2 . Because samples in mineral dissolution experiments generally have small specific surface areas (e.g. $< 1 \text{ m}^2\cdot\text{g}^{-1}$), Kr may thus give higher and more accurate surface area estimates than N_2 . Given the molecular structure of the three gases, Ar estimates should be more in accord with Kr estimates than with N_2 estimates (Gregg and Sing, 1982). Furthermore, for small specific surface areas, adsorbate gases with a relatively low vapour pressure, such as Kr, are preferred to minimize the dead space correction (IUPAC, 1985). Throughout the BET measurements performed in the context of this thesis Kr was used as the adsorbate gas.

2.2. Theoretical considerations

Ground size fractions from much larger, naturally weathered mineral fragments are normally assumed to consist only of freshly created surface area. Hereafter, a model will be derived to test the validity of this assumption. In the model, all surface area of unfractured naturally weathered fragments is by definition naturally weathered surface area. Furthermore, it is assumed that all surface area additionally created by grinding is surface area of freshly exposed mineral bulk, i.e. freshly created surface area. This is a reasonable assumption because all naturally weathered surface area is already exposed (to the measurement

technique) at the start of the grinding process.

The ratio of freshly created to measured (freshly created plus naturally weathered) actual surface area of a ground sample (F_f) is defined by:

$$F_f \equiv S_f/S_g \tag{2.3}$$

where S_f is the freshly created actual surface area of the ground sample, and S_g is the measured actual surface area of the ground sample. The ratio of freshly created to measured geometric surface area of a ground sample (f_f) is defined by:

$$f_f \equiv s_f/s_g \tag{2.4}$$

where s_f is the freshly created geometric surface area of the ground sample, and s_g is the measured geometric surface area of the ground sample. From eq. (2.1) we may now write:

$$\lambda_g = S_g/s_g \tag{2.5}$$

where λ_g is the surface roughness factor of the ground sample as a whole, and:

$$\lambda_f = S_f/s_f \tag{2.6}$$

where λ_f is the roughness factor of the freshly created surfaces in the sample. Because the ground sample contains only freshly created and naturally weathered surfaces, it follows that:

$$\lambda_w = (S_g - S_f)/(s_g - s_f) \tag{2.7}$$

where λ_w is the roughness factor of the naturally weathered surfaces in the sample, originating from the unfractured material. Eqs. (2.3), (2.5), (2.6) and (2.7) combine to:

$$F_f = [\lambda_f(\lambda_w - \lambda_g)]/[\lambda_g(\lambda_w - \lambda_f)] \tag{2.8}$$

From eqs. (2.3), (2.4), (2.5), (2.6) and (2.8) it follows that:

$$f_f = (\lambda_w - \lambda_g)/(\lambda_w - \lambda_f) \tag{2.9}$$

According to eqs. (2.8) and (2.9), the assumption that intensively ground samples contain only freshly created surface area can be tested for both the geometric and the actual

surfaces if λ_f , λ_w and λ_g are known. λ_w and λ_g can be obtained from actual and geometric surface area measurements on the unfractured and ground material, respectively. However, large unfractured fragments may not fit into experimental equipment. λ_f may be found from surface area measurements on identical sample material that has never been exposed to weathering conditions. However, this material may not be available. λ_w and λ_f may alternatively be estimated from values of λ_g , as will be shown hereafter. If the sample mass is constant during grinding, it follows that, at all grain diameters:

$$S_g - S_f = S_w \quad (2.10)$$

where S_w is the actual surface area of the unfractured fragments. Eqs. (2.1), (2.7) and (2.10) give:

$$s_g - s_f = s_w \quad (2.11)$$

where s_w is the geometric surface area of the unfractured fragments. Eqs. (2.1), (2.5), (2.6), (2.10) and (2.11) can be combined to:

$$\lambda_g = \lambda_f + (\lambda_w - \lambda_f) s_w / s_g \quad (2.12)$$

If the sample mass and the value of ϕ do not change during grinding, it follows from eq. (2.2) that:

$$s_w / s_g = d_g / d_w \quad (2.13)$$

where d_g is the average grain diameter of the ground sample, and d_w is the average diameter of the unfractured naturally weathered fragments. Eqs. (2.12) and (2.13) give:

$$\lambda_g = \lambda_f + (\lambda_w - \lambda_f) d_g / d_w \quad (2.14)$$

Thus, under the restrictions mentioned, a plot of λ_g versus d_g results in a straight line with slope $(\lambda_w - \lambda_f) / d_w$ and intercept λ_f . Estimates of λ_w and λ_f may then be found from data extrapolation.

As will be shown in the section hereafter, eq. (2.14) may not hold for ground sample material when sieving is applied. λ_g and d_g may then have a non-linear relationship (eq. 2.18) of the type shown in Fig. 2.1. The non-linearity manifests itself primarily at relatively small

grain diameters, so an alternative approach must be used to estimate λ_f . Upon grinding and sieving, λ_f equals the ratio of the total increase in actual surface area to the total increase in geometric surface area. Denoting individual ground size fractions by the subscript i , it follows that:

$$\lambda_f = (\sum_i S_{g,i} - S_w) / (\sum_i s_{g,i} - s_w) \tag{2.15}$$

under the condition that:

$$\sum_i g_{g,i} = g_w \tag{2.16}$$

In eq. (2.15), $S_{g,i}$ and $s_{g,i}$ are the actual and the geometric surface area, respectively, of a ground size fraction i . In eq. (2.16), $g_{g,i}$ is the sample mass of a ground size fraction i , and g_w is the sample mass of unfractured material.

The fact that non-linearity of λ_g versus d_g may be related to combined grinding and sieving can be seen from eq. (2.10). This assumes that naturally weathered surface area cannot be destroyed or created by grinding. If eq. (2.10) is correct, it will still hold for the total

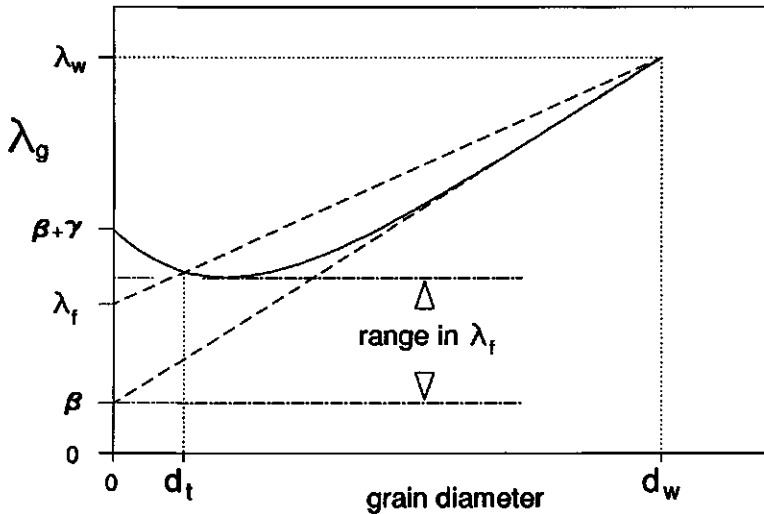


Fig. 2.1. Example of a non-linear relationship between the surface roughness factor (λ_g) and the grain diameter of ground material from large, naturally weathered mineral fragments (see eq. 2.18). The range of possible values of the roughness factor of freshly created surface area (λ_f) is indicated by arrows. The weight distribution of the ground material must be known to calculate the exact value of λ_f (eqs. 2.15 and 2.16).

mass of ground material only. Thus, when sieving is applied, eq. (2.10) must be rewritten to:

$$\sum_i (S_{g,i} - S_{f,i}) = S_w \quad (2.17)$$

where $S_{f,i}$ refers to the freshly created actual surface area of a ground size fraction i . Eq. (2.17) indicates that a linear relationship between λ_g and d_g exists only when eq. (2.10) holds for all individual size fractions after grinding and sieving. An empirical relation that describes λ_g as a function of d_g in non-linear cases is given by:

$$\lambda_g = \alpha d_g + \beta + \gamma(1 - d_g/d_w)^\delta \quad (2.18)$$

where (see Fig. 2.1) α and β are the slope and intercept of the tangent on λ_g as a function of d_g in (d_w, λ_w) , γ is a magnitude factor for the non-linear term at $d_g = 0$ μm , and δ is an exponent which is related to the range of approximate linearity of the plot at larger grain diameters. α , β , γ and δ may be estimated by rewriting eq. (2.18) to:

$$\log(\lambda_g - \lambda_g^\circ) = \log \gamma + \delta \log(1 - d_g/d_w) \quad (2.19)$$

$$\lambda_g^\circ = \alpha d_g + \beta \quad (2.20)$$

When sufficient data are available for values of d_g for which the non-linear term in eq. (2.18) is insignificant, α and β can be estimated by the linear approach according to eq. (2.20). For all other data, λ_g° can then be calculated and linear regression from eq. (2.19) leads to best estimates of γ and δ .

Non-linearity upon grinding and sieving can be explained from preferential fracturing of naturally weathered material relative to fresh mineral bulk. Differentiation into weathered outer layers and relatively fresh inner cores has been observed both in large rock fragments and in large individual crystals (e.g. Delvigne, 1965; Colman, 1986; Whitehouse *et al.*, 1986; A.G. Jongmans, pers. comm.). Under such conditions, preferential fracturing of weathered material creates a relatively large amount of small particles with higher values of λ_g than predicted from their diameter (eq. 2.14). Upon sieving, the finer size fractions will be relatively rich in particles with high values of λ , causing relative enrichment of the coarser size fractions with low- λ particles. Accordingly, non-linearity can be described by a concentration factor (Ω_g). For equal masses of ground and unfractured material, Ω_g is defined by:

$$\Omega_g = (S_g - S_f)/S_w \quad (2.21)$$

Because eq. (2.10) holds for the total mass of ground material, it follows from eqs. (2.10) and (2.21) that:

$$\left. \begin{array}{l} g_g = g_w \\ g_g = 0 \end{array} \right| \Omega_g d g_g = g_w \quad (2.22)$$

where g_g is the sample mass of ground material. For a number of i individual ground size fractions, eq. (2.22) transforms into:

$$\sum_i (\Omega_{g,i} g_{g,i}) = g_w \quad (2.23)$$

where $\Omega_{g,i}$ is the concentration factor of a ground size fraction i . From eqs. (2.1), (2.4), (2.5), (2.6), (2.9), (2.13) and (2.21) it follows that:

$$\Omega_g = [d_w (\lambda_g - \lambda_f)] / [d_g (\lambda_w - \lambda_f)] \quad (2.24)$$

which may be rewritten to solve for λ_g according to:

$$\lambda_g = \lambda_f + \Omega_g (\lambda_w - \lambda_f) d_g / d_w \quad (2.25)$$

Combination of Fig. 2.1 and eqs. (2.14) and (2.25) demonstrates the existence of the "transition" grain diameter (d_t) for which Ω_g equals unity again. At grain diameter d_t , enrichment of high- λ particles in finer size fractions and consequent enrichment of low- λ particles in coarser size fractions balances, and eqs. (2.10) and (2.14) apply. In the absence of exact relationships to determine the value of λ_f in non-linear cases, it follows from the existence of the "transition" grain diameter that the minimum value of λ_f is given by β , while the maximum value of λ_f is given by the minimum in the λ_g -curve, which follows from the fact that $\lambda_f \leq \lambda_g$ for all $d_g \geq 0 \mu\text{m}$.

2.3. Application to actual data

Holdren and Speyer (1987) report a comprehensive and internally consistent set of BET-argon surface area measurements. These were obtained for ground and sieved size fractions from much larger, naturally weathered fragments of nine different feldspars. The ground size fractions are: 0-37, 37-75, 75-150, 150-300, 300-600 and $> 600 \mu\text{m}$. The data

were analyzed by the model described before to test the hypotheses: (1) λ_g shows a linear relation with d_g as predicted by eq. (2.14); (2) values of λ_w are higher than values of λ_i ; and (3) intensively ground samples from large, naturally weathered feldspar fragments essentially contain only freshly created surface area. To simplify notations, subscripts i for individual size fractions are omitted hereafter.

From the specific BET surface areas (S_g^*), reported by Holdren and Speyer (1987), values of λ_g can be calculated once the specific geometric surface areas (s_g^*) are known. In the absence of measured data, eq. (2.2) was used to estimate s_g^* , assuming $\mathfrak{D} = 6$ and densities (g.cm^{-3}) of 2.55 for Keystone Microcline and Bancroft Microcline, 2.56 for Hybla Alkali Feldspar and Perth Perthite, 2.61 for Evje Albite, 2.65 for Mitchell Co. Oligoclase, 2.67 for Saranac Lake Andesine, 2.71 for Crystal Bay Bytownite and 2.76 for Grass Valley Anorthite. s_g^* was calculated for the two sieve openings used to collect each sample, assuming these to be limiting average grain diameters. 1200 μm was assumed to be the maximum average grain diameter for the coarsest size fraction. Plots of λ_g versus d_g for all feldspars by Holdren and Speyer (1987) are shown in Fig. 2.2.

For Bancroft Microcline, Hybla Alkali Feldspar and Grass Valley Anorthite (Figs. 2.2b, c and i), λ_g and d_g essentially show a linear relation as predicted by eq. (2.14). For the other feldspars, the relation appears to be non-linear at smaller grain diameters. For instance, for Keystone Microcline 37-75 μm and Perth Perthite 37-75 μm , the deviation from eq. (2.14) is more than 100 % (Figs. 2.2a and d). The question arises whether this non-linear effect is caused by uncertainties in λ_g . From eqs. (2.1) and (2.2), uncertainties in λ_g arise from uncertainties in S_g^* , \mathfrak{D} or d_g . For an internally consistent set of BET-krypton measurements, Casey *et al.* (1988a) found a precision in S_g^* of approximately 5 %, although the accuracy of the BET-krypton method is approximately 20 % (Gregg and Sing, 1982). Apart from two inaccurate estimates of S_g^* (Figs. 2.2h and i), the data by Holdren and Speyer (1987) indicate a precision of the same order of magnitude as found by Casey *et al.* (1988a). Thus, the non-linear effects in Fig. 2.2 cannot be explained from uncertainties in S_g^* . Furthermore, \mathfrak{D} is relatively independent of grain diameter for identical materials and methods of determination (Heywood, 1938; Cartwright, 1962). Experimental values of \mathfrak{D} ranged from 6.1 for rounded grains to 7.7 for angular grains (Fair and Hatch, 1933). This leaves inaccurate estimates of d_g as the most likely source of uncertainty. If γ is zero, the relation between λ_g and d_g is linear (eq. 2.18). A straight line, intersecting all diagonal line portions in Figs. 2.2a-i would then give more accurate estimates of d_g . However, resulting values of d_g in non-linear cases would indicate a systematic, almost total lack of grains in large portions of the distribution curve. This seems hardly possible if normal grinding procedures were followed. These findings strongly suggest that, alternatively, γ in eq. (2.18) is positive.

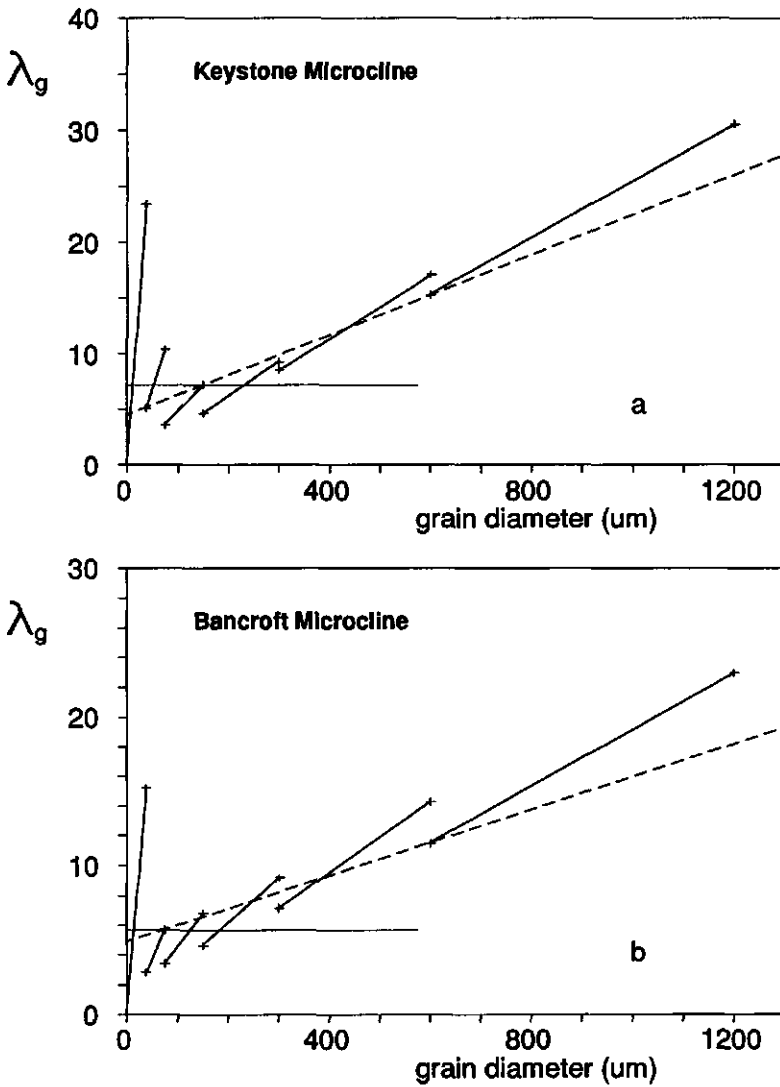


Fig. 2.2. Plots of the surface roughness factor (λ_g) versus the grain diameter for intensively ground size fractions of nine different naturally weathered feldspars. Data of specific BET-argon surface areas and sieve openings were taken from Holdren and Speyer (1987). The dotted lines for Crystal Bay Bytownite 300-600 μm (Fig. 2.2h) and Grass Valley Anorthite 600-1200 μm (Fig. 2.2i) indicate inaccurate BET surface area estimates. The specific BET surface area of Perth Perthite 150-300 μm (Fig. 2.2d), which was lost before analysis, was estimated at 500 $\text{cm}^2.\text{g}^{-1}$. Lines of minimal slope (see text) are dashed. Maximum values of the roughness factor of freshly created surfaces ($\lambda_{f\text{-max}}$) are indicated by the solid horizontal lines.

If the interpretation of surface roughness as presented here is correct, implying that $\lambda_r \leq \lambda_g \leq \lambda_w$, maximum values of λ_r follow from Fig. 2.2 without any further assumptions. These maxima are given by the minimum value of λ_g for any of the ground samples at maximum average grain diameter (horizontal lines in Fig. 2.2). If the 600-1200 μm size fractions would consist only of freshly created BET surface area, their roughness factors would obviously equal those of freshly created surfaces. However, minimum values of λ_g for all 600-1200 μm size fractions exceed maximum values of λ_r . These findings demonstrate

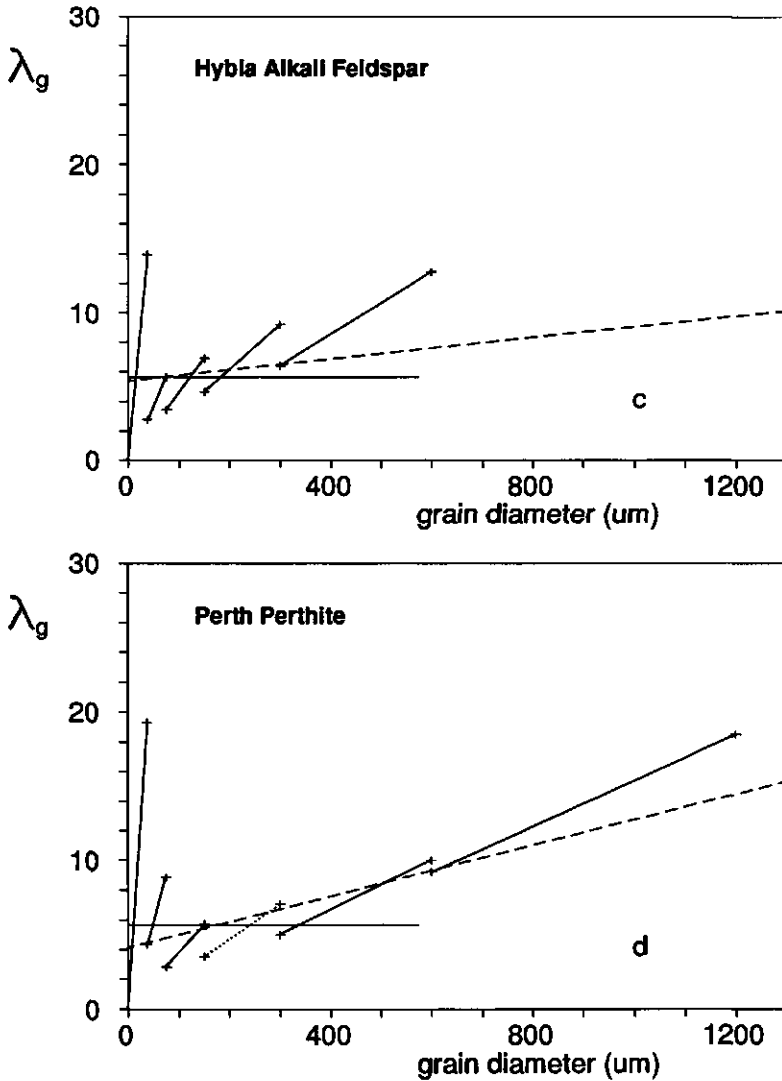


Fig. 2.2. Continued.

the presence of naturally weathered BET surface area in all 600-1200 μm fractions, regardless the validity of the model described earlier. Except for Perth Perthite (and possibly Crystal Bay Bytownite), this conclusion is valid too for the 300-600 μm size fractions.

λ_f may be estimated assuming γ to be either zero or positive. If γ is zero, straight lines intersect all λ_g ranges. Lines of minimal slope, giving lowest estimates of λ_w and highest estimates of λ_f (Table 2.1) are shown in Fig. 2.2 for all feldspars. The average diameter of the unfractured fragments was assumed to be 1 cm in all cases (Holdren and Speyer, 1987).

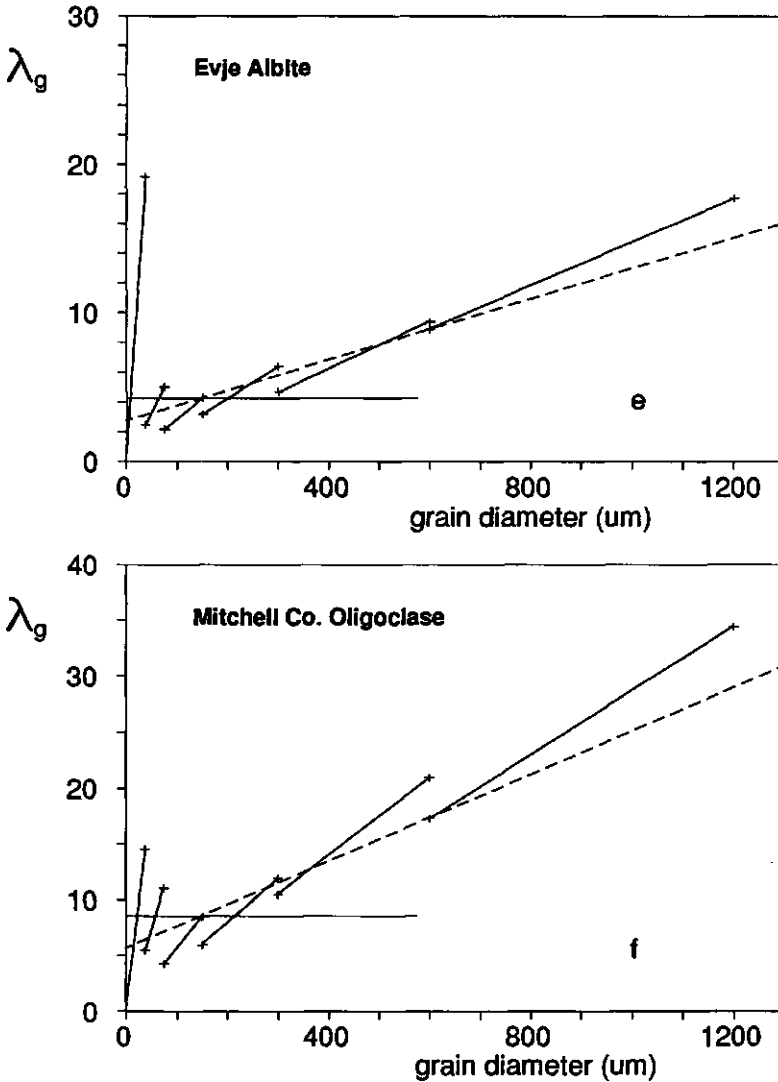


Fig. 2.2. Continued.

Alternatively, if γ is positive, λ_w may be estimated if α and β are known (see Fig. 2.1). α and β were calculated from data for the size fractions $> 150 \mu\text{m}$. For these fractions, if grinding has resulted in equal sample masses at all grain diameters between the two sieve openings, it follows from integration that:

$$d_g = [2d_p^2 d_q^2 / (d_p + d_q)]^{1/3} \quad (2.26)$$

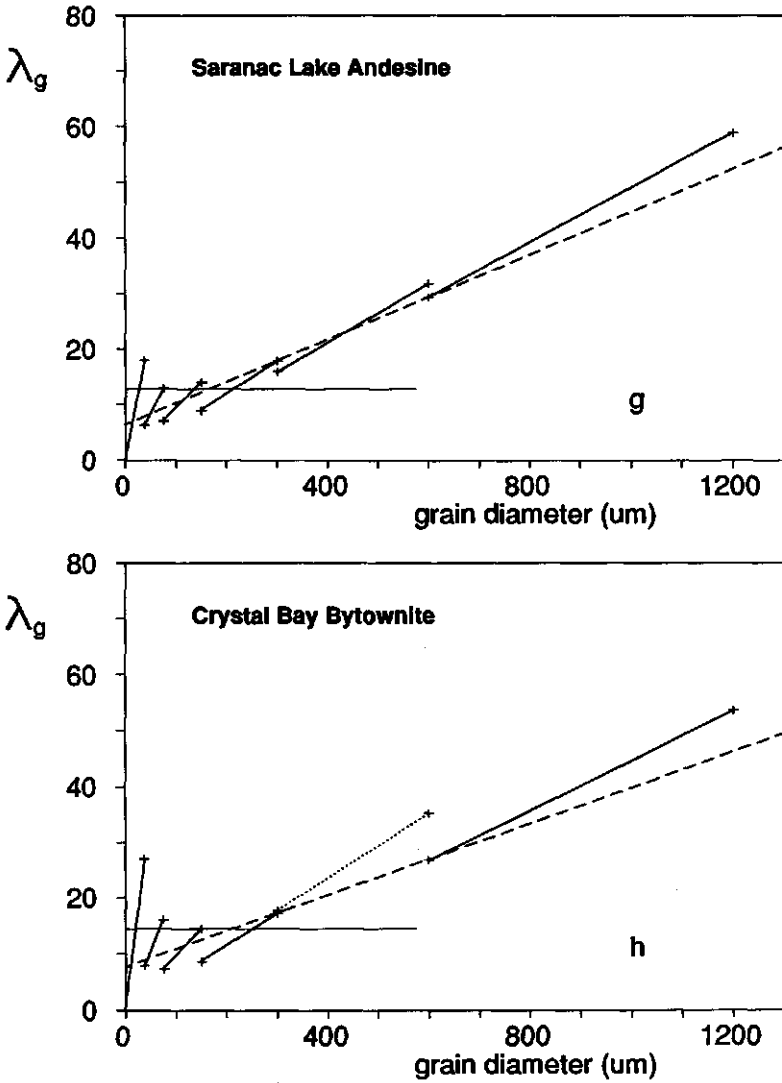


Fig. 2.2. Continued.

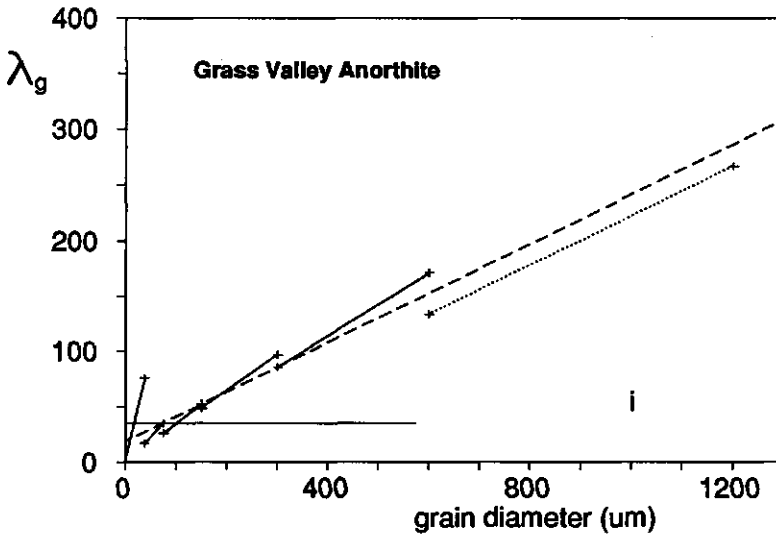


Fig. 2.2. Continued.

where d_p and d_q are the sieve openings. Unlike the frequently used average of d_p and d_q to estimate d_g , eq. (2.26) accounts - to some extent - for skewing towards smaller grain diameters in poorly defined size fractions. Estimates of α and β , and resulting estimates of λ_w , are given in Table 2.1. Because data on grain diameter and sample mass are absent, λ_f at positive values of γ could not be calculated. As discussed earlier, λ_f in non-linear cases is larger than β and smaller than the minimum value of λ_g . The actual average grain diameter of these samples is most likely smaller than the larger sieve opening and may, for instance, be given by eq. (2.26). This restricts the range of possible values of λ_f at the high side, and therefore $(2\beta + \lambda_f - \max.) / 3$ is assumed to be the best estimate of λ_f if $\gamma > 0$. Best estimates of λ_f (Table 2.1) suggest that roughness factors of freshly created alkali-feldspar surfaces are fairly constant, while those of plagioclase are related to the chemical composition. If so, in cases where eq. (2.14) applies, λ_g and F_f can simply be estimated from λ_w if the average grain diameters in the ground and unfractured samples are known.

For all feldspars by Holdren and Speyer (1987), $\lambda_w \gg \lambda_f$ and $\lambda_w \gg \lambda_g$. This simplifies eqs. (2.8) and (2.9) to:

$$F_f \approx \lambda_f / \lambda_g, \text{ and: } f_f = 1 \quad (2.27)$$

Thus, the assumption that these ground size fractions consist only of freshly created surface area is essentially true for the geometric surfaces. However, estimates of F_f from the data

Table 2.1. Estimates of λ_w , λ_f and λ_w/λ_f for samples by Holdren and Speyer (1987) using the minimal slope approximation ($\gamma = 0$), and estimates of α , β , λ_w , λ_f -max., λ_f and λ_w/λ_f for the same samples when allowing for high- λ particle enrichment ($\gamma > 0$).

Mineral component	minimal slope			α	high- λ particle enrichment				
	λ_w	λ_f	λ_w/λ_f		β	λ_w	λ_f -max.	λ_f^1	λ_w/λ_f
Keystone Microcline	184	4.5	41	0.0235	1.8	237	7.3	3.6	66
Bancroft Microcline	115	4.9	23	0.0154	3.2	157	5.7	3.2	49
Hybla Alkali Feldspar	40 ²	5.4	7 ²	0.0136	3.3	139	5.6	3.3	42
Perth Perthite	90	4.1	22	0.0135	1.5	137	5.7	2.9	47
Evje Albite	104	2.8	37	0.0128	1.6	130	4.3	2.5	52
Mitchell Co. Oligoclase	200	5.6	36	0.0247	3.6	251	8.5	5.2	48
Saranac Lake Andesine	388	6.5	60	0.0453	3.1	456	12.9	6.3	72
Crystal Bay Bytownite	328	7.6	43	0.0405	3.5	408	14.5	7.1	57
Grass Valley Anorthite	2250	18.4	122	0.2607	10.6	2618	35.2	10.6	247

¹ estimated as $(2\beta + \lambda_f\text{-max.})/3$ in cases of non-linear behaviour.

² values should not be compared to other estimates of λ_w and λ_w/λ_f , because the size fraction 600-1200 μm could not be taken into account.

Table 2.2. Estimates of F_f for the ground size fractions by Holdren and Speyer (1987) between 37 and 1200 μm .

Mineral component	37-75	75-150	150-300	300-600	600-1200
Keystone Microcline	0.49	0.71	0.55	0.29	0.16
Bancroft Microcline	0.81	0.67	0.49	0.31	0.18
Hybla Alkali Feldspar	0.86	0.69	0.51	0.36	
Perth Perthite	0.47	0.73	0.65	0.41	0.21
Evje Albite	0.71	0.83	0.55	0.37	0.19
Mitchell Co. Oligoclase	0.68	0.88	0.62	0.34	0.20
Saranac Lake Andesine	0.71	0.65	0.50	0.28	0.14
Crystal Bay Bytownite	0.64	0.70	0.59	0.28	0.18
Grass Valley Anorthite	0.44	0.29	0.16	0.09	0.05

in Table 2.1 and Fig. 2.2 vary over almost the complete range from 0 to 1. Because data on grain diameter are absent, exact values of F_f could not be calculated. Estimates of F_f using eq. (2.26) for the samples $> 37 \mu\text{m}$ (Table 2.2) show that in most cases, and even for the finest size fractions considered, grinding was highly ineffective in creating samples with fresh BET surface area only. These findings indicate that earlier dissolution studies assuming all BET surface area to be freshly created may need reinterpretation.

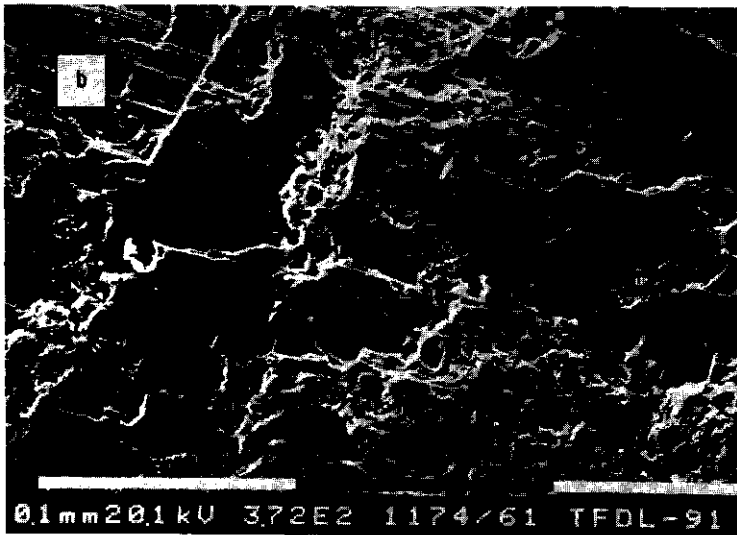


Fig. 2.3. SEM images of two feldspars by Holdren and Speyer (1987). a: freshly created (left) and naturally weathered surfaces of Crystal Bay Bytownite; b: naturally weathered surface of Grass Valley Anorthite. λ_w from SEM analysis is approximately 2 in both cases.

Scanning electron microscopy has revealed the presence of etch pits on surfaces of both naturally and artificially weathered feldspars (e.g. Tchoubar, 1965; Lundström, 1974; Berner and Holdren, 1979; Robert *et al.*, 1980; Hochella *et al.*, 1987). Analysis of SEM

images indicates that the maximum value of λ_w , resulting from etch pitting, is approximately 10 to 30 (Helgeson *et al.*, 1984). λ_w from SEM analysis is approximately 2 (Fig. 2.3) for the Crystal Bay Bytownite and the Grass Valley Anorthite by Holdren and Speyer (1987). These estimates are two to three orders of magnitude lower than those from BET analysis (Table 2.1), and include effects from etch pitting. The most likely source of naturally weathered BET surface area that may explain this discrepancy is internal surface area from porosity. Macropores (diameters > 50 nm; Gregg and Sing, 1982) have been observed in naturally weathered feldspar grains (e.g. Brace *et al.*, 1972; Montgomery and Brace, 1975; Ferry, 1985; Guthrie and Veblen, 1988; Worden *et al.*, 1990; Walker, 1990). The macropores may result from the formation of fluid inclusions during the initial cooling of the pluton, followed by leakage and weathering under earth surface conditions (Parsons *et al.*, 1988). Micropores and mesopores (diameters \leq 50 nm; Gregg and Sing, 1982) have been observed in various silicates after dissolution experiments (e.g. Pacco *et al.*, 1976; Chon *et al.*, 1978; Levine and Garofalini, 1987; Bunker *et al.*, 1988; Casey *et al.*, 1989b; Zhang *et al.*, 1993). These may form, for instance, at crystal defects (Bennema and Van Enkevort, 1979; Van Der Hoek *et al.*, 1982; Lasaga and Blum, 1986), or during the formation of leached layers (Doremus, 1983; Casey and Bunker, 1990). These findings indicate that, during the natural weathering of feldspar, the mineral surface area enlargement from pore formation is far more important than that from etch pitting (see also Appendix 1 for pore formation during the natural weathering of hornblende).

2.4. Conclusions

Laboratory dissolution studies commonly involve the use of ground samples, derived from much larger, naturally weathered mineral fragments. In this chapter, a model has been developed that relates the surface roughness factor of such samples to the grain diameter. The model can be used to: (1) estimate the roughness factors of the freshly created and naturally weathered surfaces in the ground samples; (2) estimate the ratio of freshly created to measured surface area for the ground samples, both for the geometric and for the BET surfaces; and (3) test the internal consistency of surface area estimates. Literature data for intensively ground samples from nine different, naturally weathered feldspars were evaluated. Roughness factors of the freshly created surfaces ranged from 2.5 to 11. Roughness factors of the naturally weathered surfaces ranged from 130 to 2600, which is much higher than is generally recognized for feldspar. Additional SEM observations strongly suggest that virtually all BET surface area, created during natural weathering, is present as internal surface structures such as micropores. Due to the large amount of naturally weathered internal

surface area, grinding is highly ineffective in creating large proportions of fresh BET surface area. In these samples, the ratio of freshly created BET to measured BET surface area varied over almost the entire range from 0 to 1, depending on the grain diameter after grinding and on the specific feldspar type. These findings may affect the interpretation of dissolution data from ground samples in several ways, for instance, if the freshly created and naturally weathered surfaces have different dissolution rates. Thus, earlier dissolution studies assuming all BET surface area of ground samples to be freshly created may need reinterpretation. Reinterpretation of dissolution data obtained for the nine feldspars discussed here is dealt with in the next chapter.

Acknowledgements

I am especially indebted to Edward Meijer, Nico van Breemen and Leendert van der Plas of the Department of Soil Science and Geology, Agricultural University of Wageningen, The Netherlands, for their creative ideas and critical comments during this research. I gratefully acknowledge the help of Bram Boekestein for the use of SEM facilities at the TFDL, Wageningen. G.R. Holdren, Jr., kindly supplied samples of Crystal Bay Bytownite and Grass Valley Anorthite. The thoughtful and thorough review by M.F. Hochella, Jr., greatly improved the quality of the original manuscript.

This chapter was published in *Geochimica et Cosmochimica Acta*, vol. 56, pp. 1461-1469. Editorial handling for *Geochimica et Cosmochimica Acta*: T. Pačes.

Final remarks

The theoretical considerations and the extrapolated values of λ_w from this chapter, presented in 1992 in *Geochimica et Cosmochimica Acta*, were recently put to the test (see A.E. Blum, in press). For eight 2 mm sized, strongly weathered (age 500-1000 Kyr), unfractured oligoclase and alkali feldspar samples, BET and geometric surface area measurements gave λ_w that varied between 83 and 1029 (A.E. Blum, in press). These findings confirm that "freshly ground" mineral samples as frequently used in dissolution experiments may still contain large proportions of naturally weathered, internal BET surface area.

The dissolution of ground feldspar samples in the laboratory

Chapter 3. The effect of grain diameter after grinding

Abstract

Ground samples from naturally weathered mineral fragments can still contain substantial proportions of weathered surface area. If the freshly created and naturally weathered surfaces in such samples have different dissolution rates, experimental dissolution data must be interpreted by a kinetic model in terms of both types of surface area. Such a kinetic model is presented. The model was used to reexamine literature data for ground size fractions from nine different naturally weathered feldspars. Ratios of dissolution reactive BET to measured (dissolution reactive plus non-reactive) BET surface area were analyzed as a function of the grain diameter, both for the freshly created and the naturally weathered surfaces in the samples. For the naturally weathered surfaces, the ratio of reactive BET to measured BET surface area was most likely independent of the grain diameter. If so, grinding does not destroy or create naturally weathered reactive surface area (relative to naturally weathered surface area). For the freshly created surfaces, the ratio of reactive BET to measured BET surface area was approximately proportional to the grain diameter. Thus, grinding destroys freshly created reactive surface area (relative to freshly created surface area). Additional dissolution experiments on feldspar samples, essentially containing only freshly created surface area, have confirmed this finding.

In the literature, ground samples from large, naturally weathered mineral fragments are frequently implied to contain only freshly created BET surface area. Experimental dissolution data can then be explained if the dissolution rate, normalized to freshly created BET surface area, is essentially independent of the grain diameter after grinding. In fact, however, two (partly) counteracting processes appear to be active during grinding. These are: (1) increase of the proportion of measured BET surface area which is freshly created; and (2) decrease of the proportion of freshly created BET surface area which is dissolution reactive. These observations demonstrate that rate "constants" and dissolution rates, normalized to the freshly created BET surface area, are valid at one grain diameter only. Tentative calculations suggest that, for fresh-surface feldspar grains, either the dissolution rate of the reactive sites or the density of the reactive sites is approximately two orders of magnitude higher than for equally sized naturally weathered grains.

3.1. Introduction

The mechanism and kinetics of mineral dissolution have been long and intensively studied, both in the laboratory and in the field (e.g. Correns and Von Engelhart, 1938; Arrhenius, 1954; Garrels and Mackenzie, 1967; Bricker *et al.*, 1968; Petrovich *et al.*, 1976; Holdren and Berner, 1979; Wollast and Chou, 1985; Schott and Berner, 1985; Cronan, 1985; Ovalle, 1987; Casey *et al.*, 1988a,b, 1991; Amrhein and Suarez, 1992). Laboratory data are usually evaluated as dissolution rates, normalized to the mineral surface area (e.g. $\text{mol.cm}^{-2}.\text{s}^{-1}$). Therefore, the specific surface areas of the investigated samples are frequently reported. Specific surface areas can be estimated from various techniques.

Some techniques account only for the overall size and shape of the mineral grains (geometric surface area), while others partly or totally account for existing surface details (actual surface area). The geometric surface area may, for instance, be estimated by assuming a sample to consist of spherical grains of average diameter (e.g. Lagache, 1965; Helgeson *et al.*, 1984; Knauss and Wolery, 1986), or from observations on the size and geometry of individual grains (e.g. Evans, 1965; Fler, 1982). The actual surface area may, for instance, be estimated from the gas adsorption isotherm (BET method; Brunauer *et al.*, 1938; Gregg and Sing, 1982). BET measurements normally involve nitrogen, argon or krypton as the adsorbate gas, with or without prior removal of adhering ultrafines from grinding procedures (e.g. Busenberg and Clemency, 1976; Chou and Wollast, 1984; Holdren and Speyer, 1985, 1987; Knauss and Wolery, 1986; Sverdrup and Warfvinge, 1988; Casey *et al.*, 1988a; White and Peterson, 1990). This wide variety of measurement techniques and sample pretreatments makes it difficult to assess the interchangeability of surface area estimates in kinetic dissolution models. Furthermore, surface area estimates frequently cover a range of grain diameters, both within and between individual samples. In this chapter, we will first examine some of the problems that may arise when dissolution rates are normalized to mineral surface area. Next, dissolution rates of ground feldspar samples in the laboratory are discussed in relation to their dependence on the grain diameter after grinding.

Several workers concluded that actual surface areas are larger than geometric surface areas (Leamson *et al.*, 1969; Mandelbrot, 1983; Helgeson *et al.*, 1984; Siegel and Pfannkuch, 1984; Knauss and Wolery, 1986). The first systematic attempt to correlate actual and geometric surface area over a wide range of mineral types, grain diameters and measurement techniques was conducted by White and Peterson (1990). From literature data, these authors calculated a surface roughness factor (λ), defined by (Jaycock and Parfitt, 1981):

$$\lambda \equiv S/s \tag{3.1}$$

where S is the actual surface area (cm^2) and s is the geometric surface area (cm^2), which is the area of a hypothetical smooth surface enveloping the actual surface. From about 40 studies on both natural and synthetic mineral specimens, White and Peterson (1990) found the mean value of λ to be approximately 7, regardless of grain diameter. λ ranged from 1.08 for mica (Nonaka, 1984) to 540 for biogenic carbonate sediments (Walter and Morse, 1984). Using the BET-nitrogen method, White and Peterson (1990) found λ of four naturally weathered mineral assemblages that varied between approximately 20 and 200. These relatively high values primarily resulted from the iron hydroxides and mafic minerals in the

samples (White and Peterson, 1990). BET-argon measurements for ground size fractions from nine different, naturally weathered feldspars by Holdren and Speyer (1987) give extrapolated λ of the unfractured, naturally weathered fragments that vary between 130 and 2600 (chapter 2). These values are much higher than is generally recognized for feldspar.

Clearly, at $\lambda > 1$, dissolution rates normalized to the mineral surface area vary with the measurement technique. Values of $\lambda > 1$ may also affect interpretation of results from other techniques such as Auger electron spectroscopy and X-Ray photoelectron spectroscopy (Holloway, 1978; DeBernardez *et al.*, 1984; Wehbi and Roques-Carnes, 1985).

A second complication in normalizing dissolution rates to surface area arises when naturally weathered mineral fragments are used as starting material. Normally, such fragments are intensively ground to obtain samples dominated by freshly created surface area (e.g. Luce *et al.*, 1972; Berner, 1976; Plummer and Wigley, 1976; Grandstaff, 1977; Schott *et al.*, 1981; Chou and Wollast, 1984; Knauss and Wolery, 1986; McKibben and Barnes, 1986; Casey *et al.*, 1988a). However, for nine different feldspars by Holdren and Speyer (1987), grinding was highly ineffective in creating samples with fresh BET surface area only (chapter 2). Depending on the surface morphology of the starting fragments, this may also apply for minerals other than feldspar (chapter 2; see also Appendix 1 for hornblende).

The fraction of the BET surface area of a ground sample occupied by freshly created BET surface area (F_f) is defined by:

$$F_f \equiv S_f/S_g \quad (3.2)$$

where S_f is the freshly created BET surface area by grinding (cm^2), and S_g is the BET surface area of the sample as a whole (cm^2). F_f is found from (chapter 2):

$$F_f = [\lambda_f(\lambda_w - \lambda_g)]/[\lambda_g(\lambda_w - \lambda_f)] \quad (3.3)$$

where λ_f is the roughness factor of the freshly created surfaces in the ground sample, λ_w is the roughness factor of the naturally weathered surfaces in the ground sample, and λ_g is the surface roughness factor of the ground sample as a whole. For intensively ground feldspar samples, it was shown in chapter 2 that $\lambda_w \gg \lambda_f$ and $\lambda_w \gg \lambda_g$. This simplifies eq. (3.3) to:

$$F_f \approx \lambda_f/\lambda_g \quad (3.4)$$

In eq. (3.4), inaccuracies in λ_w from extrapolation have no effect on estimates of F_1 . For instance, Knauss and Wolery (1986) report λ_g of their Evje (Norway) Albite samples, obtained from naturally weathered fragments, to be 3.5 to 4.0. In chapter 2, λ_f of Evje Albite was estimated to be 2.5. λ_g and λ_f may be inaccurate, and λ_f from the albite specimen and sample pretreatment by Holdren and Speyer (1987) may differ from that for the specimen and pretreatment by Knauss and Wolery (1986). However, the data indicate that the samples by Knauss and Wolery contained approximately 30 to 40 % of naturally weathered BET surface area. Likewise, the Amelia Albite samples by Chou and Wollast (1984) may have contained some 20 % of naturally weathered BET surface area in runs 1 and 3. Proportions of naturally weathered BET surface area in ground feldspar samples $> 37 \mu\text{m}$ by Holdren and Speyer (1987) ranged from approximately 10 to 95 %, depending on grain diameter and feldspar type (chapter 2). Proportions of naturally weathered BET surface area in ground hornblende samples by Zhang *et al.* (1993) ranged from approximately 40 to 85 %, depending on grain diameter (Appendix 1). If the naturally weathered and freshly created surfaces in such samples have different dissolution rates, the experimental rates hold for the "average" surface morphology, rather than for freshly created surfaces. In such cases, dissolution data should be explained from freshly created and naturally weathered surface area in one sample.

A third complication in normalizing dissolution rates to surface area is due to the fact that the relation between measured (geometric or BET) surface area and dissolution reactive (geometric or BET) surface area is not yet clear. Helgeson *et al.* (1984) defined the reactive geometric surface area as the number of dissolution reactive sites, multiplied by their mean geometric surface area. They estimated the ratio of reactive to measured geometric surface area to be approximately 0.01 for the $100 \mu\text{m}$ Amelia Albite grains used by Holdren and Berner (1979). The estimate was obtained by assuming all geometric surface area of ultrafines from grinding to be reactive. At equal λ of ultrafines and $100 \mu\text{m}$ grains (to convert geometric surface area to BET surface area), this would indicate that dissolution rates normalized to reactive BET surface area are approximately two orders of magnitude higher than those normalized to measured BET surface area. For intensively ground samples from nine different naturally weathered feldspars, Holdren and Speyer (1985, 1987) tested the hypothesis that experimental dissolution rates normalized to BET-argon surface area are independent of the grain diameter after grinding. They found this to be approximately true at grain diameters $> 75 \mu\text{m}$. This would indicate that ratios of reactive to measured BET-argon surface area are essentially constant with grain diameter above $75 \mu\text{m}$. As discussed earlier, their results may have been influenced, however, by the presence of varying proportions of freshly created and naturally weathered surface areas, dissolving at different rates. This hypothesis will be examined in greater detail in the sections hereafter.

3.2. Model description

Hereafter, a model is derived to analyse experimental dissolution data in terms of freshly created and naturally weathered, and in terms of reactive and non-reactive BET surface areas. In the model, all surface area of unfractured naturally weathered mineral fragments is by definition naturally weathered surface area. Furthermore, it is assumed that all surface area additionally created by grinding is surface area of freshly exposed mineral bulk, i.e. freshly created surface area. This is a reasonable assumption because all naturally weathered surface area is already exposed (to the measurement technique) at the start of the grinding process.

To discriminate between the different types of surface area, first consider the apparent dissolution rate (R), which is defined by (Helgeson *et al.*, 1984):

$$R \equiv - (1/S)(dn/dt) \quad (3.5)$$

where R is in mol.cm^{-2} of (measured) BET surface. s^{-1} , S is the BET surface area in cm^2 , n is the number of moles, and t is time in seconds. The ratio dn/dt for a ground sample as a whole, $(dn/dt)_g$, is found by summation of the respective ratios dn/dt for the fresh and weathered surfaces in the sample. Thus, according to eq. (3.5):

$$- (dn/dt)_g = S_g R_g = S_f R_f + (S_g - S_f) R_w \quad (3.6)$$

where R_g is the apparent dissolution rate of the ground sample as a whole, and R_f and R_w are the apparent dissolution rates of the fresh and weathered surfaces, respectively. Combination of eqs. (3.2) and (3.6) gives:

$$R_g = (R_f - R_w) F_f + R_w \quad (3.7)$$

In the literature, R_f and R_w are frequently implied to be independent of the grain diameter. However, it will be shown hereafter (Fig. 3.1) that application of eq. (3.7) to experimental data strongly suggests that for feldspars, either R_f or R_w or both vary with the grain diameter instead.

Variations in the apparent dissolution rates R_f and R_w with grain diameter may arise from variations in (Aagaard and Helgeson, 1982; Helgeson *et al.*, 1984; Holdren and Speyer, 1985, 1987): (1) the density of dissolution reactive sites (cm^{-2} of BET surface); (2) the mean BET surface area per reactive site; and/or (3) the mean effective dissolution rate of the

reactive sites. The effective dissolution rate (\bar{R}) is defined by (Aagaard and Helgeson, 1982):

$$\bar{R} \equiv - (1/\bar{S}) (dn/dt) \quad (3.8)$$

where \bar{R} is in mol.cm^{-2} of reactive BET surface. s^{-1} , and \bar{S} is the reactive BET surface area in cm^2 . The product of reactive site density and mean reactive BET surface area per site equals the fraction of the BET surface area that is occupied by reactive BET surface area. For the fresh surfaces, the product (P_f) is given by:

$$P_f = \bar{S}_f/S_f \quad (3.9)$$

where \bar{S}_f is the fresh reactive BET surface area in the ground sample. The product of reactive site density and mean reactive BET surface area per site for the weathered surfaces (P_w) is given by:

$$P_w = (\bar{S}_g - \bar{S}_f)/(S_g - S_f) \quad (3.10)$$

where \bar{S}_g is the reactive BET surface area of the ground sample as a whole. It follows from eqs. (3.5), (3.8) and (3.9) that the apparent dissolution rate of the fresh surfaces is given by:

$$R_f = P_f \bar{R}_f \quad (3.11)$$

where \bar{R}_f is the effective dissolution rate of the fresh surfaces. From eqs. (3.5), (3.8) and (3.10), the apparent dissolution rate of the weathered surfaces is given by:

$$R_w = P_w \bar{R}_w \quad (3.12)$$

where \bar{R}_w is the effective dissolution rate of the weathered surfaces. Combination of eqs. (3.7), (3.11) and (3.12) gives:

$$R_g = F_f P_f \bar{R}_f + (1 - F_f) P_w \bar{R}_w \quad (3.13)$$

Unfortunately, at the present state of knowledge there is no possibility to discriminate between fresh reactive BET and weathered reactive BET surface area. Thus, in ground samples containing both fresh and weathered surfaces, P_f and P_w cannot be determined separately as functions of the grain diameter. Additional information is obtained, however, from the effective dissolution rates \bar{R}_f and \bar{R}_w . The fraction of the reactive BET surface area

of a ground sample that is occupied by fresh reactive BET surface area (\bar{F}_f) is given by:

$$\bar{F}_f = \bar{S}_f / \bar{S}_g \quad (3.14)$$

Because the ratio dn/dt for the ground sample as a whole is again found from summation of the ratios dn/dt for the fresh and weathered surfaces, it follows from eqs. (3.8) and (3.14) that, in analogy to eq. (3.7):

$$\bar{R}_g = (\bar{R}_f - \bar{R}_w) \bar{F}_f + \bar{R}_w \quad (3.15)$$

where \bar{R}_g is the effective dissolution rate of the ground sample as a whole. Unlike the apparent dissolution rates R_f and R_w , the effective dissolution rates \bar{R}_f and \bar{R}_w are independent of the density and the mean reactive surface area of dissolution sites. Hereafter, it is assumed that \bar{R}_f and \bar{R}_w are independent of the grain diameter. This is a reasonable assumption if the dissolution reaction takes place far from equilibrium (Lasaga, 1981a; Aagaard and Helgeson, 1982; Helgeson *et al.*, 1984). From eqs. (3.11) and (3.12), the assumption is critical only for the origin, but not for the magnitude, of variations in R_f and R_w with grain diameter. According to eqs. (3.5) and (3.8):

$$\bar{R}_g = R_g S_g / \bar{S}_g \quad (3.16)$$

so eqs. (3.2), (3.9), (3.10) and (3.16) can be combined to:

$$\bar{R}_g = R_g / [F_f P_f + (1 - F_f) P_w] \quad (3.17)$$

and eqs. (3.2), (3.9), (3.10) and (3.14) to:

$$\bar{F}_f = F_f P_f / [F_f P_f + (1 - F_f) P_w] \quad (3.18)$$

Because the magnitude of variations in R_f and R_w with grain diameter may be analyzed by assuming \bar{R}_f and \bar{R}_w to be independent of the grain diameter, eq. (3.15) should result in a straight line if \bar{R}_g is plotted versus \bar{F}_f . Thus, if hypothetical R_f and R_w do not explain experimental data from eq. (3.7), linearity according to eq. (3.15) can be used to determine possible alternatives for P_f and P_w as functions of grain diameter. These can be tested in experiments on samples containing only fresh or weathered BET surface area (see hereafter).

3.3. Materials and methods

Data from the literature

Holdren and Speyer (1985, 1987) report a comprehensive set of specific BET-argon surface areas (S_g^* ; $\text{cm}^2.\text{g}^{-1}$) and apparent dissolution rates (R_g) for ground size fractions of nine different feldspars. The size fractions are: 0-37, 37-75, 75-150, 150-300, 300-600 and $> 600 \mu\text{m}$. In chapter 2, the proportion of fresh BET surface area (F_f) was estimated for all samples $> 37 \mu\text{m}$ (see Table 2.2). Once values of F_f are known for the 0-37 μm fractions, all data (F_f, R_g) can be interpreted by the model described in the previous section to test the hypothesis advanced by Holdren and Speyer (1985, 1987) that apparent dissolution rates of freshly created surfaces, normalized to BET area, are essentially independent of the grain diameter above 75 μm .

Estimates of λ_f and λ_w (Table 3.1; see also chapter 2) give estimates of F_f for the samples 0-37 μm once their values of λ_g are known (eq. 3.3). For these samples, λ_g may be estimated from (chapter 2):

$$\lambda_g = \alpha d_g + \beta + \gamma(1 - d_g/d_w)^\delta \quad (3.19)$$

where α, β, γ and δ are independent of the grain diameter, d_g is the average grain diameter of the ground sample, and d_w is the average grain diameter of the weathered starting

Table 3.1. $\lambda_f, \lambda_w, \alpha, \beta, \gamma$ and δ for the feldspar samples by Holdren and Speyer (1985, 1987), and F_f for the size fractions 0-37 μm (see Table 2.2 for F_f of the size fractions $> 37 \mu\text{m}$).

	λ_f	λ_w	α	β	γ	δ	$F_f(0-37)$
Keystone Microcline	3.6	237	0.0235	1.8	23	325	0.25
Bancroft Microcline	3.2	157	0.0154	3.2	0	1	0.92
Hybla Alkali Feldspar	3.3	139	0.0136	3.3	0	1	0.93
Perth Perthite	2.9	137	0.0135	1.5	15	250	0.26
Evje Albite	2.5	130	0.0128	1.6	7.5	325	0.44
Mitchell Co. Oligoclase	5.2	251	0.0247	3.6	26	400	0.33
Saranac Lake Andesine	6.3	456	0.0453	3.1	6	105	0.70
Crystal Bay Bytownite	7.1	408	0.0405	3.5	12	150	0.52
Grass Valley Anorthite	10.6	2618	0.2607	10.6	0	1	0.76

material. A detailed discussion of eq. (3.19) is given in chapter 2, and only two aspects are repeated here: (1) if $\gamma = 0$, the relation is linear and $\beta = \lambda_f$; in such cases, all BET area at grain diameter zero is freshly created by grinding (eq. 3.3); and (2) inaccuracies in d_w have little effect on λ_g at small grain diameters if α , β , γ and δ are estimated from experimental data for ground samples. Here, d_w is approximately 1 cm in all cases (Holdren and Speyer, 1985, 1987). α , β , γ and δ (Table 3.1) were calculated from linear regression (chapter 2) for all nine feldspars using data for the samples $> 37 \mu\text{m}$. Resulting estimates of F_f at 0 and $37 \mu\text{m}$ were averaged to estimate F_f for the size fractions $0\text{-}37 \mu\text{m}$ (Table 3.1). These should be accurate within 0.1 units of F_f .

For an internally consistent set of BET-krypton measurements, Casey *et al.* (1988a) found a precision in the specific BET area (S_g^*) of approximately 5 %, although the accuracy of the BET-krypton method is approximately 20 % (Gregg and Sing, 1982). Apart from two inaccurate estimates of S_g^* , the data by Holdren and Speyer (1987) indicate the same order of precision of approximately 5 % (chapter 2). Beside the two inaccurate estimates of S_g^* (Crystal Bay Bytownite $300\text{-}600 \mu\text{m}$ and Grass Valley Anorthite $> 600 \mu\text{m}$), Holdren and Speyer (1987) slightly overestimated S_g^* for Perth Perthite $150\text{-}300 \mu\text{m}$, which was lost before BET analysis. From chapter 2, values of S_g^* for these three samples of 1080, 5960 and $500 \text{cm}^2\cdot\text{g}^{-1}$, respectively, are internally consistent with the other BET measurements. These were used to recalculate the apparent dissolution rates R_g from data by Holdren and Speyer (1987).

Additional experiments

To determine P_f as a function of grain diameter in samples with fresh BET surface area only, dissolution experiments were performed on adularia and labradorite specimens from Vals (Switzerland) and from Ylijärvi (Finland), respectively. No particular care was taken to create fresh surfaces which are fully comparable to those by Holdren and Speyer (1987).

By careful wet-sawing, fracturing and handpicking, "fresh" inner core material was collected from large, naturally weathered single crystals. The core materials were ground in a mortar and dry-sieved to different size fractions (Table 3.2). Three ultrasonic cleaning steps were applied of 10 minutes each, followed by thorough washing with deionized water after each step. From earlier experience with the equipment used, this suffices to remove most of the adhering ultrafines from grinding procedures. To allow for initial changes in surface morphology during dissolution, the samples were preconditioned in static batches for three weeks, using a pH 3 HCl solution and a liquid to solid mass ratio of 100. Solutions were refreshed twice weekly and batches were stirred daily. According to initial studies on these

Table 3.2. Dissolution data for Vals Adularia and Ylijärvi Labradorite (see text). Apparent dissolution rates R_g in 10^{-17} mol.cm⁻² of BET surface.s⁻¹. Bulk dissolution rates R_g^* in 10^{-14} mol.g⁻¹.s⁻¹.

	Vals Adularia				Ylijärvi Labradorite		
fraction (μm)	53-105	105-210	210-300	600-850	53-75	105-150	300-425
S_g^{*1} (cm ² .g ⁻¹)	1460	750	410	160	2360	1270	540
d_g^2 (μm)	73	146	250	711	63	125	355
λ_g	4.5	4.7	4.4	4.8	6.7	7.1	8.6
F_f	0.99	0.99	0.98	0.94	0.94	0.88	0.73
R_g Al	8.6 ± 0.9	3.2 ± 0.5	7.0 ± 0.6	9.8 ± 1.1	34 ± 3	68 ± 4	150 ± 17
R_g Si	36 ± 2	16 ± 3	33 ± 4	50 ± 5	170 ± 21	350 ± 24	710 ± 36
R_g^* Al	12 ± 1	2.4 ± 0.4	2.9 ± 0.2	1.6 ± 0.2	80 ± 7	86 ± 5	82 ± 9
R_g^* Si	53 ± 3	12 ± 2	13 ± 2	8.0 ± 0.9	410 ± 50	450 ± 31	380 ± 19

¹ specific BET surface area, estimated from 3-point BET-krypton; accuracy ± 20 %.

² average spherical grain diameter, estimated from eq. (3.20).

specimens (unpublished data), evaluated using GEOCHEM (Mattigod and Sposito, 1978), this suffices to keep the aqueous concentrations below the saturation level of common secondary phases, except perhaps during the first few days when highly reactive ultrafines from grinding may still be present (Holdren and Berner, 1979; Gillman and Sumner, 1987). After preconditioning, BET-krypton surface areas were determined for all samples (Table 3.2) using the method by De Kanel and Morse (1979). Average grain diameters (Table 3.2) were estimated assuming each size fraction to contain equal sample masses at all grain diameters between the two sieve openings. The average grain diameter (d_g) is then given by:

$$d_g = [2d_p^2d_q^2/(d_p + d_q)]^{1/3} \quad (3.20)$$

where d_p and d_q are the two sieve openings. Unlike the frequently used average of the two sieve openings to estimate d_g , eq. (3.20) accounts - to some extent - for skewing towards smaller grain diameters in poorly defined size fractions. The specific geometric surface area of the samples (s_g^*) was estimated from (Cartwright, 1962):

$$s_g^* = \mathfrak{D}/(\rho d_g) \quad (3.21)$$

where \mathfrak{D} is a geometry factor related to the average shape of the grains, and ρ is the density (g.cm⁻³). A spherical grain geometry was assumed ($\mathfrak{D} = 6$ if d_g is in cm). The data indicate a

linear relation between d_g and λ_g for both the adularia and the labradorite samples (Table 3.2). Thus, $\gamma \approx 0$ and $\beta \approx \lambda_g$ in eq. (3.19). Resulting estimates of F_f (Table 3.2) indicate that the samples are largely dominated by fresh BET surface area.

In the final experiments, dissolution rates of Al and Si were determined using single-pass flow-through reaction cells (Levenspiel, 1972; Weed and Jackson, 1979), a pH 3 HCl input solution, and a flow rate of $1.03 \pm 0.08 \text{ ml.hr}^{-1}$. Temperature was $21 \pm 3 \text{ }^\circ\text{C}$. One blank was run to check for leachant composition. Three feldspars (adularia, albite and labradorite), dissolving at steady state pH 3 HCl before the final experiments started, were used to test analysis equipment performance. Leachates, removed on a 3 to 4 days interval basis, were analyzed using a Varian SpectrAA 300 graphite tube autoanalyzer. Analyses showed that, after eight weeks of running time, approximate steady state was reached for all samples. Analyses over the next three weeks were averaged to calculate mean steady state dissolution rates (Table 3.2).

3.4. Results

Data from the literature

Plots of all data (F_f , R_g) for the samples by Holdren and Speyer (1985, 1987) are given in Figs. 3.1a-j. The dissolution data were obtained for Si at pH 3 HCl, except for the Bancroft Microcline (pH 2 HCl). The estimates of F_f for the samples $> 37 \text{ }\mu\text{m}$ hold for average grain diameters from eq. (3.20), assuming $d_q = 1200 \text{ }\mu\text{m}$ for the samples $> 600 \text{ }\mu\text{m}$. Eq. (3.20) cannot be used for the fractions $0\text{-}37 \text{ }\mu\text{m}$, but back-calculation from their estimates of F_f indicates average grain diameters between 15 and 20 μm in most cases.

Two main types of dissolution behaviour can be distinguished, depending on whether F_f increases or decreases below about 100 μm . A decrease in F_f with decreasing grain diameter can be explained from preferential fracturing of weathered outer layers of grains, relative to fresh inner core material (chapter 2). The decrease in F_f is equivalent to a positive value of γ in eq. (3.19). Keystone Microcline, Perth Perthite, Evje Albite, Mitchell Co. Oligoclase, Saranac Lake Andesine and Crystal Bay Bytownite are referred to hereafter as $\gamma > 0$ feldspars (Table 3.1). Bancroft Microcline, Hybla Alkali Feldspar and Grass Valley Anorthite are referred to hereafter as $\gamma = 0$ feldspars. Unless the high value of R_g for the coarsest size fraction of Crystal Bay Bytownite (Fig. 3.1i) is caused by experimental error, this feldspar may represent a third type of dissolution behaviour.

To illustrate the essence of the problem in Fig. 3.1, assume that the apparent dissolution rates R_f and R_w are independent of the grain diameter, as frequently implied in

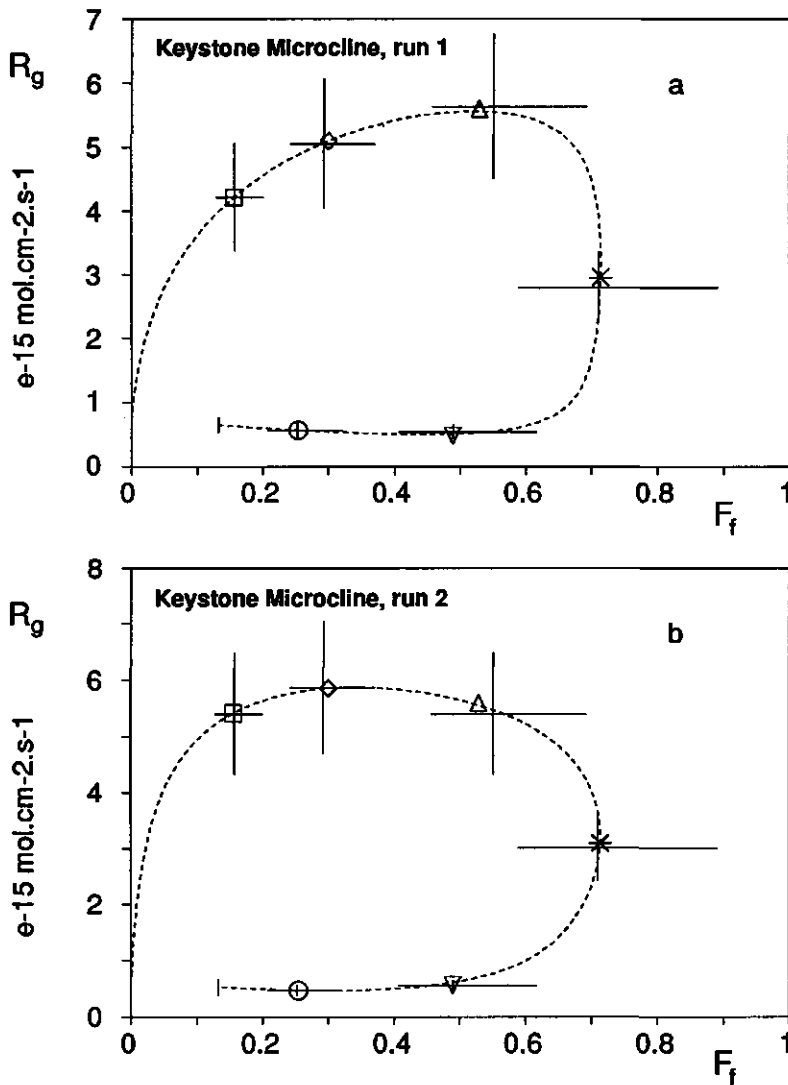


Fig. 3.1. Plots of the apparent dissolution rate (R_g) versus the ratio of fresh BET to BET surface area (F_f) for the ground feldspar samples by Holdren and Speyer (1985, 1987). The actual data are indicated by their error bars, which hold for estimates of R_g and the surface roughness factor (λ_g ; see eq. 3.3) that are accurate within 20%. The dashed curves are modeled relations, with symbols indicating model values at average grain diameters as estimated for the samples. \square : 600-1200 μm ; \diamond : 300-600 μm ; \triangle : 150-300 μm ; $*$: 75-150 μm ; ∇ : 37-75 μm ; \circ : 0-37 μm . The small vertical lines at the end of the dashed curves indicate F_f at grain diameter 0 μm . For Bancroft Microcline, Hybla Alkali Feldspar and Grass Valley Anorthite, $F_f = 1$ at grain diameter 0 μm . Symbols are repeated for actual data of Crystal Bay Bytownite (whose poor fit is due to the limitations of eq. 3.23).

the literature. R_t and R_w in ground samples should then be independent of the proportion of fresh BET surface area (F_f), which is a function of the grain diameter. It follows from eq. (3.7) that, if R_t equals R_w , R_g should be independent of F_f . This is obviously incorrect for all feldspars in Fig. 3.1. If, alternatively, R_t does not equal R_w , a plot of R_g versus F_f should result in a straight line (eq. 3.7). However, a linear relation is found only for Bancroft Microcline (Fig. 3.1c) and Hybla Alkali Feldspar (Fig. 3.1d; the non-linear curves in Fig. 3.1 are explained later and should not be considered here). Furthermore, extrapolation to $F_f = 1$

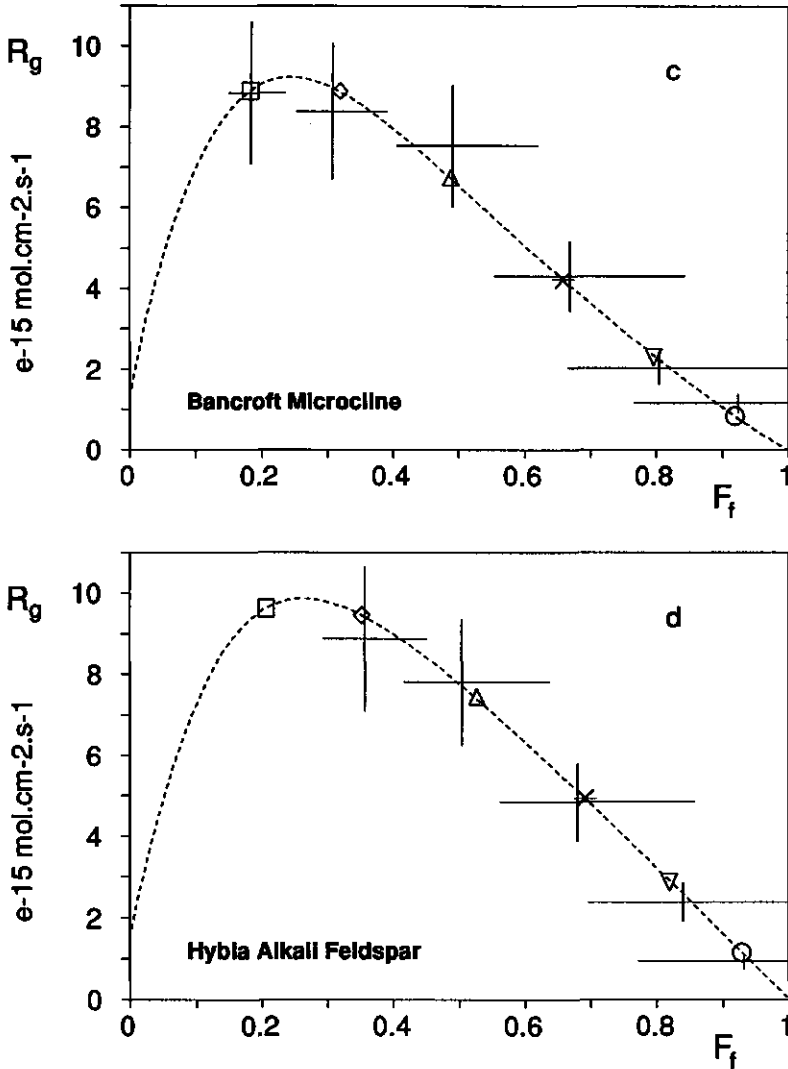


Fig. 3.1. Continued.

in Figs. 3.1c and d shows that $R_f = 0$ (eq. 3.7). Because R_f was assumed independent of the grain diameter, consequently, the fresh surfaces would hardly dissolve at all in any size fraction of these two feldspars. These findings leave little doubt that the original assumption is incorrect, so either R_f or R_w or both are a function of grain diameter in these experiments.

To determine possible alternatives for the dependence of R_f and R_w on grain diameter, plots of \bar{R}_g versus \bar{F}_f were tested for linearity of data (eq. 3.15), using several combinations of P_f and P_w as functions of grain diameter (\bar{R}_g is the effective dissolution rate of a ground

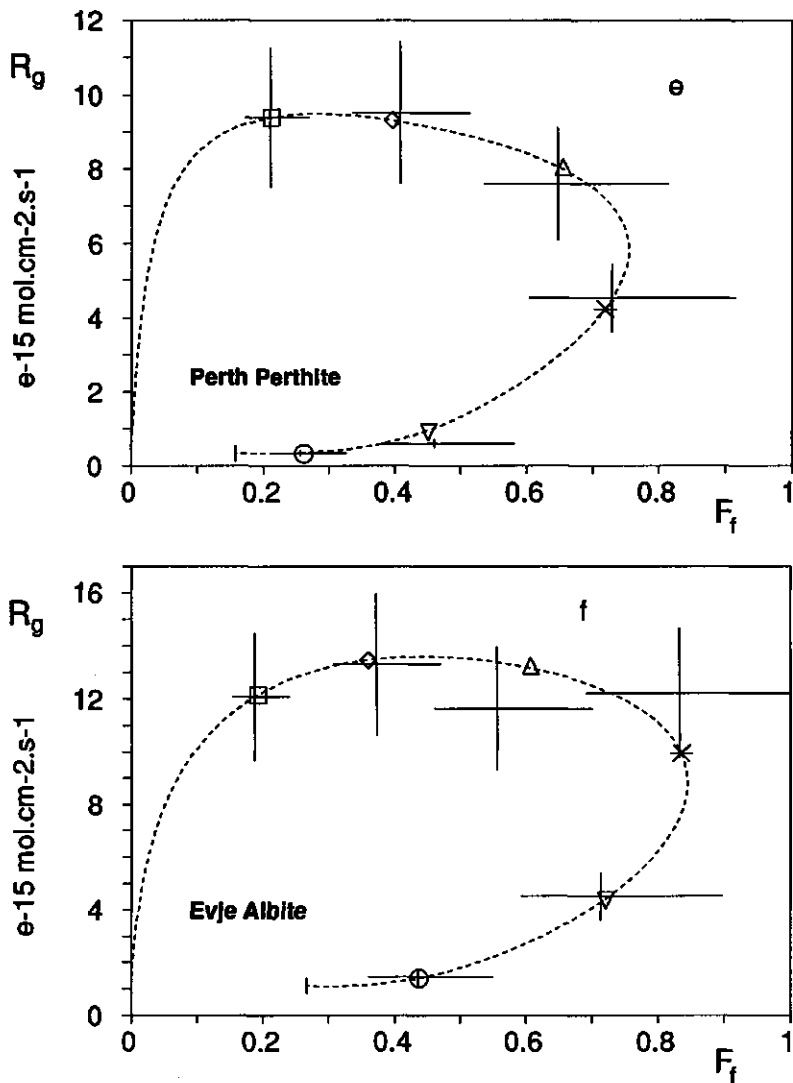


Fig. 3.1. Continued.

sample, \bar{F}_f is the ratio of fresh reactive BET to reactive BET surface area, P_f is the ratio of fresh reactive BET to fresh BET surface area, and P_w is the ratio of weathered reactive BET to weathered BET surface area). Because actual values of P_f and P_w are unknown, functions were arbitrarily defined between minimum and maximum values of zero and unity, respectively, within the range of grain diameters investigated. The validity of this approach can be seen from eqs. (3.11) and (3.12). If actual values of \bar{R}_f , \bar{R}_w , P_f and P_w (as opposed to their model assumptions) are denoted by the superscript #, it follows that $P_f^\#$ and $P_w^\#$ differ

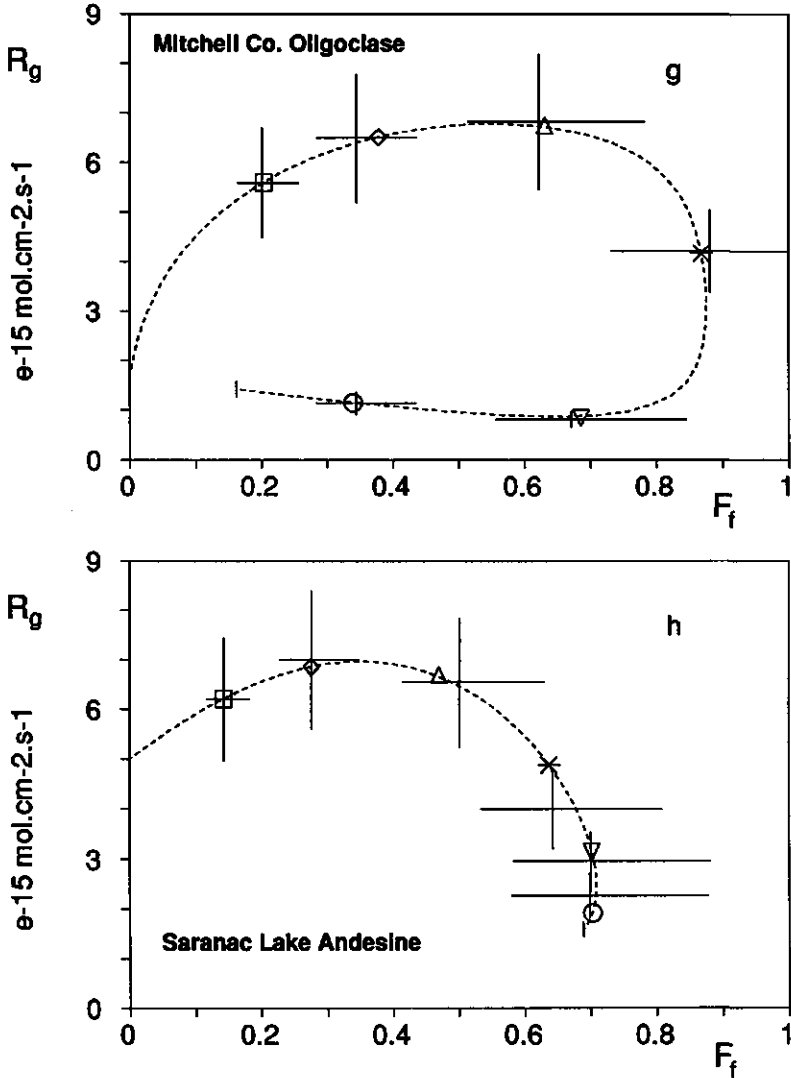


Fig. 3.1. Continued.

from P_f and P_w only by constant multiplication factors \bar{R}_f^*/\bar{R}_f and \bar{R}_w^*/\bar{R}_w , respectively, at all relevant grain diameters. A total of nine functions, including linear and non-linear forms, were analyzed on their capability to explain the experimental data. Two functions showed a minimum or a maximum, respectively, at intermediate grain diameters. However, functions of P_f or P_w showing minima and/or maxima seem rather unlikely, because they would indicate that grinding creates reactive surface area (relative to measured surface area) at some grain diameters, while destroying reactive surface area (relative to measured surface area) at

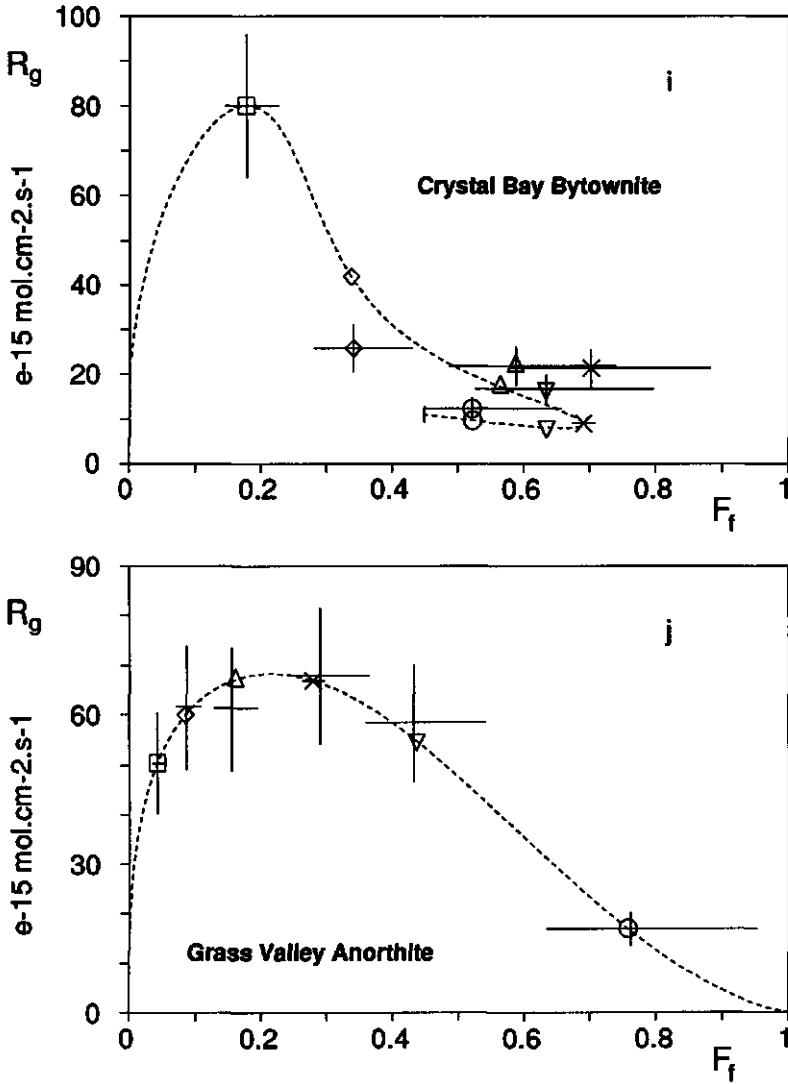


Fig. 3.1. Continued.

others. Most of the tested combinations could not explain the experimental data, or, alternatively, led to almost similar conclusions as for the (linear) functions in the analysis hereafter.

Within the range of available grain diameters, P_f and P_w were independently allowed to either remain constant or to decrease (relative destruction of reactive surface area by grinding) or increase linearly with decreasing grain diameter. P_f and P_w were defined by $P = 1$, $P = d_g/d_r$, or $P = 1 - d_g/d_r$, where d_r is a reference grain diameter. Here, $d_r = 832 \mu\text{m}$, which is the average grain diameter of the coarsest size fraction according to eq. (3.20). Perhaps it should be emphasized that \bar{F}_f is an intricate function of the grain diameter, so the linear shape of P_f and P_w with grain diameter is not a simple explanation for any linearity of data (\bar{F}_f, \bar{R}_g) hereafter.

Typical examples of plots \bar{R}_g versus \bar{F}_f are given for Keystone Microcline, run 1 (Figs. 3.2a-c) and for Bancroft Microcline (Fig. 3.2d). A highly significant linear relationship was observed in a number of cases (Table 3.3). Furthermore, eq. (3.15) states that, if \bar{F}_f is independent of the grain diameter, \bar{R}_g should be independent of the grain diameter too (i.e. data clustering). Significant data clustering was observed for $\gamma = 0$, $P_f = d_g/d_r$ and $P_w = 1$

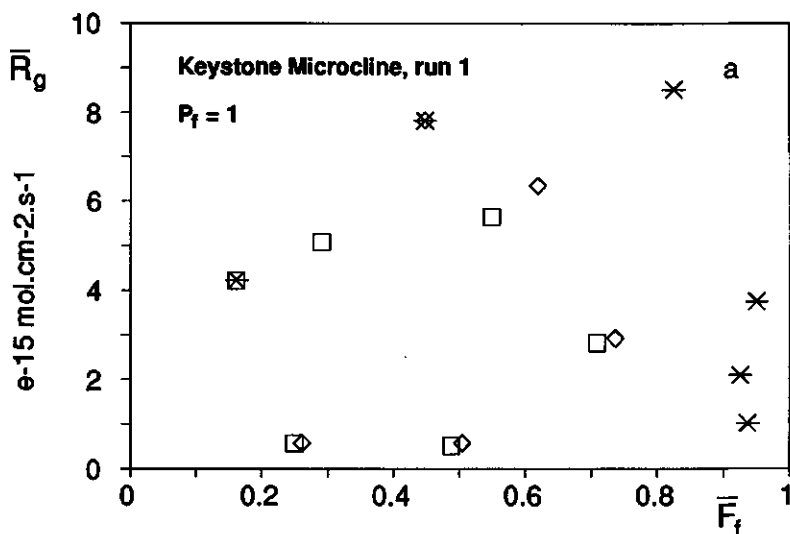


Fig. 3.2. Typical plots of the effective dissolution rate (\bar{R}_g) versus the ratio of fresh reactive BET to reactive BET surface area (\bar{F}_f) for the ground feldspar samples by Holdren and Speyer (1985, 1987). Correlation coefficients of the plots are given in Table 3.3. \square : $P_w = 1$; \diamond : $P_w = 1 - d_g/d_r$; $*$: $P_w = d_g/d_r$. For Keystone Microcline run 1, additional datapoints outside the plot ranges are: $\bar{F}_f = 1, \bar{R}_g = 26.9 \cdot 10^{-15} \text{ mol.cm}^{-2} \cdot \text{s}^{-1}$ (plot a, $P_w = 1 - d_g/d_r$), and $\bar{F}_f = 0.16, \bar{R}_g = \infty$ (plot b, $P_w = 1 - d_g/d_r$).

(Table 3.3; see also Fig. 3.2d and Appendix 2). For Bancroft Microcline and Hybla Alkali Feldspar, highly significant linear relationships were found if P_f and/or P_w are 1 or $1 - d_g/d_r$ (Table 3.3). From model analysis, these reflect the linearity of the original dataset (Figs. 3.1c and d), rather than implying from their slope and intercept that fresh surfaces do not dissolve. Thus, for the functions analyzed, and apart from the Crystal Bay Bytownite, the dissolution behaviour of the fresh surfaces in these feldspars can be explained only if $P_f = d_g/d_r$ (Table 3.3). This was not recognized by Holdren and Speyer (1987) because they did not recognize

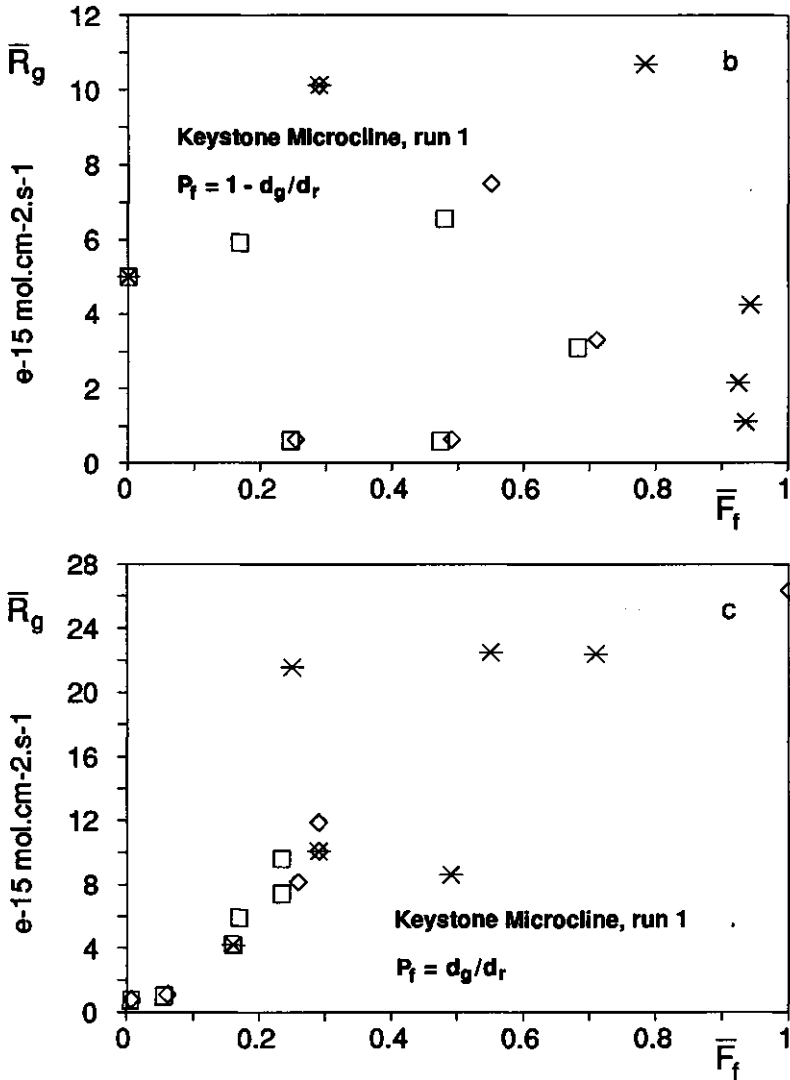


Fig. 3.2. Continued.

the presence of varying proportions of weathered BET surface area in their samples. In feldspar samples with essentially fresh BET surface area only, the same trend of P_f with grain diameter was observed (see hereafter).

The general trend of $P_f \approx d_g/d_r$ shows that the effect of grinding is approximately similar for all feldspars analyzed. This seems logical: if grinding destroys fresh reactive surface area in one feldspar, it is unlikely that it would create fresh reactive surface area in

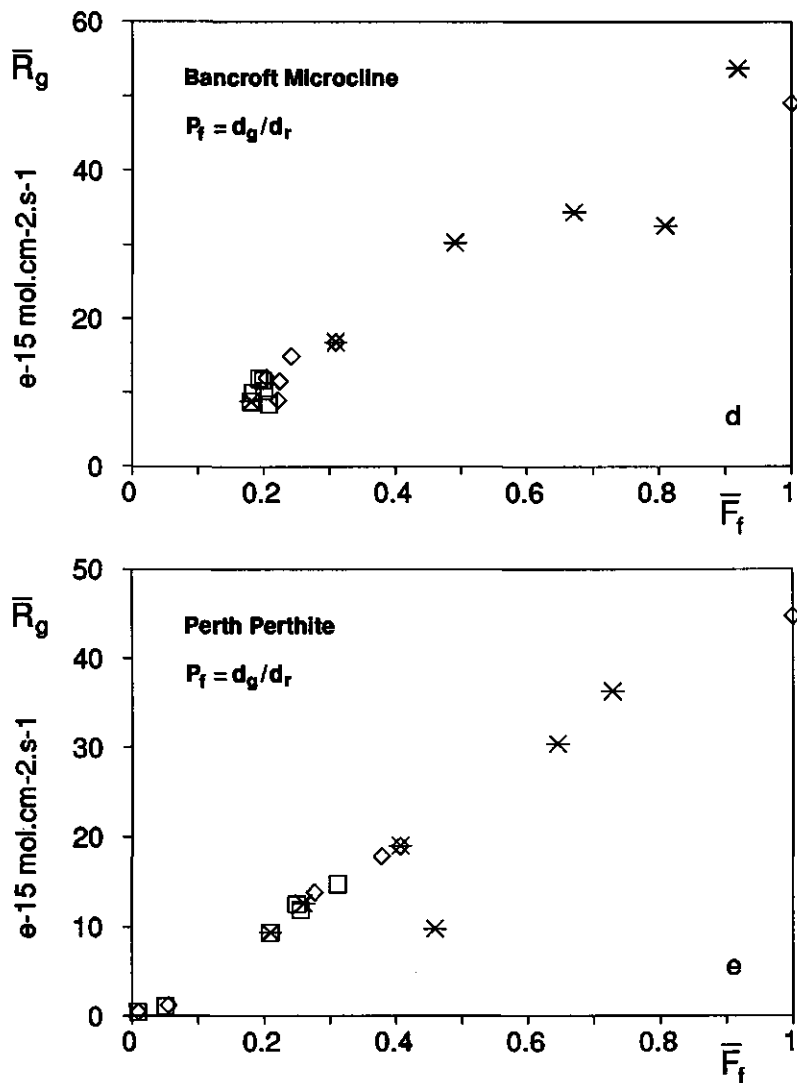


Fig. 3.2. Continued.

Table 3.3. Linear correlation coefficients from eq. (3.15) for ground feldspar samples by Holdren and Speyer (1985, 1987). Data clustering (D.C.) and data linearity of more than 99 % statistical significance is underlined in bold printing. The number of data is 6 for all feldspars, except for HAF (n = 5). For explanation and interpretation: see text.

	KM1 ¹	KM2	BM	HAF	PP	EA	MCO	SLA	CBB	GVA
$P_f=1, P_w=1$	-.02	-.15	<u>-.97</u>	<u>-.99</u>	-.00	-.14	-.16	-.83	-.81	-.74
$P_f=1, P_w=d_g/d_r$	-.34	-.51	-.63	-.86	-.57	-.38	-.40	-.43	<u>-.94</u>	+0.03
$P_f=1, P_w=1-d_g/d_r$	+0.79	+0.79	+0.40	<u>-.97</u>	+0.80	+0.73	+0.62	+0.70	+0.88	-.53
$P_f=d_g/d_r, P_w=1$	<u>+.96</u>	<u>+.98</u>	<u>D.C.</u>	<u>D.C.</u>	<u>+.99</u>	<u>+.94</u>	<u>+.97</u>	+0.61	+0.34	<u>D.C.</u>
$P_f=d_g/d_r, P_w=d_g/d_r$	+0.59	+0.71	<u>+.94</u>	+0.93	<u>+.90</u>	<u>+.94</u>	+0.29	+0.67	+0.33	<u>+.96</u>
$P_f=d_g/d_r, P_w=1-d_g/d_r$	<u>+.98</u>	<u>+.99</u>	<u>+.99</u>	+0.79	<u>+.99</u>	<u>+.94</u>	<u>+.96</u>	<u>+.99</u>	<u>+.95</u>	<u>+.99</u>
$P_f=1-d_g/d_r, P_w=1$	-.24	-.37	<u>-.98</u>	<u>-.99</u>	-.34	-.36	-.35	-.86	-.84	-.75
$P_f=1-d_g/d_r, P_w=d_g/d_r$	-.39	-.54	-.65	-.88	-.61	-.45	-.45	-.47	<u>-.95</u>	-.01
$P_f=1-d_g/d_r, P_w=1-d_g/d_r$	-.59	-.59	-.65	<u>-.98</u>	-.57	-.69	-.59	-.73	-.78	-.46

¹ from left to right: Keystone Microcline runs 1 and 2, Bancroft Microcline, Hybla Alkali Feldspar, Perth Perthite, Evje Albite, Mitchell Co. Oligoclase, Saranac Lake Andesine, Crystal Bay Bytownite, and Grass Valley Anorthite, respectively.

another. All available data in Table 3.3 for $P_f = d_g/d_r$ show that slopes in eq. (3.15) are positive, so $\bar{R}_f > \bar{R}_w$. Furthermore, the dissolution behaviour of Bancroft Microcline, Perth Perthite, Evje Albite and Grass Valley Anorthite is largely independent of P_w as a function of grain diameter (Table 3.3). This can be explained only if $\bar{R}_f \gg \bar{R}_w$ for these feldspars (e.g. Fig. 3.2e for Perth Perthite). For instance, in the limiting case of $\bar{R}_w = 0$, the contribution of the weathered surface area to the total dissolution kinetics is zero for any P_w as a function of grain diameter. According to the other feldspars, either $P_w \approx 1$ or $P_w \approx 1 - d_g/d_r$ (Table 3.3). However, if $P_w \approx 1 - d_g/d_r$, weathered reactive surface area would be created by grinding. This seems impossible almost by definition, so P_w was most likely independent of grain diameter in these experiments.

For Keystone Microcline and Bancroft Microcline, the theoretical effect of P_w and \bar{R}_w on R_g , using $P_f = d_g/d_r$ and $\bar{R}_f \gg \bar{R}_w$ is shown in Figs. 3.3a and b. Both plots reflect the earlier findings from Figs. 3.1 and 3.2. Note also that at 100 μm , $R_g \approx 0.01 \bar{R}_f$ for both (and, from similar plots, for all) feldspars. This agrees well with the findings by Helgeson *et al.* (1984), discussed in the introduction.

Hereafter, it is assumed that $P_f \approx d_g/d_r$ ($P_f \equiv 0$ at $d_g = 0$ and $P_f \equiv 1$ at $d_g = d_r$), and that $P_w \approx 1$ or $P_w \approx 1 - d_g/d_r$ ($P_w \equiv 1$ at $d_g = 0$ and $P_w \equiv 0$ at $d_g = d_r$). Methods are discussed to estimate the effective dissolution rates \bar{R}_f and \bar{R}_w from experimental data, and

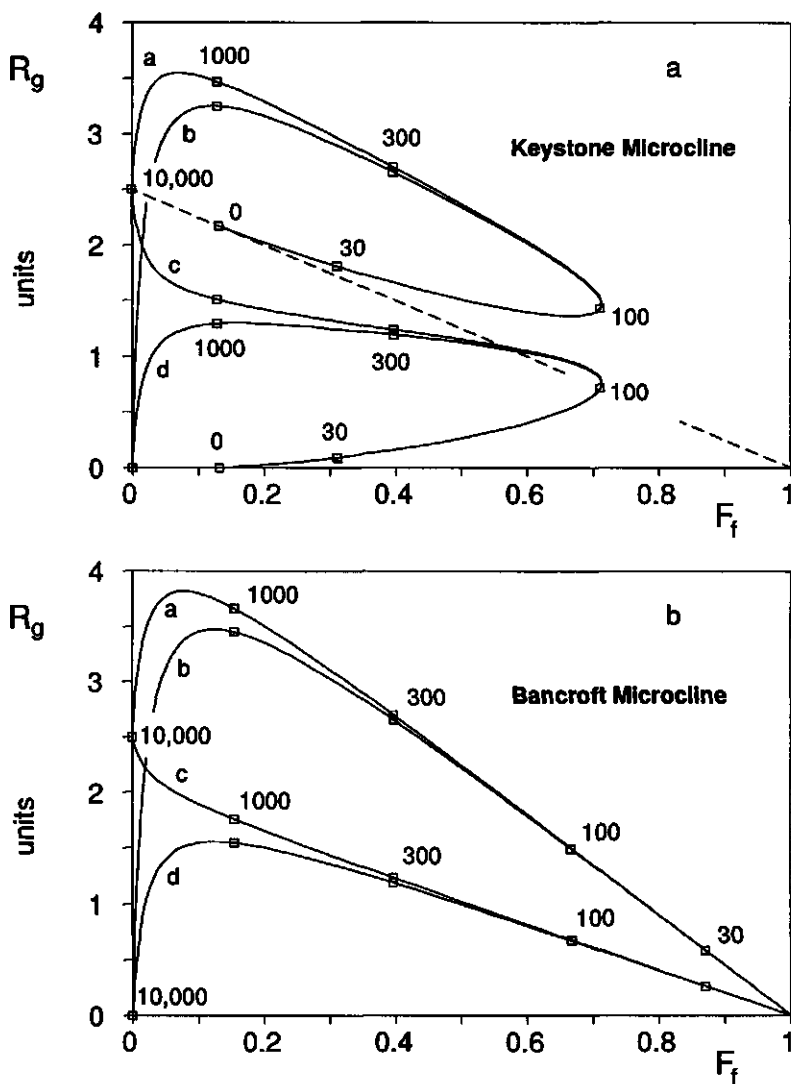


Fig. 3.3. Plots of the theoretical effect of grain diameter on the apparent dissolution rate (R_g) and on the ratio of fresh BET to BET surface area (F_f) for ground feldspar samples by Holdren and Speyer (1985, 1987). Plot a: Keystone Microcline; plot b: Bancroft Microcline. In both plots: $P_f = d_g/d_r$, $\bar{R}_f = 100$ units and $d_r = 10,000 \mu\text{m}$, which is the average diameter of the unfractured sample material. Datapoints of (F_f , R_g) are indicated in μm at several grain diameters. Curves a: $\bar{R}_w = 2.5$ units, $P_w = 1$; curves b: $\bar{R}_w = 2.5$ units, $P_w = 1 - d_g/d_r$; curves c: $\bar{R}_w = 2.5$ units, $P_w = d_g/d_r$; curves d: $\bar{R}_w = 0$. Dashed line in plot a: see eq. (3.22).

to evaluate possible deviations in the ratio of fresh reactive BET to fresh BET surface area from the simple approximation used so far ($P_f = d_g/d_r$). It is repeated that values of P_f , P_w , \bar{R}_f and \bar{R}_w are correct on an internal basis only, but that they can be used to calculate actual values of the apparent dissolution rates R_f and R_w at all grain diameters from eqs. (3.11) and (3.12).

\bar{R}_w in most of these experiments is too small for accurate extrapolation in plots of the effective dissolution rate (\bar{R}_g) versus the ratio of fresh reactive BET to reactive BET surface area (\bar{F}_f) (see, for instance, Figs. 3.2c and e). However, at $d_g = 0 \mu\text{m}$ it follows from eq. (3.13) that both for $P_w = 1$ and for $P_w = 1 - d_g/d_r$:

$$R_g = (1 - F_f)\bar{R}_w \quad (3.22)$$

According to eq. (3.22), a straight line through $(F_f, R_g) = (1, 0)$ and (F_f, R_g) at $d_g = 0 \mu\text{m}$ gives \bar{R}_w as the y-intercept at $F_f = 0$. This relation is plotted by the dashed line in Fig. 3.3a. Once \bar{R}_w has been estimated, the corresponding value of \bar{R}_f is found from F_f and R_g at grain diameter d_r (F_f and R_f). This estimate of \bar{R}_f can be checked from a plot \bar{R}_g versus \bar{F}_f . For instance, for Keystone Microcline run 1, $\bar{R}_w \approx 0.75 \cdot 10^{-15} \text{ mol.cm}^{-2} \cdot \text{s}^{-1}$ (Fig. 3.1a) and $\bar{R}_f \approx 23 \cdot 10^{-15} \text{ mol.cm}^{-2} \cdot \text{s}^{-1}$ if $P_w \approx 1$, or $\bar{R}_f \approx 27 \cdot 10^{-15} \text{ mol.cm}^{-2} \cdot \text{s}^{-1}$ if $P_w \approx 1 - d_g/d_r$ (eq. 3.13). Both estimates of \bar{R}_f are in general agreement with Fig. 3.2c. Estimates of \bar{R}_f for

Table 3.4. \bar{R}_f and \bar{R}_w ($10^{-15} \text{ mol.cm}^{-2}$ of reactive BET surface. s^{-1}), and P_f of the intermediate size fractions (see text) for samples by Holdren and Speyer (1985, 1987).

	\bar{R}_f	\bar{R}_w	P_f 0.37 μm	P_f 52 μm^1	P_f 104 μm^1	P_f 208 μm^1	P_f 416 μm^1
Keystone Microcline run 1	23.0	0.75	0.002	0.014	0.158	0.440	0.660
Keystone Microcline run 2	31.5	0.60	0.003	0.015	0.126	0.315	0.580
Bancroft Microcline	52.2	1.66	0.027	0.053	0.137	0.330	0.550
Hybla Alkali Feldspar	51.6	2.00	0.022	0.064	0.155	0.330	0.554
Perth Perthite	43.0	0.40	0.004	0.020	0.143	0.265	0.550
Evje Albite	57.0	1.50	0.024	0.100	0.251	0.370	0.605
Mitchell Co. Oligoclase	20.8	1.70	0.001	0.020	0.220	0.473	0.690
Saranac Lake Andesine ²	13.5	5.0	0.084	0.154	0.253	0.615	0.905
Crystal Bay Bytownite ²	360	20	0.015	0.042	0.060	0.065	0.105
Grass Valley Anorthite	1610	31	0.022	0.148	0.263	0.410	0.640

¹ average spherical grain diameter, estimated from eq. (3.20).

² inaccurate values, due to likely extrapolation and/or experimental error.

$P_w = 1$, and of \bar{R}_w , are given in Table 3.4 for all $\gamma > 0$ feldspars. Except for Saranac Lake Andesine, estimates of \bar{R}_f are much higher than those of \bar{R}_w . The deviate estimates for Saranac Lake Andesine may be due to extrapolation error in \bar{R}_w and/or to the relatively high value of R_g at 0-37 μm , compared to other identical size fractions (Fig. 3.1h).

For $\gamma = 0$ feldspars, \bar{R}_w (and, consequently, \bar{R}_f) cannot be estimated from eq. (3.22) because, at $d_g = 0 \mu\text{m}$, $F_f = 1$. However, if $P_w \approx 1$, the data tend to cluster, so, for instance, for Bancroft Microcline: $0.20 \bar{R}_f + 0.80 \bar{R}_w \approx 10^{-14} \text{ mol.cm}^{-2}.\text{s}^{-1}$ (eq. 3.15 and Fig. 3.2d). It was shown for Bancroft Microcline that $\bar{R}_f \gg \bar{R}_w$, so $\bar{R}_f \approx 5.0 \cdot 10^{-14} \text{ mol.cm}^{-2}.\text{s}^{-1}$. If, alternatively, $P_w \approx 1 - d_g/d_f$, it follows that $\bar{R}_f \approx R_f/F_f$ (eq. 3.13), so $\bar{R}_f \approx 4.8 \cdot 10^{-14} \text{ mol.cm}^{-2}.\text{s}^{-1}$ instead. Unfortunately, there seems to be no reasonably accurate procedure to estimate \bar{R}_w for $\gamma = 0$ feldspars, other than to determine the dissolution rate of the unfractured material. If $P_w \approx 1 - d_g/d_f$, a first estimate of \bar{R}_w can be found from the best line in a plot of \bar{R}_g versus \bar{F}_f . Estimates of \bar{R}_f for $P_w = 1$ and $\bar{R}_f \gg \bar{R}_w$ are given in Table 3.4 for the $\gamma = 0$ feldspars. The estimates of \bar{R}_w for the $\gamma = 0$ feldspars (Table 3.4) are from best lines in plots of \bar{R}_g versus \bar{F}_f assuming $P_w = 1 - d_g/d_f$.

Theoretical plots of the apparent dissolution rate of ground samples (R_g) versus the ratio of fresh BET to BET surface area (F_f), using $P_f = d_g/d_f$, are not fully identical to experimental plots (e.g. Figs. 3.1a and b versus Fig. 3.3a). From model analysis, variations in P_w as a function of grain diameter, and in d_f , λ_f and d_w (and, consequently, λ_w), have little

Table 3.5. C_1 , C_2 , C_3 , P_f at grain diameter d_w , $P_f^{\#}$ at grain diameter d_w , $\bar{R}_f^{\#}$ and $\bar{R}_w^{\#}$ (see text) for ground feldspar samples by Holdren and Speyer (1985, 1987).

	C_1	C_2	C_3	$P_f(d_w)$	$P_f^{\#}(d_w)$	$\bar{R}_f^{\#}$	$\bar{R}_w^{\#1}$
Keystone Microcline run 1	50	0.12	0.58	4.3	0.27	$4 \cdot 10^{-13}$	$3 \cdot 10^{-15}$
Keystone Microcline run 2	25	0.10	0.77	6.9	0.55	$4 \cdot 10^{-13}$	$1 \cdot 10^{-15}$
Bancroft Microcline	1.5	0.10	0.12	2.1	0.15	$7 \cdot 10^{-13}$	$1 \cdot 10^{-14}$
Hybla Alkali Feldspar	1	0	0	1.9	0.12	$8 \cdot 10^{-13}$	$2 \cdot 10^{-14}$
Perth Perthite	30	0.06	0.88	9.0	0.63	$6 \cdot 10^{-13}$	$1 \cdot 10^{-15}$
Evje Albite	25	0.02	0.68	5.5	0.22	$1 \cdot 10^{-12}$	$7 \cdot 10^{-15}$
Mitchell Co. Oligoclase	35	0.11	0.51	3.6	0.16	$5 \cdot 10^{-13}$	$1 \cdot 10^{-14}$
Saranac Lake Andesine ²	5	0.07	0	1.1	0.04	$3 \cdot 10^{-13}$	$1 \cdot 10^{-13}$
Crystal Bay Bytownite ²	5	0.60	0.50	4.1	0.69	$2 \cdot 10^{-12}$	$3 \cdot 10^{-14}$
Grass Valley Anorthite	25	0.02	0.59	4.4	0.17	$4 \cdot 10^{-11}$	$2 \cdot 10^{-13}$

¹ obtained by assuming $P_f^{\#}(d_w) = P_w^{\#}(d_w)$ (see text).

² inaccurate values, due to likely extrapolation and/or experimental error.

effect on the explanation of the actual data. However, deviations from $P_f = d_g/d_r$ may explain the discrepancies between model predictions so far and the data in Fig. 3.1. This was analyzed in case of $P_w = 1$. Although P_w possibly equals $1 - d_g/d_r$ instead, and although estimates of \bar{R}_w for the $\gamma=0$ feldspars may be inaccurate, ratios of \bar{R}_f to \bar{R}_w (Table 3.4) show that the contribution of the weathered surfaces to the total dissolution kinetics is relatively small for all feldspars except perhaps for Saranac Lake Andesine. Thus, with the possible exception of Saranac Lake Andesine, the analysis of P_f hereafter is approximately independent of P_w as a function of grain diameter, and holds also for reasonable alternative estimates of \bar{R}_w for the $\gamma=0$ feldspars.

From eq. (3.13), P_f was estimated at grain diameters smaller than d_r for all feldspars, using $P_f \equiv 1$ at grain diameter d_r (Table 3.4). For most feldspars, P_f as a function of d_g/d_r can be described empirically by:

$$P_f = \frac{\arctan [C_1(d_g/d_r - C_2)] + \arctan (C_1 C_2)}{\arctan [C_1(1 - C_2)] + \arctan (C_1 C_2)} (d_g/d_r)^{C_3} \quad (3.23)$$

where C_1 , C_2 and C_3 are independent of the grain diameter. C_1 is related to the maximum slope of the arctan fraction. C_2 equals d_g/d_r where the slope of the arctan fraction is at maximum. C_3 accounts for additional deviations from linearity. The arctan fraction models the observation that several $\gamma>0$ feldspars show a marked decrease in P_f at grain diameters around 100 μm . This was also observed by Holdren and Speyer (1985, 1987). If the high value of R_g at 832 μm for the Crystal Bay Bytownite is not an experimental error, then according to this model, a marked decrease in P_f occurs at grain diameters around 600 μm to a fairly constant level at smaller grain diameters (Table 3.4). The data in Table 3.4 were used to estimate C_1 , C_2 , C_3 and P_f at grain diameter d_w (Table 3.5). Resulting plots of P_f versus d_g/d_r are shown in Fig. 3.4. Using the data from Fig. 3.1 and Tables 3.1, 3.4 and 3.5, modeled relations of R_g versus F_f are shown in Fig. 3.1. The poor fit for Crystal Bay Bytownite (Fig. 3.1i) is due to the limitations of eq. (3.23).

Additional experiments

The apparent dissolution rate (R_g) in the Vals Adularia and Ylijärvi Labradorite experiments essentially equals that of the fresh surfaces in these samples (Table 3.2). Apart from the finest adularia fraction, R_g of both feldspars, both for Al and Si, is approximately proportional to the grain diameter (Table 3.2). This confirms the earlier finding that $P_f \approx d_g/d_r$ in the experiments by Holdren and Speyer (1985, 1987). The data were also interpreted in

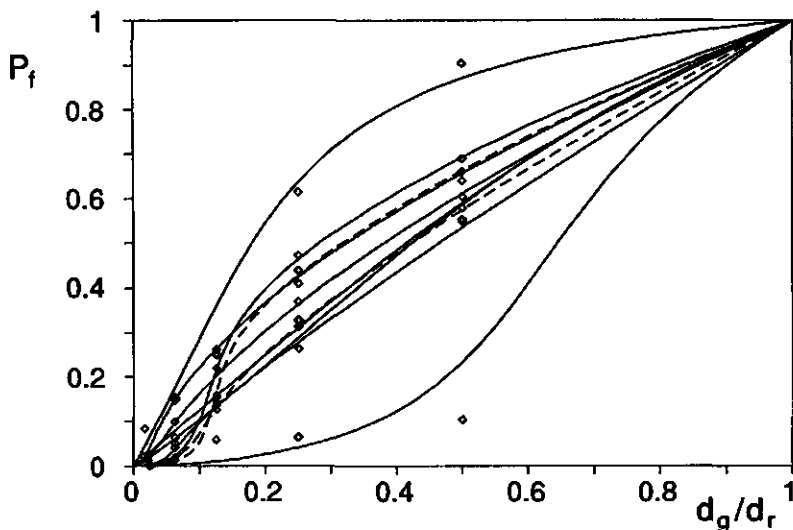


Fig. 3.4. Plot of all data (d_g/d_r , P_f) from Table 3.4 and fits from eq. (3.23) used to generate the curves in Fig. 3.1. Dashed curves are for Keystone Microcline run 1 and 2, indicating the variation between duplos. At $d_g/d_r = 0.25$, from top to bottom: Saranac Lake Andesine, Mitchell Co. Oligoclase, Keystone Microcline run 1, Grass Valley Anorthite, Evje Albite, Keystone Microcline run 2, Hybla Alkali Feldspar, Bancroft Microcline, Perth Perthite and Crystal Bay Bytownite. The deviations from $P_f = d_g/d_r$ (and $P_w = 1$) for Saranac Lake Andesine and Crystal Bay Bytownite may also be seen from Table 3.3, and may be due to experimental and/or extrapolation error (see text).

terms of bulk dissolution rates (R_g^* ; $\text{mol}\cdot\text{g}^{-1}\cdot\text{s}^{-1}$; Table 3.2). This eliminates all possible effects from surface area measurements. For these samples, the bulk dissolution rates should be approximately independent of grain diameter if $P_f = d_g/d_r$ (Appendix 3). Apart from the finest adularia fraction, the results again confirm the earlier findings on P_f . In batch-type dissolution experiments on the same labradorite specimen as used here, similar results were obtained (L.G. Wesselink, pers. comm.).

3.5. Discussion

The preceding analysis strongly suggests that the ratio of fresh reactive BET to fresh BET surface area (P_f) is approximately proportional to the grain diameter within the range of grain diameters investigated. This indicates that experimentally derived rate "constants" and apparent dissolution rates of fresh feldspar surfaces, when normalized to their BET area, are

valid at one grain diameter only. Correction procedures for differences in grain diameter should be applied with care, because from this research it is not yet fully clear if relationships between P_f and grain diameter are identical for all feldspars. Also, methods and artifacts of grinding have widely recognized effects on apparent dissolution rates for a variety of minerals (e.g. Boldyrev, 1979; Rimstidt and Barnes, 1980; Petrovich, 1981a,b; Sangwal, 1982, 1987; Eggleston *et al.*, 1989).

The observed trend of decreasing amounts of fresh reactive BET surface area at all grain diameters (relative to fresh BET surface area) can be explained if preferential fracture planes have a relatively high density of potentially dissolution reactive sites. This can be seen as follows. At some grain diameter after grinding, the exposed fresh surfaces have a given average density of dissolution sites. As grinding continues, surfaces with increasingly smaller density of dissolution sites will be exposed, thereby decreasing the average density at all grain diameters. If so, fresh reactive BET surface area is "diluted" rather than "destroyed" by grinding. For the weathered surfaces, originating from the unfractured grains, the dissolution site density is determined by the initial grain diameter rather than by the grain diameter after grinding. This explains the observation that, contrary to P_f , P_w does not decrease with grain diameter in the samples by Holdren and Speyer (1985, 1987).

Casey *et al.* (1991) determined the relation between chemical composition and apparent dissolution rate for a number of plagioclases. They found the apparent dissolution rate of Pacaya Anorthite, reported by Fleer (1982), to be approximately 75 times higher than expected from the other data. The present analysis offers an explanation for this discrepancy. From the description by Casey *et al.* (1991), the single crystal used by Fleer (1982) was much larger than the average grain diameter of the other plagioclases in their study. Thus, its ratio of reactive BET to BET surface area may have been much larger too. Even if the effective dissolution rates of all anorthites in their study would be of comparable value, the Pacaya Anorthite may well have had a much higher apparent dissolution rate. Furthermore, Fleer (1982) estimated the geometric, rather than the actual surface area as for the other samples in their study (Casey *et al.*, 1991). The roughness factor of fresh anorthite surfaces is approximately 10, however (Table 3.1).

Brady and Walther (1989) determined the relation between the apparent dissolution rate at pH 8 and the mean electrostatic site potential for a number of silicates. They found the apparent dissolution rate of nepheline, reported by Tole *et al.* (1986), to be two orders of magnitude higher than predicted from the other data. Again, from the description by Tole *et al.* (1986), differences in grain diameter may explain this discrepancy if the findings on P_f from the present analysis hold for silicates in general.

Specific surface areas have been estimated from genetic considerations, geometric surface area calculations and BET measurements for a number of weathered silicates in natural systems (e.g. Hurd, 1973; White and Claassen, 1979; Claassen and White, 1979; Pačes, 1983; Siegel 1984; Velbel, 1985; Gislason and Eugster, 1987a,b; Schnoor, 1990; Swoboda-Colberg and Drever, 1993). For most of these systems, calculated aqueous concentrations from laboratory derived rate constants significantly exceed the observed concentrations. In contrast, Gislason and Eugster (1987a,b) found aqueous concentrations from pebble sized silicates in a N.E. Iceland aquifer that exceeded calculated concentrations from laboratory experiments. However, they determined rate constants for the naturally weathered, pebble sized materials from dissolution experiments on ground 125-250 μm samples. The studied materials were rhyolitic ash from the Askja 1875 eruption, and basaltic glass from the Krafla 1981 eruption (Gislason and Eugster, 1987a,b). The eruption dates indicate that the materials possibly differed in degree of natural weathering, and thus, in the comparability to freshly created surfaces by grinding. Also, naturally weathered surfaces may still have been present in the ground samples. The findings on P_f from the present analysis may not apply to their experiments, but alternatively, rate "constants" for the pebble sized materials may have been higher than those for the ground 125-250 μm grains by more than an order of magnitude. If so, this would bring their results in much better agreement with those of similar studies.

Ratios of the number of dissolution reactive surface sites to the total number of surface sites have been related to the surface roughness factor (Helgeson *et al.*, 1984), to the fractal dimension of mineral grains (Avnir *et al.*, 1985), to the morphology of etch pits (Lasaga and Blum, 1986), to the activation energy of the dissolution reaction (Wehrli, 1989b), and to the kinetic effect of cation adsorption (Wehrli *et al.*, 1990). For instance, Helgeson *et al.* (1984) estimated the actual value of P_f ($P_f^\#$) to be approximately 0.01 for the 100 μm Amelia Albite grains used by Holdren and Berner (1979). The estimate of 0.01 was obtained by assuming $P_f^\#$ of ultrafines to be unity, and may therefore represent a maximum. Also, λ was assumed to be unity. The value of 0.01 will be used hereafter to derive tentative estimates of $P_f^\#$, $P_w^\#$, $\bar{R}_f^\#$, and $\bar{R}_w^\#$ for the feldspars by Holdren and Speyer (1985, 1987).

Because the value of 0.01 holds for geometric surface areas ($\lambda = 1$), it should first be recalculated to BET surface area. According to their description, Holdren and Berner (1979) used naturally weathered albite fragments of perhaps 1 cm average diameter as starting material. If so, 100 μm grains, obtained from grinding and sieving, have a λ_g and F_f of about 3.0 and 0.83 respectively (chapter 2). If the albite ultrafines consist of freshly created surface area only, then $\lambda_{\text{ultrafines}} \approx 2.5$ (Table 3.1). These data indicate that $P_f^\#$ for the 100 μm Amelia Albite, normalized to BET surface area, essentially equals $P_f^\#$, normalized to geometric

surface area. Assuming the value of 0.01 to be approximately correct for all feldspars by Holdren and Speyer (1985, 1987) at 100 μm (p. 63, 2nd par.), it follows from eq. (3.11) that $0.01/P_{f,100\mu\text{m}}$ can be used as a multiplication constant to estimate $P_f^\#$ at all grain diameters from eq. (3.23). Resulting estimates of $P_f^\#$ at grain diameter d_w (Table 3.5) suggest that for hypothetical 1 cm sized fresh-surface feldspar fragments, the fraction of the BET surface area occupied by reactive BET surface area ranges from approximately 0.1 to 0.7, provided that all BET area of ultrafines is reactive. These estimates are much higher than that for the 100 μm Amelia Albite by Helgeson *et al.* (1984).

The ratio of P_f to $P_f^\#$ at grain diameter d_w can be used to calculate $\bar{R}_f^\#$ from \bar{R}_f (eq. 3.11). First estimates of $\bar{R}_f^\#$ (Table 3.5) are approximately two to three orders of magnitude higher than the apparent dissolution rates of these samples.

Estimates of $\bar{R}_w^\#$ depend on the relation between $P_f^\#$ and $P_w^\#$. If $P_f^\# \approx P_w^\#$ at grain diameter d_w (i.e. fresh and weathered BET surfaces on similarly sized grains have similar densities of identical dissolution sites), $\bar{R}_w^\#$ would be approximately two orders of magnitude smaller than $\bar{R}_f^\#$ (Table 3.5). However, an alternative explanation for these data would be that $\bar{R}_f^\# \approx \bar{R}_w^\#$, so that $P_f^\# \approx 100 P_w^\#$ at grain diameter d_w (eq. 3.12). It will be shown in chapter 7 that the second explanation is, in fact, the most accurate.

3.6. Conclusions

A kinetic model is presented for the analysis of experimental dissolution data in terms of both fresh and weathered mineral surfaces. These may be simultaneously present, for instance, in ground samples from naturally weathered mineral fragments. Literature data for nine different feldspars were reinterpreted to yield the proportion of the BET surface area which is dissolution reactive as a function of the grain diameter. For the weathered surfaces (originating from the unfractured fragments), the proportion of the BET surface area which is dissolution reactive was most likely independent of the grain diameter. If so, grinding does not destroy or create weathered reactive BET surface area, relative to weathered BET surface area. For the fresh surfaces, the proportion of the BET surface area which is dissolution reactive was approximately proportional to the grain diameter. Thus, grinding destroys fresh reactive BET surface area, relative to fresh BET surface area, at all grain diameters. This can be explained if preferential fracture planes have relatively high densities of potentially dissolution reactive sites. Fresh reactive BET surface area is then "diluted", rather than "destroyed" by grinding. These findings demonstrate that experimental feldspar dissolution rates cannot be compared if the grain diameters are different. They also demonstrate that the proposed nature of dissolution reactive sites in the literature so far is

incorrect. Tentative calculations suggest that the ratio of reactive BET to measured BET surface area for hypothetical, 1 μm sized fresh-surface feldspar fragments ranges from approximately 0.1 to 0.7, if all BET surface area of ultrafine particles from grinding is reactive. These estimates are much higher than literature estimates for grain diameters, normally used in dissolution studies. Tentative calculations also suggest that, at pH 3 HCl: (1) the dissolution rate of reactive sites, normalized to their BET area, is approximately two orders of magnitude higher for fresh than for weathered feldspar surfaces; or (2) the density of reactive sites, normalized to BET area, is approximately two orders of magnitude higher for fresh than for weathered feldspar surfaces.

Acknowledgements

I am greatly indebted to Nico van Breemen, Edward Meijer and Leendert van der Plas of the Department of Soil Science and Geology, Agricultural University of Wageningen, The Netherlands, for their creative ideas, constant support and critical comments during this research. I thank Barend van Lagen of the same Department for performing the chemical analyses. I gratefully acknowledge the help of Joop Harmsen in providing the graphite tube autoanalyzer system at the ICW, Wageningen, and the help of Paul van Ekeren and Aad van Genderen for the use of high-vacuum equipment at the Center of Thermodynamics, University of Utrecht, The Netherlands.

This chapter was published in *Geochimica et Cosmochimica Acta*, vol. 56, pp. 3957-3970. Editorial handling for *Geochimica et Cosmochimica Acta*: M.F. Hochella, Jr.

**The dissolution of ground feldspar samples
in the laboratory**

**Chapter 4. The effect of grain diameter in the
starting material**

Abstract

Surface area measurements and dissolution experiments were performed on a naturally weathered feldspar-quartz assemblage. The surface areas of the unfractured (612 μm) and ground samples were measured at different levels of surface detail, using a dissecting microscope, scanning electron microscopy (SEM) and the BET-krypton method. Roughness factors of the freshly created surfaces by grinding were 2.1 (SEM at 10,000x magnification) and 4.8 (BET) respectively. Roughness factors of the naturally weathered surfaces were 2.8 (SEM at 10,000x; including effects from etch pitting) and 34 (BET) respectively. These data indicate that: (1) a large amount of BET surface area was created during natural weathering; and (2) etch pits do not contribute significantly to the BET surface area created during natural weathering. Comparison of these and earlier results suggests that the surface roughness factor of unfractured naturally weathered feldspar grains decreases with decreasing grain diameter.

Dissolution experiments at pH 3 and 5 HCl showed that, at 612 μm , freshly created BET surfaces dissolve approximately one order of magnitude faster than their naturally weathered counterparts. Comparison with earlier results indicates that this discrepancy in dissolution rate, at equal diameters of freshly created and naturally weathered grains, decreases with decreasing grain diameter. This can be explained from the suggested decreasing surface roughness with decreasing grain diameter if the BET surface area created during natural weathering is non-reactive.

Dissolution rates of freshly created feldspar surfaces in the laboratory are frequently up to several orders of magnitude higher than those of naturally weathered feldspar surfaces in actual field situations. The findings from this research help to explain these discrepancies. However, effects from other factors, such as imperfect contact between solution and solids, the presence of organic ligands, etc., should also be considered.

4.1. Introduction

Over the past several decades, many authors have reported on the kinetics of mineral dissolution in the laboratory (e.g. Lagache, 1965; Berner and Holdren, 1977; Chou and Wollast, 1984; Holdren and Speyer, 1985, 1987; Knauss and Wolery, 1986; Grandstaff, 1986; Casey *et al.*, 1989a,b). The kinetics of mineral dissolution have also been studied in natural systems (e.g. Garrels, 1967; Pačes, 1983; Velbel, 1985; Bruton, 1986; Olsson and Melkerud, 1987; Matzner, 1987; Sverdrup and Warfvinge, 1987, 1988). Dissolution rates from laboratory experiments are frequently normalized to the mineral surface (e.g. $\text{mol}\cdot\text{cm}^{-2}\cdot\text{s}^{-1}$). Dissolution rates in natural systems, normally obtained from budget studies, are frequently normalized to the landscape surface (e.g. $\text{kmol}\cdot\text{ha}^{-1}\cdot\text{yr}^{-1}$). If the amount of mineral surface per unit of landscape surface is estimated, dissolution rates in natural systems can be compared to those in the laboratory. In this way, Pačes (1983) found natural weathering rates of oligoclase in some Czechoslovakian drainage basins that are one to three orders of magnitude lower

than feldspar dissolution rates in the laboratory. Velbel (1985) found oligoclase weathering rates in a North Carolina watershed that are approximately one to two orders of magnitude lower than feldspar dissolution rates in the laboratory. In contrast, Knauss and Wolery (1986) found laboratory rates for Evje Albite at 25 °C that are comparable to natural oligoclase rates by Velbel (1985). However, Knauss and Wolery (1986) reported dissolution rates in mol.cm^{-2} of BET-argon surface. s^{-1} , where Velbel (1985) reported rates in mol.cm^{-2} of geometric surface. s^{-1} . For nine different, 1 cm sized naturally weathered feldspars by Holdren and Speyer (1987), it was shown in chapter 2 that their BET-argon surface area is two to three orders of magnitude larger than their geometric surface area. If this discrepancy holds also for the naturally weathered oligoclase by Velbel (1985), its dissolution rate normalized to the BET-argon surface would be two to three orders of magnitude lower than that for the albite by Knauss and Wolery (1986). Based on similar arguments, the discrepancy between field rates (in mol.cm^{-2} of geometric surface. s^{-1}) and laboratory rates (in mol.cm^{-2} of BET surface. s^{-1}) as reported by Pačes (1983) and Velbel (1985) would probably be larger still if the field rates were normalized to the BET surface.

Discrepancies between natural and laboratory dissolution rates may arise from differences in such factors as: pH, P_{CO_2} , the proportion of mineral surface in contact with the solution, concentrations of organic ligands, concentrations of inorganic solutes, liquid-flux, temperature, and the character of the mineral surfaces (Velbel, 1985, 1986; Furrer and Stumm, 1986; Amrhein and Suarez, 1988; Sverdrup and Warfvinge, 1988; Van Grinsven and Van Riemsdijk, 1992). In a comparison between laboratory feldspar dissolution rates and natural weathering rates of oligoclase, Velbel (1985, 1986) proposed that the two most likely sources of rate discrepancy were: (1) difficulties in estimating the reactive mineral surface area in natural systems; and (2) the reactive character of freshly created feldspar surfaces by grinding in the laboratory, relative to their naturally weathered counterparts.

Sverdrup and Warfvinge (1988) and Sverdrup (1990) studied the natural weathering of a number of minerals in the Gårdsjön watershed (Sweden). By using a kinetic expression to calculate natural weathering rates from laboratory dissolution data, they concluded that weathering rates in the Gårdsjön watershed can be explained satisfactory from the dissolution rates of ground samples. Uncertainties in their data still allow for rate discrepancies up to one order of magnitude, however. Moreover, they assumed that all BET surface area in their laboratory samples was freshly created by grinding. However, their samples presumably still contained substantial proportions of naturally weathered BET surface area, dissolving at a much lower rate (chapters 2 and 3). Furthermore, Sverdrup and Warfvinge (1988) and Sverdrup (1990) did not recognize the proportionality between dissolution rates of freshly created feldspar surfaces and grain diameter (chapter 3), and did not consider this possibility

for minerals other than feldspar. For instance, if the grain diameter after grinding were 10 % of the original grain diameter, this would explain approximately one order of magnitude in rate discrepancy. Finally, Sverdrup and Warfvinge (1988) and Sverdrup (1990) estimated specific BET surface areas ($\text{cm}^2 \cdot \text{g}^{-1}$) in the Gårdsjön watershed by assuming that the magnitude of surface roughness of the naturally weathered grains was similar to that of grains in their ground samples. However, roughness factors of naturally weathered surfaces may be up to several orders of magnitude larger than those of freshly created surfaces by grinding (chapter 2). If this were true for the samples by Sverdrup and Warfvinge (1988) and Sverdrup (1990), natural weathering rates in the Gårdsjön watershed, normalized to BET surface area, would be an additional few orders of magnitude smaller than calculated by these authors.

In chapter 3, the dissolution rates of freshly created and naturally weathered surfaces were compared for nine different, 1 cm sized feldspars used by Holdren and Speyer (1985, 1987). However, the diameter of naturally weathered grains in actual field situations is generally much smaller than 1 cm. In this chapter, the dissolution rates of freshly created and naturally weathered surfaces are compared for a mineral assemblage of much smaller average grain diameter ($612 \mu\text{m}$). Additionally, the results at this smaller grain diameter are compared to the earlier results from chapters 2 and 3 for the 1 cm sized fragments.

4.2. Theoretical considerations

In the analysis hereafter, all surface area of unfractured naturally weathered grains is by definition naturally weathered surface area. Furthermore, it is assumed that all surface area additionally created by grinding is surface area of freshly exposed mineral bulk, i.e. freshly created surface area. This is a reasonable assumption because all naturally weathered surface area is already exposed (to the measurement technique) at the start of the grinding process.

The effect of natural weathering on the dissolution rate can be quantified by the rate discrepancy factor, R_f/R_w , where R_f ($\text{mol} \cdot \text{cm}^{-2}$ of freshly created BET surface $\cdot \text{s}^{-1}$) and R_w ($\text{mol} \cdot \text{cm}^{-2}$ of naturally weathered BET surface $\cdot \text{s}^{-1}$) are the dissolution rates of freshly created and naturally weathered surfaces, respectively. R_w can be determined directly from dissolution experiments on unfractured naturally weathered sample material. Normally, however, R_f must be determined from experiments on ground samples containing both freshly created and naturally weathered surfaces (chapter 2). In such samples, R_f decreases with decreasing grain diameter, for instance, because the average density of dissolution reactive sites on freshly created surfaces decreases during grinding (chapter 3). R_f is actually the

hypothetical dissolution rate of the unfractured sample material, provided that it had not weathered. Therefore, R_f must be determined at the grain diameter of the unfractured sample material. In artificially ground samples, R_f is given by (see eq. 3.7):

$$R_f = (R_g - R_w)/F_f + R_w \quad (4.1)$$

where R_g (mol.cm^{-2} of BET surface. s^{-1}) is the dissolution rate of the ground sample as a whole, and where F_f is the proportion of the BET surface area of the ground sample which is freshly created by grinding. Thus, if R_f is calculated from eq. (4.1) at several grain diameters after grinding, R_f at the grain diameter of the unfractured material can be estimated from data extrapolation. For ground samples from nine different feldspars by Holdren and Speyer (1985, 1987), it was shown in chapter 3 that: (1) R_f is approximately proportional to the grain diameter below 1000 μm (for instance, because preferential fracture planes have relatively high densities of dissolution reactive sites); and (2) at infinitely large grain diameter, R_f reaches a maximum (for instance, because the density of dissolution reactive sites reaches a maximum). R_f may then be described empirically as a function of grain diameter by:

$$R_f = \frac{d_g}{d_g + d_r} R_{f\text{-max.}} \quad (4.2)$$

where d_g is the average grain diameter of the ground material, d_r is a reference grain diameter (for which $R_f = 0.5 R_{f\text{-max.}}$), and $R_{f\text{-max.}}$ is the hypothetical dissolution rate of freshly created surfaces at infinitely large grain diameter.

Determination of the proportion of freshly created BET surface area (F_f) in artificially ground samples is dealt with in chapter 2. Briefly, the surface roughness factor (λ) of ground sample material equals the ratio of the BET surface area (S ; cm^2) to the geometric surface area (s ; cm^2):

$$\lambda = S/s \quad (4.3)$$

For ground sample material, derived from naturally weathered grains, the surface roughness factor (λ_g) can be empirically described as a function of grain diameter (d_g) by (eq. 2.18):

$$\lambda_g = \alpha d_g + \beta + \gamma(1 - d_g/d_w)^\delta \quad (4.4)$$

where α (≥ 0), β (≥ 1), γ (≥ 0) and δ (≥ 1) are independent of the grain diameter and may

be estimated from data extrapolation, and where d_w is the average grain diameter of the naturally weathered starting material. Eq. (4.4) can be used to estimate the roughness factors of the freshly created surfaces (λ_f) and naturally weathered surfaces (λ_w) in the ground sample material. For instance, if $\gamma = 0$, the relation is linear and β equals λ_f (chapter 2). Once λ_f and λ_w are estimated, F_f is found from (eq. 2.8):

$$F_f = [\lambda_f(\lambda_w - \lambda_g)] / [\lambda_g(\lambda_w - \lambda_f)] \quad (4.5)$$

It follows from eq. (4.5) that $F_f = 0$ for the unfractured material ($\lambda_g = \lambda_w$). It follows from eqs. (4.4) and (4.5) that, at grain diameter $0 \mu\text{m}$, $F_f = 1$ if $\gamma = 0$ ($\lambda_g = \beta = \lambda_f$ if $\gamma = 0$).

4.3. Sample preparation and characterization

One of the research aims was to relate the mineralogy of exposed surfaces in the samples to the bulk mineralogical composition. Therefore, preliminary studies using scanning electron microscopy (SEM), optical microscopy and X-Ray diffraction were performed on unfractured naturally weathered grains of several candidate samples to select material: (1) free from secondary mineral coatings; and (2) with the constituent minerals homogeneously distributed over the grains. The selected material was a non-calcareous coastal sand from Tatamagouche Bay, Nova Scotia, Canada, containing approximately 50, 33 and 7 % by mass of quartz, microcline-perthite and plagioclase, respectively. Its nature and geologic setting are discussed in more detail by Loring and Nota (1973).

All available material was dry-sieved to collect the coarsest size fraction (600-850 μm). The feldspar (and quartz) in the 600-850 μm fraction was concentrated by removing grains with densities smaller than 2.56 and larger than 2.88 g.cm^{-3} using bromoform and a mixture of bromoform and decaline (Van Der Plas, 1966). The feldspar concentrate (8 g) was washed with ethanol to remove the bromoform and decaline, and with deionized water to remove the ethanol. 6 g was ground in a mortar by applying a few light strokes at a time, followed by dry-sieving to fractions 300-425 μm (2 g), 105-210 μm (2 g), 53-105 μm (0.8 g) and < 53 μm . The ground samples and the remaining unfractured concentrate were washed with deionized water until the supernatant was clear immediately after settling of the bulk. Grains < 5 μm were washed from the sample < 53 μm . Three mild (low intensity) ultrasonic cleaning steps of 10 minutes each, followed by washing with deionized water after each step, were applied to all samples. In our experience, this should suffice to remove most of the adhering ultrafines produced by grinding. However, after the third cleaning step the supernatants were

Table 4.1. X-Ray fluorescence spectrometry data.

fraction (μm)	600-850	300-425	105-210	53-105	< 53
Na_2O^1	2.66/ 2.69	2.70/ 2.63	2.74/ 2.59	2.65/ 2.72	2.02/ 1.89
K_2O	3.70/ 3.62	3.73/ 3.69	3.55/ 3.68	3.68/ 3.67	3.79/ 3.70
CaO	0.46/ 0.38	0.39/ 0.50	0.40/ 0.42	0.41/ 0.36	0.15/ 0.21
Al_2O_3	11.66/11.40	11.91/11.59	11.23/11.57	11.31/11.48	10.43/10.01
MgO	0.11/ 0.14	0.11/ 0.07	0.04/ 0.13	0.16/ 0.10	0.24/ 0.21
Fe_2O_3	0.23/ 0.32	0.32/ 0.22	0.32/ 0.26	0.16/ 0.29	1.40/ 1.32
SiO_2	81.01/80.57	81.46/81.11	80.99/80.43	79.98/80.24	82.97/82.43
others ²	0.09/ 0.17	0.10/ 0.13	0.06/ 0.13	0.10/ 0.26	0.22/ 0.12
sum	99.92/99.29	100.72/99.94	99.33/99.21	98.45/99.12	101.22/99.89

¹ all oxides in duplicate, expressed as weight %.

² $\text{BaO} + \text{TiO}_2 + \text{MnO}$.

still slightly cloudy for all samples. The cloudiness of the unfractured sample indicates that (part of) the suspended ultrafines did not result from grinding. Given the careful sample selection, the cloudiness most likely can not be attributed to secondary phases. Alternatively, it may be due to the presence of finely divided primary phases, or of residual layers from natural weathering on the primary phases. To avoid further possible damage of existing surface structures, the ultrasonic cleaning was restricted to 30 minutes total for all samples.

All samples were analyzed by X-Ray fluorescence spectrometry (XRFS; Table 4.1), X-Ray diffraction and optical microscopy for normative calculations (Brown and Skinner, 1974; Davis, 1986). Powder diffraction patterns were obtained from a Guinier camera. Optical polarizing microscopy (Van Der Plas, 1966) and X-Ray diffraction data indicate that all samples are composed of microcline-perthite (≈ 33 weight %, assumed to consist of a pure albite, $\text{NaAlSi}_3\text{O}_8$, and a pure microcline, KAlSi_3O_8 , component), plagioclase (≈ 7 weight %, according to the method by Tobi (1963) consisting of oligoclase and andesine of approximate average composition $\text{Ab}_{70}\text{An}_{30}$), quartz (≈ 50 weight %, assumed pure SiO_2), muscovite (≈ 9 weight %, assumed pure $\text{KAl}_3\text{Si}_3\text{O}_{10}(\text{OH})_2$) and biotite (≈ 1 weight %, assumed pure $\text{K}(\text{Mg},\text{Fe}^{++})_3\text{AlSi}_3\text{O}_{10}(\text{OH})_2$). According to XRFS, the summed mass fraction of oxides of other elements (Ba, Ti and Mn) was < 0.2 % in all samples. Optical microscopy showed that the samples contain approximately 5 % of rock fragments with very small amounts (≈ 0.1 % of total mass) of amphibole, hypersthene and garnet. The results of the normative calculations are given in Table 4.2.

Using the method by De Kanel and Morse (1979), specific BET surface areas were estimated for all samples from a 3-point krypton adsorption isotherm (Table 4.2). General

Table 4.2. Sample characterization.

fraction (μm)	600-850	300-425	105-210	53-105	< 53
albite ¹	693/.18	673/.17	695/.18	716/.18	554/.15
microcline	523/.15	519/.15	522/.14	542/.15	461/.13
plagioclase ²	251/.07	264/.07	247/.07	233/.07	107/.03
muscovite	237/.09	249/.10	233/.09	229/.09	256/.10
biotite	22/.01	19/.01	19/.01	20/.01	75/.03
quartz	8419/.50	8408/.50	8473/.51	8371/.50	9385/.56
S^* ($\text{cm}^2\cdot\text{g}^{-1}$) ³	1730	1780	2200	3900	13650
s^* ($\text{cm}^2\cdot\text{g}^{-1}$) ⁴	50.4	87.9	144	482	
d (μm) ⁵	612	346	205	69	14

¹ all minerals expressed as $\mu\text{mol}\cdot\text{g}^{-1}$ sample/mass fraction; the albite and microcline are mainly present as microcline-perthite.

² present as oligoclase and andesine ($\text{Ab}_{70}\text{An}_{30}$).

³ specific BET-krypton surface area; estimated accuracy $\pm 20\%$, estimated precision $\pm 5\%$.

⁴ specific geometric surface area; estimated accuracy $\pm 10\%$.

⁵ average equivalent spherical grain diameter; estimated accuracy $\pm 10\%$.

equations were derived for 17 different types of grain geometry (ellipsoids, prisms, pyramids, etc., and combinations) to calculate the volume and geometric surface area of individual grains from variable linear grain dimensions. This allows determination of the average equivalent spherical grain diameter and of the specific geometric surface area of samples in terms of an almost infinitely large number of possible grain shapes. The linear dimensions of 50 individual grains in each of the samples $> 53 \mu\text{m}$ were determined from observation by a dissecting microscope (40x). At this scale of surface detail, etch pits and pores are not observed and have no effect on the surface area estimate. Dimensions parallel to the microscope axis were obtained from measurement of shadows, cast by a rotatable light source at known angles. The average equivalent spherical grain diameter of the sample $< 53 \mu\text{m}$ was estimated from microscopic observation at 250x magnification (Ellison, 1954; Robins, 1954). Data on specific geometric surface area and average equivalent spherical grain diameter are given in Table 4.2.

The surface morphology of grains in the unfractured 600-850 μm and in the ground 105-210 μm material was examined by SEM. The unfractured material contains only few and small etch pits (Fig. 4.1). Apart from the etch pits, no other weathering-related surface details were found with magnifications up to 10,000x. Geometric calculations on SEM images of

representative surfaces at 1000x (taken at different angles to obtain 3-dimensional

Table 4.1. X-Ray fluorescence spectrometry data.

fraction (μm)	600-850	300-425	105-210	53-105	< 53
Na ₂ O ¹	2.66/ 2.69	2.70/ 2.63	2.74/ 2.59	2.65/ 2.72	2.02/ 1.89
K ₂ O	3.70/ 3.62	3.73/ 3.69	3.55/ 3.68	3.68/ 3.67	3.79/ 3.70
CaO	0.46/ 0.38	0.39/ 0.50	0.40/ 0.42	0.41/ 0.36	0.15/ 0.21
Al ₂ O ₃	11.66/11.40	11.91/11.59	11.23/11.57	11.31/11.48	10.43/10.01
MgO	0.11/ 0.14	0.11/ 0.07	0.04/ 0.13	0.16/ 0.10	0.24/ 0.21
Fe ₂ O ₃	0.23/ 0.32	0.32/ 0.22	0.32/ 0.26	0.16/ 0.29	1.40/ 1.32
SiO ₂	81.01/80.57	81.46/81.11	80.99/80.43	79.98/80.24	82.97/82.43
others ²	0.09/ 0.17	0.10/ 0.13	0.06/ 0.13	0.10/ 0.26	0.22/ 0.12
sum	99.92/99.29	100.72/99.94	99.33/99.21	98.45/99.12	101.22/99.89

¹ all oxides in duplicate, expressed as weight %.

² BaO + TiO₂ + MnO.

still slightly cloudy for all samples. The cloudiness of the unfractured sample indicates that (part of) the suspended ultrafines did not result from grinding. Given the careful sample selection, the cloudiness most likely can not be attributed to secondary phases. Alternatively, it may be due to the presence of finely divided primary phases, or of residual layers from natural weathering on the primary phases. To avoid further possible damage of existing surface structures, the ultrasonic cleaning was restricted to 30 minutes total for all samples.

All samples were analyzed by X-Ray fluorescence spectrometry (XRFS; Table 4.1), X-Ray diffraction and optical microscopy for normative calculations (Brown and Skinner, 1974; Davis, 1986). Powder diffraction patterns were obtained from a Guinier camera. Optical polarizing microscopy (Van Der Plas, 1966) and X-Ray diffraction data indicate that all samples are composed of microcline-perthite (\approx 33 weight %, assumed to consist of a pure albite, NaAlSi₃O₈, and a pure microcline, KAlSi₃O₈, component), plagioclase (\approx 7 weight %, according to the method by Tobi (1963) consisting of oligoclase and andesine of approximate average composition Ab₇₀An₃₀), quartz (\approx 50 weight %, assumed pure SiO₂), muscovite (\approx 9 weight %, assumed pure KAl₃Si₃O₁₀(OH)₂) and biotite (\approx 1 weight %, assumed pure K(Mg,Fe⁺⁺)₃AlSi₃O₁₀(OH)₂). According to XRFS, the summed mass fraction of oxides of other elements (Ba, Ti and Mn) was < 0.2 % in all samples. Optical microscopy showed that the samples contain approximately 5 % of rock fragments with very small amounts (\approx 0.1 % of total mass) of amphibole, hypersthene and garnet. The results of the normative calculations are given in Table 4.2.

Using the method by De Kanel and Morse (1979), specific BET surface areas were estimated for all samples from a 3-point krypton adsorption isotherm (Table 4.2). General

Table 4.2. Sample characterization.

fraction (μm)	600-850	300-425	105-210	53-105	< 53
albite ¹	693/.18	673/.17	695/.18	716/.18	554/.15
microcline	523/.15	519/.15	522/.14	542/.15	461/.13
plagioclase ²	251/.07	264/.07	247/.07	233/.07	107/.03
muscovite	237/.09	249/.10	233/.09	229/.09	256/.10
biotite	22/.01	19/.01	19/.01	20/.01	75/.03
quartz	8419/.50	8408/.50	8473/.51	8371/.50	9385/.56
S^* ($\text{cm}^2 \cdot \text{g}^{-1}$) ³	1730	1780	2200	3900	13650
s^* ($\text{cm}^2 \cdot \text{g}^{-1}$) ⁴	50.4	87.9	144	482	
d (μm) ⁵	612	346	205	69	14

¹ all minerals expressed as $\mu\text{mol} \cdot \text{g}^{-1}$ sample/mass fraction; the albite and microcline are mainly present as microcline-perthite.

² present as oligoclase and andesine ($\text{Ab}_{70}\text{An}_{30}$).

³ specific BET-krypton surface area; estimated accuracy $\pm 20\%$, estimated precision $\pm 5\%$.

⁴ specific geometric surface area; estimated accuracy $\pm 10\%$.

⁵ average equivalent spherical grain diameter; estimated accuracy $\pm 10\%$.

equations were derived for 17 different types of grain geometry (ellipsoids, prisms, pyramids, etc., and combinations) to calculate the volume and geometric surface area of individual grains from variable linear grain dimensions. This allows determination of the average equivalent spherical grain diameter and of the specific geometric surface area of samples in terms of an almost infinitely large number of possible grain shapes. The linear dimensions of 50 individual grains in each of the samples $> 53 \mu\text{m}$ were determined from observation by a dissecting microscope (40x). At this scale of surface detail, etch pits and pores are not observed and have no effect on the surface area estimate. Dimensions parallel to the microscope axis were obtained from measurement of shadows, cast by a rotatable light source at known angles. The average equivalent spherical grain diameter of the sample $< 53 \mu\text{m}$ was estimated from microscopic observation at 250x magnification (Ellison, 1954; Robins, 1954). Data on specific geometric surface area and average equivalent spherical grain diameter are given in Table 4.2.

The surface morphology of grains in the unfractured 600-850 μm and in the ground 105-210 μm material was examined by SEM. The unfractured material contains only few and small etch pits (Fig. 4.1). Apart from the etch pits, no other weathering-related surface details were found with magnifications up to 10,000x. Geometric calculations on SEM images of representative surfaces at 1000x (taken at different angles to obtain 3-dimensional information) give an estimated roughness factor of approximately 2.2 ± 0.3 for naturally



Fig. 4.1. Morphology of naturally weathered surfaces in the 600-850 μm fraction as viewed by SEM, prior to experiments. a: microcline-perthite surface with few and small etch pits; $\lambda_w \approx 1.3$; the central, triangular feature is not an etch pit. b: small microcline-perthite (lower left) and large quartz crystals on a very rough surface; $\lambda_w \approx 3$ to 4; notice the absence of etch pits in the quartz.

weathered surfaces (Fig. 4.1) and 1.6 ± 0.2 for freshly created surfaces. Roughness factors were also estimated from SEM images of representative surfaces at 10,000x. Due to the increased surface detail these were higher than those at 1000x, and were approximately 2.8 ± 0.4 and 2.1 ± 0.3 for the naturally weathered and freshly created surfaces, respectively.

4.4. Dissolution experiments

Single-pass flow-through reaction cells (Levenspiel, 1972; Weed and Jackson, 1979) were used for experiments. Their advantages over static and multiple-pass dynamic systems are: (1) no precipitation of secondary solids at sufficiently high flow rates; (2) dissolving minerals are easily kept far from equilibrium; (3) aqueous concentrations in the reaction cells are essentially constant with time; and (4) close simulation of the leaching action of dilute solutions in saturated groundwater systems. The samples and two blanks on empty cells were leached with HCl solutions at pH 3 and pH 5. Due to atmospheric CO_2 , pH 5 was reached at a slightly lower HCl concentration than in pure $\text{H}_2\text{O}/\text{HCl}$. The pH was set by a voltmeter and was periodically checked, both in the leachants and in the leachates of all runs. Variations in pH of the leachants were always within 0.1 units and usually within 0.04 units. All H_2O was obtained from an ELGASTAT UHQ unit. All pH 5 leachates were acidified to pH 3 by adding 1 M HCl before storage. Samples were analyzed for Na, K, Ca, Al and Si at 1 to 3 weeks intervals using a Varian SpectrAA 300 graphite tube autoanalyzer. The experiments were run at 21 ± 3 °C. Leachates were collected at 3 to 4 days intervals.

The experimental equipment consists of: (1) several three-liter hospital infusion bags as closed leachant supply tanks; (2) peristaltic pumps at a flow rate of 0.48 ± 0.03 ml.hr⁻¹; (3) polycarbonate in-line filter holders, switched for upward flow, as reaction cells; (4) 100 ml plastic bottles to collect leachates; and (5) waterseals to avoid atmospheric contamination in the collection bottles over sampling intervals. Capillary polyethylene tubing and polycarbonate mini-corks were used for interconnections, except for flexible PVC tubing to feed the leachant through the pumps. Sample chambers were teflon rings (5 mm height and inner diameter of 30 mm) inside the filter holders, fitted with 0.1 μm nylon membrane filters on both ends. The average residence time of leachant in the sample chambers was approximately 6.5 hrs. Sample heights were about 1 mm, so concentration gradients were essentially absent. The upward flow in the sample chambers (0.07 cm.hr⁻¹) may have lifted mineral particles of up to approximately 0.5 μm maximum diameter. Some of these may have passed the top filter to accumulate in the collection bottles. During storage at pH 3 they probably dissolve entirely,

causing false dissolution data for the first few days when ultrafines may still be present (Holdren and Berner, 1979). However, calculations hereafter involve steady state dissolution rates, which were reached after several months of leaching, so all material passing the 0.1 μm membrane filters was assumed to be effectively in solution. Alkali- and alkaline earth cations in freshly created surficial layers are generally highly reactive in acid aqueous solutions, causing non-stoichiometric dissolution during the initial periods of experiments (e.g. Chou and Wollast, 1984; Murphy and Helgeson, 1987). Washing upon sonification during the pretreatment may thus have "preweathered" the ground samples. However, the effect of such initial reactions on the steady state dissolution rates of Na, K and Ca in this type of experiments can be neglected (Murphy and Helgeson, 1987).

Experiments at pH 3 (days 0 to 141) were run for all samples. Experiments at pH 5 (days 141 to 305) were run for the samples 600-850, 300-425, 105-210, and $< 53 \mu\text{m}$. Occasional duplicates indicate that typical analytic errors are 5 % for Si, 10 % for Al, 15 % for Ca, and 20 % for K and Na. Acceptable data for K and Na are not available for the 300-425 μm and $< 53 \mu\text{m}$ sample and can be compared to data for the other samples only for portions of total running time. However, these include large parts of the steady state periods.

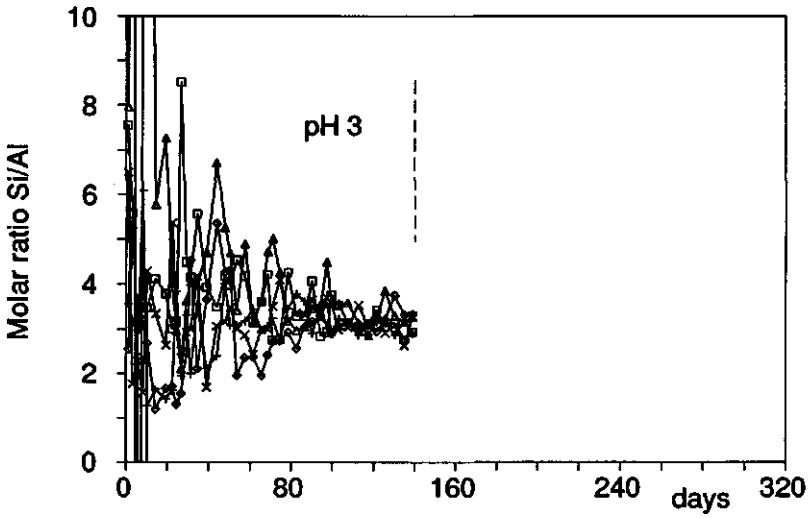


Fig. 4.2. Molar ratios Si/Al versus time during the pH 3 stage of the dissolution experiments. \square : 600-850 μm (unfractured); + : 300-425 μm (ground); \diamond : 105-210 μm (ground); \triangle : 53-105 μm (ground); \times : $< 53 \mu\text{m}$ (ground).

4.5. Results

Molar ratios of Si to Al in the pH 3 leachates (Fig. 4.2) invariably showed high initial scattering, but gradually leveled off to a final value of 3.0 to 3.5. From day 108 onward, steady state was assumed for all samples (Figs. 4.2 and 4.3a-e). Initial dissolution rates of Al (Fig. 4.3a) and Si (Fig. 4.3b) were high for approximately three weeks. This holds also for the unfractured sample, so the high initial rates cannot be caused solely by the dissolution of ultrafines from grinding. Al and Si rates stabilized over the course of several months. At pH 3 steady state, Al and Si showed a maximum dissolution rate at an intermediate grain diameter (105-210 μm).

Switching the input solution to pH 5 caused an immediate, large decrease in Al concentrations (Fig. 4.3a). This remained during total running time of the experiments. The increase in pH caused a small initial drop in Si dissolution rates, followed by a slow decrease to a new steady state level which was reached at approximately day 240 (Fig. 4.3b). For Si at pH 5, the dissolution rate was again highest for the 105-210 μm sample.

For Na and Ca, dissolution rates at pH 3 steady state were again highest for the 105-210 μm sample (Figs. 4.3c and d). In contrast, K dissolution rates at pH 3 were of approximately the same order of magnitude (Fig. 4.3e). Upon changing the pH from 3 to 5, dissolution rates of Na, Ca and K quickly dropped to much lower levels. The data over the

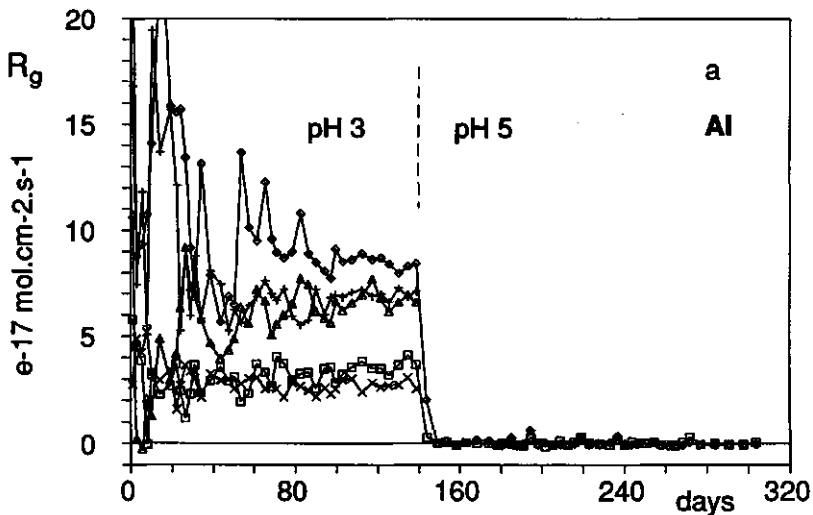


Fig. 4.3. Experimental dissolution rates normalized to BET surface (R_g) versus time. \square : 600-850 μm (unfractured); + : 300-425 μm (ground); \diamond : 105-210 μm (ground); \triangle : 53-105 μm (ground); \times : < 53 μm (ground). a: Al; b: Si; c: Na; d: Ca; e: K.

steady state periods at pH 3 and 5 were used to calculate the mean dissolution rates and standard deviations, normalized to BET-krypton surface area (Table 4.3). The dissolution rates at pH 5 may differ from those without prior experiments at pH 3.

Occasional measurements showed that, at pH 3, leachant pH was not affected significantly by mineral dissolution. Equilibrium calculations (GEOCHEM; Mattigod and Sposito, 1978; Nordstrom *et al.*, 1978) for the quartz and feldspar at pH 3 showed that they

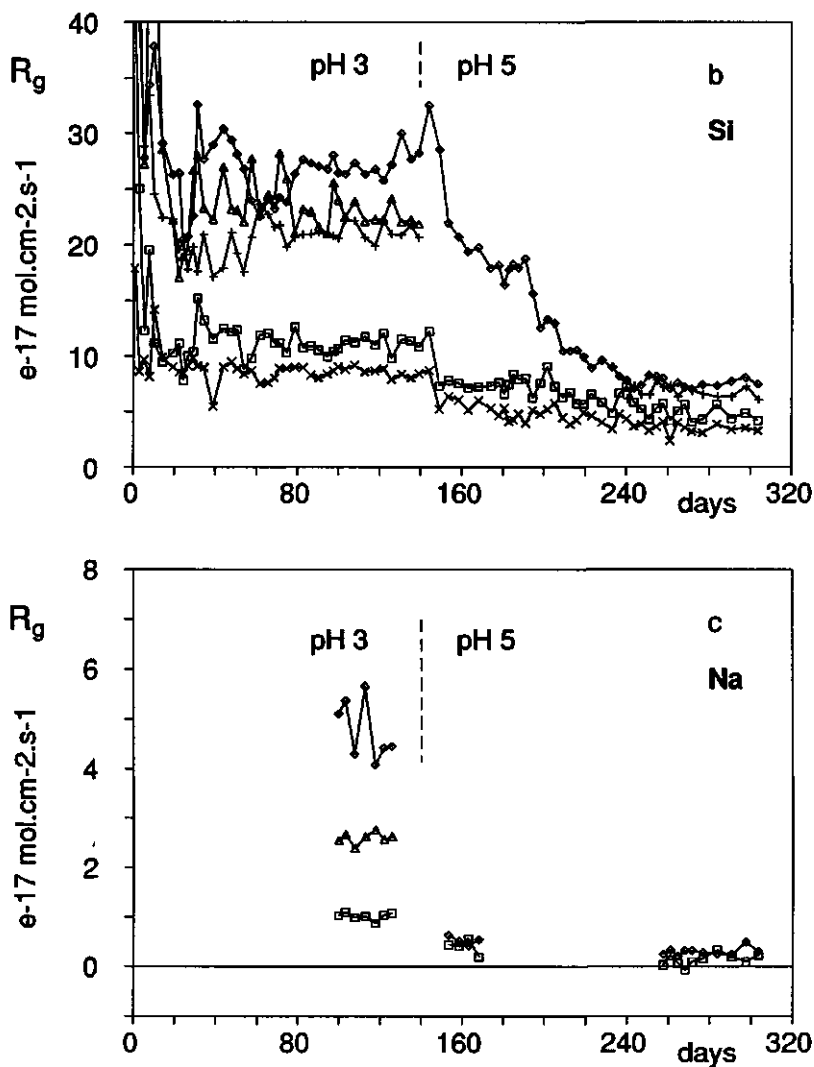


Fig. 4.3. Continued.

dissolve far from equilibrium (saturation indices of quartz ≈ -3 ; saturation indices of feldspar ≈ -20). At pH 5, the pH of leachates from the 105-210 μm sample at days 163, 219 and 261 was 5.13 ± 0.1 , 5.17 ± 0.1 and 5.07 ± 0.1 , respectively. Equilibrium calculations (GEOCHEM) for a number of common secondary phases indicate that the leachates were undersaturated for all phases considered. Highest saturation indices were found at pH 5.17 for gibbsite (-0.34) and kaolinite (-0.36).

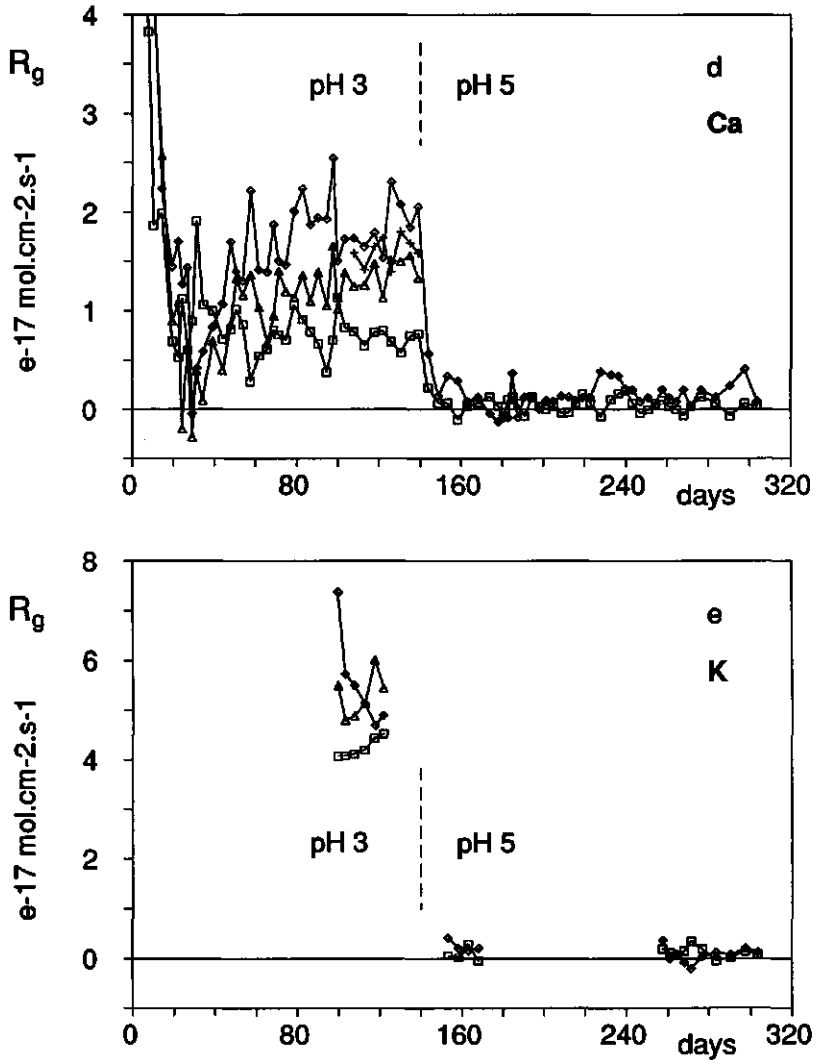


Fig. 4.3. Continued.

Table 4.3. Mean dissolution rates and standard deviations in 10^{-17} mol.cm⁻² of BET surface.s⁻¹ at steady state pH 3 and pH 5 HCl.

fraction (μm)	600-850	300-425	105-210	53-105	<53
Na pH 3	1.01 \pm 0.08		4.59 \pm 0.62	2.59 \pm 0.13	
K pH 3	4.33 \pm 0.19		5.06 \pm 0.35	5.37 \pm 0.49	
Ca pH 3	0.73 \pm 0.08	1.61 \pm 0.14	1.88 \pm 0.25	1.38 \pm 0.16	
Al pH 3	3.65 \pm 0.26	7.02 \pm 0.21	8.53 \pm 0.29	6.88 \pm 0.45	2.76 \pm 0.22
Si pH 3	11.3 \pm 0.7	21.2 \pm 0.8	27.4 \pm 1.3	22.6 \pm 0.9	8.54 \pm 0.42
Na pH 5	0.15 \pm 0.10		0.30 \pm 0.08		
K pH 5	0.14 \pm 0.11		0.09 \pm 0.13		
Ca pH 5	0.04 \pm 0.07		0.16 \pm 0.10		
Al pH 5	0.03 \pm 0.10		-0.04 \pm 0.05		
Si pH 5	5.09 \pm 0.89	6.92 \pm 0.53	7.61 \pm 0.41		3.54 \pm 0.48

4.6. Discussion

The surface roughness factor (λ_g) of the samples $> 53 \mu\text{m}$ was plotted versus the average equivalent spherical grain diameter (d_g) from the data in Table 4.2 (Fig. 4.4). Over the entire range of grain diameters the relation between λ_g and d_g is linear, so $\gamma = 0$ in eq. (4.4), and:

$$\lambda_g = 0.0477 d_g + 4.8 \quad (r^2 = 0.99) \quad (4.6)$$

Substituting values of d_g (Table 4.2) into eq. (4.6) gives: $\lambda_w(600-850 \mu\text{m}) = 34.0$, $\lambda_g(300-425 \mu\text{m}) = 21.3$, $\lambda_g(105-210 \mu\text{m}) = 14.6$, $\lambda_g(53-105 \mu\text{m}) = 8.1$, $\lambda_g(< 53 \mu\text{m}) = 5.5$ and $\lambda_f = 4.8$. Consequently, estimates of F_f (eq. 4.5) are: $F_f(300-425 \mu\text{m}) = 0.10$, $F_f(105-210 \mu\text{m}) = 0.22$, $F_f(53-105 \mu\text{m}) = 0.53$ and $F_f(< 53 \mu\text{m}) = 0.85$. These values will be used throughout the calculations hereafter. Given the high value of r^2 in eq. (4.6), estimates of F_f should be internally consistent within approximately 0.05 units. From the estimated accuracy of specific surfaces areas and grain diameters (Table 4.2), the maximum error in F_f is approximately 0.2 units, but will generally be smaller than 0.1 units (chapter 3).

SEM, optical microscopy and X-Ray diffraction gave no evidence for the presence of secondary mineral coatings on the naturally weathered grains. Differences between the roughness factor of freshly created surfaces (λ_f) and of naturally weathered surfaces (λ_w) must then be attributed to additionally created BET surface area in the primary phases, for

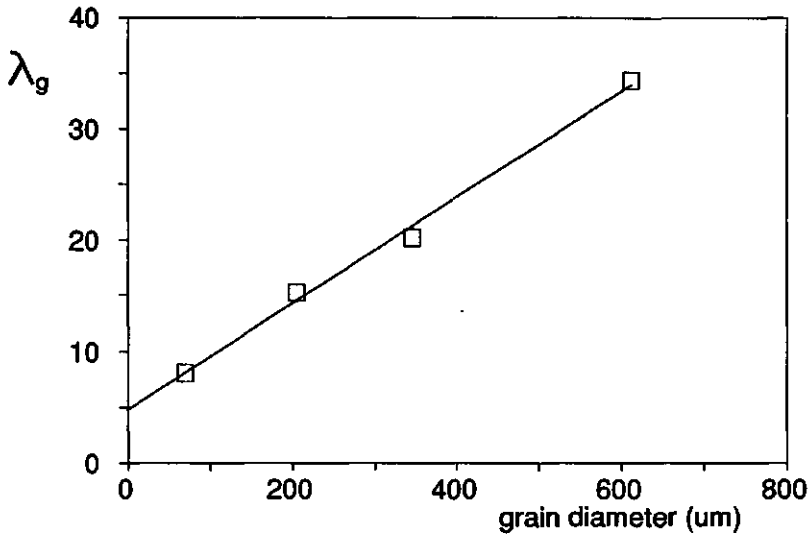


Fig. 4.4. Surface roughness factor (λ_g) versus the grain diameter (d_g ; μm) using the data from Table 4.2.

instance, by etch pitting (Helgeson *et al.*, 1984). However, λ_w from BET analysis is 34.0 and far exceeds the value of 2.8 estimated from SEM observation at 10,000x. This indicates that only small part of the BET area created during natural weathering can be explained from etch pits (whose effect on λ_w is included in the SEM estimate). Other sources of BET area that may explain the discrepancy between λ_w from SEM analysis and from the BET method are:

(1) Macropores (diameters > 50 nm); these have been observed throughout the bulk of naturally weathered feldspar grains (e.g. Montgomery and Brace, 1975; Ferry, 1985; Worden *et al.*, 1990). The macropores may result from fluid inclusions that formed during the initial cooling of the pluton, followed by leakage and weathering under earth surface conditions (Parsons *et al.*, 1988).

(2) Micropores (diameters ≤ 2 nm) and mesopores ($2 < \text{diameters} \leq 50$ nm); these have been observed in surficial layers of silicates after dissolution experiments (e.g. Pacco *et al.*, 1976; Bunker *et al.*, 1988; Casey *et al.*, 1989a,b; Zhang *et al.*, 1993). The micropores may form during leached layer formation (Doremus, 1983; Casey and Bunker, 1990); micropores and/or mesopores may form at crystal defects (Van Der Hoek *et al.*, 1982; Lasaga and Blum, 1986; see also chapter 7).

(3) Surface details other than pores, created during natural weathering and smaller than approximately 100 nm; these are detected by the BET method but not by SEM at 10,000x.

Because the origin of the BET surface area created during natural weathering is not critical for determining values of R_t/R_w , this was not investigated any further in the present

research (see chapter 5 for a detailed discussion on this subject).

For nine different, 1 cm sized naturally weathered feldspars by Holdren and Speyer (1985, 1987), it was shown in chapter 2 that λ_w from BET-argon analysis ranges from approximately 130 to 2600. The smaller λ_w of 34.0 for the Nova Scotia sample 600-850 μm may be due to the presence of quartz or to a shorter period of exposure to natural weathering conditions. Alternatively, λ_w may be smaller as a result of the smaller average diameter of the unfractured Nova Scotia grains. It was proposed in chapter 3 that the average density of dissolution reactive sites on freshly created feldspar surfaces (cm^{-2} of BET surface) decreases with decreasing grain diameter. If so, the average density of dissolution reactive sites on freshly created feldspar surfaces in the natural environment, for instance, by the mechanical action of rivers, glaciers, etc., probably decreases with decreasing grain diameter too. Subsequent weathering, creating additional BET surface area at dissolution reactive sites, would then give rougher surfaces (and, consequently, larger λ_w) at larger grain diameters.

The dissolution rate of the freshly created surfaces in the ground samples (R_f) was calculated from eq. (4.1) and from the data in Table 4.3. Plots of R_f versus the average equivalent spherical grain diameter (Fig. 4.5) show that dissolution rates of the freshly created surfaces decrease with decreasing grain diameter. Except perhaps for K, they approach zero at very small grain diameters. Steady state dissolution rates at pH 5 for elements other than Si are inaccurate (Fig. 4.3) and were not used to estimate values of R_f/R_w . Eq. (4.2) was used to fit the data in Fig. 4.5, giving estimates of d_f and $R_f\text{-max}$. (Table 4.4). These were used to extrapolate R_f at the grain diameter of the unfractured material, leading to estimates of R_f/R_w (Table 4.4). The estimates indicate that dissolution rates of freshly created surfaces at 612 μm are approximately one order of magnitude higher than those of the naturally weathered surfaces in these samples. The results for Si indicate that R_f/R_w increases with decreasing pH (Table 4.4).

In a simplified model, the BET surface area exists of a number of dissolution reactive sites and a number of non-reactive sites (Helgeson *et al.*, 1984). The discrepancy in dissolution rates at 612 μm between the freshly created and the naturally weathered surfaces may then be explained in two ways: (1) the ratio of the number of dissolution reactive sites to the total number of sites is larger for the freshly created than for the naturally weathered BET surfaces; or (2) the dissolution rate, normalized to the dissolution reactive surface area, is higher for the freshly created surfaces than for the naturally weathered surfaces. However, at pH 3 HCl, explanation (2) seems unlikely because dissolution took place far from equilibrium.

Under these conditions, dissolution rates normalized to the reactive surface area are essentially independent of surface morphology (Helgeson *et al.*, 1984; see also chapter 7). Explanation (1) is true, for instance, if most or all surface sites additionally created during natural weathering are non-reactive. Possible examples are: (1) the development of leached

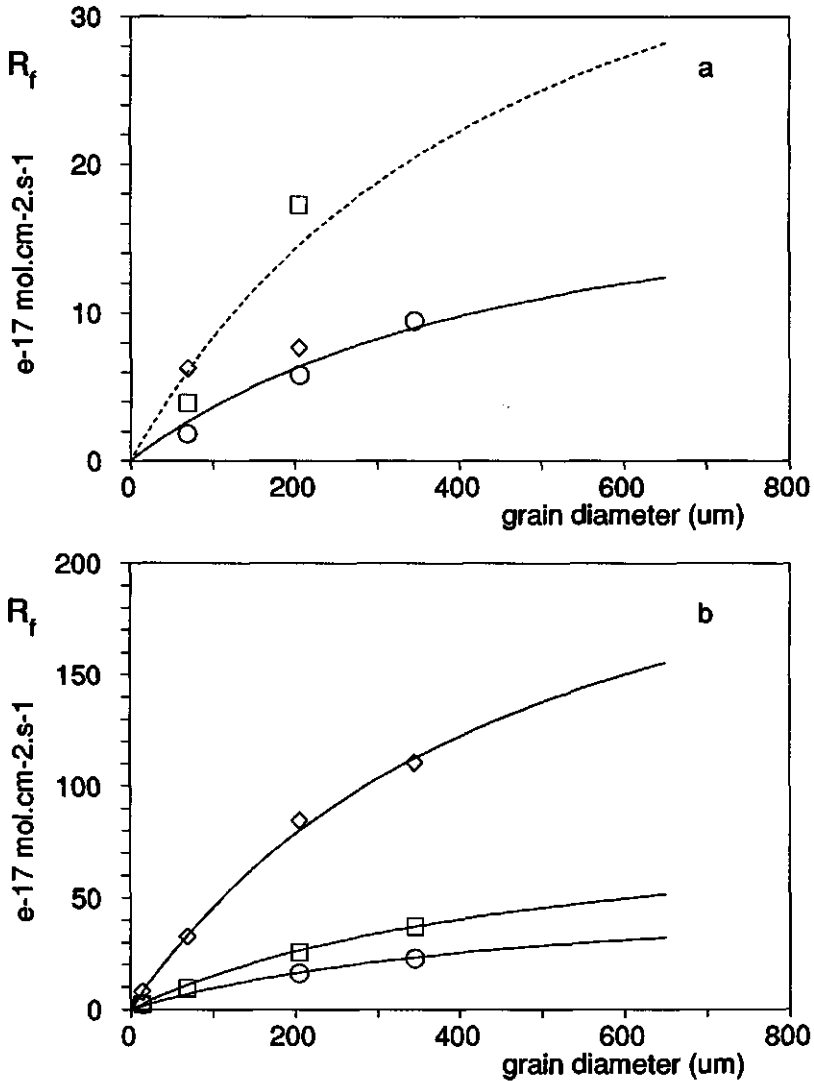


Fig. 4.5. Dissolution rate, normalized to the freshly created BET surface area (R_f), versus the grain diameter (d_g ; μm). Plot a: \square : Na (pH 3); \diamond : K (pH 3); \circ : Ca (pH 3); dashed curve for Na may be inaccurate; curve for K not plotted (see also Table 4.4). Plot b: \square : Al (pH 3); \diamond : Si (pH 3); \circ : Si (pH 5).

Table 4.4. Estimates of d_r and R_f -max. (see eq. 4.2), and of R_f and R_f/R_w at 612 μm . R_f -max. and R_f at 612 μm are in 10^{-17} mol.cm $^{-2}$ of BET surface.s $^{-1}$.

	Na pH 3	K ¹ pH 3	K ² pH 3	Ca pH 3	Al pH 3	Si pH 3	Si pH 5
d_r (μm)	500	500	500	500	500	500	500
R_f -max.	50	27	52	22	91	275	57
R_f at 612 μm	28	15	29	12	50	151	31
R_f/R_w at 612 μm ³	28 \pm 8	4 \pm 1	7 \pm 2	16 \pm 5	14 \pm 2	13 \pm 2	6 \pm 3

¹ estimated assuming the dissolution rate of the 105-210 μm fraction to be correct (Fig. 4.5a).

² estimated assuming the dissolution rate of the 53-105 μm fraction to be correct (Fig. 4.5a).

³ error indications for R_f/R_w are calculated from dissolution rates of the fractions 600-850 and 105-210 μm that differ by one standard deviation from their mean values (Table 4.3), except for the alternative estimate of R_f/R_w for K, where the dissolution rate and standard deviation of the 53-105 μm fraction were used instead.

layers; obviously, the BET surface area in leached layers is less- or non-reactive, at least for the leached substances; or (2) the development of micropores/mesopores at crystal defects; because pore growth at crystal defects proceeds by increasing the depth and not the diameter (Van Der Hoek *et al.*, 1982; see also chapter 7), the BET area perpendicular to the mineral surface (the pore "walls") is, in fact, non-reactive.

From the preceding, the difference in surface area character between freshly created and naturally weathered surfaces in ground samples can be explained as a function of grain diameter as follows. Grinding of large, hypothetical fresh-surface grains gradually decreases the dissolution site density (cm $^{-2}$ of BET surface) with decreasing grain diameter. Large, naturally weathered grains of similar diameter as their fresh-surface counterparts have a (much) lower dissolution site density because most of the BET surface area additionally created during natural weathering is non-reactive. However, the naturally weathered surfaces after grinding originate from the unfractured grains (chapter 3), so their dissolution site density is independent of grain diameter, and is determined by the grain diameter prior to grinding, and not by the grain diameter after grinding. Thus, there exists a grain diameter in the ground material where the dissolution site densities (and dissolution rates normalized to BET surface) of the freshly created and naturally weathered surfaces are similar. At larger grain diameters, the freshly created surfaces are more reactive than the naturally weathered surfaces; at smaller grain diameters, they are less reactive.

The steady state dissolution rates of Al and Si (Table 4.3) were plotted versus the proportion of freshly created BET surface area F_f (Fig. 4.6). The plots closely resemble those,

discussed in chapter 3 for the ground feldspar samples by Holdren and Speyer (1985, 1987) in case where $\gamma = 0$ as for the Nova Scotia samples. From the preceding, the shape of the plots can be explained as follows. At the grain diameter of the unfractured sample ($F_f = 0$), the experimental dissolution rate equals that of the naturally weathered surfaces. At infinitely small grain diameter, essentially all surface area is freshly created ($F_f = 1$), but the dissolution rate of the freshly created surfaces is approximately zero. At grain diameters which are not too small, the proportion of freshly created BET surface area is relatively large, and the dissolution site density of the freshly created BET surfaces is relatively high. This causes the experimental dissolution rate to reach a maximum at some intermediate grain diameter, i.e. at an intermediate value of F_f .

The steady state dissolution rates in Table 4.3 represent averages for the entire mineral composition of the samples. Yet, the dissolution rates at pH 3 are probably determined by the feldspar, because: (1) the stoichiometry indicates dissolution of feldspar (and, possibly, the trace mineral biotite), rather than of quartz and/or muscovite (Fig. 4.2); and (2) in a review of available data from the literature, Helgeson *et al.* (1984) found that, at pH 3 and 25 °C, the dissolution rate of Si from ground feldspar samples is $(26 \pm 9) \cdot 10^{-17}$ mol.cm⁻² of BET

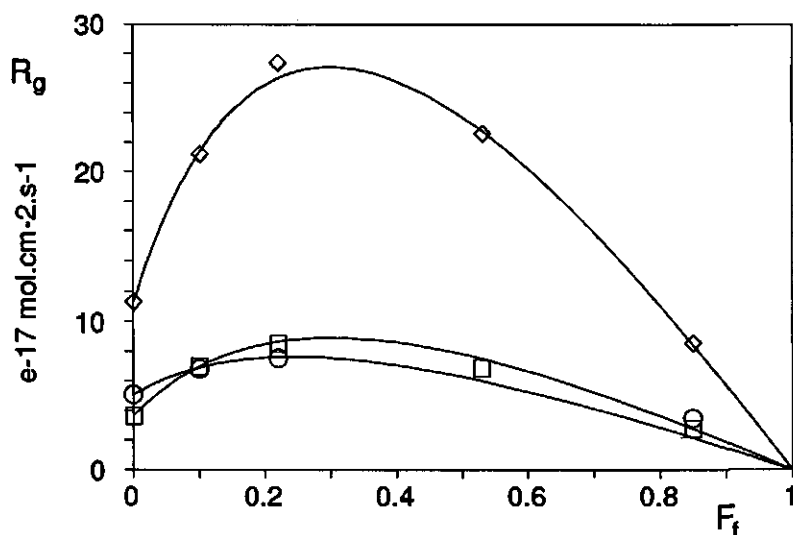


Fig. 4.6. Steady state dissolution rates of Al and Si normalized to BET surface (R_g) versus the proportion of freshly created BET surface area (F_f). \square : Al (pH 3); \diamond : Si (pH 3); \circ : Si (pH 5). The curves were generated from a rewritten version of eq. (4.1): $R_g = F_f R_f + (1 - F_f) R_w$, where F_f is found from eqs. (4.5) and (4.6), and where R_f is found from eq. (4.2) and from the data in Table 4.4.

surface. s^{-1} . This value corresponds nicely to the Si dissolution rates at pH 3 of the ground samples in this study (Table 4.3). Thus, values of R_f/R_w at pH 3 suggest that the discrepancy in dissolution rate between freshly created and naturally weathered surfaces increases in the order: microcline (K) < oligoclase and andesine (Ca) < oligoclase, andesine and albite (Na).

So far, R_f/R_w holds only at the grain diameter of the unfractured sample material. The question arises how R_f/R_w is related to the grain diameter. First, we should distinguish between naturally weathered surfaces in artificially ground samples and naturally weathered surfaces in the field. As discussed earlier, the naturally weathered surfaces in artificially ground samples originate from the unfractured grains, so their dissolution site density and dissolution rate are approximately independent of the grain diameter after grinding. However, the dissolution site density of naturally weathered surfaces in the field probably decreases with decreasing grain diameter, as for the freshly created surfaces by the mechanical action of rivers, glaciers, etc., from which they have developed. So, in analogy to eq. (4.2), the dissolution rate of naturally weathered surfaces in the field may depend on grain diameter according to:

$$R_w = \frac{d_g}{d_g + d_f} R_{w-max}. \quad (4.7)$$

where R_{w-max} is R_w at infinitely large grain diameter. According to eqs. (4.2) and (4.7), R_f/R_w equals $R_f-max./R_{w-max.}$, which is independent of the grain diameter. However, if the density of dissolution reactive sites on freshly created surfaces in the field decreases with decreasing grain diameter, this would also affect the amount of BET surface area additionally created during natural weathering. This can be seen, for instance, from the earlier discussion on the decrease of λ_w with decreasing grain diameter. If the BET surface area additionally created during natural weathering is essentially non-reactive, larger (=rougher) grains have a smaller proportion of dissolution reactive BET surface area than predicted from their diameter. This causes the dissolution rate of larger grains to be smaller than predicted by eq. (4.7). If so, R_f/R_w decreases with decreasing grain diameter, rather than being independent of grain diameter. Values of R_f/R_w for the 1 cm sized feldspars by Holdren and Speyer (1985, 1987), estimated from Si dissolution at pH 3 HCl, vary from 40 to 600 (see eqs. 3.11 and 3.12 and the data in Table 3.5). The smaller R_f/R_w of 13 (Table 4.4) for the 612 μm Nova Scotia material suggests that R_f/R_w indeed decreases with decreasing grain diameter (see also the kinetic model in chapter 7).

4.7. Conclusions

Surface area measurements at different levels of surface detail and dissolution experiments were performed on a naturally weathered assemblage of feldspar and quartz. The results from this and earlier studies (Holdren and Speyer, 1985, 1987; this thesis, chapter 2 and 3) indicate that dissolution of freshly created and naturally weathered feldspar surfaces in artificially ground samples proceeds as follows. Starting with large, hypothetical fresh-surface feldspar grains, the average dissolution site density (cm^{-2} of BET surface area) gradually decreases with decreasing grain diameter during grinding. This can be explained if preferential fracture planes have relatively high densities of dissolution reactive sites. Natural weathering of the fresh-surface grains without changing their diameter lowers the dissolution site density (cm^{-2} of BET surface area), because the BET surface area additionally created during natural weathering is essentially non-reactive. During artificial grinding, the dissolution site density of the naturally weathered surfaces is constant with grain diameter, because the surfaces originate from the unfractured grains. Thus, there exists a grain diameter in the ground material where the dissolution site density (and the dissolution rate normalized to BET area) of the freshly created surfaces equals that of the naturally weathered surfaces. At larger grain diameters, the freshly created BET surfaces are more reactive than the naturally weathered BET surfaces; at smaller grain diameters, they are less reactive.

Dissolution rates of freshly created feldspar surfaces in the laboratory are frequently up to several orders of magnitude higher than those of naturally weathered feldspar surfaces in the field. For the unfractured (612 μm) feldspar-quartz assemblage in this study, and for four ground samples of increasingly smaller grain diameter, the steady state dissolution rates of Na, K, Ca, Al and Si were determined at pH 3 and pH 5 HCl. The results indicate that, at 612 μm , dissolution rates of freshly created feldspar surfaces are approximately one order of magnitude higher than those of naturally weathered feldspar surfaces under similar hydrogeochemical conditions (all rates normalized to BET surface area). Comparison with the results from chapter 3 strongly suggests that this discrepancy factor increases with increasing grain diameter. These findings help to explain the observed discrepancies between feldspar dissolution rates in the laboratory and in the field. However, additional factors (such as pH, concentrations of organic ligands and/or inorganic solutes, the proportion of mineral surface in contact with the solution, etc.) should also be considered in explaining the discrepancies.

Acknowledgements

I am especially indebted to Edward Meijer, Nico van Breemen and Leendert van der Plas of the Department of Soil Science and Geology, Agricultural University of Wageningen, The Netherlands, for their creative ideas, critical comments and practical help during this research. I thank Leo Begheyn and Barend van Lagen of the same Department for performing the chemical analyses. I gratefully acknowledge the help of Joop Harmsen in providing the graphite tube autoanalyzer system at the ICW, Wageningen, of Bram Boekestein for the use of SEM facilities at the TFDL, Wageningen, of Paul van Ekeren and Aad van Genderen for the use of high-vacuum equipment at the Center of Thermodynamics, University of Utrecht, The Netherlands, and of Anton Korteweg, Department of Physical and Colloid Chemistry, Agricultural University of Wageningen, for his practical help during the BET analyses. Prof. L.I. Staffansson of the University of Stockholm, Sweden, kindly performed cross-analysis of some BET-krypton surfaces. The thoughtful and thorough review by William P. Inskeep greatly improved the quality of the original manuscript.

This chapter was published in *Geochimica et Cosmochimica Acta*, vol. 57, pp. 4963-4975. Editorial handling for *Geochimica et Cosmochimica Acta*: J.I. Drever.

Part B

The dissolution of naturally weathered feldspar and quartz

Chapter 5. Results from surface roughness data

(co-authored by N. van Breemen, L. van der Plas and E.L. Meijer)

Abstract

The effect of sample pretreatment, secondary mineral coatings, etch pits and pores on surface roughness was investigated for feldspar and quartz in a naturally weathered mineral assemblage. The assemblage was fractionated to four different ranges of grain density, each of which was sieved to three different size fractions. The gas adsorbed (BET-krypton) surface area, the geometric surface area, the mineralogical composition and the average grain diameter were determined for all samples. The data showed that: (1) surface roughness factors of the samples were generally much higher than those of freshly created surfaces; and (2) for individual density ranges (i.e. at constant mineralogical composition), the surface roughness factor decreased linearly with decreasing grain diameter. Theoretical considerations and scanning electron microscopy showed that contributions to the surface roughness factor of secondary mineral coatings, macropores (diameters > 50 nm) and etch pits were insignificant. Krypton adsorption data showed that by far most surface roughness was due to the presence of micropores and mesopores (diameters ≤ 50 nm). These findings demonstrate that, during natural weathering, micropores/mesopores develop at dissolution reactive sites whose density (cm⁻² of geometric surface area) is approximately proportional to grain diameter.

Multivariate linear regression was used to interpret the surface roughness factors of the samples in terms of the surface roughness factors of the constituent minerals. The model showed that, during natural weathering, micropores/mesopores develop in feldspar but not in quartz grains. At similar grain diameters, the pore density increases in the order: quartz < microcline < albite < oligoclase/andesine. This sequence is similar to the well-known sequence of relative weatherability of these minerals, suggesting a relationship between weatherability and micropore/mesopore density. Moreover, the results imply that sequences of relative weatherability are valid only at similar grain diameter of the minerals considered.

5.1. Introduction

The aqueous dissolution of minerals has been intensively studied over the past several decades, both in the laboratory (e.g. Busenberg and Clemency, 1976; Chou and Wollast, 1984; Holdren and Speyer, 1985, 1987; Brantley *et al.*, 1986; Knauss and Wolery, 1986; Casey *et al.*, 1988a,b) and in the field (e.g. April and Newton, 1983; Pačes, 1983; Delany, 1985; Fölster, 1985; Hultberg, 1985; Velbel, 1985; Clayton, 1986; Olsson and Melkerud, 1987). Experiments have shown that artificial and natural weathering of primary minerals such as feldspar and quartz proceeds as a non-uniform chemical attack of exposed surfaces, leading to the formation of etch pits (e.g. Wilson, 1975; Berner and Holdren, 1977, 1979; Robert *et al.*, 1980; Hochella *et al.*, 1987) and/or pores (e.g. Petit *et al.*, 1987a; Casey *et al.*, 1989a; Walker, 1990; Worden *et al.*, 1990; Zhang *et al.*, 1993). Etch pits develop from enhanced dissolution at surface sites of high internal energy, such as crystal defects, if the dissolution rate is limited by the rate of a chemical reaction step at the mineral-water interface

(Berner and Holdren, 1977, 1979; Helgeson *et al.*, 1984; Lasaga and Blum, 1986). Several models have been proposed to explain the formation of pores during mineral dissolution: (1) like the etch pits, micropores (diameters ≤ 2 nm) and mesopores ($2 \text{ nm} < \text{diameters} \leq 50$ nm) may form at crystal defects if the dissolution rate is limited by the rate of a chemical reaction step at the mineral-water interface (Van Der Hoek *et al.*, 1982; Lasaga and Blum, 1986); (2) a leached microporous surface layer may form if the dissolution rate is limited by the rate of a transport step, such as diffusion of aqueous reactants and products (Doremus, 1983; Chou and Wollast, 1984; Casey and Bunker, 1990); and (3) macropores (diameters > 50 nm) may result from the formation of fluid inclusions during the initial cooling of the pluton, followed by leakage and weathering under earth surface conditions (Parsons *et al.*, 1988).

Dissolution rates in the literature are normally expressed per unit of "average" mineral surface area (e.g. mol.cm^{-2} of BET surface. s^{-1}). However, the etch pits, micro-, meso- and macropores, and possibly still other surface details, may all dissolve at their own characteristic rate. Furthermore, the formation of etch pits and pores during dissolution affects the amount of surface area - and thus, the dissolution rate - in a way that may vary from sample to sample (Helgeson *et al.*, 1984; White and Peterson, 1990; see also chapter 2). This demonstrates that the relationship between experimental dissolution rates, normalized to "average" surface area, and the nature, morphology and relative amounts of the various surface details is of great importance to our understanding of the dissolution process.

In the previous chapters, porosity has been proposed as the most likely explanation for the high surface roughness factors of naturally weathered feldspar grains. In this chapter, the effect of secondary coatings, etch pits and pores on surface roughness is discussed for feldspar and quartz in a naturally weathered mineral assemblage. In the following chapter, dissolution experiments on the same mineral assemblage are discussed in the light of findings from the present research.

The surface morphology of mineral grains can be quantified by the surface roughness factor (λ). λ is defined as the ratio of the actual surface area (S ; cm^2) to the geometric surface area (s ; cm^2), which is the area of a hypothetical smooth surface enveloping the actual surface (Jaycock and Parfitt, 1981):

$$\lambda \equiv S/s \quad (5.1)$$

Both the actual and the geometric surface area are in fact scale dependent. The actual surface area may, for instance, be approximated by the BET method (Brunauer *et al.*, 1938; Gregg and Sing, 1982). The specific geometric surface area (s^* ; $\text{cm}^2.\text{g}^{-1}$) may, for instance,

be found from (Cartwright, 1962):

$$s^* = \mathcal{F}/(\rho d) \quad (5.2)$$

where \mathcal{F} is a geometry factor related to the average shape of the grains, ρ is the density (g.cm^{-3}), and d is the average grain diameter. For spherical grains, \mathcal{F} equals 6 if d is in cm. More accurate values of \mathcal{F} may be found, for instance, from microscopic observation of grains at low magnification (e.g. Fair and Hatch, 1933; Cartwright, 1962).

5.2. Materials and methods

We wanted to relate unambiguously the mineralogy of exposed surfaces in our samples to the bulk mineralogical composition. Therefore, preliminary studies using optical microscopy, scanning electron microscopy (SEM), and X-Ray diffraction were performed on several naturally weathered samples to select material: (1) free from secondary mineral coatings; and (2) with the constituent minerals homogeneously distributed over the grains. The selected sample was a mineral assemblage from Fiesch (Switzerland), collected three kilometers south of the Fiescher glacier. The sample consists of glacial deposits of low-grade metamorphic Central Aar granite, and essentially contains only feldspar and quartz. The material has been exposed to leaching for at least 400 years (when the glacier retreated from the sampling site). Grain diameters vary from approximately 100 to 1000 μm . Organic matter and secondary minerals were not detected during sample selection. The alkali feldspars in the Central Aar granites are generally perthitic, consisting of low albite and low microcline (Bambauer and Bernotat, 1982; Bernotat and Bambauer, 1982). The Ca bearing plagioclases are generally oligoclase and andesine (Steck, 1976). During the period of Alpine metamorphism, temperature in the Central Aar granites did not exceed 450 $^{\circ}\text{C}$ (Schaltegger and Von Quadt, 1990).

The sample was given a mild (low intensity) ultrasonic cleaning for three times 10 minutes, each time followed by profuse washing with deionized water. By sedimentation in bromoform/decane mixtures (Van Der Plas, 1966), the sample was fractionated to four ranges of different grain density (2.56-2.59, 2.59-2.63, 2.63-2.67 and 2.67-2.88 g.cm^{-3}). These were washed with ethanol to remove the bromoform and decane, washed with deionized water to remove the ethanol, oven-dried, and dry-sieved to fractions 600-850, 300-425 and 105-210 μm . All samples were analyzed by X-Ray fluorescence spectrometry (XRFS; Table 5.1), X-Ray diffraction, and point counting with optical microscopy to estimate the bulk mineralogical composition from normative calculations (Brown and Skinner, 1974).

Table 5.1. Elemental composition ($\mu\text{mol.g}^{-1}$ sample) according to XRFs.

sample ¹	Na	K	Ca	Al	Si	Mg+Fe
Ac	735	2730	<5	3618	10993	27
Am	747	2724	<5	3675	10938	27
Af	964	2404	<5	3581	11146	36
Bc	1545	1646	23	3510	11444	78
Bm	2309	1001	39	3646	11442	74
Bf	1692	922	25	2896	12488	62
Cc	1591	363	63	2283	13422	107
Cm	1581	256	50	2129	13688	78
Cf	932	99	38	1238	14939	62
Dc	1962	355	452	3466	11656	325
Dm	2047	331	443	3574	11566	302
Df	1942	393	570	3628	11282	417

¹ A = 2.56-2.59 g.cm^{-3} ; B = 2.59-2.63 g.cm^{-3} ; C = 2.63-2.67 g.cm^{-3} ; D = 2.67-2.88 g.cm^{-3} , c = 600-850 μm ; m = 300-425 μm ; f = 105-210 μm .

Optical microscopy showed that the samples contain on average 20 % of rock fragments of varying composition. Optical microscopy and X-Ray data showed that the samples are mainly composed of microcline (assumed pure KAlSi_3O_8), albite (assumed pure $\text{NaAlSi}_3\text{O}_8$), microcline-perthite, consisting of a microcline and an albite component, plagioclase which according to the method by Tobi (1963) consists of oligoclase and andesine (assumed pure $\text{Ab}_{70}\text{An}_{30}$), and quartz (assumed pure SiO_2). Also, a few % of muscovite (assumed pure $\text{KAl}_3\text{Si}_3\text{O}_{10}(\text{OH})_2$) and biotite (assumed pure $\text{K}(\text{Mg},\text{Fe}^{++})_3\text{AlSi}_3\text{O}_{10}(\text{OH})_2$), and traces of amphibole, epidote and tourmaline are present in most samples. According to the XRFs data, the summed mass fraction of oxides of other elements (Ba, Ti and Mn) is invariably < 0.2 %. Optical microscopy and normative calculations showed that large differences in mineralogical composition exist between samples of different density range (Fig. 5.1). For size fractions of similar density range, however, variations in mineralogical composition are small, and deviations from average mass fractions seldomly exceed 10 % (Tables 5.2 and 5.3). The incomplete purification by density fractionation (Fig. 5.1) results from the presence of the perthites and the rock fragments.

Using the method by De Kanel and Morse (1979), the specific BET surface area (S^* ; $\text{cm}^2.\text{g}^{-1}$) was estimated for all samples from a 3-point krypton adsorption isotherm. General equations were derived for 17 different types of grain geometry (ellipsoids, prisms, pyramids, etc., and combinations) to calculate the volume and the geometric surface area of individual

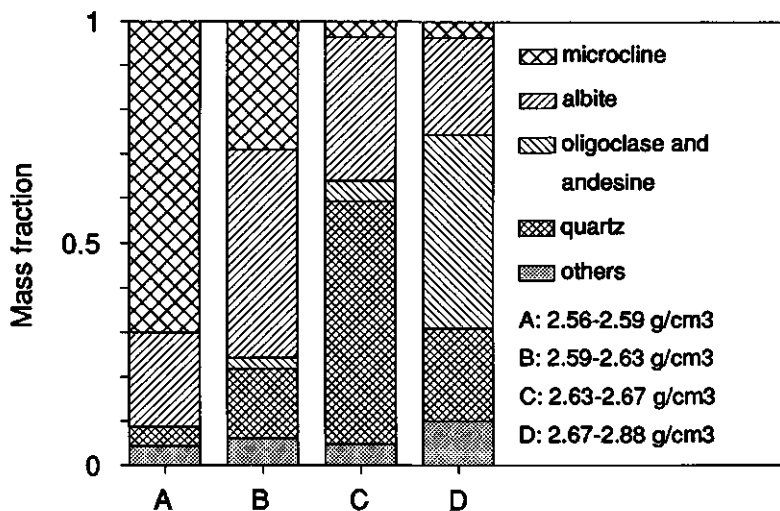


Fig. 5.1. Average mineralogical composition of the four density ranges (Tables 5.2 and 5.3). "Others" includes muscovite and biotite, and traces of amphibole, epidote and tourmaline.

grains from variable linear grain dimensions. In this way, the average equivalent spherical grain diameter and the specific geometric surface area of samples can be estimated in terms of an almost infinitely large number of possible grain shapes. The linear dimensions of 30 individual grains were determined in all samples from observation by a dissecting microscope at 40x magnification. At this scale of surface detail, etch pits and pores are not observed and have no effect on the surface area estimate. Dimensions parallel to the microscope axis were obtained from measurement of shadows, cast by a rotatable light source at known angles. Essential data on all samples are given in Tables 5.2 and 5.3.

To determine the effect of ultrasonic cleaning on the surface roughness of the samples (Cremeens *et al.*, 1987), 10 g of untreated sample material was gently washed with deionized water during 5 minutes and wet-sieved using a 600 and a 210 μm sieve. The mineral fragments $> 1000 \mu\text{m}$ were handpicked from the fraction $> 600 \mu\text{m}$, and the grains $<$ approximately $100 \mu\text{m}$ were decanted from the fraction $< 210 \mu\text{m}$. The geometric and BET surface area of these minimally treated samples $600\text{-}1000 \mu\text{m}$ and $100\text{-}210 \mu\text{m}$ were determined as for the other samples.

The effect of etch pitting on surface morphology was investigated by SEM for the three samples of density $2.67\text{-}2.88 \text{ g.cm}^{-3}$ (Fig. 5.2a and hereafter). The $600\text{-}850 \mu\text{m}$, $2.67\text{-}2.88 \text{ g.cm}^{-3}$ sample was used in three additional experiments to further evaluate the nature of the BET surfaces.

Table 5.2. Characterization of samples in the grain density ranges 2.56-2.59 and 2.59-2.63 g.cm⁻³.

density (g.cm ⁻³)	2.56-2.59			2.59-2.63		
	600-850	300-425	105-210	600-850	300-425	105-210
fraction (μm)	762	366	194	825	402	235
d _w (μm) ¹	762	366	194	825	402	235
S _w [*] (cm ² .g ⁻¹) ¹	1400	1600	1480	1650	2030	1890
s _w [*] (cm ² .g ⁻¹) ¹	38.8	80.8	151	34.8	73.9	124
microcline ²	0.737	0.727	0.636	0.414	0.236	0.219
albite	0.192	0.196	0.253	0.391	0.581	0.427
Ab ₇₀ An ₃₀ ³	0	0	0	0.020	0.035	0.022
quartz	0.036	0.032	0.063	0.109	0.086	0.276
muscovite	0.031	0.041	0.042	0.054	0.051	0.046
biotite	0.004	0.004	0.006	0.012	0.011	0.010
∅ _w (-) ⁴	7.61	7.62	7.57	7.48	7.77	7.64
λ _w (-) ¹	36.1	19.8	9.8	47.4	27.5	15.2

¹ d_w is the average spherical grain diameter; S_w^{*} is the specific BET surface area; s_w^{*} is the specific geometric surface area; λ_w is the surface roughness factor.

² all minerals expressed as mass fractions.

³ oligoclase and andesine.

⁴ ∅_w is the geometry factor, calculated assuming densities (g.cm⁻³) of: microcline = 2.55; albite = 2.61; Ab₇₀An₃₀ = 2.66; quartz = 2.65; muscovite = 2.82; biotite = 2.84.

Table 5.3. Characterization of samples in the grain density ranges 2.63-2.67 and 2.67-2.88 g.cm⁻³.

density (g.cm ⁻³)	2.63-2.67			2.67-2.88		
	600-850	300-425	105-210	600-850	300-425	105-210
fraction (μm)	839	419	187	676	383	217
d _w (μm) ¹	839	419	187	676	383	217
S _w [*] (cm ² .g ⁻¹) ¹	1470	1460	1240	2990	3510	3420
s _w [*] (cm ² .g ⁻¹) ¹	34.8	68.6	156	42.8	73.9	131
microcline ²	0.063	0.038	0.003	0.035	0.021	0.049
albite	0.378	0.383	0.221	0.238	0.265	0.161
Ab ₇₀ An ₃₀ ³	0.056	0.045	0.034	0.400	0.392	0.506
quartz	0.446	0.484	0.706	0.228	0.213	0.189
muscovite	0.040	0.038	0.026	0.049	0.062	0.030
biotite	0.017	0.012	0.010	0.050	0.047	0.065
∅ _w (-) ⁴	7.71	7.59	7.72	7.69	7.53	7.56
λ _w (-) ¹	42.2	21.3	8.0	69.9	47.5	26.1

^{1,2,3,4} see notes Table 5.2.

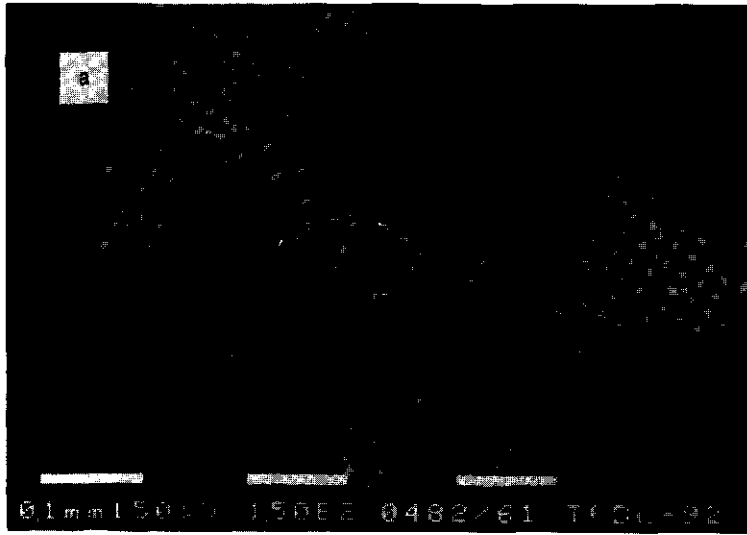


Fig. 5.2. a: scanning electron microscope image of an albite grain in the 600-850 μm , 2.67-2.88 $\text{g}\cdot\text{cm}^{-3}$ sample. The general shape of the grain is representative for essentially all grains in all samples. At this scale of surface detail, the roughness factor is approximately 2. b: scanning electron microscope image of a polished cross-section of a randomly oriented microcline grain in the 600-850 μm , 2.67-2.88 $\text{g}\cdot\text{cm}^{-3}$ sample. This particular grain shows a very high density of internal cavities, which may be macropores (see text).

In the first experiment, a small amount of sample was immersed in commercial grade synolite lacquer. After hardening, the resulting stub was sawed and carefully polished, exposing cross-sections of randomly oriented grains. The presence of macropores throughout the bulk of the grains (Worden *et al.*, 1990; Walker, 1990) was investigated using SEM (Worden *et al.*, 1990) at magnifications up to 20,000x (Fig. 5.2b and hereafter).

In the second experiment, the krypton adsorption isotherm of the sample was compared to that of a reference sample. This technique gives an estimate of their difference in micropore volume ($\text{cm}^3 \cdot \text{g}^{-1}$ sample; Lippens and De Boer, 1965). The reference sample was a pure, ground 53-105 μm adularia fraction, freshly derived from the inner core material of a 10 cm large naturally weathered single crystal. The ground adularia was cleaned ultrasonically in ethanol three times for 10 minutes, each time followed by washing with ethanol. The ground, clean adularia fraction is similar to that used in earlier experiments (chapter 3). Its BET surface area is 99 % freshly created by grinding (Table 3.2), so etch pits, pores, secondary mineral coatings, etc., from natural weathering are virtually absent.

The third experiment was to determine whether the BET surface area is located near the surface of the grains or throughout the bulk of the grains. 2.0082 g of 600-850 μm , 2.67-2.88 $\text{g} \cdot \text{cm}^{-3}$ sample was mixed with 0.2410 g of 10 μm corund powder in a 5 ml plastic container. 0.8 ml of deionized water was added, and the resulting slurry was vigorously shaken mechanically for about 7 hours. The fine and coarse grains were then carefully separated by repeated sedimentation in deionized water until the supernatant was totally clear. Velocities of sedimentation showed that the mechanical treatment had not caused any significant fracturing of the coarse grains, so their numbers before and after treatment are essentially the same. Both size fractions were oven-dried, collected, cooled to room temperature and reweighed. The coarse size fraction was again ultrasonically cleaned three times for 10 minutes, and its specific BET surface area was determined.

5.3. Results and discussion

Using the data in Tables 5.2 and 5.3, the surface roughness factor of the naturally weathered samples (λ_w) was plotted versus their average equivalent spherical grain diameter (d_w ; Fig. 5.3). The results show that the surface roughness factor of samples of comparable mineralogical composition decreases approximately linearly with decreasing grain diameter. We can think of three reasonable ways to explain these findings: (1) effects from the presence of unobserved secondary mineral coatings; (2) effects from the sample pretreatment (ultrasonic cleaning and dry-sieving); or (3) effects from the primary phases. These are discussed in greater detail hereafter.

(1) Secondary mineral coatings

Secondary mineral coatings can be highly porous, and may contribute to the BET surface area of naturally weathered samples (White and Peterson, 1990). At constant composition of a secondary coating, its porous character can be quantified by a constant (C_4 ; cm^{-1}) denoting the equivalent BET surface area of the gas absorbed per cm^3 of coating material. The BET surface area of coating material (S_c ; cm^2) in a sample is then given by:

$$S_c = V_c C_4 \quad (5.3)$$

where V_c is the volume of coating material. Eq. (5.3) can be used to quantify the effect of secondary coatings on the surface roughness factor of a naturally weathered sample as follows. If, during natural weathering, the surface roughness factor changes only as a result of formation of secondary coatings, the surface roughness factor of the primary phases does not change and equals that of their freshly created counterparts. For freshly created spherical primary grains, covered by secondary coating material, it follows from eq. (5.3) and from

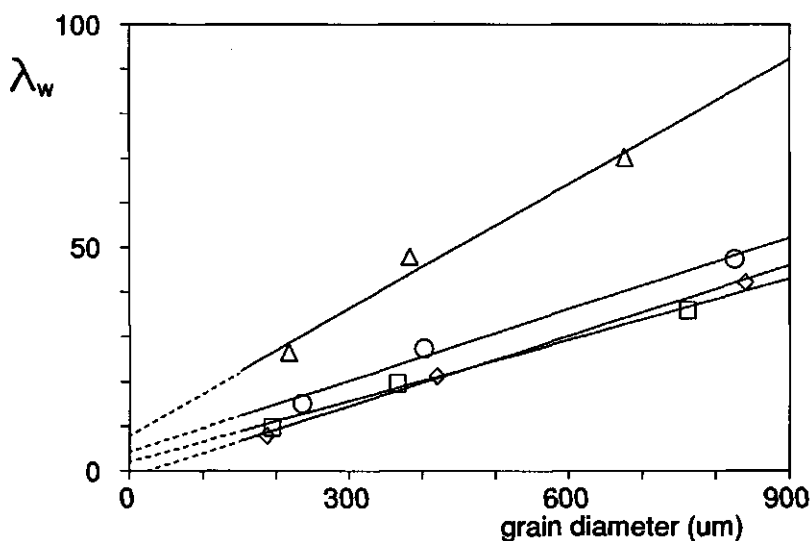


Fig. 5.3. Plot of the surface roughness factor (λ_w) versus the average spherical grain diameter (d_w ; μm). Estimated accuracy of $\lambda_w \pm 20\%$; estimated precision of $\lambda_w \pm 5\%$. Estimated accuracy of $d_w \pm 10\%$. \square : $2.56\text{-}2.59 \text{ g.cm}^{-3}$, $\lambda_w = 0.0454 d_w + 1.9$ ($r^2 = 1.00$); \circ : $2.59\text{-}2.63 \text{ g.cm}^{-3}$, $\lambda_w = 0.0531 d_w + 4.2$ ($r^2 = 0.99$); \diamond : $2.63\text{-}2.67 \text{ g.cm}^{-3}$, $\lambda_w = 0.0523 d_w - 1.3$ ($r^2 = 1.00$); \triangle : $2.67\text{-}2.88 \text{ g.cm}^{-3}$, $\lambda_w = 0.0931 d_w + 8.2$ ($r^2 = 0.99$). Extrapolated intercepts may be inaccurate, due to lack of data at small grain diameters.

simple geometry that:

$$\lambda_w = \lambda_f + C_4[d_c - 2d_c^2/d_w + 4d_c^3/(3d_w^2)] \quad (5.4)$$

where λ_f is the surface roughness factor of the freshly created primary grains, d_c is the average thickness of the coating, and d_w is the average grain diameter including the coating. In the samples used here (grain diameters > 100 μm), secondary coatings in the order of nm thickness may have remained unobserved during sample selection. For such coatings ($d_c \ll d_w$), eq. (5.4) simplifies to:

$$\lambda_w \approx \lambda_f + C_4 d_c \quad (5.5)$$

At constant composition of the primary phases, λ_f is independent of the grain diameter (chapter 2). Thus, eq. (5.5) indicates that the actual relationships in Fig. 5.3 can be explained from the presence of secondary coatings only if, far from reason, the increase in coating thickness were proportional to the increase in grain diameter of the primary phases. Furthermore, the value of C_4 for secondary iron (hydr)oxides in Tahoe Granite is in the order of $40,000 \text{ cm}^{-1}$ (White and Peterson, 1990). An increase in the coating thickness of 0.25 μm would then increase λ_w by one unit (eq. 5.5). Thus, iron (hydr)oxide coatings on the 650-800 μm grains in these samples would be approximately 10 μm thick over the entire geometric surface (Fig. 5.3). Both from SEM and from X-Ray diffraction, such coatings would have been easily observed during sample selection.

(2) Sample pretreatment

In general, abrasion of grains during ultrasonic cleaning and/or dry-sieving gives higher (or lower) λ only if the surface details which are destroyed have lower (or higher) λ than those which are created. For instance, Cremeens *et al.* (1987) found that abrasion of fresh mineral surfaces by grinding created additional surface roughness at the scale of observation by SEM. In contrast, we found a decrease in surface roughness from BET analysis in the corund experiment (see hereafter). This suggests that λ of surface details created by abrasion is intermediate between λ_f from SEM analysis and λ_w from the BET method. The vigorous treatment in the corund experiment abraded 32 % of the BET surface area of the 600-850 μm , 2.67-2.88 g.cm^{-3} sample (see hereafter). Therefore, the much less vigorous and much shorter ultrasonic treatment could not have abraded, for instance, 63 % of the BET surface area of the 105-210 μm , 2.67-2.88 g.cm^{-3} sample, needed to decrease its λ_w from

69.9 to 26.1 (Table 5.3). The specific surface areas from the experiment using minimal sample pretreatment were ($\text{cm}^2\text{.g}^{-1}$): 37.3 (geometric; 600-1000 μm), 172 (geometric; 100-200 μm), 1910 (BET; 600-1000 μm), and 3270 (BET; 100-200 μm), respectively. Thus, the surface roughness factors were 51.2 (600-1000 μm), and 19.0 (100-200 μm), respectively. Realizing that both samples cover the entire range of grain densities, these values are in good agreement with the data in Fig. 5.3.

In conclusion, we are confident that most or all of the differences in surface roughness of these samples are inherent to the primary phases, and not to secondary coatings or to the sample pretreatment.

(3) Primary phases

In the samples of density 2.67-2.88 g.cm^{-3} , λ_w from scanning electron microscopy at 1000x magnification was approximately 2.0, including effects from etch pitting (Fig. 5.2a for the 600-850 μm fraction). From point counting on representative SEM images, etch pit densities (cm^{-2} of geometric surface) were approximately 3600 ± 1200 (105-210 μm), 2800 ± 1000 (300-425 μm), and 4000 ± 1400 (600-850 μm), respectively. The average etch pit diameter was approximately 1.5 μm in all three samples. If the average depth of the etch pits is, for instance, 1 μm , the proportion of the SEM area occupied by etch pits is approximately 0.01 % for all three samples. However, surface roughness factors from BET analysis (Table 5.3) are much higher than those from SEM observation (Fig. 5.2a). This demonstrates that the formation of etch pits during natural weathering does not explain the high λ_w from BET analysis in these samples.

Macropore porosities from leakage and weathering of fluid inclusions may reach several % by volume within parts of selected crystals, the higher values being found in rocks judged to be "wetter" on petrographic grounds (Montgomery and Brace, 1975; Worden *et al.*, 1990). If the surface roughness factor of a naturally weathered sample results only from the formation of macropores, the roughness at an atomic level, both inside and outside the macropores, does not change during natural weathering and equals that of freshly created surfaces. For cylindrically shaped pores of identical radius, distributed homogeneously throughout the bulk of spherical grains, it follows from simple geometry that:

$$\lambda_w = \lambda_1 [1 + d_w v_p / (3r)] \quad (5.6)$$

where v_p is the volume fraction of pores in the grains and r is the pore radius. From point

counting and scale measurements on representative SEM images up to 20,000x magnification, the 600-850 μm , 2.67-2.88 $\text{g}\cdot\text{cm}^{-3}$ sample has an average macropore volume fraction of approximately 0.5 % maximum, and the average macropore radius is approximately 2 μm (Fig. 5.2b). The 0.5 % is a maximum because it is not clear from the SEM observations if all cavities in the polished cross-sections are internally connected to the surface of the grains. Values of λ_r for microcline, albite, oligoclase and andesine are approximately 3.4, 2.5, 5.2 and 6.3, respectively (Table 2.1). Given its crystal structure, λ_r of quartz is probably even lower (see chapter 2). Assuming $\lambda_r = 4$ for the 600-850 μm , 2.67-2.88 $\text{g}\cdot\text{cm}^{-3}$ sample, its maximum λ_w would equal 6.3 (eq. 5.6). Thus, the formation of macropores during natural weathering does not explain the actual λ_w of 69.9 for this sample.

The krypton adsorption isotherms of the adularia reference and of the 600-850 μm , 2.67-2.88 $\text{g}\cdot\text{cm}^{-3}$ test sample are shown in Fig. 5.4a. Comparison of the two isotherms (Lippens and De Boer, 1965; Fig. 5.4b) indicates $(3.1 \pm 0.2) \cdot 10^{-5} \text{ cm}^3 \cdot \text{g}^{-1}$ more micropore volume for the test sample than for the reference sample. If the micropore volume of the reference sample equals zero, and if the micropores in the test sample are cylindrically shaped and internally smooth, this explains 620 cm^2 of BET surface $\cdot \text{g}^{-1}$ sample at maximum average micropore radius (1 nm). However, this estimate is a minimum. For instance, if the surface roughness factor at an atomic level inside the micropores equals that of freshly created surfaces (say, $\lambda_r = 4$), a micropore radius of 0.85 nm would explain all BET surface area of the sample. Additionally, the adsorption-desorption hysteresis for the test sample (Fig. 5.4a) indicates the presence of mesopores (Gregg and Sing, 1982). These findings strongly suggest that the BET surface area of these samples can be largely explained from the formation of micropores and mesopores in the primary phases during natural weathering.

Reweighing the corund-treated fractions gave 1.8117 g of coarse grains, and 0.4317 g of fine grains. Thus, the unexplained loss in total weight of solids is 0.0058 g, and the shift in mass from coarse to fine grains is 0.1936 ± 0.0029 g. For spherical grains of 338 μm radius (Table 5.3), this can be explained from the abrasion of a 11 μm thick surficial layer. The BET surface area of the coarse grains after treatment is 2030 $\text{cm}^2 \cdot \text{g}^{-1}$, compared to the original 2990 $\text{cm}^2 \cdot \text{g}^{-1}$. If the BET surface area of the 600-850 μm , 2.67-2.88 $\text{g}\cdot\text{cm}^{-3}$ sample is homogeneously distributed over the bulk of the grains, eq. (5.6) also applies to the data from the corund experiment. In that case, the change in specific geometric surface area and in surface roughness of the treated sample, due to the diminution in average grain diameter, follows from eqs. (5.2) and (5.6):

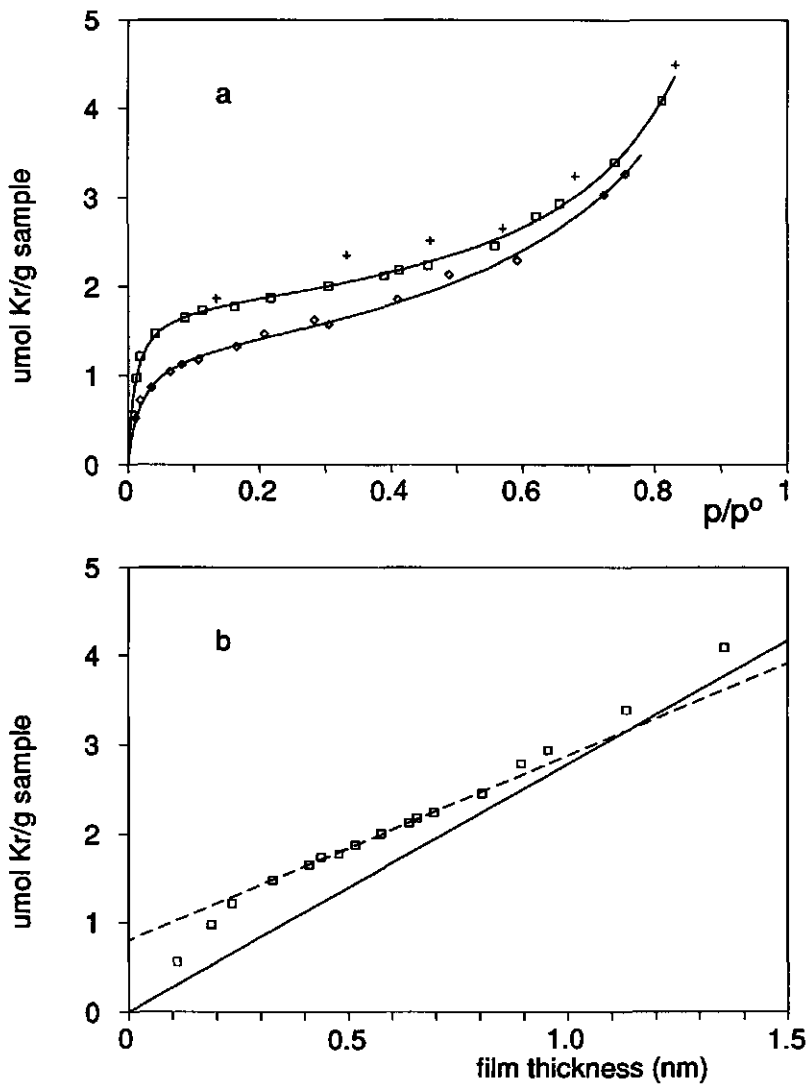


Fig. 5.4. Krypton adsorption/desorption isotherms. \square : adsorption of the 600-850 μm , 2.67-2.88 g.cm^{-3} test sample; $+$: desorption of the 600-850 μm , 2.67-2.88 g.cm^{-3} test sample; \diamond : adsorption of the 53-105 μm adularia reference sample. The samples were degassed 40 hours at 350 $^\circ\text{C}$; the data were obtained at -196 $^\circ\text{C}$. Plot a: amount adsorbed/desorbed ($\mu\text{mol.g}^{-1}$ sample) versus the relative krypton vapour pressure (p/p°). Plot b: amount adsorbed ($\mu\text{mol.g}^{-1}$ sample) versus the statistical thickness of the krypton film (nm); the y-intercept equals the difference in micropore volume between the reference sample (solid diagonal line) and the test sample (Lippens and De Boer, 1965).

$$s_a^* = \frac{\mathfrak{D}_a d_b}{\mathfrak{D}_b d_a} s_b^* \quad (5.7)$$

and, because v_p and r do not change during the corund treatment:

$$\lambda_a = \lambda_1 + (\lambda_b - \lambda_1) d_a/d_b \quad (5.8)$$

where the subscripts a and b refer to after and before treatment, respectively. Application of eqs. (5.1), (5.7) and (5.8) to the data from the corund experiment, assuming $\lambda_1 = 4$, indicates that the specific BET surface area of the treated sample is $3000 \text{ cm}^2 \cdot \text{g}^{-1}$ if $\mathfrak{D}_b = \mathfrak{D}_a$ (minimal gain of BET surface, compared to the untreated sample, if the average shape of the grains does not change). Even if the corund treatment resulted in a perfect spherical shape for all grains ($\mathfrak{D}_a = 6$), the specific BET surface area after treatment would still be $2340 \text{ cm}^2 \cdot \text{g}^{-1}$ ($\mathfrak{D}_b = 7.69$; Table 5.3). Thus, the actual BET area of $2030 \text{ cm}^2 \cdot \text{g}^{-1}$ indicates that the micropores/mesopores in the sample were, at least partly, localized near the surface of the grains. Due to the irregular shape of the grains, the actual layer thickness removed by the corund probably varied from $0 \text{ }\mu\text{m}$ at some places to more than $20 \text{ }\mu\text{m}$ at others. Therefore, the actual thickness of the layer where the BET surface area of the sample is located could not be determined, and may be any value between almost zero and several tens of μm .

If the linear relations in Fig. 5.3 hold, and if the micropores/mesopores in these samples are cylindrically shaped and perpendicular to the surface, the average pore density (p) follows from simple geometry:

$$p = \frac{\alpha d_w}{2\pi r \lambda_1 L_m} \quad (5.9)$$

where p is the number of micropores/mesopores per unit of geometric surface area, α is the slope of the linear relation between surface roughness and grain diameter (Fig. 5.3), and L_m is the average length of the pores. Thus, at constant radius and length, the micropore/mesopore density in these samples is proportional to grain diameter. Consequently, at infinitely small grain diameter their density is essentially zero. Extrapolated values of λ_w in Fig. 5.3 are indeed in general agreement with those reported for non-porous freshly created feldspar surfaces (2.5 to 11; chapter 2).

As discussed in the introduction, micropores and/or mesopores may form from enhanced dissolution at crystal defects, or from selective leaching of surficial layers. The density, depth and radius of pores in leached layers primarily depend on crystal structure,

mineral composition, temperature, pH, and reaction time (Casey and Bunker, 1990). For the Fiesch samples of similar density range, these are all essentially independent of the grain diameter. Thus, the actual relations between surface roughness and grain diameter (Fig. 5.3) suggest that leached layers, whether present or not, did not contribute significantly to the BET surface area. For instance, if density and radius of selectively leached pores are independent of grain diameter, the leached layer thickness would, far from reason, be proportional to grain diameter. Furthermore, for the nine different naturally weathered feldspars by Holdren and Speyer (1985, 1987), it was concluded in chapter 2 that the surface roughness factor of Grass Valley Anorthite was highest of all ($\lambda_w \approx 2600$). However, contrary to microcline and albite, Al-depleted leached layers in anorthite can exist only if condensation of silanol groups ($\equiv \text{Si} - \text{OH}$) into a linked structure (for instance, $\equiv \text{Si} - \text{O} - \text{Si} \equiv$) occurs (Casey and Bunker, 1990). Unless intensive condensation of silanol groups occurred in the Grass Valley Anorthite during natural weathering, its high λ_w cannot be explained from the formation of Al-depleted leached layers.

The observed dependence of surface roughness on grain diameter can be explained if preferential fracture planes have relatively high densities of dissolution reactive sites (i.e. sites where BET surface area is created during dissolution). A similar mechanism was proposed in chapter 3 to explain the dissolution behaviour of freshly created feldspar surfaces by Holdren and Speyer (1985, 1987). Under such conditions, artificial grinding in the laboratory and grinding in the field (for instance, by the mechanical action of rivers, glaciers, etc.) exposes freshly created surfaces with increasingly lower density of dissolution reactive sites, thereby decreasing the average density at all grain diameters. If, during subsequent natural weathering, BET surface area develops at such sites, smaller grains have lower surface roughness factors. This also agrees with the observation that the surface roughness factor of the naturally weathered Nova Scotia sample (612 μm ; chapter 4) is much smaller than that of the naturally weathered feldspar fragments by Holdren and Speyer (1 cm; chapter 2).

The surface roughness factors of these samples are in fact weighted averages of the surface roughness factors of the constituent minerals. Because, at constant mineralogical composition, surface roughness in Fig. 5.3 is linearly related to grain diameter, similar relationships will hold for the pure constituent minerals i according to:

$$\lambda_i = \alpha_i d_i + \beta_i \quad (5.10)$$

where λ_i is the surface roughness factor of mineral i , α_i and β_i are the slope and intercept, respectively, and d_i is the average grain diameter of mineral i . If the constituent minerals are homogeneously distributed over the grains in a sample, and if all grains in the sample are of

similar size and shape, the weighting factors are the volume fractions of the minerals i (Appendix 4), which can be obtained from mass fractions (Tables 5.2 and 5.3) and densities. The surface roughness factor of a sample w (λ_w) is then given by (Appendix 4):

$$\lambda_w = \sum_i [v_{i,w} (\alpha_i d_w + \beta_i)] \quad (5.11)$$

where $v_{i,w}$ is the volume fraction of mineral i in sample w ($\sum_i v_{i,w} \equiv 1$), and where the expression between parentheses is the surface roughness factor of mineral i in sample w . In eq. (5.11) α_i and β_i are the unknowns, so the resulting multivariate linear regression model can be solved if the number of samples $w \geq 2i$. Using the data in Tables 5.2 and 5.3 for microcline, albite, oligoclase/andesine and quartz only (no muscovite or biotite considered), the model indicates that quartz has the lowest, and oligoclase/andesine has the highest surface roughness factor in these samples. Based on the high λ_w of biotite (White and Peterson, 1990) and the low λ_w of muscovite (Nonaka, 1984), we assumed in the final analysis that α_i and β_i equal those of quartz for muscovite, and those of oligoclase/andesine for biotite. The results of the final regression analysis are shown in Fig. 5.5. At a given grain diameter, values of λ_i in these samples increase in the order: quartz < microcline < albite < oligoclase/andesine. This sequence is similar to the well-known sequence of relative

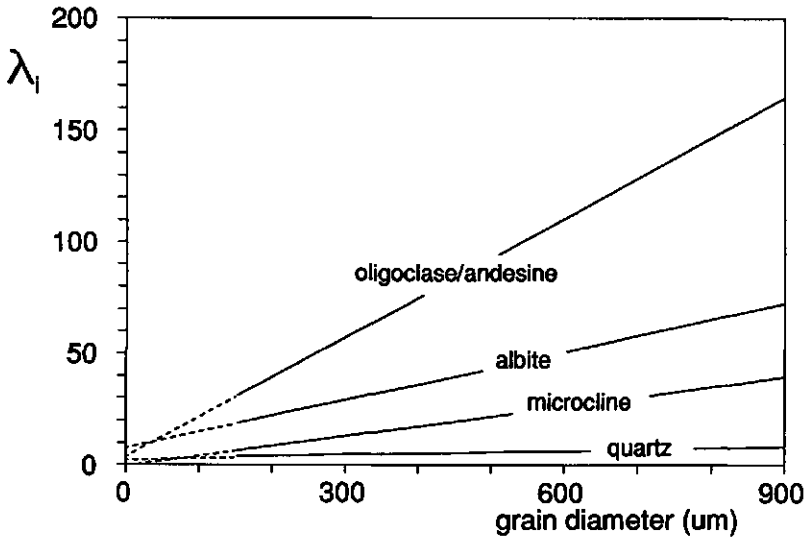


Fig. 5.5. Relations between surface roughness factor (λ_i) and grain diameter (d_w ; μm) of the predominant minerals i in the samples, as estimated from multivariate linear regression (eq. 5.11). Oligoclase/andesine: $\lambda_i = 0.1789 d_w + 3.1$; albite: $\lambda_i = 0.0717 d_w + 7.1$; microcline: $\lambda_i = 0.0439 d_w - 0.8$; quartz: $\lambda_i = 0.0062 d_w + 1.9$. $r^2 = 0.99$.

weatherability of these minerals (Goldich, 1938). That the same sequence can be derived from surface roughness data strongly supports the validity of our approach. The results indicate a relationship between the weatherability of minerals and the density of micropores/mesopores after natural weathering. This is true, for instance, if the micropores/mesopores develop at highly reactive dissolution sites (see also the following chapter). Moreover, the relations in Fig. 5.5 suggest that sequences of relative weatherability hold only at similar grain diameter of the minerals considered.

5.4. Conclusions

The effect of sample pretreatment, secondary coatings, etch pits and pores on surface roughness of mineral grains was investigated for feldspar and quartz in a naturally weathered assemblage. Roughness factors of the naturally weathered surfaces were much higher than could be explained from sample pretreatment, formation of secondary mineral coatings, etch pits or macropores. Krypton adsorption/desorption data showed that the high surface roughness factors can be explained from the presence of micropores and mesopores, concentrated near the mineral surface. Because freshly created surfaces by grinding are non-porous, these findings indicate that, during natural weathering, micropores/mesopores develop at dissolution reactive sites. The data also indicate that, at constant mineralogical composition, the micropore/mesopore density is approximately proportional to grain diameter. This suggests that leached layers, whether present or not, do not contribute significantly to the BET surface area. The data can be explained, however, if preferential fracture planes have relatively high densities of dissolution reactive sites. A similar mechanism was proposed earlier: (1) to explain the dissolution behaviour of freshly created feldspar surfaces by grinding (chapter 3); and (2) to explain the discrepancy in surface roughness between the naturally weathered Nova Scotia sample (chapter 4) and the naturally weathered feldspars by Holdren and Speyer (1985; 1987) (chapter 2).

Multivariate linear regression showed that the micropores/mesopores develop in the feldspar grains but not in the quartz grains during natural weathering. At similar grain diameters, surface roughness factors increase in the order: quartz < microcline < albite < oligoclase/andesine. This sequence is similar to the well-known sequence of relative mineral weatherability. The findings strongly suggest a relationship between the weatherability of minerals and the density of micropores/mesopores. This can be explained if micropores/mesopores develop at dissolution reactive sites. Moreover, the data indicate that sequences of relative weatherability are valid only at similar grain diameter of the minerals involved.

Acknowledgements

We thank Paul van Ekeren and Aad van Genderen for the use of high-vacuum equipment at the Center of Thermodynamics, University of Utrecht, The Netherlands, and Bram Boekestein for the use of SEM facilities at the TFDL, Wageningen. We are indebted to Paul Flapper and Luis Francisco de Morais Faria da Costa Lopes for performing the BET and dissecting microscope measurements.

A combined version of this and the following chapter has been accepted for publication in *Geochimica et Cosmochimica Acta*.

Editorial handling for *Geochimica et Cosmochimica Acta*: G. Sposito.

The multivariate linear regression model (Appendix 4) was published in the July 1993 special issue of *Chemical Geology* on the 3rd International Symposium on Geochemistry of the Earth Surface.

The dissolution of naturally weathered feldspar and quartz

Chapter 6. Results from dissolution data

(co-authored by N. van Breemen, E.L. Meijer and L. van der Plas)

Abstract

The dissolution behaviour of a naturally weathered feldspar-quartz assemblage was studied at pH 3 HCl and ambient temperature. The assemblage was fractionated to four different ranges of grain density, each of which was sieved to three different size fractions. Dissolution rates of Na, K, Ca, Al and Si, normalized to the gas adsorbed (BET) surface area, were essentially independent of the grain diameter. Due to effects from surface roughness, dissolution rates normalized to the geometric surface area were essentially proportional to grain diameter. Combination of these and earlier findings indicates that the micropores and mesopores (which are present in the feldspar but not in the quartz grains) were the dissolution reactive sites, rather than the etch pits. Theoretical arguments indicate that the pore area perpendicular to the mineral surface (i.e. the pore "walls") is essentially non-reactive, and that the dissolution rates are largely determined by the pore area parallel to the mineral surface (the pore "bottoms"). The pore area parallel to the mineral surface is equivalent to: (1) the leached layer/fresh mineral interface, if the micropores/mesopores develop in leached layers; or (2) the dislocation outcrops where strained mineral material is in contact with the solution, if the micropores/mesopores develop at crystal defects. Tentative calculations suggest that, during the previous natural weathering of these samples, dissolution occurred from the micropore "bottoms", rather than from the etch pits, too.

Due to the absence of micropores/mesopores in naturally weathered quartz, its dissolution behaviour differs distinctly from that of feldspar. The data imply that quartz dissolves primarily from the etch pits, and that its dissolution rate, normalized to either BET or to geometric surface area, and both for freshly ground and for naturally weathered grains, is independent of the grain diameter. The absence of highly reactive sites on freshly created quartz surfaces (i.e. sites where micropores/mesopores form) may explain their low dissolution rate, compared to freshly created feldspar surfaces. The absence of non-reactive micropore "walls" in naturally weathered quartz may explain why large discrepancies between dissolution rates of freshly created and naturally weathered surfaces have been reported for feldspar, but not (yet) for quartz.

6.1. Introduction

Over the past several decades many authors have reported on the kinetics of mineral dissolution, both in the laboratory and in the field (e.g. Lagache, 1965; Wollast, 1967; Cleaves *et al.*, 1970, 1974; Pačes, 1973, 1983, 1986; Petrovich, 1976; Balek *et al.*, 1978; Åberg and Jacks, 1985; Knauss and Wolery, 1986; Brantley *et al.*, 1986; Casey *et al.*, 1989a,b). Experimental dissolution data are usually evaluated by a kinetic model, several of which are available from the literature (e.g. Aagaard and Helgeson, 1982; Helgeson *et al.*, 1984; Chou and Wollast, 1984; Wintsch and Dunning, 1985; Murphy and Helgeson, 1987; Wieland *et al.*, 1988). Virtually all kinetic models yield dissolution rates normalized to mineral surface area. Therefore, authors frequently include data on the specific surface areas of their

samples (e.g. Lagache, 1965; Busenburg and Clemency, 1976; Chou and Wollast, 1984; Holdren and Speyer, 1985, 1987; Knauss and Wolery, 1986; Casey *et al.*, 1988a).

Kinetic models normally contain only one surface area parameter. This implies that dissolution rates are expressed per unit of "average" surface area, and hold for individual surface sites only if all surface area dissolves equally fast. However, mineral dissolution is a non-uniform chemical attack of exposed surfaces, leading to the formation of etch pits (e.g. Wilson, 1975; Berner and Holdren, 1977, 1979; Robert *et al.*, 1980; Hochella *et al.*, 1987), macropores (diameters > 50 nm; e.g. Ferry, 1985; Guthrie and Veblen, 1988; Worden *et al.*, 1990; Walker, 1990) and micropores/mesopores (diameters ≤ 2 nm and 2 nm < diameters ≤ 50 nm; e.g. Petit *et al.*, 1987a; Bunker *et al.*, 1988; Casey *et al.*, 1989a; Hellmann *et al.*, 1990; Zhang *et al.*, 1993; see also chapters 2 and 5).

The non-uniform chemical attack of mineral surfaces is inconsistent with the implicit assumption in kinetic models that all surface area dissolves equally fast. In chapter 5, the effect of etch pits and pores on the BET (gas adsorbed) surface area was investigated for feldspar and quartz in a naturally weathered assemblage. In this chapter, experimental dissolution data for the same assemblage are analyzed using the findings from chapter 5. The main objective is to determine the reactivity of the etch pits, relative to that of the pores, under acid leaching conditions.

6.2. Materials and methods

The starting material was a naturally weathered feldspar-quartz assemblage from glacial deposits of the low-grade metamorphic Central Aar granite. The material has been exposed to leaching for at least 400 years (when the glacier retreated from the sampling site). Grain diameters vary from 100 to 1000 μm . Organic matter and secondary minerals are virtually absent. The starting material is described in more detail in chapter 5.

HF/H₂SO₄ and ultrasonic pretreatment are frequently used in dissolution studies to remove unwanted adhering fine particles (e.g. Perry *et al.*, 1983; Creméens *et al.*, 1987). To determine the effect of these pretreatments on the dissolution of Al and Si, 5 g of the starting material was split into four equal portions for a preliminary dissolution test run. The sample portions were either: (1) submersed for 10 minutes in a mixture of equal volumes of a 10 % HF and a 0.1 N H₂SO₄ solution (Perry *et al.*, 1983); and/or (2) ultrasonically cleaned at low intensity for three times 10 minutes, each time followed by washing with deionized water. Thus, sample 1 is untreated, sample 2 is HF/H₂SO₄ treated, sample 3 is ultrasonically treated and sample 4 is HF/H₂SO₄ plus ultrasonically treated.

In the final dissolution experiments, the starting material was given mild (low intensity) ultrasonic cleaning for three times 10 minutes, each time followed by washing with deionized water. The cleaned material was fractionated to four different ranges of grain density (2.56-2.59, 2.59-2.63, 2.63-2.67 and 2.67-2.88 g.cm^{-3}) using bromoform and mixtures of bromoform and decaline (Van Der Plas, 1966). These were dry-sieved to fractions 600-850, 300-425 and 105-210 μm . The BET-krypton surface area, the geometric surface area, the average equivalent spherical grain diameter, and the mineralogical composition were determined for all samples (Tables 5.2 and 5.3). Optical microscopy and X-Ray diffraction showed that all samples essentially consist of quartz, microcline, microcline-perthite, albite, and oligoclase/andesine (assumed average composition $\text{Ab}_{70}\text{An}_{30}$). Optical microscopy, X-Ray fluorescence spectrometry and normative calculations (Brown and Skinner, 1974) showed that relative amounts of these minerals in individual samples varied with the density range. Optical microscopy also showed that small amounts of muscovite and biotite were present in all samples (Tables 5.2 and 5.3).

The design of the dissolution experiments was similar to that in chapter 4. Teflon single-pass flow-through reaction cells, switched for upward flow, were used in combination with peristaltic pumps and PVC and PE tubing. Non-duplicated experiments were carried out for two months (test runs) and for six months (final runs), respectively, at pH 3 and pH 5 HCl and 21 ± 3 °C. Two blanks (empty reaction cells) were run during all experiments to check for leachant composition. Three pure feldspars (adularia, albite and labradorite), dissolving at steady state pH 3 throughout the experiments, were used to test the analytical equipment performance. Sample heights in the reaction cells were about 1 mm, so concentration gradients were virtually absent. The reaction cells were fitted with 0.1 μm nylon membrane filters on both ends. The flow rate was maintained at 0.98 ± 0.08 ml.hr^{-1} for all runs. During the first few days of experiments, ultrafine particles not removed by the ultrasonic cleaning may have passed the top filter, causing false dissolution data (Holdren and Berner, 1979; Gillman and Sumner, 1987). However, calculations hereafter involve steady state rates, which were reached after several months of running time. So, all material passing the top filter was assumed to be effectively in solution. Leachates, removed at 3 to 4 days intervals, were analyzed for Na, K, Ca, Al, and Si at 1 to 3 weeks intervals using a Varian SpectraAA 300 graphite tube autoanalyzer. Leachates collected during the pH 5 stage of the runs were acidified to pH 3 with 1 M HCl before storage. Periodic duplicates showed that analytic errors in leachate concentrations are in the order of 5 % for Al and Si, 10 % for Ca and Na, and 20 % for K.

6.3. Results

Test runs

At pH 3, the effect of HF/H₂SO₄ and mild ultrasonic pretreatment on bulk dissolution rates (mol.g⁻¹.s⁻¹) from the starting material is shown in Fig. 6.1. The rates were highest for HF/H₂SO₄ pretreatment during the first month of the experiments. This may be due to fluorination of the mineral surface (Perry *et al.*, 1983). Ultrasonic pretreatment had much less effect on dissolution rates (Fig. 6.1), and was used during preparation of the final samples.

Dissolution experiments

Dissolution data for the samples of density ranges 2.56-2.59 and 2.59-2.63 g.cm⁻³ were obtained at pH 3 HCl (days 0 to 156) and at pH 5 HCl (days 156 to 186), respectively. Dissolution data for the samples of density ranges 2.63-2.67 and 2.67-2.88 g.cm⁻³ were obtained at pH 3 HCl (days 0 to 115 and 157 to 183) and at pH 5 HCl (days 115 to 157), respectively. Typical dissolution runs are shown in Fig. 6.2. Normally, dissolution rates showed high initial values in the first few months, and leveled off to lower, more or less

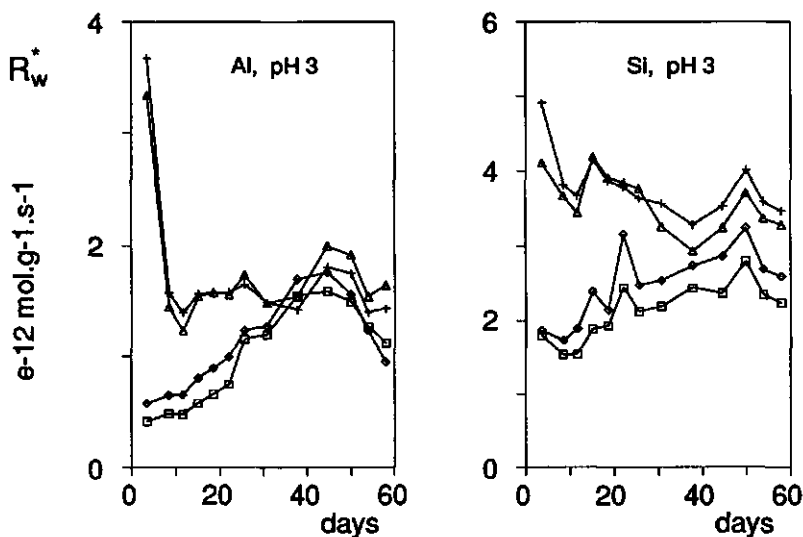


Fig. 6.1. Plots of Al and Si bulk dissolution rates (R_w^* ; in $10^{-12} \text{ mol.g}^{-1}.\text{s}^{-1}$) versus time for the starting material in the test runs (pH 3 HCl). \square : no pretreatment; $+$: HF/H₂SO₄ treated; \diamond : ultrasonically treated; Δ : HF/H₂SO₄ and ultrasonically treated.

constant values over the next few months. After switching from pH 3 to pH 5, concentrations of Na, K, Ca, and Al generally dropped quickly to much lower levels (sometimes within the range of the blanks), while concentrations of Si generally stayed relatively high. The results at pH 5 may not be similar to those without prior dissolution at pH 3. Results from similar dissolution experiments (chapter 4) suggest that concentrations of Na, K, Ca, and Al remain low at pH 5, while concentrations of Si take several months to reach new steady state values.

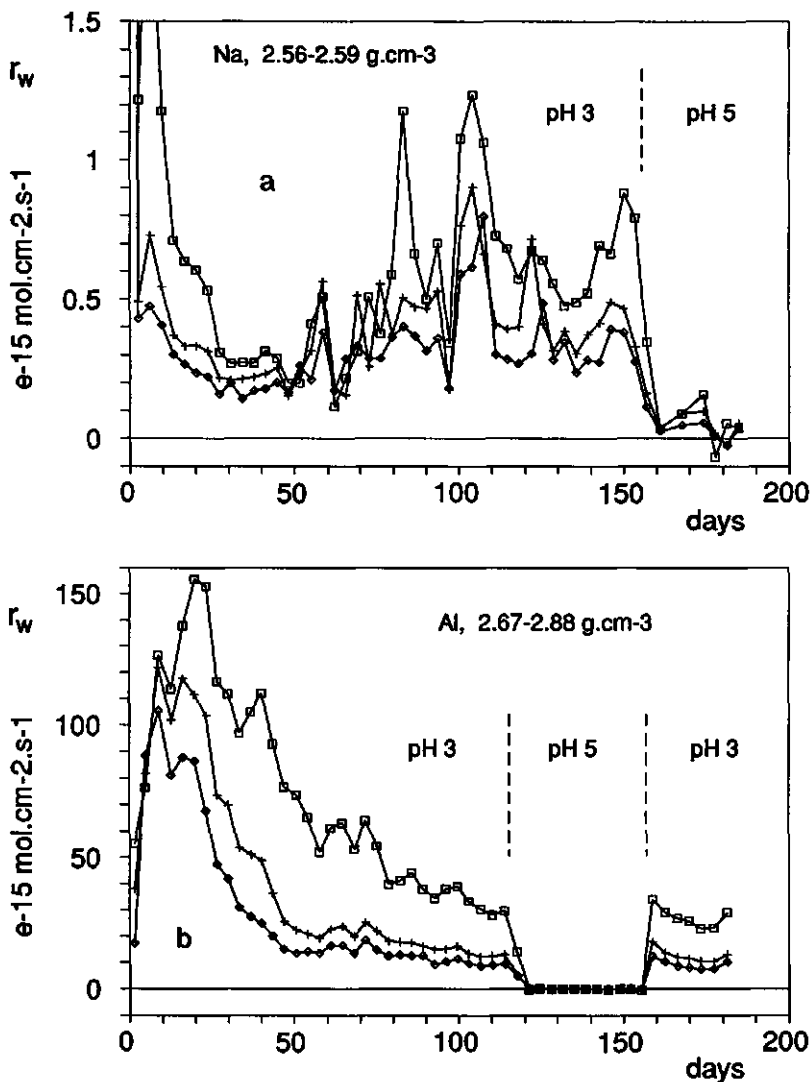


Fig. 6.2. Examples of plots of dissolution rates (r_w ; in $10^{-15} \text{ mol.cm}^{-2}$ of geometric surface area. s^{-1}) versus time. \square : 600-850 μm ; $+$: 300-425 μm ; \diamond : 105-210 μm .

Table 6.1. Dissolution rates (R_w) at pH 3 HCl (average \pm standard deviation in 10^{-17} mol.cm $^{-2}$ of BET surface.s $^{-1}$), normalized to reference sample composition for each density range (see text).

sample ¹	Na	K	Ca	Al	Si
Ac	1.97 \pm 0.38	7.05 \pm 3.03	2.25 \pm 0.49	19.5 \pm 2.1	55.9 \pm 8.8
Am	2.32 \pm 0.63	7.35 \pm 2.84	1.87 \pm 0.39	18.8 \pm 1.9	59.4 \pm 11.2
Af	2.82 \pm 0.61	10.5 \pm 4.2	1.33 \pm 0.30	25.6 \pm 2.3	76.8 \pm 14.7
Bc	2.84 \pm 0.35	5.07 \pm 2.10	3.06 \pm 0.68	20.1 \pm 1.9	62.4 \pm 11.0
Bm	2.39 \pm 0.30	5.98 \pm 2.45	1.29 \pm 0.28	15.6 \pm 1.6	52.7 \pm 9.2
Bf	2.73 \pm 0.46	5.41 \pm 2.32	1.63 \pm 0.86	18.4 \pm 2.6	40.1 \pm 7.5
Cc	5.16 \pm 0.64	7.28 \pm 1.76	2.60 \pm 0.57	19.4 \pm 3.4	84.8 \pm 10.5
Cm	4.13 \pm 0.70	7.58 \pm 3.31	1.83 \pm 0.83	12.7 \pm 2.2	49.6 \pm 6.4
Cf	3.48 \pm 0.83	17.0 \pm 8.1	1.54 \pm 0.65	15.2 \pm 3.0	28.0 \pm 5.9
Dc	4.34 \pm 0.39	26.5 \pm 3.8	7.83 \pm 2.32	52.5 \pm 7.4	125 \pm 11
Dm	5.16 \pm 0.71	18.7 \pm 2.9	3.71 \pm 0.82	31.3 \pm 4.0	90.6 \pm 9.6
Df	5.62 \pm 0.99	17.4 \pm 4.4	3.03 \pm 0.45	39.9 \pm 5.8	126 \pm 10

¹ A = 2.56-2.59 g.cm $^{-3}$; B = 2.59-2.63 g.cm $^{-3}$; C = 2.63-2.67 g.cm $^{-3}$; D = 2.67-2.88 g.cm $^{-3}$; c = 600-850 μ m; m = 300-425 μ m; f = 105-210 μ m.

Table 6.2. Dissolution rates (r_w) at pH 3 HCl (average \pm standard deviation in 10^{-16} mol.cm $^{-2}$ of geometric surface.s $^{-1}$), normalized to reference sample composition for each density range (see text).

sample ¹	Na	K	Ca	Al	Si
Ac	7.11 \pm 1.39	25.4 \pm 10.9	8.11 \pm 1.78	70.5 \pm 7.7	202 \pm 32
Am	4.60 \pm 1.25	14.5 \pm 5.6	3.70 \pm 0.76	37.2 \pm 3.8	118 \pm 22
Af	2.77 \pm 0.60	10.3 \pm 4.1	1.30 \pm 0.29	25.1 \pm 2.3	75.3 \pm 14.4
Bc	13.5 \pm 1.7	24.0 \pm 10.0	14.5 \pm 3.2	95.2 \pm 9.2	296 \pm 52
Bm	6.57 \pm 0.82	16.4 \pm 6.7	3.54 \pm 0.76	42.9 \pm 4.3	145 \pm 25
Bf	4.16 \pm 0.70	8.25 \pm 3.53	2.49 \pm 1.32	28.1 \pm 3.9	61.2 \pm 11.5
Cc	21.8 \pm 2.7	30.7 \pm 7.4	11.0 \pm 2.4	82.1 \pm 14.5	358 \pm 44
Cm	8.78 \pm 1.49	16.1 \pm 7.0	3.89 \pm 1.76	27.0 \pm 4.8	106 \pm 14
Cf	2.76 \pm 0.66	13.6 \pm 6.4	1.22 \pm 0.52	12.1 \pm 2.4	22.3 \pm 4.7
Dc	30.3 \pm 2.7	185 \pm 26	54.7 \pm 16.2	367 \pm 52	873 \pm 74
Dm	24.5 \pm 3.4	88.6 \pm 13.6	17.6 \pm 3.9	149 \pm 19	430 \pm 46
Df	14.7 \pm 2.6	45.4 \pm 11.5	7.91 \pm 1.18	104 \pm 15	328 \pm 27

¹ see note Table 6.1.

Therefore, the pH 5 experiments were not continued any further, and results at pH 5 are ignored hereafter.

Average steady state dissolution rates at pH 3, normalized to geometric and to BET surface area, were estimated from the 10 last data before switching to pH 5. The average steady state rates were further normalized to a reference sample composition for each density range (Tables 6.1 and 6.2). This eliminates differences in dissolution rate, due to differences in mineralogical composition for samples of similar density range. The average composition of all samples in a density range was used as the reference composition. For instance, the 600-850 μm , 2.56-2.59 $\text{g}\cdot\text{cm}^{-3}$ sample contains 735 $\mu\text{mol Na}\cdot\text{g}^{-1}$ sample, and a reference sample of 2.56-2.59 $\text{g}\cdot\text{cm}^{-3}$ contains 815 $\mu\text{mol Na}\cdot\text{g}^{-1}$ sample (Table 5.1). The estimated pH 3 steady state dissolution rate of Na in the 600-850 μm , 2.56-2.59 $\text{g}\cdot\text{cm}^{-3}$ sample is $(6.41 \pm 1.25) \cdot 10^{-16} \text{ mol}\cdot\text{cm}^{-2}$ of geometric surface area $\cdot\text{s}^{-1}$ (Fig. 6.2a). Thus, a 600-850 μm , 2.56-2.59 $\text{g}\cdot\text{cm}^{-3}$ sample of reference composition has a Na dissolution rate of $815/735 \cdot (6.41 \pm 1.25) \cdot 10^{-16} = (7.11 \pm 1.39) \cdot 10^{-16} \text{ mol}\cdot\text{cm}^{-2}$ of geometric surface area $\cdot\text{s}^{-1}$ (Table 6.2).

6.4. Discussion

Using the data in Table 6.1, the molar ratio of Al to Si in the leachates was plotted versus time (Fig. 6.3). If Al and Si dissolve stoichiometrically, the ratio of Al to Si is 0 for the quartz, 0.33 for the albite, the microcline and the trace mineral biotite, 0.48 for the oligoclase and andesine of assumed average composition $\text{Ab}_{70}\text{An}_{30}$, and 1.00 for the trace mineral muscovite. The experimental ratios at pH 3 steady state vary between 0.3 and 0.5 (Fig. 6.3), indicating that dissolution rates were largely determined by the feldspars, and possibly the trace mineral biotite. In chapter 4, similar results were found for dissolution from the Nova Scotia feldspar-quartz assemblage.

For the purpose of graphic presentation, the relative grain diameter of a sample w (d'_w) is defined as the ratio of the grain diameter of that sample (d_w) to the average grain diameter over all (three) samples in that density range:

$$d'_w \equiv 3d_w / (d_c + d_m + d_f) \quad (6.1)$$

where the subscripts c, m, and f refer to the coarse (600-850 μm), medium (300-425 μm), and fine (105-210 μm) fractions in that density range, respectively. In analogy, the relative dissolution rate normalized to the BET surface area (R'_w) is defined as:

$$R'_w \equiv 3R_w / (R_c + R_m + R_f) \quad (6.2)$$

and the relative dissolution rate normalized to the geometric surface area (r'_w) is defined as:

$$r'_w \equiv 3r_w / (r_c + r_m + r_f) \quad (6.3)$$

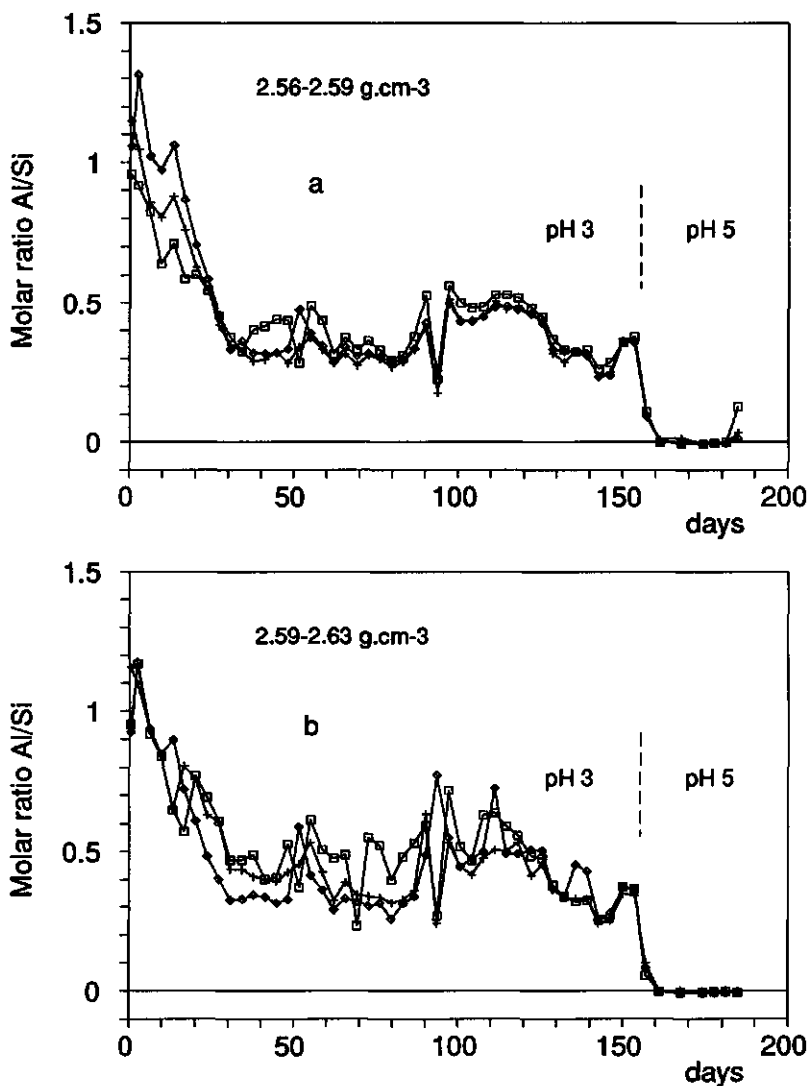


Fig. 6.3. Molar ratios of Al to Si at pH 3 and pH 5 HCl. \square : 600-850 μm ; $+$: 300-425 μm ; \diamond : 105-210 μm . Plot a: 2.56-2.59 g.cm^{-3} ; plot b: 2.59-2.63 g.cm^{-3} ; plot c: 2.63-2.67 g.cm^{-3} ; plot d: 2.67-2.88 g.cm^{-3} .

It follows from eqs. (6.1), (6.2) and (6.3) that the relative grain diameters and dissolution rates (d'_w , R'_w and r'_w) differ from the actual grain diameters and dissolution rates (d_w , R_w and r_w) only by a constant factor for samples of similar density range.

In the literature, dissolution rates normalized to the BET surface area are frequently implied to be independent of grain diameter. However, for freshly created surfaces of nine different feldspars by Holdren and Speyer (1985, 1987), dissolution rates normalized to the

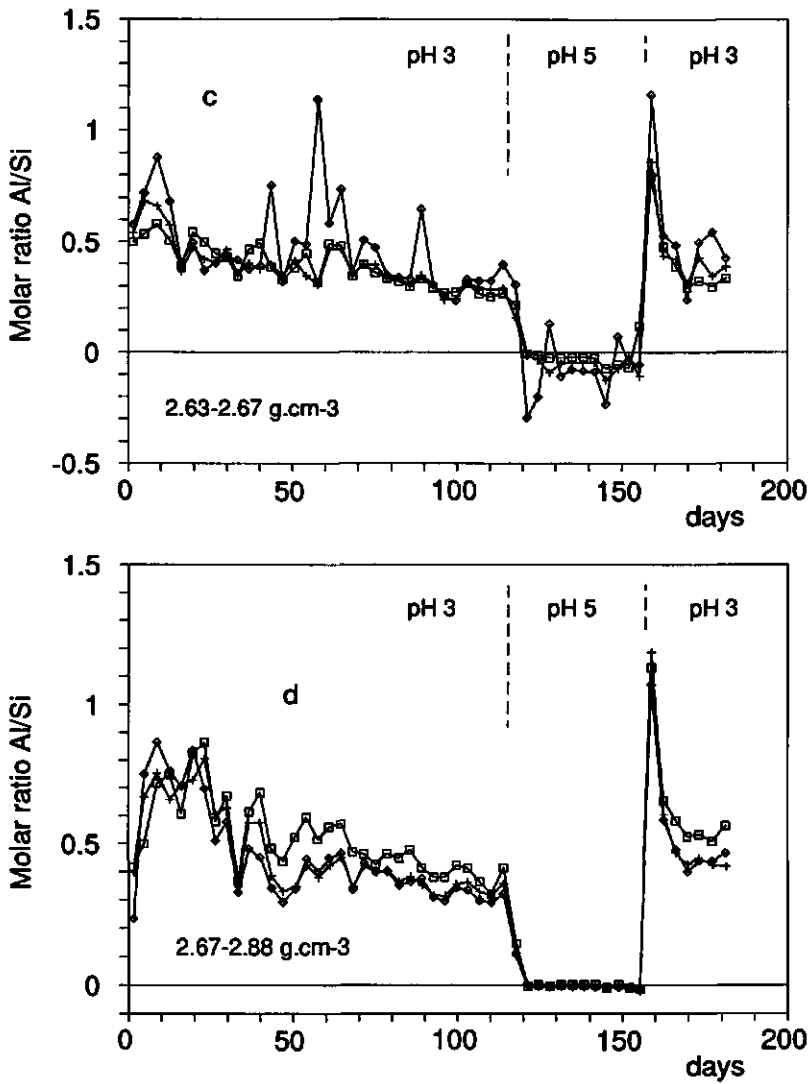


Fig. 6.3. Continued.

BET surface area are approximately proportional to grain diameter instead (chapter 3). This can be explained if preferential fracture planes have relatively high densities of dissolution reactive sites. Grinding would then expose freshly created surfaces with increasingly lower density of dissolution sites, thereby decreasing the average density at all grain diameters (chapter 3; see also Fig. 6.4). To determine the relationship between dissolution rates normalized to BET surface and grain diameter in these naturally weathered samples, R_w' (calculated from the data in Table 6.1) was plotted versus d_w' (calculated from the data in Tables 5.2 and 5.3) for all elements analyzed (Fig. 6.5). Square sums were calculated for the data in Fig. 6.5, assuming: (1) dissolution rates normalized to the BET surface area are independent of grain diameter; or (2) dissolution rates normalized to the BET surface area are proportional to grain diameter (Table 6.3). The results show that, except for Ca, model

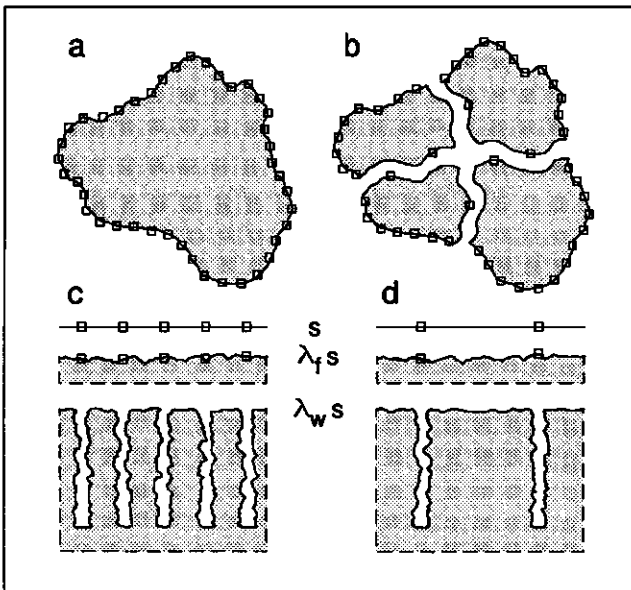


Fig. 6.4. Schematic surfaces of feldspar grains. a: a hypothetical grain with freshly created surface area only; the surface has a high density of dissolution reactive sites (indicated by squares). b: fracturing creates additional fresh surface area, and decreases the average density of dissolution sites. c,d: schematic surfaces of a large (left) and a small grain. From top to bottom: the geometric surface (s), the freshly created BET surface ($\lambda_f s$; λ_f is the roughness factor of the freshly created surfaces, which is independent of grain diameter), and the porous, naturally weathered BET surface ($\lambda_w s$; λ_w is the roughness factor of the naturally weathered surfaces, which decreases linearly with decreasing grain diameter). Etch pits and macropores have only small effects on the BET surface area and are not shown.

predictions based on dissolution rates independent of grain diameter explain the actual data better than those based on dissolution rates proportional to grain diameter. Thus, dissolution rates of these samples, normalized to BET area, largely conform to literature assumptions.

Table 6.3. Square sums for the data in Figs. 6.5 and 6.6, assuming dissolution rates normalized to BET surface area (Fig. 6.5) and to geometric surface area (Fig. 6.6) to be independent of (dashed horizontal lines) or proportional to (dashed diagonal lines) grain diameter.

	Na	K	Ca	Al	Si
Fig. 6.5, hor. lines	0.19	0.79	1.30	0.32	0.78
Fig. 6.5, diag. lines	3.47	5.22	0.91	2.79	2.33
Fig. 6.6, hor. lines	2.90	2.23	6.61	3.97	4.39
Fig. 6.6, diag. lines	0.29	0.33	0.78	0.24	0.43

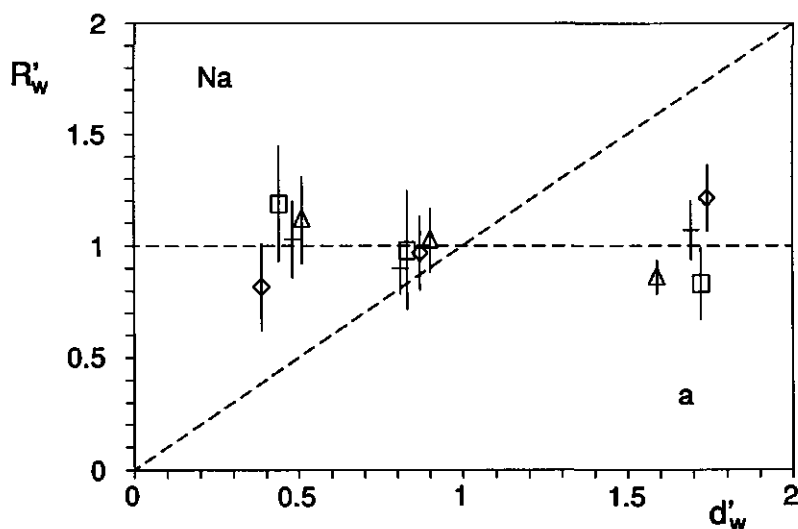


Fig. 6.5. Plots of the relative dissolution rate normalized to BET surface area (R'_w ; eq. 6.2) versus the relative grain diameter (d'_w ; eq. 6.1) at pH 3 HCl. Data of R'_w were calculated from Table 6.1; data of d'_w were calculated from Tables 5.2 and 5.3. Dashed lines are model predictions, based on dissolution rates normalized to BET surface area that are independent of grain diameter (horizontal lines) or proportional to grain diameter (diagonal lines). \square : 2.56-2.59 g.cm^{-3} ; $+$: 2.59-2.63 g.cm^{-3} ; \diamond : 2.63-2.67 g.cm^{-3} ; \triangle : 2.67-2.88 g.cm^{-3} . Plot a: Na; b: K; c: Ca; d: Al; e: Si.

As discussed in the introduction, dissolution rates normalized to BET surface area hold for the "average" BET surface, and would hold for individual surface sites only if all BET surface area dissolves equally fast. Analysis of surface morphologies in these samples (chapter 5) showed that: (1) micropores, mesopores and etch pits are the most likely dissolution reactive sites; (2) the micropores and mesopores are present in the feldspar but not in the quartz; at constant mineralogical composition, their density (cm^{-2} of geometric surface) is essentially proportional to grain diameter; and (3) the etch pits are present both in

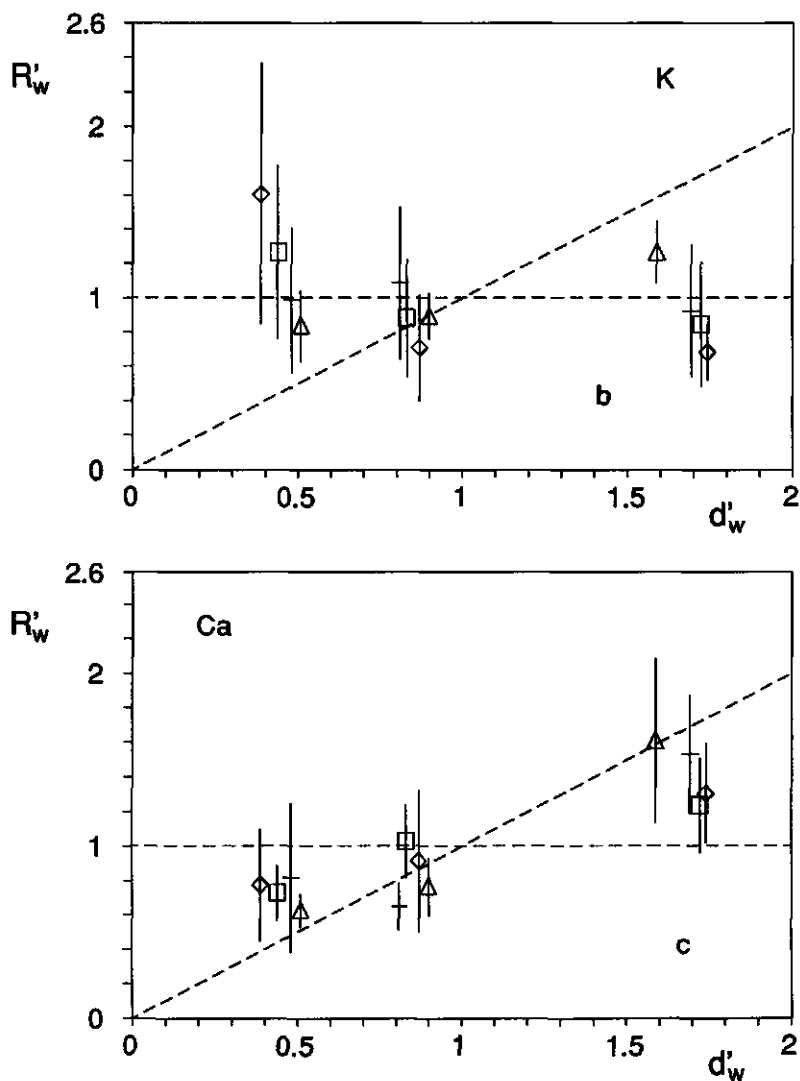


Fig. 6.5. Continued.

the feldspar and in the quartz; at constant mineralogical composition, their density (cm^{-2} of geometric surface) is essentially independent of grain diameter. To determine the reactivity of the micropores/mesopores relative to that of the etch pits, dissolution rates normalized to the geometric surface area (r'_w ; calculated from the data in Table 6.2) were plotted versus d'_w (Fig. 6.6). Square sums were calculated for the data in Fig. 6.6, assuming: (1) dissolution rates normalized to the geometric surface area are independent of grain diameter; or (2) dissolution rates normalized to the geometric surface area are proportional to grain diameter

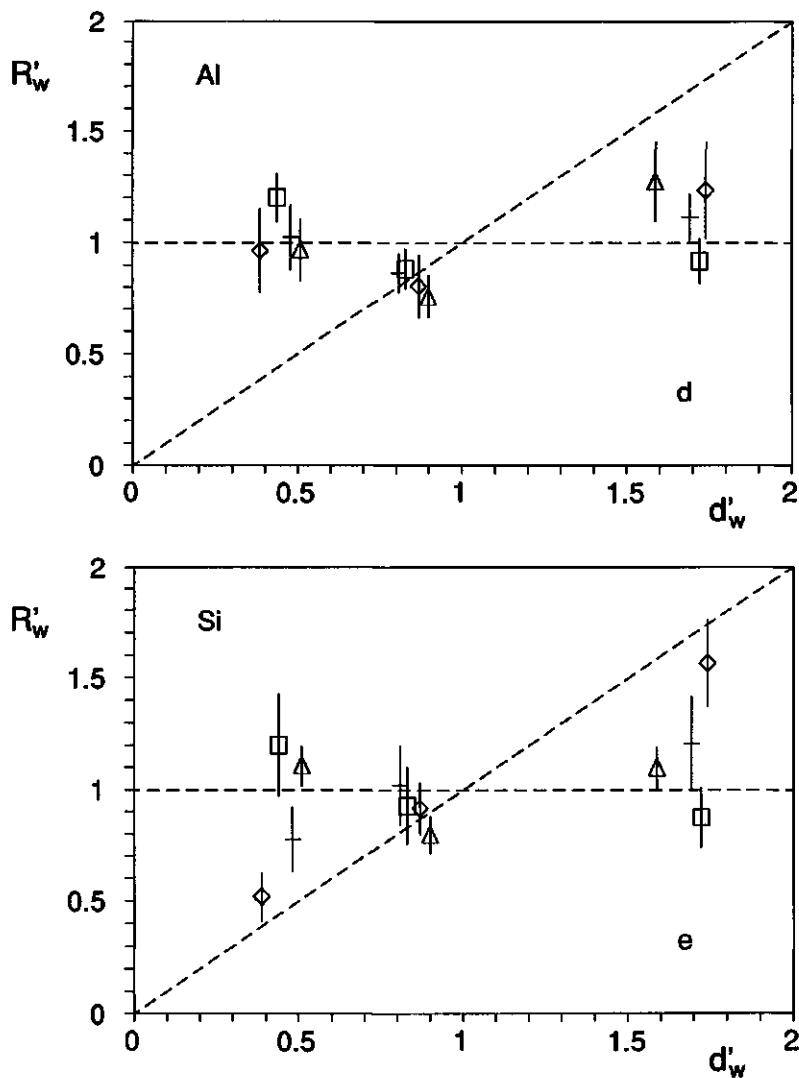


Fig. 6.5. Continued.

(Table 6.3). The results show that model predictions based on dissolution rates proportional to grain diameter explain the actual data better than those based on dissolution rates independent of grain diameter. Thus, the etch pit and pore densities, and the results in Fig. 6.6 indicate that the micropores/mesopores are the reactive sites, rather than the etch pits. Note that the independence on grain diameter of dissolution rates normalized to the BET surface area (Fig. 6.5) cannot be explained from the independence on grain diameter of the etch pit density (in cm^{-2} of geometric surface area).

Micropores may form from the development of leached layers (Chou and Wollast, 1984; Nesbitt and Muir, 1988; Casey and Bunker, 1990), and micropores/mesopores may form from enhanced dissolution at dislocations (i.e. crystal line defects; Van Der Hoek *et al.*, 1982; Lasaga and Blum, 1986). If the micropores in these feldspars formed from the development of leached layers during natural weathering, the BET surface area of the leached material (i.e. the micropore "walls" in Fig. 6.4) is essentially non-reactive, at least for the leached substances (Casey *et al.*, 1989a; Muir *et al.*, 1989, 1990; Hellmann *et al.*, 1990). However,

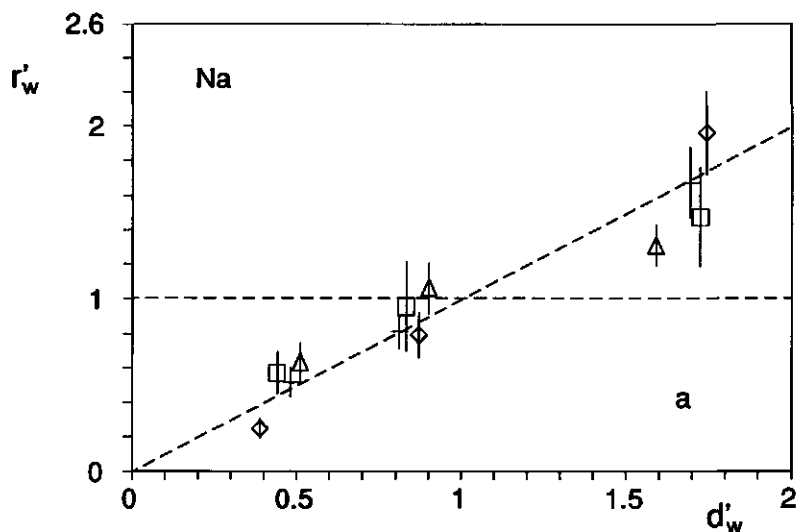


Fig. 6.6. Plots of the relative dissolution rate normalized to geometric surface area (r'_w ; eq. 6.3) versus the relative grain diameter (d'_w ; eq. 6.1) at pH 3 HCl. Data of r'_w were calculated from Table 6.2; data of d'_w were calculated from Tables 5.2 and 5.3. Dashed lines are model predictions, based on dissolution rates normalized to geometric surface area that are independent of grain diameter (horizontal lines) or proportional to grain diameter (diagonal lines). \square : 2.56-2.59 g.cm^{-3} ; $+$: 2.59-2.63 g.cm^{-3} ; \diamond : 2.63-2.67 g.cm^{-3} ; Δ : 2.67-2.88 g.cm^{-3} . Plot a: Na; b: K; c: Ca; d: Al; e: Si.

analysis of surface morphologies suggests that leached layers, whether present or not, do not contribute significantly to the BET surface area of these samples (chapter 5). If, alternatively, the micropores (and mesopores) formed from enhanced dissolution at crystal defects, the BET surface area of the pore "walls" is essentially non-reactive too, because micropores/mesopores at crystal defects develop by increasing their depth rather than their diameter (Van Der Hoek *et al.*, 1982; Lasaga and Blum, 1986; see also chapter 7).

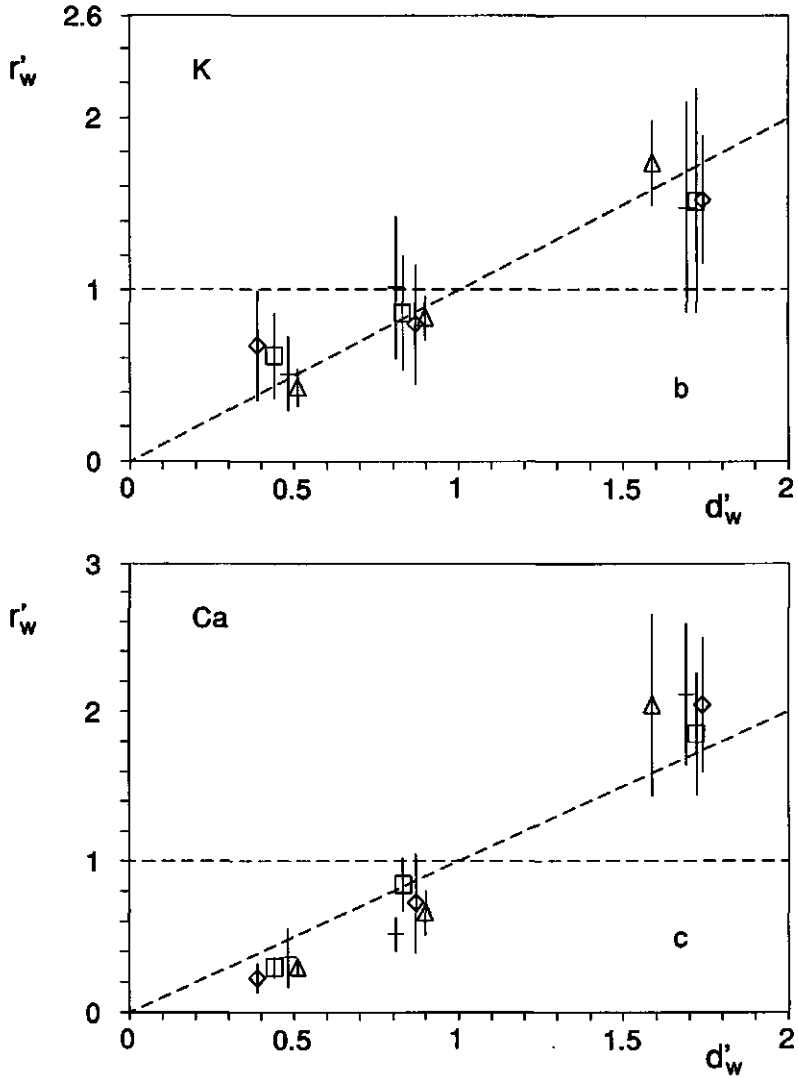


Fig. 6.6. Continued.

Although the micropore/mesopore "walls" were most likely non-reactive, dissolution may have occurred at the pore "bottoms" (i.e. the leached layer/fresh mineral interface, or the dislocation outcrops where strained mineral material is in contact with the solution). If so, the proportion of the geometric surface area occupied by reactive surface area is proportional to grain diameter, because the density of micropores/mesopores (cm^{-2} of geometric surface area) is proportional to grain diameter (see also Fig. 6.4). Thus, dissolution at micropore/mesopore "bottoms" explains the relationships between dissolution rates

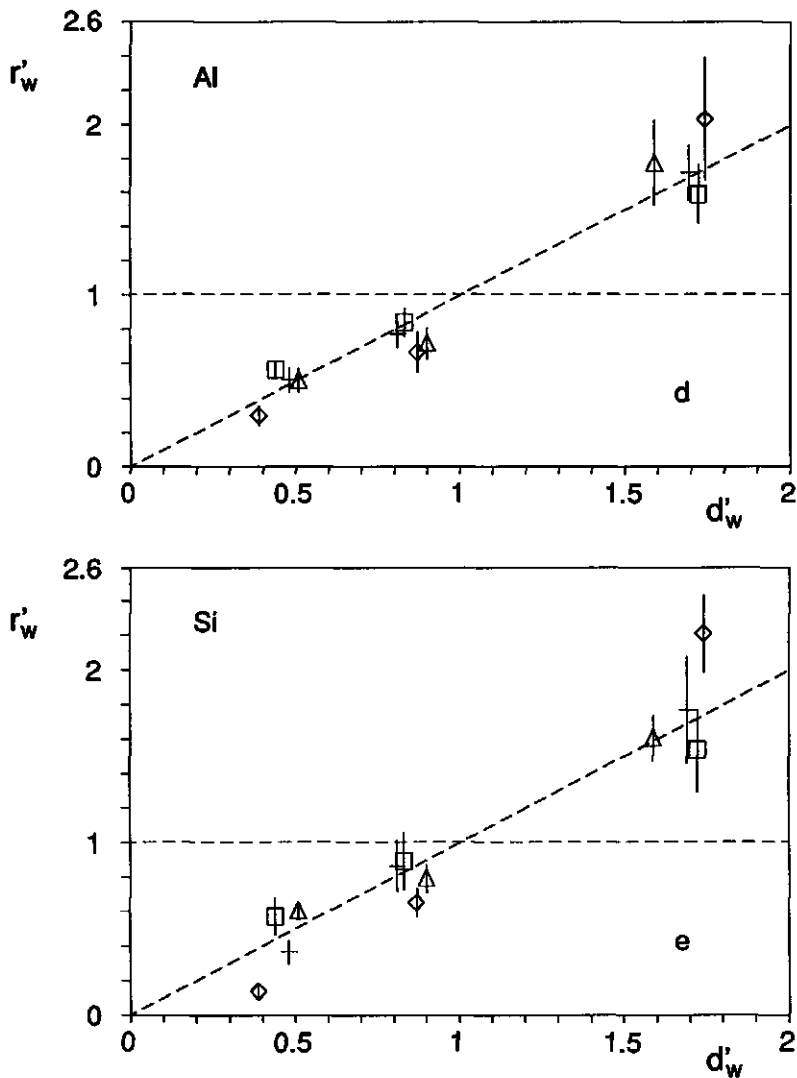


Fig. 6.6. Continued.

normalized to geometric surface area and grain diameter (Fig. 6.6). Note that the proportion of the BET area inside the pores which is occupied by the pore "bottoms" is independent of the grain diameter (Fig. 6.4). Because the BET area of the samples essentially equals that of the micropores/mesopores (chapter 5), this explains why dissolution rates normalized to the BET surface area are independent of the grain diameter (Fig. 6.5). So, the independence on grain diameter of dissolution rates normalized to the BET area indicates that the ratio of pore diameter to pore length, and not the density of dissolution sites, is independent of grain diameter. These findings also agree with the findings in chapter 3 that dissolution rates of freshly created feldspar surfaces normalized to their BET area are proportional to grain diameter, and not independent of grain diameter (Fig. 6.4).

Because micropores/mesopores are absent in the quartz (chapter 5), its dissolution rate is probably determined by the less reactive etch pits. This may explain the low dissolution rate of quartz compared to feldspar. If quartz dissolution is indeed determined by the etch pits, dissolution rates of quartz, normalized to the geometric surface area, should be independent of grain diameter (because the density of etch pits is independent of grain diameter). Due to the absence of micropores/mesopores, the surface roughness factor (i.e. the ratio of BET to geometric surface area) of quartz in these samples is essentially independent of grain diameter (chapter 5). Because dissolution rates normalized to BET surface area are by definition a factor surface roughness smaller than those normalized to geometric surface area, quartz dissolution rates, normalized to BET surface area, should be independent of grain diameter too.

Discrepancies up to several orders of magnitude between field- and laboratory derived dissolution rates have been reported for feldspar (Pačes, 1983; Velbel, 1985), but not (yet) for quartz. Part of this discrepancy may be related to the fact that most surface area of naturally weathered feldspar grains is present as non-reactive micropore/mesopore "walls", which are absent on freshly created feldspar surfaces in the laboratory. Because micropores/mesopores are absent both on freshly created and naturally weathered quartz surfaces, the discrepancy between field- and laboratory derived dissolution rates for quartz should be small relative to that for feldspar.

In the 600-850 μm , 2.67-2.88 $\text{g}\cdot\text{cm}^{-3}$ sample, the micropore volume is approximately $3.1\cdot 10^{-5} \text{ cm}^3\cdot\text{g}^{-1}$, the etch pit density is approximately 4000 cm^{-2} of geometric surface area, and the average etch pit diameter is approximately $1.5 \mu\text{m}$ (chapter 5). The volume of mesopores is not well-known and is ignored hereafter. If the etch pits and micropores were cylindrically shaped and internally smooth, if the micropore "walls" were non-reactive, and if the average depth of the etch pits and micropores were, for instance, $1 \mu\text{m}$, the volume

amount dissolved during natural weathering ($\text{cm}^3 \cdot \text{cm}^{-2}$ of reactive surface area) is $2.7 \cdot 10^{-5}$ for the etch pits, and $1.0 \cdot 10^{-4}$ for the micropores. This suggests that field weathering rates, normalized to reactive surface area, were of approximately the same order of magnitude for the etch pits and the micropores. However, the reactive surface areas ($\text{cm}^2 \cdot \text{g}^{-1}$ sample) are 0.011 for the etch pits, and 0.313 for the micropores. Furthermore, the reactive surface area of the etch pits was smaller than 0.011 during the initial stages of natural weathering (because the etch pits were smaller), while the reactive surface area of the micropores was probably constant throughout the exposure time (because micropore growth increases only the amount of non-reactive surface area). These tentative calculations suggest that - as in the laboratory - dissolution rates during the previous natural weathering of the sample material were determined by the micropore "bottoms", rather than by the etch pits. The calculations also suggest that the contribution of etch pits to the dissolution of feldspar, relative to the contribution of micropores, increases with increasing exposure time to natural weathering.

6.5. Conclusions

Steady state dissolution rates of Na, K, Ca, Al and Si were determined at pH 3 HCl for subsamples from a naturally weathered assemblage of feldspar and quartz. The subsamples were obtained from fractionation to four different ranges of grain density, each of which was sieved to three different size fractions. The dissolution data, and analysis of surface morphology (chapter 5), indicate that micropores and mesopores (present in the feldspar but not in the quartz) are the dissolution reactive sites, rather than the etch pits (present in both the feldspar and the quartz). Theoretical arguments indicate that the pore area perpendicular to the grain surface (i.e. the micropore/mesopore "walls") is essentially non-reactive. This strongly suggests that dissolution rates in these samples are largely determined by the area of the micropore/mesopore "bottoms" in the feldspar, which is equivalent to: (1) the leached layer/fresh mineral interface if pores develop from selective leaching; or (2) the dislocation outcrops where strained mineral material is in contact with the solution if pores develop at crystal defects. Tentative calculations suggest that dissolution during natural weathering prior to the experiments was determined - as in the laboratory - by the pore "bottoms" in the feldspar.

The results from this and the earlier chapters indicate that the dissolution of feldspar and quartz proceeds as follows. Dissolution rates of fresh-surface feldspar grains, normalized to the geometric or to the BET surface area are approximately proportional to grain diameter (chapter 3). This can be explained from the density of dissolution reactive sites (i.e. sites where micropores and mesopores develop during natural weathering), which is approximately

proportional to grain diameter (chapter 3). During the first stages of natural weathering, the amounts of reactive and geometric surface area are constant with time. So, dissolution rates of naturally weathered feldspar grains, normalized to the geometric surface area, equal those of similarly sized fresh-surface feldspar grains, and are approximately proportional to grain diameter. Dissolution rates normalized to the BET surface area are by definition a factor surface roughness smaller than those normalized to the geometric surface area. Due to the development of micropores/mesopores at the dissolution reactive sites, it holds for naturally weathered feldspar grains that: (1) surface roughness factors decrease linearly with decreasing grain diameter; and (2) dissolution rates, normalized to the BET surface area, are approximately independent of grain diameter. Thus, the independence on grain diameter of feldspar dissolution rates normalized to the BET area does not provide any significant information other than the fact that the ratio of pore diameter to pore depth is independent of grain diameter after natural weathering. These findings indicate that, for proper comparison of data from different experiments, feldspar dissolution rates should be normalized to the geometric, rather than to the BET surface area. Because micropores/mesopores do not form in quartz during natural weathering, its dissolution rate is probably determined by the less reactive etch pits. This may explain the low dissolution rate of quartz compared to feldspar. Because the density of etch pits on quartz surfaces (cm^{-2} of geometric surface area) is independent of grain diameter (chapter 5), the dissolution rate of quartz, either normalized to BET or to geometric surface area, and both for freshly created and for naturally weathered surfaces, should be independent of grain diameter. The absence of non-reactive BET area of micropore/mesopore "walls" in quartz may help to explain why large discrepancies between field- and laboratory derived dissolution rates have been reported for feldspar, but not (yet) for quartz.

Acknowledgements

We are greatly indebted to Joop Harmsen for providing the graphite tube autoanalyzer system at the ICW, Wageningen, The Netherlands. We thank Leo Begheyn and Barend van Lagen of the Department of Soil Science and Geology, Agricultural University, Wageningen, for performing the chemical analyses.

A combined version of this and the previous chapter has been accepted for publication in *Geochimica et Cosmochimica Acta*.

Editorial handling for *Geochimica et Cosmochimica Acta*: G. Sposito.

The dissolution of naturally weathered feldspar and quartz

Chapter 7. Crystal defects, micropores, and the reactivity of mineral surfaces; a theoretical study

(co-authored by P. Verburg and E.L. Meijer)

Abstract

Minerals differ in the way their surface is affected by weathering. Little or no change may occur if the mineral is resistant, while etch pits and micropores may develop in reactive minerals. We surveyed the conditions leading to the formation of micropores at dislocations for two contrasting minerals (sanidine and quartz) and investigated the effect of micropores on dissolution rates. Thermodynamical considerations indicate that, for sanidine in contact with moderately undersaturated solutions: (1) micropores (radii up to 5 nm) and etch pits develop at dislocations; and (2) at solution composition constant with time, the surface area of micropore "walls" is non-reactive. In contrast, no micropores develop at dislocations in quartz, regardless of solution composition. These findings agree with earlier observations for a naturally weathered feldspar-quartz assemblage.

We introduced one-dimensional aqueous diffusion into an existing Monte Carlo program to simulate the development of dissolution holes at dislocations with time. The simulations showed that, as the depth of a dissolution hole (proto etch pit or micropore) increases with time, the dissolution rate at the bottom of the hole decreases, due to the increasing diffusion path length. Finally, a steady state depth up to several μm is reached, during which the dissolution rate at the bottom of the hole equals the (very slow) rate outside the hole. The simulations showed that, due to diffusion inside the holes, micropores form during the natural weathering of sanidine, even though the free energy change of the bulk solution indicates that etch pitting should occur. Both for sanidine and for quartz, the simulations showed that the effect of diffusion is insufficient to prevent the formation of etch pits at dislocations under highly undersaturated laboratory conditions. The simulations confirmed the hypothesis that micropore "walls" are essentially non-reactive.

A kinetic model was derived to implement the non-reactive character of micropore "walls". Application of this model to literature data for naturally weathered feldspar showed that, after correction for the non-reactivity of the micropore "walls", the dissolution rate of the remaining surface area is approximately similar to that of freshly created feldspar surfaces under similar hydrogeochemical conditions. Thus, the formation of non-reactive micropore "walls" at dislocations probably represents the most essential change in surface area character during the natural weathering of feldspar.

7.1. Introduction

Dissolution of primary minerals such as feldspar and quartz proceeds as a non-uniform chemical attack of exposed surfaces, leading to the formation of etch pits (e.g. Lazorina and Soroka, 1974; Berner and Holdren, 1979; Wegner and Christie, 1983; Brantley *et al.*, 1986; Hochella. *et al.*, 1987) and/or pores (e.g. Petit *et al.*, 1987a; Casey *et al.*, 1989a; Worden *et al.*, 1990; see also chapter 5). Etch pits develop from enhanced dissolution at surface sites of high internal energy if the dissolution rate is limited by the rate of a chemical reaction step at the mineral-water interface (Berner and Holdren, 1977, 1979; Berner 1981; Helgeson *et al.*,

1984). In particular, dislocation (i.e. crystal line defect) outcrops favor the development of etch pits (Patel *et al.*, 1965; Joshi and Vagh, 1968; Joshi *et al.*, 1970; Heimann, 1982). Several models have been proposed to explain the formation of pores during mineral dissolution: (1) micropores and/or mesopores (diameters ≤ 50 nm) may develop from enhanced dissolution at dislocation outcrops if the dissolution rate is limited by the rate of a chemical reaction step at the mineral-water interface (Van Der Hoek *et al.*, 1982; Lasaga and Blum, 1986); (2) a selectively leached microporous surface layer may develop if the dissolution rate is limited by the rate of a transport step, e.g. diffusion of aqueous reactants and products (Doremus, 1983; Chou and Wollast, 1984; Casey and Bunker, 1990); and (3) macropores (diameters > 50 nm) may develop from the leakage of fluid inclusions formed during the initial cooling of the pluton (Parsons *et al.*, 1988).

Dislocations are present in virtually all crystalline solids, although their density is highly variable. In primary minerals such as feldspar and quartz, relatively low dislocation densities of 10^5 cm⁻² are typical for slow crystal growth, while densities as high as 10^{10} cm⁻² may be found in plastically deformed low metamorphic rocks (Blum *et al.*, 1990). The distribution of dislocations may be spatially variable, and densities as high as 10^{12} cm⁻² have been reported spotwise in quartz (Liddell *et al.*, 1976).

Although dislocations hardly affect the bulk thermodynamic properties of minerals (Helgeson *et al.*, 1984, Blum *et al.*, 1990), their effect on dissolution rates can be dramatic (Lasaga, 1983; Helgeson *et al.*, 1984; Lasaga and Blum, 1986). At very high degrees of undersaturation, dissolution rates are relatively independent of the dislocation density (Murr and Hiskey, 1981; Casey *et al.*, 1988a; Holdren *et al.*, 1988; Murphy, 1988, 1989; Blum *et al.*, 1990). Under such conditions the kinetics of mineral dissolution are more likely controlled by impurities in the crystal lattice (Blum *et al.*, 1990). Closer to equilibrium, however, dislocation densities above a critical limit considerably affect dissolution rates (Wintsch and Dunning, 1985; Schott *et al.*, 1989). The microstructure of dislocations is most likely another important factor in their control of dissolution rates (Meike, 1990).

In the literature so far, the possible role of dislocations on mineral dissolution has been largely confined to the development of etch pits. However, for a naturally weathered feldspar-quartz assemblage from low-grade metamorphic Central Aar granite (Switzerland), it was concluded in chapters 5 and 6 that: (1) during natural weathering, micropores detected by the BET-krypton method had developed in the feldspar grains but not in the quartz grains; (2) the micropores detected by the BET-krypton method had developed from dissolution at dislocations, rather than from selective leaching; and (3) during natural weathering, and in subsequent laboratory experiments at pH 3 HCl on unfractured samples, dissolution rates

normalized to the BET-krypton surface area were controlled by the micropores, rather than by the etch pits. These findings indicate that the development of micropores at dislocations is probably of great importance to our understanding of the mineral dissolution process. For the naturally weathered assemblage from Switzerland, it was estimated in chapter 5 that the micropores should be several μm deep to explain the micropore volume derived from the BET data. However, hydrogen depth profiling techniques suggest that chemical alterations in weathered mineral surface layers extend only to a depth of 100 nm or so (Petit *et al.*, 1987a; Nesbitt and Muir, 1988; Mogk and Locke, 1988; Althaus and Tirtadinata, 1989; Casey *et al.*, 1989a; Goossens *et al.*, 1989).

This paper is a continuation of work by Cabrera and Levine (1956), Van Der Hoek *et al.* (1982) and Lasaga and Blum (1986) on the role of dislocations in mineral dissolution. Emphasis is on the formation of micropores at dislocations, and on their possible effect on dissolution rates. More specifically, we concentrated on the following questions:

- 1) Why do micropores develop in feldspar grains but not in quartz grains during natural weathering?
- 2) Can micropores and etch pits coexist on naturally weathered feldspar surfaces?
- 3) To what extent is diffusion of aqueous reactants and products rate-limiting inside the micropores (i.e. can micropores be several μm deep as estimated in chapter 5)?
- 4) How does the surface area of micropores affect dissolution rates?

In the sections hereafter, we will first consider some thermodynamic aspects. Next, we present and discuss the results of some Monte Carlo simulations. Finally, we present a kinetic model that includes the most important findings from the thermodynamic and Monte Carlo sections.

7.2. Thermodynamic considerations

The immediate area around a dislocation contains strain energy, emanating from the crystal lattice distortion induced by the dislocation (Fig. 7.1). Upon dissolution the strain energy is released and enhanced dissolution at dislocations may result. Dissolution is most favorable at the dislocation outcrop itself, where the strain energy density is highest. As a result, a microscopic hole tends to form with the dislocation at its centre. Depending on the overall energetics of the process, dissolution may then proceed until the microscopic hole becomes a macroscopic hole (etch pit). To determine the outcome of dissolution at a dislocation, the EMC-diagram (i.e. the "phase" diagram in Van Der Hoek *et al.*, 1982) is a very powerful concept. The theoretical considerations leading to the construction of the EMC-diagram are briefly repeated hereafter from the earlier literature.

For a dislocation perpendicular to the mineral surface, the change in free energy (dG ; kJ) upon increasing the radius r of a cylindrical microscopic hole by infinitesimal dr is given by (Lasaga and Blum, 1986):

$$dG = (\Delta G/V)2\pi rL dr + \sigma 2\pi L dr - u_r 2\pi rL dr \quad (7.1)$$

where ΔG ($\text{kJ}\cdot\text{mol}^{-1}$) is the molar free energy change of the dissolution reaction of unstrained mineral bulk, V is the molar volume of the mineral, L is the length of the hole (so $2\pi rL$ dr is the volume of material that dissolves in the infinitesimal step), σ ($\text{kJ}\cdot\text{nm}^{-2}$) is the free energy needed to create one unit amount of surface area, and u_r ($\text{kJ}\cdot\text{nm}^{-3}$) is the strain energy density as a function of r . In eq. (7.1), the creation of additional surface area upon dissolution to a larger radius increases dG (hence the positive sign), the release of strain energy upon dissolution decreases dG (hence the negative sign), and the free energy change of dissolution of unstrained mineral bulk either increases dG at supersaturation ($\Delta G > 0$), or decreases dG at undersaturation ($\Delta G < 0$). ΔG is found from:

$$\Delta G = \mathfrak{R}T \ln \left[\frac{(\prod_i a_i^{q_i})}{K_{eq}} \right] \quad (7.2)$$

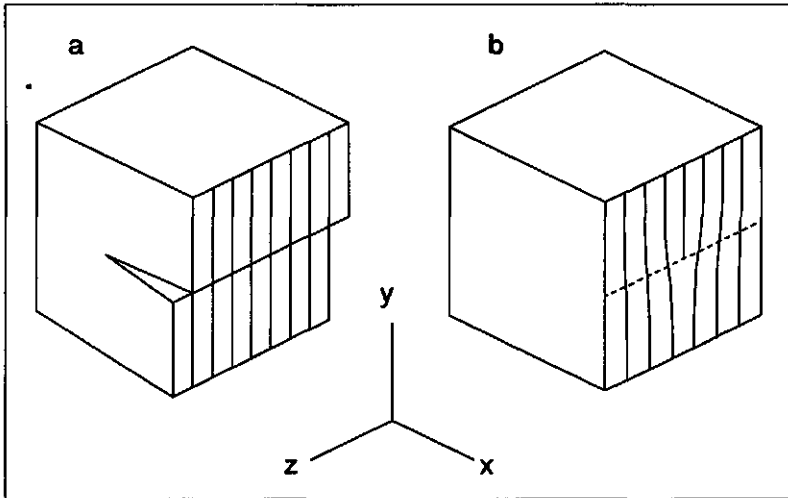


Fig. 7.1. Morphology of dislocations. a: pure screw dislocation; the Burgers vector (i.e. the "distortion" vector in the lattice) and the dislocation line (i.e. the line connecting all Burgers vectors) are both parallel to z . b: pure edge dislocation; the Burgers vector is parallel to z , and the dislocation line is parallel to x .

where \mathcal{R} is the gas constant, T (K) is temperature, a_i is the aqueous activity of species i in the dissolution reaction, q_i is the stoichiometric coefficient of the aqueous species i (which is positive for products and negative for reactants), and K_{eq} is the equilibrium constant of the dissolution reaction for unstrained mineral bulk.

At a distance r greater than approximately 1 nm, the strain energy in the distorted crystal lattice can be described using ideal elastic behaviour (Lasaga and Blum, 1986). At closer distance to the dislocation, the elastic continuum theory is no longer valid and several *ad hoc* functions have been proposed to describe the non-ideal elastic behaviour within this region. Van Der Hoek *et al.* (1982) proposed a continuous function u_r which, beyond approximately 1 nm from the dislocation, approaches ideal elastic behaviour:

$$u_r = \frac{\mu b^2}{8\pi^2 \mathcal{K} (r^2 + r_h^2)} \quad (7.3)$$

where μ ($\text{kJ}\cdot\text{nm}^{-3}$) is the bulk shear modulus, b (nm) is the magnitude of the Burgers vector of the dislocation, \mathcal{K} is a geometry factor related to the type of dislocation, r is again the distance from the dislocation, and r_h is Hooke's radius (see below). \mathcal{K} is found from (Lasaga and Blum, 1986):

$$\mathcal{K} = \left\{ \frac{\sin^2 \Psi}{1 - p} + \cos^2 \Psi \right\}^{-1} \quad (7.4)$$

where Ψ is the angle between the dislocation and the Burgers vector, and p is Poisson's ratio. \mathcal{K} equals unity for a pure screw dislocation ($\Psi = 0^\circ$; Fig. 7.1a), and \mathcal{K} equals $1 - p$ for a pure edge dislocation ($\Psi = 90^\circ$; Fig. 7.1b). For other values of Ψ , $b \sin \Psi$ is the edge component, and $b \cos \Psi$ is the screw component of the Burgers vector. r_h equals the distance r from the dislocation where the strain energy density u_r has dropped to 50 % of its value at $r = 0$ (eq. 7.3). r_h is given by (Van Der Hoek *et al.*, 1982):

$$r_h = (r_f \sigma / u_0)^{1/2} \quad (7.5)$$

where r_f is Frank's radius, and u_0 is the strain energy density at $r = 0$. r_f is the radius of the cylindrical dissolution hole at equilibrium ($\Delta G = 0$) in the special case where $r_h = 0$, and is found from (Frank, 1949):

$$r_f = \frac{\mu b^2}{8\pi^2 \mathcal{K} \sigma} \quad (7.6)$$

Mineral dissolution at dislocations, leading to microscopic or macroscopic holes, will proceed as long as free energy is gained by the process. Thus, the dynamics of formation of micropores and/or etch pits at dislocations ultimately depends on the shape of the integrated free energy function of eq. (7.1). Using eq. (7.3), integration and multiplication by N_{av}/L gives (Lasaga and Blum, 1986):

$$\Delta G_{pit} = N_{av} \left\{ \frac{\pi \Delta G}{V} r^2 + 2\pi \sigma r - \frac{\mu b^2}{8\pi \kappa} \ln [1 + (r/r_h)^2] \right\} \quad (7.7)$$

where ΔG_{pit} ($\text{kJ} \cdot \text{mol}^{-1} \cdot \text{nm}^{-1}$) is the total free energy change per unit depth upon dissolution from radius 0 to radius r , and where N_{av} is Avogadro's constant (mol^{-1}). The general shape of ΔG_{pit} as a function of r is plotted in the EMC-diagram on the presence of etch pits, micropores and closed dislocations at mineral surfaces (Fig. 7.2). The x- and y-values in the EMC-diagram are given by r_f/r_h and r_f/r_c , respectively, where r_c is the critical radius of two-dimensional nucleation. r_c is found from (Van Der Hoek *et al.*, 1982):

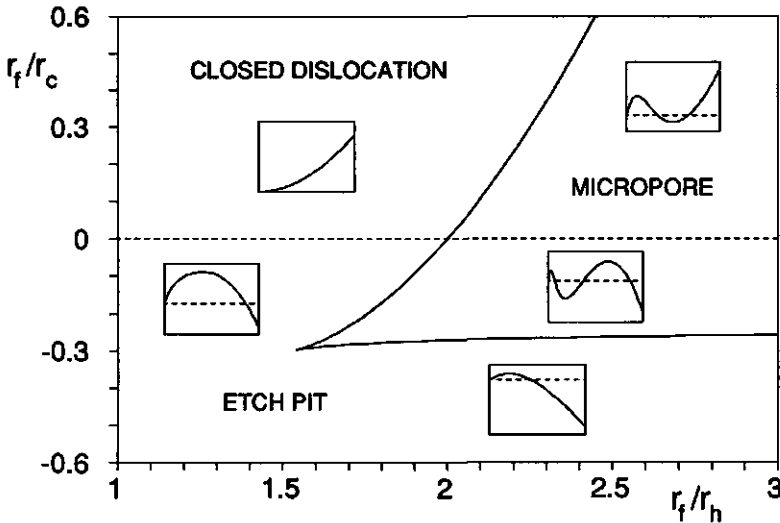


Fig. 7.2. EMC-diagram of etch pitting and micropore formation in minerals. The x-axis depends on mineral parameters only, and the y-axis depends on both mineral and aqueous solution parameters (see text). Inserts are examples of ΔG_{pit} versus r (eq. 7.7) in corresponding regions, showing respectively: (1) no minima or maxima (closed dislocations); (2) one maximum (etch pits); (3) one maximum and one minimum (stable micropores); and (4) two maxima and one minimum (metastable micropores).

$$r_c = \sigma V / \Delta G \quad (7.8)$$

which is positive for precipitation, and negative for dissolution. From eqs. (7.5) and (7.6) it follows that:

$$\frac{r_f}{r_h} = \frac{b}{\sigma} \left\{ \frac{\mu u_0}{8\pi^2 \kappa} \right\}^{1/2} \quad (7.9)$$

and from eqs. (7.6) and (7.8):

$$\frac{r_f}{r_c} = \frac{\mu b^2 \Delta G}{8\pi^2 \kappa \sigma^2 V} \quad (7.10)$$

According to eqs. (7.9) and (7.10), the x-value in the EMC-diagram depends on mineral parameters only, whereas the y-value depends on both mineral and aqueous solution parameters. In the region labeled "micropore" (Fig. 7.2), all ΔG_{pit} -curves have a minimum, so dissolution holes of a finite radius r are (meta)stable. Outside this region the curves show no minima, so if the solution is undersaturated ($r_f/r_c < 0$), free energy is gained by the dissolution process at all r larger than a critical value. This leads to the formation of etch pits, provided that the energy barrier at small r can be surmounted. In general, the height of the energy barrier decreases with increasing degree of undersaturation. At supersaturation outside the micropore region, the ΔG_{pit} -curve increases monotonically with increasing r , so dislocations remain closed and neither etch pits nor micropores tend to form.

Application to quartz and sanidine

Parameters needed to apply this model to the dissolution of minerals include the surface free energy σ , the bulk shear modulus μ , Poisson's ratio ν , the magnitude of the Burgers vector b , and the strain energy density at the dislocation u_0 (see Table 7.1 for quartz and sanidine). The data in Table 7.1 for sanidine are generally close to available data for other K-feldspars, so the conclusions hereafter are probably valid for K-feldspar as a group. Available data for Na- and Ca-feldspar are generally much closer to those for sanidine than to those for quartz.

Some critical remarks concerning the data in Table 7.1 are in order. The estimate of σ for quartz does not account for variations, due to different crystallographic orientations of mineral surfaces. However, the estimate was obtained from solubility data, and is thus an

Table 7.1. Mineral data.

	quartz	sanidine
σ (10^{-22} kJ.nm ⁻²)	3.50 ¹	2.00 ²
μ (10^{-22} kJ.nm ⁻³)	444 ³	287 ³
p (-)	0.077 ⁴	0.278 ⁴
b (most frequent; nm)	0.49 ⁵	1.12 ⁶
b (next frequent; nm)	0.73 ⁵	0.86 ⁷
ΔH_m (kJ.mol ⁻¹)	8.17 ⁸	61.6 ⁴
V (cm ³ .mol ⁻¹)	22.69 ⁹	109.1 ⁹

¹ Parks (1984); ² theoretical value for orthoclase; Brace and Walsh (1962); ³ Heinisch *et al.* (1975); ⁴ Lasaga and Blum (1986); ⁵ Doukhan and Trepied (1979); ⁶ Sacerdoti *et al.* (1980); ⁷ Willaime and Gandais (1977); ⁸ data for cristobalite; Lasaga and Blum (1986); ⁹ Robie *et al.* (1978).

average experimental value over the entire surface (Parks, 1984). Experimental values of σ for feldspar are not well-established. Brace and Walsh (1962) calculated a theoretical value of $2.00 \cdot 10^{-22}$ kJ.nm⁻² for orthoclase, and we adopted this value for sanidine. The estimates of μ and p do not account for anisotropy, present in most minerals. However, the isotropic case is probably a fairly good approximation, at least beyond approximately one nm from the dislocation (Lasaga and Blum, 1986). Table 7.1 lists the magnitude of some of the most frequently observed Burgers vectors for dislocations in quartz and K-feldspar. Smaller Burgers vectors may be found, for instance, at "partial dislocations" (Christie and Ardell, 1976), or at point defects such as Al substitution in quartz (Blum *et al.*, 1990). Larger Burgers vectors may be found, for instance, at "super dislocations", consisting of two closely spaced dislocations showing mutual interaction (Van Der Biest and Thomas, 1976). Finally, u_0 may be estimated by assuming that the strain energy associated with the thorough disordering of chemical bonds at the dislocation equals the energy needed to disorder the crystal into a melt (Van Der Hoek *et al.*, 1982; Lasaga and Blum, 1986). u_0 (kJ.nm⁻³) may then be calculated from the molar enthalpy of melting (ΔH_m) and the molar volume. Other contributions of dislocations to the internal energy of crystals, such as changes in the configurational entropy and in the vibrational energy of the lattice, are very small compared to the strain energy and can be neglected (Cottrell, 1953).

For nine different naturally weathered feldspars used by Holdren and Speyer (1985, 1987), it was concluded in chapter 2 that by far most BET-argon surface area could not be detected by scanning electron microscopy, and must be present as internal surface structures

such as pores. For an assemblage of naturally weathered feldspar and quartz, it was concluded in chapter 5 that the BET-krypton surface area was largely present as micropores in the feldspar but not in the quartz grains. The assemblage developed from the low-grade metamorphic Central Aar granite (< 450 °C; Schaltegger and Von Quadt, 1990), so a high dislocation density is expected in both the feldspar and quartz grains (Blum *et al.*, 1990). Using the data in Table 7.1, values of r_f/r_h for common dislocations in sanidine are 2.54 (screw, $b = 1.12$ nm), 2.98 (edge, $b = 1.12$ nm), 1.95 (screw, $b = 0.86$ nm), and 2.29 (edge, $b = 0.86$ nm), respectively. Plotting these values in Fig. 7.2 explains the presence of micropores in naturally weathered sanidine from enhanced dissolution at dislocations if ΔG of the aqueous solution is intermediate between values where etch pits or closed dislocations dominate. For common dislocations in quartz, values of r_f/r_h are 0.63 (screw, $b = 0.49$ nm), 0.66 (edge, $b = 0.49$ nm), 0.94 (screw, $b = 0.73$ nm), and 0.98 (edge, $b = 0.73$ nm), respectively. Plotting these values in Fig. 7.2 indicates that micropores do not form in quartz from dissolution at dislocations, regardless of solution composition.

Values of r_f/r_c in Fig. 7.2 can be calculated from the data in Table 7.1 once ΔG of the aqueous solution is known. Table 7.2 gives the composition of five selected aqueous solutions, representing a variety of conditions. Assuming activity coefficients to be unity, the data were used to calculate ΔG for quartz and sanidine from their equilibrium constants (Table 7.3). For sanidine, $a_{Al^{3+}}$ in eq. (7.2) was calculated from:

$$a_{Al^{3+}} = \frac{c_{Al(tot)}}{1 + K_1 10^{pH} + K_2 10^{2pH} + K_3 10^{3pH} + K_4 10^{4pH}} \quad (7.11)$$

where $c_{Al(tot)}$ is the total concentration of Al (Table 7.2) and where K_1 , K_2 , K_3 and K_4 are the hydrolysis constants for the aluminum complexes considered (Table 7.3). Resulting values of ΔG (Table 7.2) indicate that many soil solutions are supersaturated or near equilibrium with respect to quartz, and are undersaturated with respect to sanidine. In contrast, frequently used laboratory solutions are undersaturated and highly undersaturated with respect to quartz and sanidine, respectively. Many low-temperature groundwaters are supersaturated with respect to quartz (Holland, 1978) and feldspar (Pačes, 1973; Holland, 1978). This is also true for the groundwater selected in Table 7.2.

From the data in Tables 7.1 and 7.2, values of r_f/r_c for the soil solution of pH 4 vary between +0.33 and +0.79 for common dislocations in quartz, and between -0.31 and -0.72 for common dislocations in sanidine. In combination with calculated values of r_f/r_h , this indicates that dislocations remain closed in quartz, and form etch pits in sanidine (Fig. 7.2). For the soil solution of pH 6.2, values of r_f/r_c vary between -0.04 and -0.10 for common dislocations in quartz, and between -0.71 and -1.67 for those in sanidine. This indicates

Table 7.2. Aqueous solution data (in mol.l⁻¹) and the resulting molar free energy changes ΔG (in kJ.mol⁻¹) for the dissolution of unstrained quartz (Q) and sanidine (S).

	H ⁺	K ⁺	H ₄ SiO ₄	Al(tot)	ΔG (Q)	ΔG (S)
soil, pH 4 ¹	1.0·10 ⁻⁴	1.2·10 ⁻⁴	1.5·10 ⁻³	7.2·10 ⁻⁴	+6.70	-4.99
soil, pH 6.2 ²	5.9·10 ⁻⁷	2.3·10 ⁻⁵	7.1·10 ⁻⁵	3.7·10 ⁻⁶	-0.84	-11.56
lab., pH 3 HCl ³	1.0·10 ⁻³	1.2·10 ⁻⁶	3.3·10 ⁻⁶	9.5·10 ⁻⁷	-8.46	-101.0
lab., pH 5 HCl ³	1.0·10 ⁻⁵	6.0·10 ⁻⁸	1.5·10 ⁻⁶	1.0·10 ⁻⁸	-10.43	-83.4
groundwater ⁴	2.5·10 ⁻⁷	3.6·10 ⁻⁵	6.5·10 ⁻⁴	3.3·10 ⁻⁵	+4.65	+13.03

¹ acidified spodosol (Mulder, 1988); ² granitic soil (adapted from Tardy, 1971); ³ unpublished data for feldspar-rich quartz sand (Anbeek, 1993); ⁴ Ellicott granite (Holland, 1978).

Table 7.3. Equilibrium constants (25 °C, 1 bar).

SiO ₂ (s) + 2H ₂ O = H ₄ SiO ₄ (aq);	$K_{eq} = 10^{-4.00}$	(1)
KAlSi ₃ O ₈ (s) + qH ⁺ + (8 - q)H ₂ O = K ⁺ + Al(OH) _{4-q} ^{(q-1)+} + 3H ₄ SiO ₄ (aq);	$K_{eq} = 10^{+1.29}$ if q = 4	(2)
Al ³⁺ + H ₂ O = Al(OH) ²⁺ + H ⁺ ;	$K_1 = 10^{-5.02}$	(3)
Al ³⁺ + 2H ₂ O = Al(OH) ₂ ⁺ + 2H ⁺ ;	$K_2 = 10^{-9.7}$	(3)
Al ³⁺ + 3H ₂ O = Al(OH) ₃ ^o + 3H ⁺ ;	$K_3 = 10^{-16.3}$	(4)
Al ³⁺ + 4H ₂ O = Al(OH) ₄ ⁻ + 4H ⁺ ;	$K_4 = 10^{-22.2}$	(5)

¹ Garrels and Christ (1965); ² data for microcline; Van Breemen and Brinkman (1978); ³ Sillen and Martell (1964); ⁴ Nazarenko and Nevskaya (1969); ⁵ Couturier *et al.* (1984).

that, under these conditions, etch pits would form in both quartz and sanidine. However, r_t/r_c in quartz is only slightly negative, and energy barriers against etch pitting are much higher than for sanidine (Fig. 7.3). For quartz, the energy barrier against etch pitting is not greatly affected by the presence of screw dislocations, and equals approximately 3500 to 6000 kJ.mol⁻¹.nm⁻¹ (Fig. 7.3a). For sanidine, the effect of screw dislocations on ΔG_{pit} is much more pronounced, and energy barriers against etch pitting at dislocations are approximately 100 kJ.mol⁻¹.nm⁻¹ (Fig. 7.3b). From similar plots, essentially the same applies for edge dislocations. Furthermore, the critical radius (after which etch pitting proceeds spontaneously at dislocations) is approximately 9 nm for quartz and 0.3 nm for sanidine. Because the fundamental unit of dissolution in these minerals is the Si/Al tetrahedron ($r_{Si-O} = 0.16$ nm), the critical radius for etch pitting in sanidine equals only some two tetrahedra in length. Thus, the continuous nature of the curves in Fig. 7.3b is most likely incorrect at small r , so the effect of

the energy barrier is even further reduced. These findings suggest that in many soil solutions of low or near-neutral pH etch pits develop primarily in sanidine, relative to quartz. The presence of etch pits in feldspar but not in quartz under similar geochemical conditions has indeed been observed in naturally weathered sample material (Fig. 4.1b).

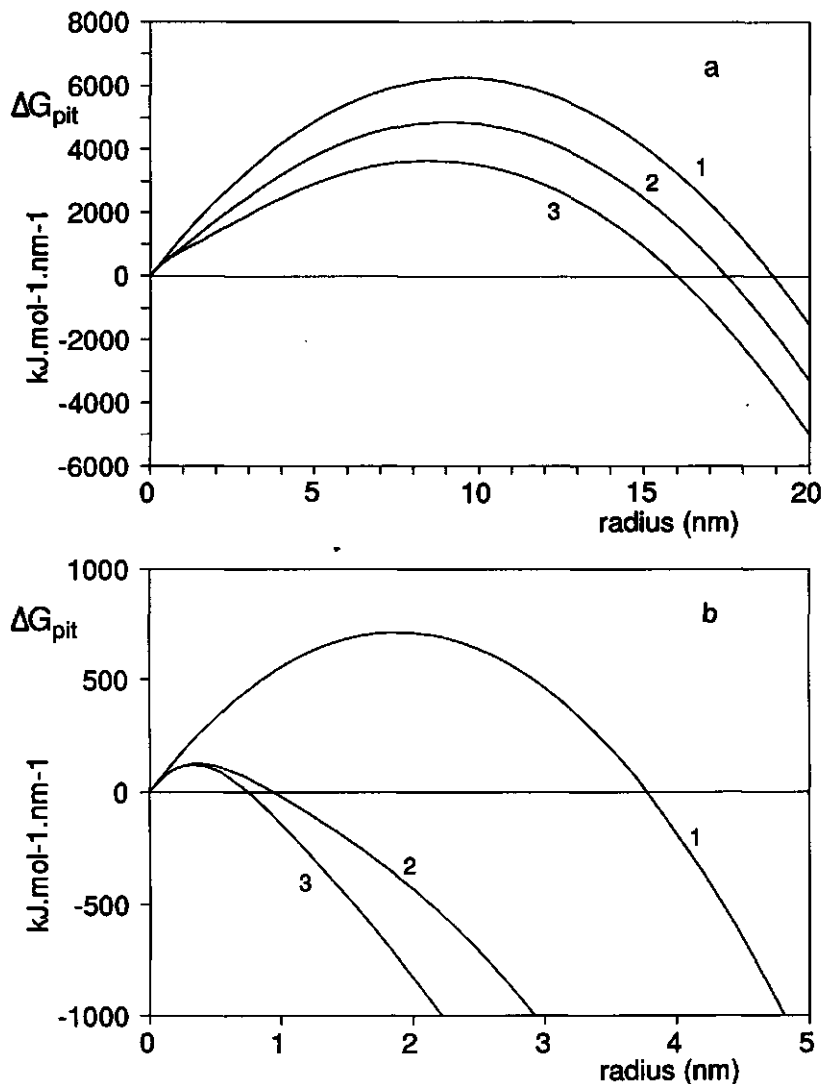


Fig. 7.3. The effect of screw dislocations on ΔG_{pit} as a function of radius r for quartz and sanidine in contact with the soil solution of pH 6.2 (Table 7.2). Plot a (quartz): curve 1: defect-free surface ($b = 0$ nm); 2: $b = 0.49$ nm; 3: $b = 0.73$ nm. Plot b (sanidine): curve 1: defect-free surface; 2: $b = 0.86$ nm; 3: $b = 1.12$ nm.

Fig. 7.4 illustrates the effect of the aqueous solution composition (ΔG) on the formation of etch pits and micropores at screw dislocations in quartz and sanidine. At undersaturation for quartz (Fig. 7.4a, curves 1, 2 and 3), the energy barrier against etch pitting and the radius at which the energy barrier is at its maximum increase with less negative ΔG . At equilibrium

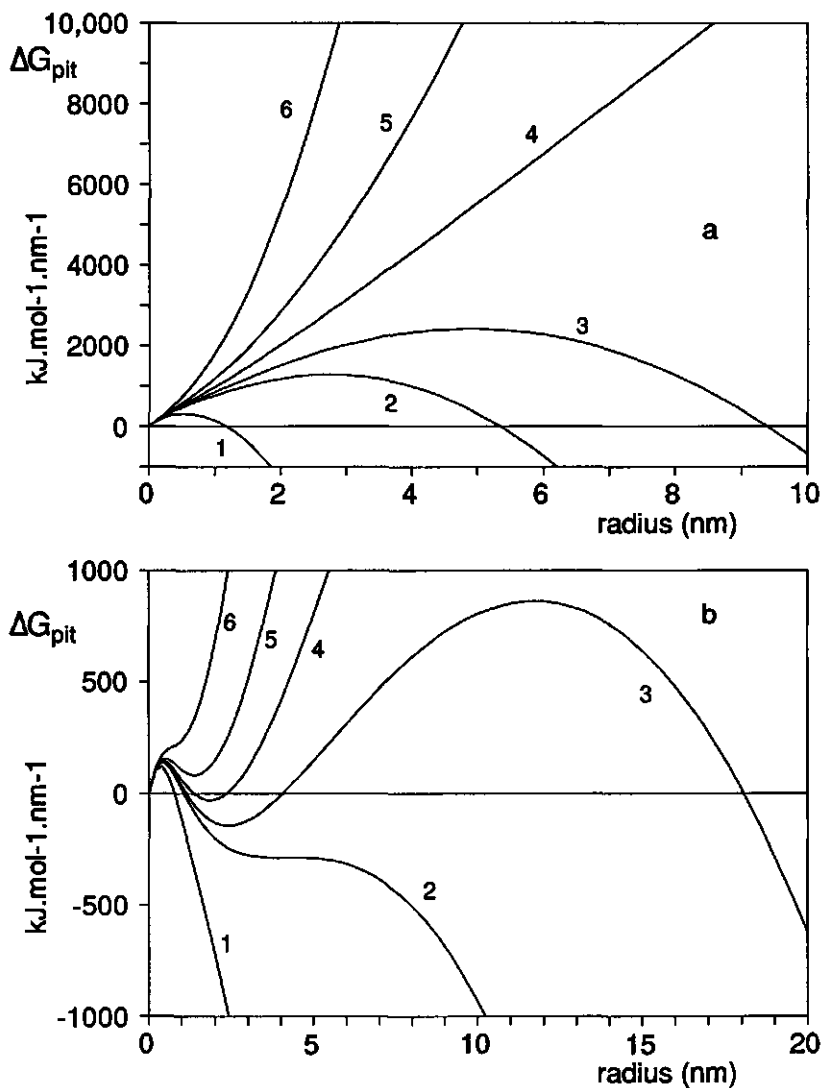


Fig. 7.4. The effect of aqueous solution composition (ΔG) on ΔG_{pit} as a function of radius r for quartz and sanidine. Plot a (quartz): $b = 0.49$ nm screw dislocation. Plot b (sanidine): $b = 1.12$ nm screw dislocation. ΔG (kJ.mol^{-1}) = -10.0 (curves 1), -2.5 (2), -1.5 (3), 0 (4), $+2.5$ (5), and $+10.0$ (6), respectively.

and at supersaturation for quartz (Fig. 7.4a, curves 4, 5 and 6), the dislocations remain closed. For sanidine (Fig. 7.4b), the energy barrier is not greatly affected by changes in ΔG , and the critical radius is again in the order of only a few tetrahedra. In sanidine, etch pits form at relatively large negative ΔG (curves 1 and 2), dislocations remain closed at relatively large positive ΔG (curve 6), and (meta)stable micropores form at intermediate ΔG . According to Fig. 7.4b, pore radii at 1.12 nm screw dislocations in sanidine vary between approximately 1.5 and 3.0 nm. From similar plots, pore radii at other common edge and screw dislocations in sanidine (Table 7.1) vary between approximately 1.0 and 5.0 nm. The curves in Fig. 7.4b indicate that, at constant ΔG of the aqueous solution for sanidine, the radius of pores in equilibrium with that solution is constant too. So, according to this model, all micropore surface area perpendicular to the mineral surface (i.e. the micropore "walls") does not dissolve if the solution composition is constant with time. Changes in solution composition would lead to dissolution (larger radius at more negative ΔG) or growth (smaller radius at more positive ΔG) at the micropore walls if equilibrium were maintained.

Experimental data (chapter 5) show that etch pits and micropores may develop simultaneously on feldspar surfaces during natural weathering. This can be explained from dissolution at dislocations as follows. Combination of eqs. (7.9) and (7.10) gives:

$$\frac{r_f}{r_c} = \frac{\Delta G}{\Delta H_m} \left\{ \frac{r_f}{r_h} \right\}^2 \quad (7.12)$$

In the EMC-diagram, these are parabola with their minimum/maximum at the origin (Fig. 7.5). For individual mineral grains r_f/r_h may vary, for instance, with the Burgers vector. Thus, if ΔG of a solution in contact with sanidine is, for instance, $+4.0 \text{ kJ.mol}^{-1}$ (Fig. 7.5, curve 1), screw dislocations with $b < 1.0 \text{ nm}$ remain closed and those with $b > 1.0 \text{ nm}$ form micropores. At $\Delta G = -3.0 \text{ kJ.mol}^{-1}$ (Fig. 7.5, curve 3), screw dislocations with $b < 0.8 \text{ nm}$ or $b > 1.0 \text{ nm}$ form etch pits, while micropores form at dislocations with intermediate values of b .

Summarizing, it was concluded in this section that: (1) if solutions are undersaturated, etch pits may develop at dislocations in both quartz and sanidine; however, in typical soil solutions, etch pits tend to develop predominantly in sanidine; (2) if solutions are not too highly under- or supersaturated, micropores with radii between approximately 1 and 5 nm tend to develop at common dislocations in sanidine; (3) if solutions are not too highly undersaturated, micropores and etch pits may coexist on surfaces of sanidine grains; and (4) if the solution composition is constant with time, the surface area of the micropore walls is non-reactive.

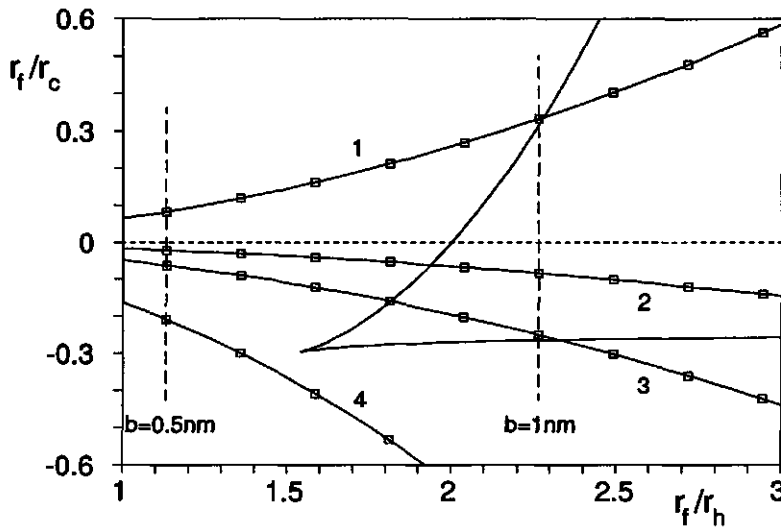


Fig. 7.5. EMC-diagram, showing the effect of the magnitude of the Burgers vector (b) and of the aqueous solution composition (ΔG) on etch pitting and micropore formation at screw dislocations in sanidine. Squares indicate values of the Burgers vector at 0.1 nm intervals. ΔG (kJ.mol^{-1}) = +4.0 (curve 1), -1.0 (2), -3.0 (3), and -10.0 (4), respectively.

7.3. Monte Carlo simulations

One problem which has not been discussed so far is that micropores seem to be present in virtually all naturally weathered feldspars (chapters 2 and 5), although ΔG of most soil solutions seems sufficiently negative to prevent their formation (compare Table 7.2 and Fig. 7.5). We hypothesized that this may be due to diffusion of aqueous reactants and products inside the dissolution holes, leading to a ΔG at the bottom of the hole (where most dissolution takes place) which is higher than the ΔG of the bulk solution. To test this hypothesis, Monte Carlo simulations (Gilmer, 1976, 1980) were applied as an alternative for the many differential equations involved in the analytic solution of the problem. Essentially, a matrix of m by m individual surface sites was defined, and for each site the kinetic rate constants of dissolution and precipitation were replaced by the probabilities of the corresponding events. Next, random numbers were used to select individual sites, and to determine whether dissolution or precipitation should occur. After each event, the probabilities were recalculated for all sites. The principles of Monte Carlo simulations assuming constant solution composition are discussed elsewhere (Lasaga and Blum, 1986; Blum and Lasaga, 1987). The Monte Carlo program SCSV.FOR by these authors models dissolution and

precipitation at a screw dislocation in a cubic crystal (the dislocation outcrop is situated at the centre of the matrix and the dislocation line is perpendicular to the initial surface). We adapted this program by introducing diffusion of aqueous reactants and products inside the dissolution hole (Appendix 5). In the program, each surface site is represented by a cube. Since Al/Si tetrahedra are the structural units of dissolution in quartz and sanidine, we decided that each cube should represent one tetrahedron. Thus, one mole of quartz contains N_{av} cubes, and one mole of sanidine contains $4N_{av}$ cubes. The corresponding edge length (e) of the cubes in the Monte Carlo matrix can then be calculated from the molar volume (Table 7.4).

One of the initial tasks is to translate the thermodynamic parameters b , ΔH_m , σ and μ from the previous section into suitable input parameters for the Monte Carlo program. Because the thermodynamic rate constants are replaced by probabilities, the Monte Carlo equivalents of b , ΔH_m , σ and μ should be dimensionless (Lasaga and Blum, 1986). Therefore, energy terms are normalized to kT units, and distances are normalized to the edge length of the cube. The dimensionless equivalent of the magnitude of the Burgers vector is then given by b/e . Hooke's radius r_h is a convenient parameter to define the strain energy density function u_r in Monte Carlo simulations. Its dimensionless equivalent is given by r_h/e , where r_h is related to ΔH_m according to (eqs. 7.5 and 7.6):

$$r_h = \left\{ \frac{\mu b^2 V}{8\pi^2 k \Delta H_m} \right\}^{1/2} \quad (7.13)$$

The surface free energy (σ) is related to the bond energy B (kJ) between surfaces of adjacent cubes in the Monte Carlo matrix. This can be seen from the fact that for each bond

Table 7.4. Monte Carlo parameters for screw dislocations at 300 K, and resulting values of the related thermodynamic quantities.

		quartz	sanidine
e	(nm)	0.335	0.356
b/e	(-)	2 ($b = 0.670$ nm)	3 ($b = 1.068$ nm)
r_h/e	(-)	2.49 ($\Delta H_m = 8.18$ kJ.mol ⁻¹)	2.41 ($\Delta H_m = 61.6$ kJ.mol ⁻¹)
b/e	(-)		5 ($b = 1.780$ nm)
r_h/e	(-)		4.01 ($\Delta H_m = 61.6$ kJ.mol ⁻¹)
$B/(kT)$	(-)	9.5 ($\sigma = 3.51 \cdot 10^{-22}$ kJ.nm ⁻²)	6 ($\sigma = 1.96 \cdot 10^{-22}$ kJ.nm ⁻²)
			8 ($\sigma = 2.62 \cdot 10^{-22}$ kJ.nm ⁻²)
$\mu/(kT)$	(-)	403 ($\mu = 444 \cdot 10^{-22}$ kJ.nm ⁻³)	312 ($\mu = 287 \cdot 10^{-22}$ kJ.nm ⁻³)

to be broken $2e^2$ surface area must be created. For a cubic crystal, the dimensionless bond energy or bond "strength" $B/(kT)$ is found from σ according to (Lasaga and Blum, 1986):

$$B/(kT) = 7244 \sigma e^2 / T \quad (7.14)$$

where σ is in 10^{-22} kJ.nm⁻², e is in nm, and T is in K. The dimensionless bulk shear modulus $\mu/(kT)$ is found from (Lasaga and Blum, 1986):

$$\mu/(kT) = 7244 \mu e^3 / T \quad (7.15)$$

where μ is in 10^{-22} kJ.nm⁻³, e is in nm, and T is in K. Finally, time in Monte Carlo simulations is calculated from probabilities, and is a dimensionless quantity (Blum and Lasaga, 1987). Time (t) in seconds is found from the dimensionless Monte Carlo time (τ) according to $t = \tau/\nu$, where ν is a frequency factor (s^{-1}) which is approximately equal to kT/h , where h is Planck's constant (Lasaga, 1981b). Table 7.4 lists values of the dimensionless Monte Carlo parameters that were used in the simulations hereafter, and the corresponding values of the related thermodynamic quantities.

Application to quartz and sanidine

The Monte Carlo simulations including diffusion of aqueous species inside the dissolution holes require input of the dissolution rate at the bottom of the hole if no diffusion occurs (see Appendix 5). These can be obtained from simulations of the type described by Lasaga and Blum (1986), where one ΔG holds for all sites and over total computing time. Some results for sanidine in contact with the soil solution of pH 4 (Table 7.2) are shown in Fig. 7.6. After a short initial period, when a distinct dissolution hole has yet to be formed on the originally flat surface, the dissolution rate at the bottom of the hole stabilizes. However, its value largely depends on the bond strength $B/(kT)$ (Fig. 7.6). If dislocations are the primary dissolution reactive sites on surfaces of sanidine grains, the Monte Carlo rate at the bottom of the hole essentially equals the experimental dissolution rate normalized to the reactive surface area of the grains. It was concluded in chapter 3 that, for nine different freshly created feldspars used by Holdren and Speyer (1985, 1987), dissolution rates at pH 3 HCl, normalized to the reactive BET-argon surface area, varied between approximately $4 \cdot 10^{-11}$ (anorthite) and $4 \cdot 10^{-13}$ (microcline) mol.cm⁻².s⁻¹. Thus, if the flat matrix surface at $t = 0$ represents a freshly created sanidine surface, the Monte Carlo rates normalized to the reactive surface area (Fig. 7.6) are several orders of magnitude higher than those derived

from experimental data. Relationships between the bond strength and the Monte Carlo rate normalized to the reactive surface area are shown in Fig. 7.7 for sanidine in contact with several solutions. The simulations for the laboratory solution of pH 3 HCl show that for screw dislocations with $b/e = 3$, $B/(kT) = 9$ ($\sigma \approx 2.95 \cdot 10^{-22}$ kJ.nm⁻²) gives Monte Carlo rates in approximate agreement with experimental rates for microcline at pH 3 HCl. However, computing time of the simulations hereafter largely depended on the value of $B/(kT)$, and was several weeks of continuous running at $B/(kT) = 8$ on the VAX-8700 computer used for calculations. Simulations at $B/(kT) = 9$, which would take several months of continuous running, fall beyond the scope of this research.

The strain energy at finite distance r from a dislocation acts as one of the driving forces for mineral dissolution. This means that the equilibrium constant of the dissolution reaction of strained mineral material (K'_{eq}) increases with decreasing distance r from the dislocation, and is larger than that of unstrained mineral material (K_{eq}) at all finite r . For instance, for sanidine $K'_{eq} = K_{eq} = 10^{+1.29}$ if $r = \infty$ (Table 7.3), and $K'_{eq} = 10^{+12.07}$ if $r = 0$ (Appendix 5). The effect of

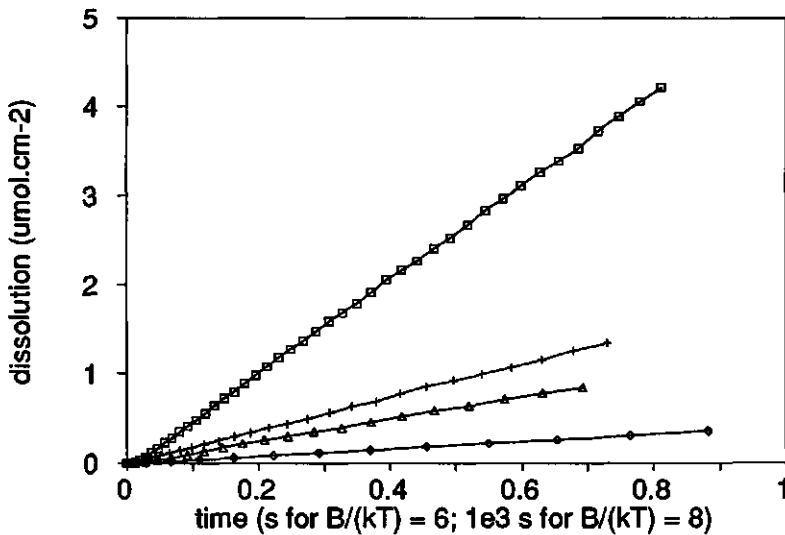


Fig. 7.6. Monte Carlo simulation of dissolution at a screw dislocation in sanidine, assuming no aqueous diffusion inside the dissolution hole. Summed dissolution at the bottom of the hole is plotted versus time. The slope equals the dissolution rate at the bottom of the hole. The simulations were obtained for the soil solution of pH 4 (Table 7.2). Each symbol represents an increase in depth of the hole, relative to the surrounding surface, of 10 cubes. \square : $B/(kT) = 6$, $b/e = 3$ (rate = $5.29 \cdot 10^{-6}$ mol.cm⁻².s⁻¹); + : $B/(kT) = 6$, $b/e = 5$ (rate = $1.85 \cdot 10^{-6}$); \diamond : $B/(kT) = 8$, $b/e = 3$ (rate = $4.05 \cdot 10^{-10}$); \triangle : $B/(kT) = 8$, $b/e = 5$ (rate = $1.25 \cdot 10^{-9}$).

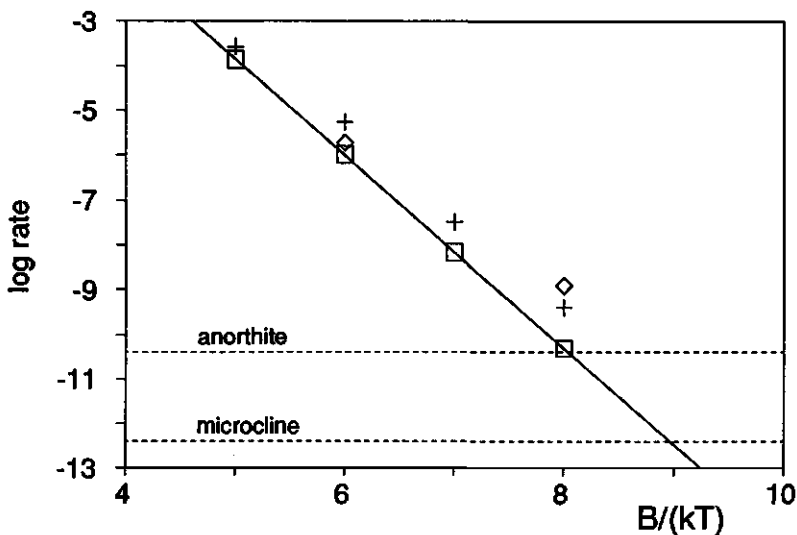


Fig. 7.7. Monte Carlo simulation of dissolution at a screw dislocation in sanidine, assuming no aqueous diffusion inside the dissolution hole. The logarithm of the dissolution rate at the bottom of the hole is plotted versus the bond strength $B/(kT)$. □ : laboratory solution of pH 3 HCl (Table 7.2), and $b/e = 3$; + : soil solution of pH 4 (Table 7.2), and $b/e = 3$; ◇ : soil solution of pH 4, and $b/e = 5$. The dashed horizontal lines are estimates of the dissolution rate at the bottom of the hole, derived from experimental data (see text and Table 3.5), for freshly created anorthite and microcline at pH 3 HCl.

this increase in K_{eq} at finite r is that dissolution proceeds even at supersaturation for the unstrained mineral bulk. This is demonstrated by the results of the simulations for sanidine, assuming aqueous diffusion to occur inside the dissolution hole, using the soil solution of pH 4 as the bulk solution (Fig. 7.8). During the first stage of the simulations, the depth of the hole relative to that of the surrounding surface increases with time (Fig. 7.8a). As a result, the increasing diffusion path length causes ΔG at the bottom of the hole to increase with time too (Fig. 7.8b). Finally, a steady state depth is reached at some positive ΔG . During this stage, dissolution at the bottom of the hole proceeds at the same (very slow) rate by which the surrounding surface dissolves in contact with the bulk solution. Thus, the depth of the hole during this stage is constant with time. At $B/(kT) = 6$, the high dissolution rates at the bottom of the hole (Fig. 7.7) give large concentration gradients inside the hole. This causes ΔG at the bottom of the hole to increase by approximately 2 to 5 $\text{kJ}\cdot\text{mol}^{-1}$ for each increase in depth by one cube. Both at $b/e = 3$ and 5, the steady state depth is in the order of several cubes only. The long-term steady state averages of ΔG at the bottom of the hole for $B/(kT) = 6$ are indicated by the dashed lines in Fig. 7.8b. At $B/(kT) = 8$, dissolution rates at the

bottom of the hole are much lower, and development of the dissolution holes proceeds much more gradual. This is also shown schematically in Fig. 7.8c for $b/e = 5$. Assuming linear concentration profiles, ΔG inside the hole is given as a function of depth at steady state (Fig. 7.8c). If $B/(kT) = 8$ and $b/e = 5$, the transition from etch pit to micropore in Fig. 7.2 occurs at $\Delta G = -1.72 \text{ kJ.mol}^{-1}$. Thus, during the steady state stage, conditions are favorable for etch pitting over the first 20 % or so of depth of the hole. At greater depths inside the steady state hole, conditions are favorable for the formation of a micropore instead. The depth to

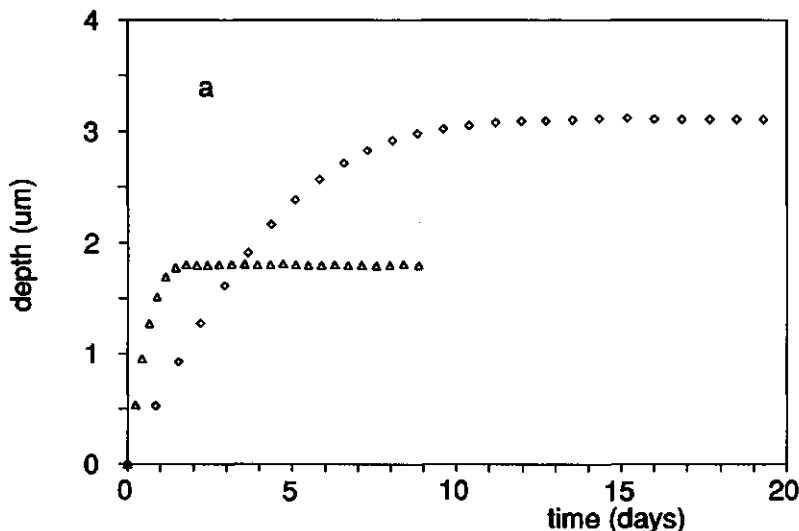


Fig. 7.8. Monte Carlo simulation of dissolution at a screw dislocation in sanidine, assuming aqueous diffusion inside the dissolution hole. The soil solution of pH 4 (Table 7.2) was used as bulk solution. In plots a and b, each symbol represents 100,000 net dissolutions (dissolutions minus precipitations) from a 40×40 matrix. \diamond : $B/(kT) = 8$, $b/e = 3$ (2,500,000 net dissolutions); \triangle : $B/(kT) = 8$, $b/e = 5$ (2,500,000 net dissolutions). Plot a: depth of the dissolution holes versus time for $B/(kT) = 8$ (depth for $B/(kT) = 6$ is in the order of several nm). Plot b: ΔG at the bottom of the dissolution holes versus time. The dashed lines indicate the long-term averages for $B/(kT) = 6$, $b/e = 3$ (lower dashed line) and $B/(kT) = 6$, $b/e = 5$. Plot c: cross-sections of the hole for $B/(kT) = 8$, $b/e = 5$ after 200,000, 400,000, 600,000, 800,000, 1,000,000 and 2,500,000 net dissolutions. The ΔG -curve (right) after 2,500,000 net dissolutions indicates the thermodynamical conditions inside the hole at steady state depth. Plot d: surface of a 80×80 matrix for $B/(kT) = 8$, $b/e = 3$ after 200,000 net dissolutions. Plot e: EMC-diagram, showing the thermodynamical conditions at the bottom of the holes during the simulations (see text). From left to right: $B/(kT) = 8$, $b/e = 3$; $B/(kT) = 6$, $b/e = 3$; $B/(kT) = 8$, $b/e = 5$; $B/(kT) = 6$, $b/e = 5$.

width ratio of the steady state hole is approximately 500 (Fig. 7.8c). If $B/(kT) = 8$ and $b/e = 3$, the transition from etch pit to micropore occurs at $\Delta G = -4.94 \text{ kJ.mol}^{-1}$. Because at all times and at any depth ΔG inside the hole $\geq -4.99 \text{ kJ.mol}^{-1}$ (Table 7.2), conditions are favorable for micropore formation over virtually the entire depth throughout running time (see also Fig. 7.8d). In Fig. 7.8e the thermodynamical conditions during the simulations are plotted in the EMC-diagram. The parabola (eq. 7.12) at negative values of r_i/r_c indicates the conditions for sanidine in contact with the soil solution of pH 4 ($\Delta G = -4.99 \text{ kJ.mol}^{-1}$). At the

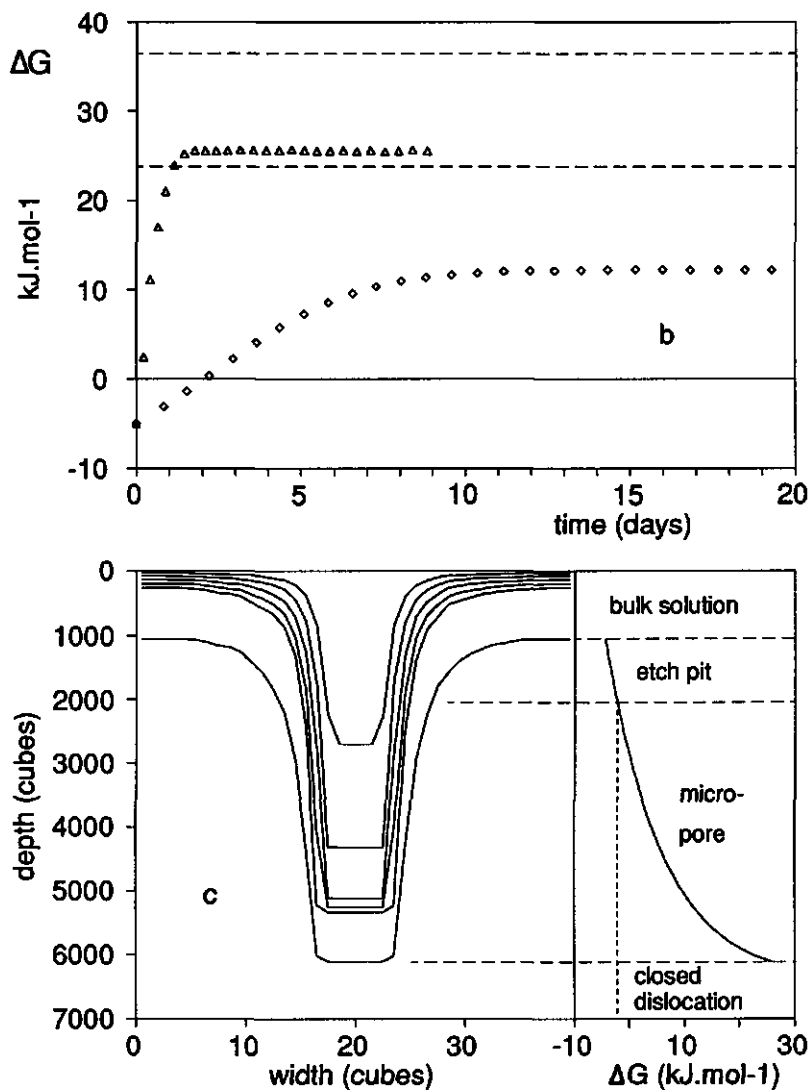


Fig. 7.8. Continued.

bottom of a dissolution hole in the case of aqueous diffusion, these conditions would hold if the depth of the hole were zero, i.e. at $t = 0$. The parabola at positive values of r_f/r_c indicates the conditions where dislocations are in equilibrium with the solution ($\Delta G = \Delta H_m$). At the bottom of a dissolution hole in the case of aqueous diffusion, the equilibrium would be reached if the concentration gradients were zero, i.e. at infinitely large depth of the hole. Thus, as actual depth increases with time, conditions at the bottom of the hole tend to shift from the lower parabola towards the upper parabola. Because final depth in the simulations

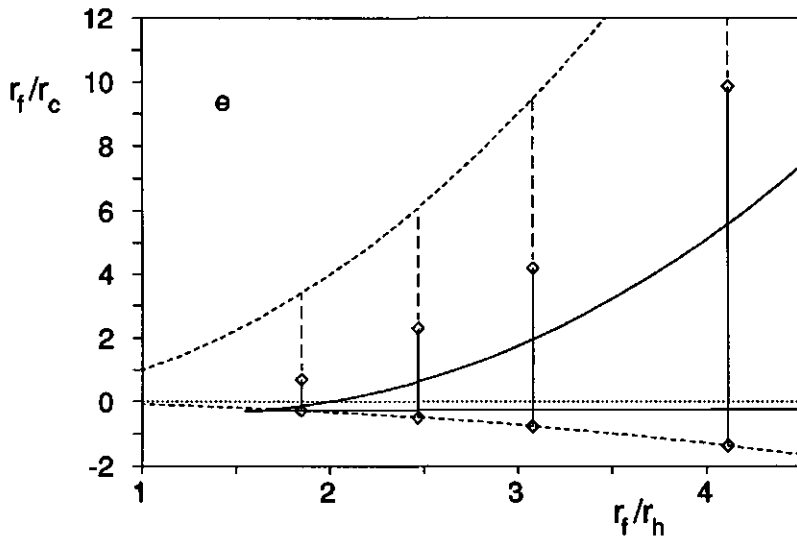
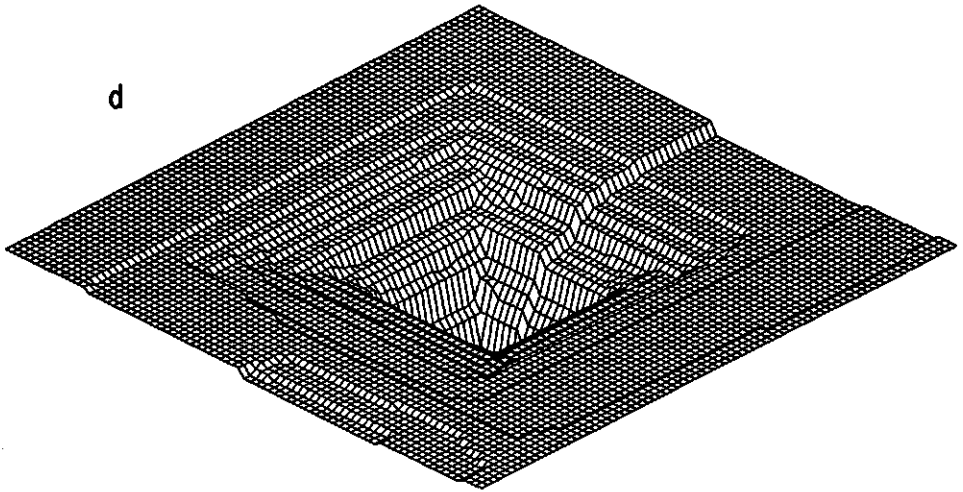


Fig. 7.8. Continued.

is finite, the upper parabola will not be reached, however. The steady state values of ΔG (Fig. 7.8b) were used to plot values of r_t/r_c in the EMC-diagram. The points obtained reflect the conditions where micropore development stops in the Monte Carlo simulations, so they are situated on the micropore/closed dislocation transition. The results show that the transition according to the Monte Carlo method is essentially similar in shape but situated at somewhat higher values of r_t/r_c than the transition predicted by the thermodynamic model.

For the simulations discussed in Fig. 7.8, K'_{eq} was used to model the dissolution rate at the bottom of the hole as a function of the aqueous concentrations at the bottom of the hole, and was calculated from ΔH_m (Appendix 5). However, K'_{eq} from ΔH_m holds only at the dislocation outcrop itself ($r = 0$), and for all $r > 0$, K'_{eq} is smaller than K_{eq} at $r = 0$. Furthermore, K'_{eq} is K_{eq} corrected for the strain energy, but not yet for the surface free energy (eq. 7.1). The "average" value of K'_{eq} over the entire bottom of the dissolution hole, corrected for the surface free energy and for values of $r > 0$, can be estimated from ΔG at maximum

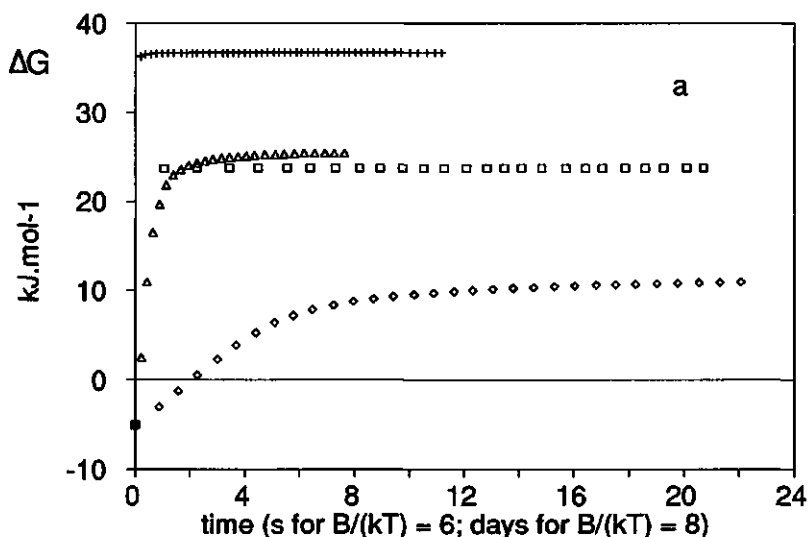


Fig. 7.9. Monte Carlo simulation of dissolution at a screw dislocation in sanidine, assuming aqueous diffusion inside the dissolution hole. Conditions are similar to those for the simulations in Fig. 7.8, except for values of K'_{eq} , which were estimated from Fig. 7.8b (see text). Each symbol represents 2000 net dissolutions from a 40 x 40 matrix if $B/(kT) = 6$, or 100,000 net dissolutions if $B/(kT) = 8$. □ : $B/(kT) = 6$, $b/e = 3$ (50,000 net dissolutions); + : $B/(kT) = 6$, $b/e = 5$ (100,000 n.d.); ◇ : $B/(kT) = 8$, $b/e = 3$ (3,000,000 n.d.); Δ : $B/(kT) = 8$, $b/e = 5$ (2,500,000 n.d.). Plots a and b: ΔG at the bottom of the dissolution holes versus time. Plot c: depth of the dissolution holes versus time.

depth in the earlier simulations (Fig. 7.8b). The effect of this Monte Carlo estimate of K'_{eq} ($= K_{M,eq}$) is that in the diffusion model the dissolution rate at the bottom of the hole approaches to zero as conditions approach the micropore/closed dislocation transition (eq. A5.15). This is in better agreement with the actual situation as in the simulations so far, where dissolution in the diffusion model is still far from equilibrium at the micropore/closed dislocation transition. The results of simulations similar to those in Fig. 7.8, but replacing K'_{eq} from ΔH_m by $K_{M,eq}$ estimated from Fig. 7.8b, are shown in Fig. 7.9. Maximum values of ΔG

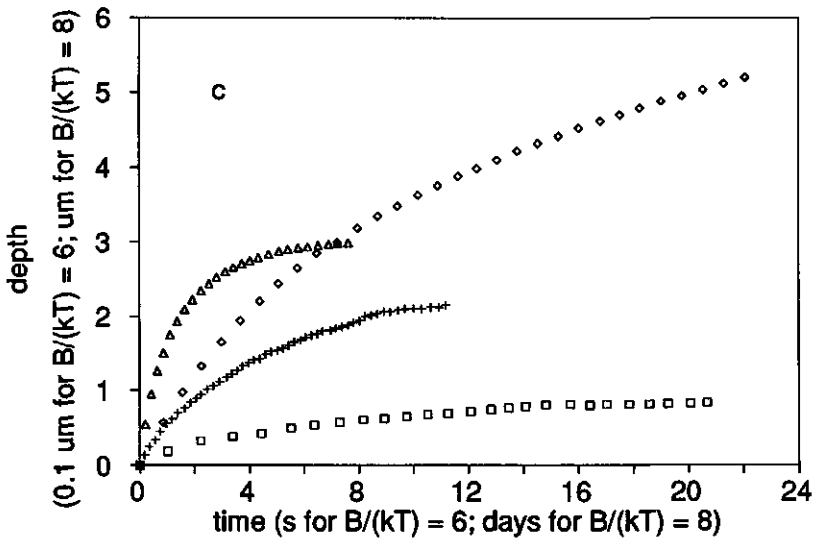
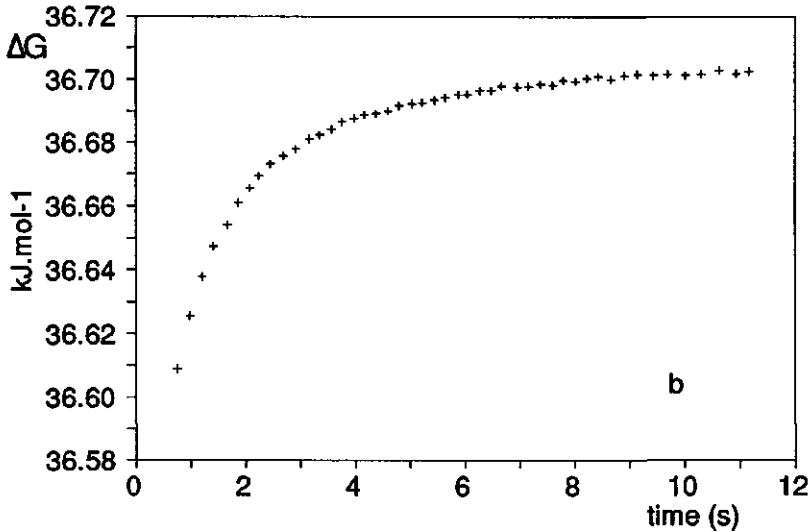


Fig. 7.9. Continued.

at the bottom of the hole (Fig. 7.9a) are essentially similar to those in Fig. 7.8b, so these are not greatly affected by replacing K'_{eq} by $K_{\text{M,eq}}$. This means that the micropore/closed dislocation transition according to the Monte Carlo model is largely independent of $K_{\text{M,eq}}$. As in the earlier simulations, the steady state value of ΔG at $B/(kT) = 6$ seems to be reached almost instantaneously (Fig. 7.9a). However, at a finer scale ΔG slowly increases throughout running time (Fig. 7.9b for $b/e = 5$). Both at $B/(kT) = 6$ and 8, the slower increase in ΔG with depth compared to the earlier simulations results in larger depth of the holes (Fig. 7.9c). The steady state micropore depth at $B/(kT) = 8$ is up to several μm . Comparison between results at $B/(kT) = 6$ and $B/(kT) = 8$ suggests that, in this pH 4 soil solution, steady state

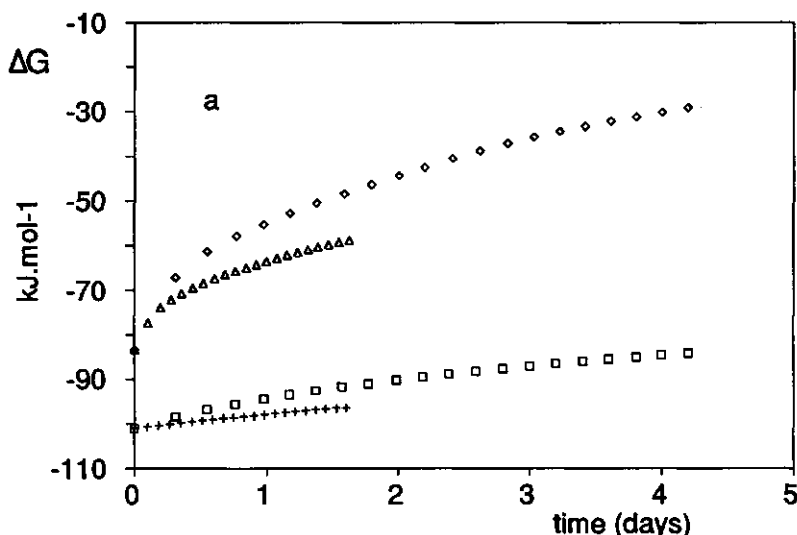


Fig. 7.10. Monte Carlo simulation of dissolution at a screw dislocation in sandine, assuming aqueous diffusion inside the dissolution hole. Values of K'_{eq} were estimated from Fig. 7.8b (see text). In plots a and b, each symbol represents 50,000 net dissolutions from a 40×40 matrix (1,000,000 net dissolutions for all runs). $B/(kT) = 8$ for all runs. \square : $b/e = 3$, and laboratory solution of pH 3 (Table 7.2) as bulk solution; $+$: $b/e = 5$, and laboratory solution of pH 3; \diamond : $b/e = 3$, and laboratory solution of pH 5; \triangle : $b/e = 5$, and laboratory solution of pH 5. Plot a: ΔG at the bottom of the dissolution holes versus time. Plot b: depth of the dissolution holes versus time. Plot c: cross-sections of the hole for $B/(kT) = 8$, $b/e = 3$ and laboratory solution of pH 3 after 40,000, 80,000, 120,000, 160,000, 200,000 and 1,000,000 net dissolutions. The ΔG -curve (right) indicates the thermodynamical conditions inside the hole after 200,000 net dissolutions. The diameter of the hole is smaller than that in Fig. 7.8c because the magnitude of the Burgers vector is smaller. Plot d: surface of a 80×80 matrix for $B/(kT) = 8$, $b/e = 3$ and laboratory solution of pH 3 after 200,000 net dissolutions.

micropore depths at $B/(kT) = 9$ are in the order of $10 \mu\text{m}$. The actual depth of etch pits at dislocations is frequently in the order of several μm too. This suggests that the physical length and/or microstructure of dislocations is not the limiting factor in reaching such micropore depths. However, the model does not account for the possible formation of secondary products, such as Al hydroxides, due to the increase in pH and in activities of Al, Si, etc., at the bottom of the hole. Secondary products, forming at some intermediate ΔG , would result in much lower diffusion coefficients, limiting further micropore development.

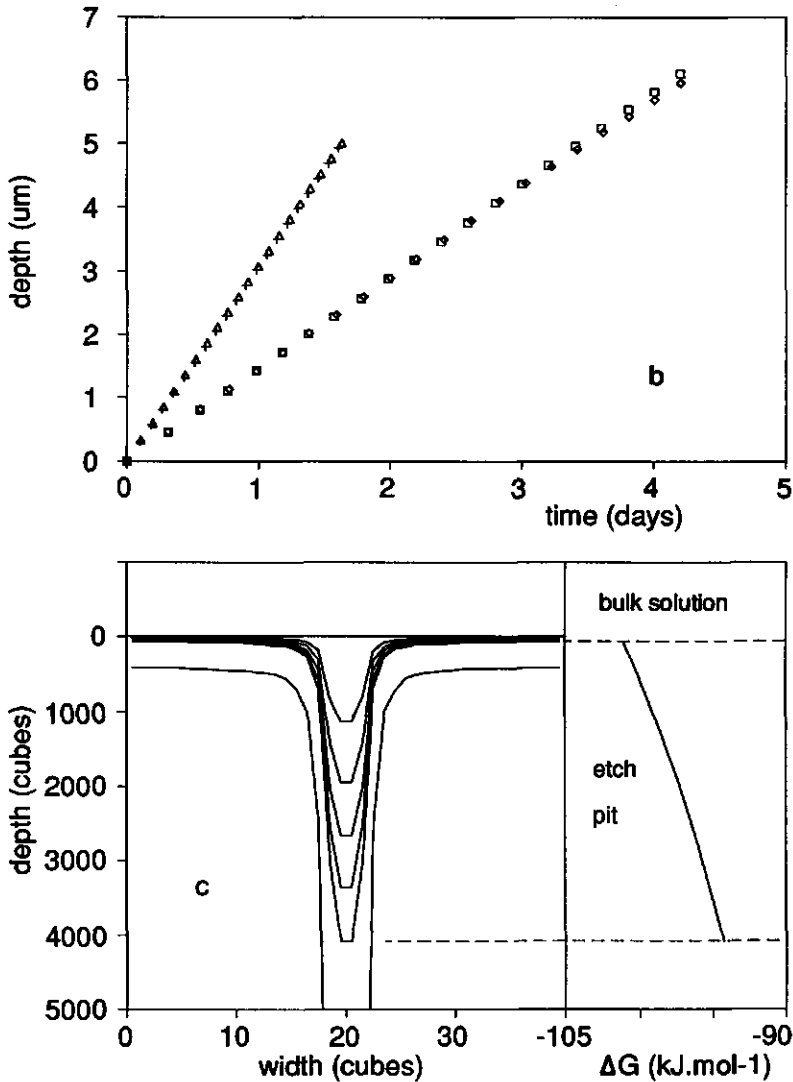


Fig. 7.10. Continued.

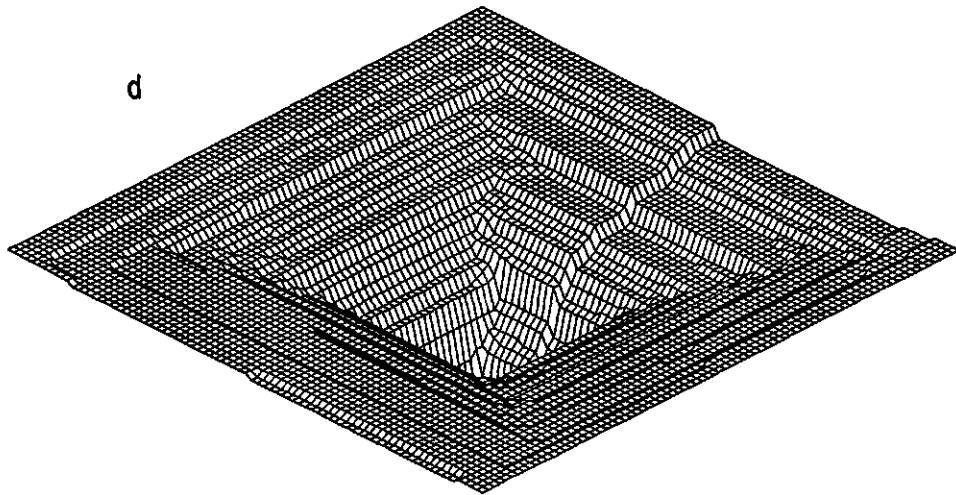


Fig. 7.10. Continued.

Results of simulations for sanidine with the laboratory solutions of pH 3 and 5 HCl (Table 7.2) as bulk solutions, assuming aqueous diffusion inside the dissolution holes, are shown in Fig. 7.10. The increase in ΔG with time at the bottom of the hole is larger at pH 5 than at pH 3 (Fig. 7.10a). This is primarily due to the higher H^+ activity at pH 3, which acts as a buffer against changes in ΔG from dissolution. At the end of the simulations, when depth has reached several μm , the growth rate of the hole is still hardly affected by diffusion (Fig. 7.10b). However, as dissolution continues, ΔG at the bottom of the hole will eventually reach the value at the micropore/closed dislocation transition. This would most likely result in a hole of several tens of μm deep at steady state, with conditions being favorable for etch pitting over many μm depth (e.g. compare the ΔG -curves in Figs. 7.8c and 7.10c). The tendency towards etch pitting under laboratory conditions may also be seen by comparing Figs. 7.8d and 7.10d. Yet, according to the Monte Carlo model, the morphology of the proto etch pit under these conditions closely resembles that of a micropore.

Results of Monte Carlo simulations for quartz are shown in Fig. 7.11. The dissolution rates at the bottom of the hole, assuming no aqueous diffusion, were determined for the soil solution of pH 6.2 and for the laboratory solution of pH 5 HCl (Fig. 7.11a). Using the soil solution of pH 6.2 as bulk solution, assuming aqueous diffusion inside the dissolution holes, screw dislocations with $b/e = 2$ remain closed, and dissolution of quartz proceeds at a very low rate over the entire surface (Fig. 7.11b). This indicates that, although ΔG of the solution is slightly negative, the energy barrier against opening of the hole is sufficiently high to

prevent etch pitting. Using the laboratory solution of pH 5 HCl as bulk solution, ΔG at the bottom of the hole is essentially constant with time because: (1) the low dissolution rate at the bottom of the hole compared to feldspar (Figs. 7.6 and 7.11a) gives relatively small concentration gradients; and (2) the small depth of the hole compared to feldspar after equal net dissolution (Figs. 7.8c and 7.11c) gives relatively small diffusion path lengths. Values of ΔG (Table 7.2) indicate that the energy barrier against etch pitting is smaller for quartz in contact with the laboratory solution of pH 5 HCl than for quartz in contact with the soil solution of pH 6.2. According to the Monte Carlo simulations, the smaller energy barrier at pH 5 HCl no longer prevents the formation of a dissolution hole in the quartz (Figs. 7.11c and d). Both from the value of r_f/r_h and from cross-sections of the hole, it is an etch pit.

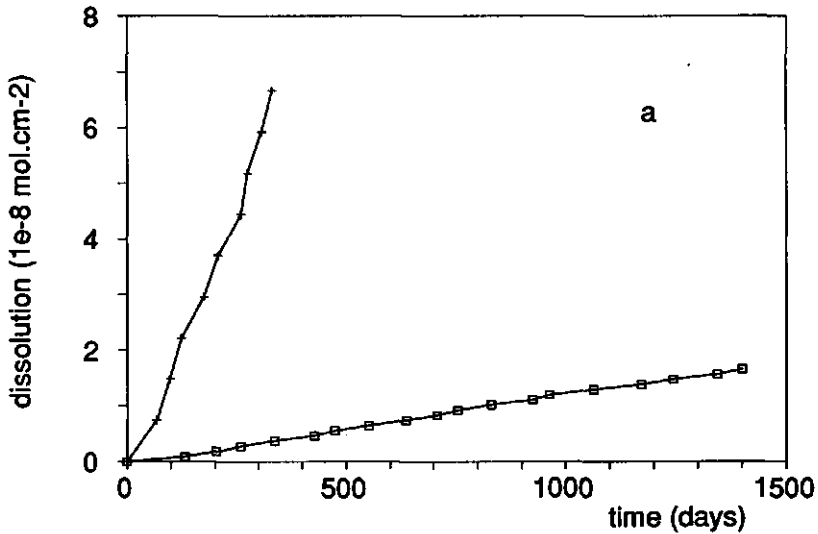


Fig. 7.11. Monte Carlo simulation of dissolution at a screw dislocation in quartz, assuming no aqueous diffusion (plot a) and aqueous diffusion (plots b, c and d) inside the dissolution hole. $B_f/(kT) = 9.5$ and $b/e = 2$ for all runs. Plot a: total dissolution (40×40 matrix) at the bottom of the hole versus time. The slope equals the dissolution rate at the bottom of the hole. \square : soil solution of pH 6.2 (Table 7.2) as bulk solution; each symbol represents 1000 net dissolutions (rate = $1.36 \cdot 10^{-16} \text{ mol.cm}^{-2} \cdot \text{s}^{-1}$); + : laboratory solution of pH 5 as bulk solution; each symbol represents an increase in depth of the hole of 5 cubes (rate = $2.12 \cdot 10^{-15} \text{ mol.cm}^{-2} \cdot \text{s}^{-1}$). Plot b: surface of a 80×80 matrix for the soil solution of pH 6.2 after 200,000 net dissolutions. Plot c: cross-sections of the hole for the laboratory solution of pH 5 after 50,000, 100,000, 150,000 and 200,000 net dissolutions. The ΔG -curve (right) indicates the thermodynamical conditions inside the hole after 200,000 net dissolutions. Plot d: surface of a 80×80 matrix for the laboratory solution of pH 5 after 200,000 net dissolutions.

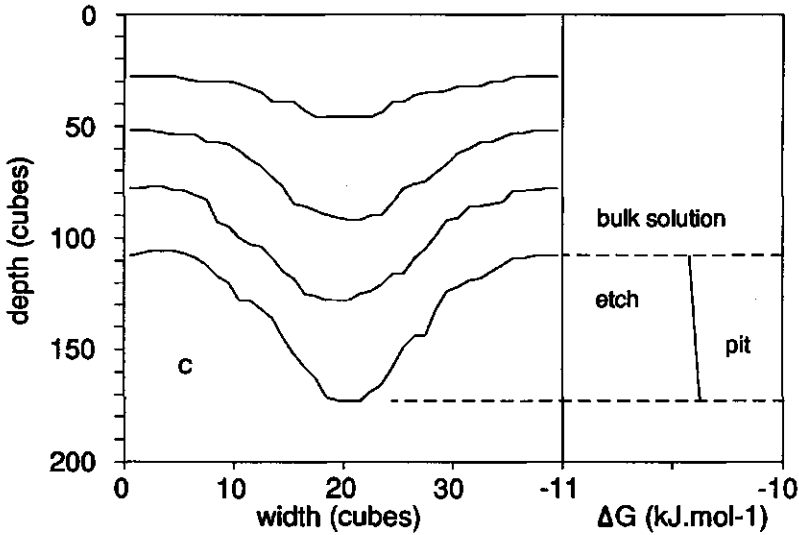
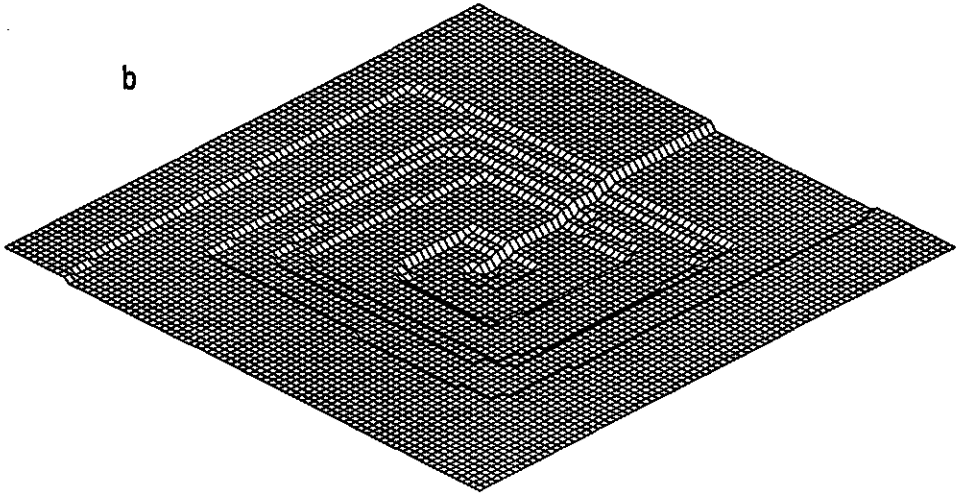


Fig. 7.11. Continued.

7.4. A kinetic model

It was shown in the thermodynamic section that the radius of a micropore in equilibrium with a solution changes only if the solution composition changes. This means that the micropore walls do not dissolve if the aqueous solution composition is constant with time. Furthermore, the Monte Carlo simulations indicate that, for micropores at dislocations,

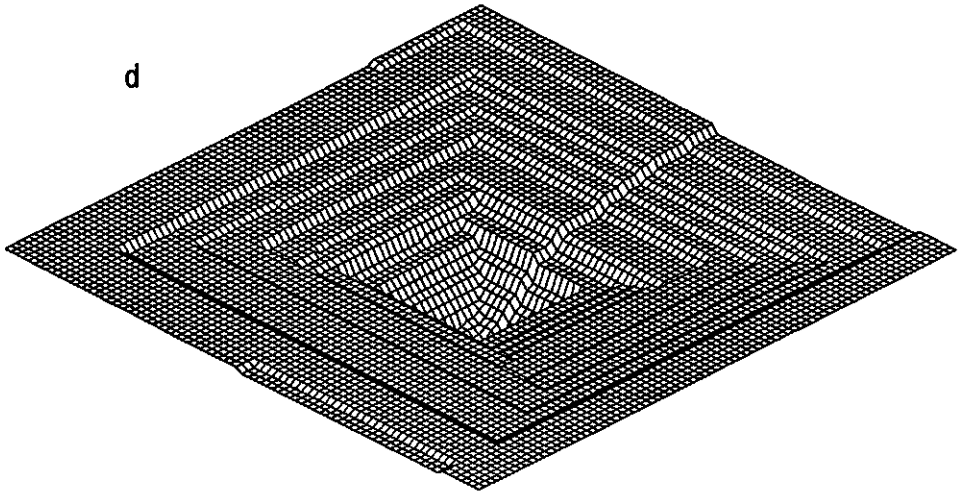


Fig. 7.11. Continued.

dissolution takes place at the bottom of the hole, rather than from the walls. Even at steady state in the Monte Carlo simulations, dissolution rates at different parts of the mineral surface largely depend on the surface area to which the rates are normalized. This can be seen as follows (Fig. 7.12a). If the geometric surface area of a grain or sample is defined as the hypothetical smooth surface enveloping the actual surface (Jaycock and Parfitt, 1981), then dissolution rates during steady state, normalized to the geometric surface area, are essentially similar over the entire geometric surface (Fig. 7.12a). However, dissolution rates normalized to the actual surface area are much smaller for the micropore walls than for the area parallel to the geometric surface (Fig. 7.12a). These findings indicate that the dissolution rate of mineral grains, normalized to actual surface area, decreases with increasing proportion of micropore wall area. Hereafter, a kinetic model is derived to account for the relative inactivity of the actual surface area of micropore walls.

The surface roughness factor (λ) of a mineral grain is defined as the ratio of the actual surface area (S ; cm^2) to the geometric surface area (s ; cm^2) (Jaycock and Parfitt, 1981):

$$\lambda \equiv S/s \quad (7.16)$$

Both the actual and the geometric surface area are in fact scale dependent. Here, the actual surface area is replaced by the BET surface area, which includes most surface area from micropores at dislocations (chapter 5). The geometric surface area may, for instance, be estimated from microscopic observation at small magnification (Fair and Hatch, 1933;

Cartwright, 1962). The proportion of the measured BET surface area of a microporous, naturally weathered grain (or sample) which is occupied by BET surface area of micropore walls (F_m) is defined by:

$$F_m \equiv S_m/S_w \quad (7.17)$$

where S_m is the BET surface area of the micropore walls, and S_w is the measured BET surface area of the naturally weathered grain (Fig. 7.12b). The BET surface area of a non-porous freshly created grain by grinding (S_f ; Fig. 7.12c) is given by:

$$S_f = \lambda_f s_f \quad (7.18)$$

where λ_f is the roughness factor of the freshly created surface, and where s_f is the freshly created geometric surface area. Because the micropores are observed by the BET method but not by geometric surface area techniques, it follows that $S_w = S_f + S_m$, and $s_w = s_f$. Under these conditions, eqs. (7.16), (7.17) and (7.18) combine to:

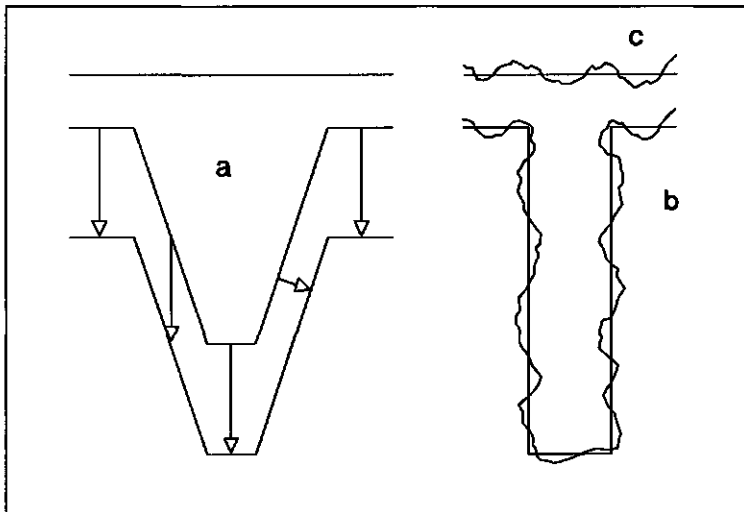


Fig. 7.12. Schematic surfaces during mineral dissolution. a: dissolution rates at steady state; the three arrows at far left indicate the magnitude of dissolution rates normalized to the geometric surface area (upper horizontal line); the three arrows at far right indicate the magnitude of dissolution rates normalized to the actual surface area. b: actual surface area of a micropore in a naturally weathered grain. c: geometric and actual surface area of a freshly created (non-porous) grain.

$$F_m = 1 - \lambda_f/\lambda_w \quad (7.19)$$

where λ_w is the roughness factor of the naturally weathered surfaces.

The apparent dissolution rate normalized to BET surface (R ; mol.cm⁻².s⁻¹) is defined by (Helgeson *et al.*, 1984):

$$R \equiv - (1/S) (dn/dt) \quad (7.20)$$

where n is the number of moles, and t is time. The ratio dn/dt for the naturally weathered grain as a whole, $(dn/dt)_w$, is found from summation of the respective ratios dn/dt for the BET surface area of the micropore walls (S_m), and for the BET surface area "parallel" to the geometric surface ($S_w - S_m$). Thus, it follows from eq. (7.20) that:

$$- (dn/dt)_w = S_w R_w = S_m R_m + (S_w - S_m) R_p \quad (7.21)$$

where R_w is the apparent dissolution rate of the naturally weathered grain as a whole, R_m is the apparent dissolution rate of the micropore walls, and R_p is the apparent dissolution rate of the naturally weathered BET surface area "parallel" to the geometric surface (which includes the micropore bottoms). Eqs. (7.17) and (7.21) give:

$$R_w = F_m R_m + (1 - F_m) R_p \quad (7.22)$$

Eqs. (7.19) and (7.22) can be combined to:

$$R_f/R_w = \frac{\lambda_w}{(\lambda_w - \lambda_f) R_m/R_f + \lambda_f R_p/R_f} \quad (7.23)$$

where R_f is the apparent dissolution rate of a fresh-surface grain of similar size as the naturally weathered grain. For instance, if micropore walls in naturally weathered grains do not dissolve ($R_m = 0$), and if the naturally weathered BET area parallel to the geometric surface dissolves at the same rate as its freshly created counterpart ($R_p = R_f$), eq. (7.23) gives: $R_f/R_w = \lambda_w/\lambda_f$. So, under these conditions, the ratio of the dissolution rates of freshly created and naturally weathered mineral grains, normalized to the BET surface area, equals the reciprocal of the ratio of the respective surface roughness factors. This relation is plotted by the diagonal line in Fig. 7.13. It follows from eq. (7.23) that $R_f/R_w > \lambda_w/\lambda_f$ if $(\lambda_w/\lambda_f - 1) R_m + R_p < R_f$. This is true, for instance, if $R_m = 0$ and $R_p < R_f$. Alternatively, $R_f/R_w < \lambda_w/\lambda_f$ if $(\lambda_w/\lambda_f - 1) R_m + R_p > R_f$. This is true, for instance, if $R_m > 0$ and

$R_p = R_f$. In the limiting case where $R_m = R_p = R_f$, eq. (7.23) gives $R_f/R_w = 1$.

Available data of R_f/R_w and λ_w/λ_f are plotted in Fig. 7.13. Apart from one inaccurate dataset (Saranac Lake Andesine; see chapter 3) for which $R_f/R_w \ll \lambda_w/\lambda_f$, and two datasets for which $R_f/R_w \gg \lambda_w/\lambda_f$ (Perth Perthite and Keystone Microcline, run 2), the data are within a factor 2 or so in agreement with $R_f/R_w = \lambda_w/\lambda_f$. In general, it follows from

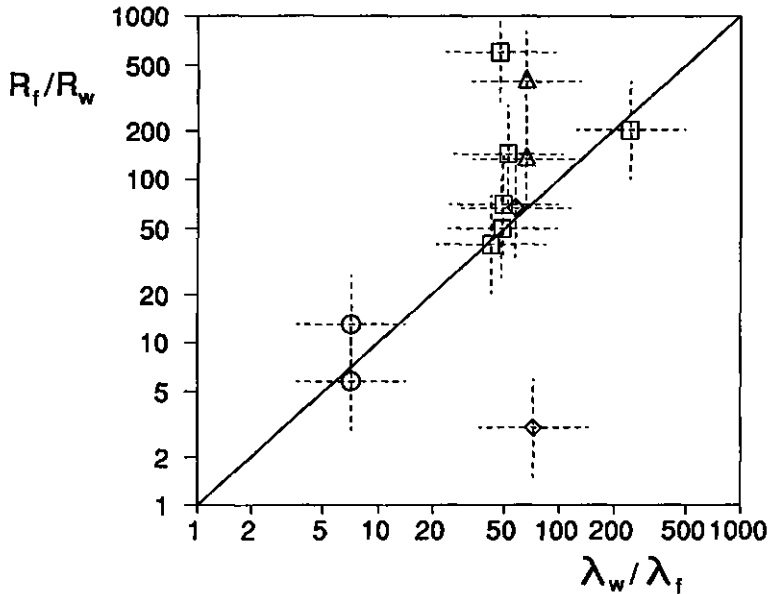


Fig. 7.13. The ratio of dissolution rates of fresh-surface grains to that of similarly sized naturally weathered grains (R_f/R_w), plotted versus the reciprocal of the ratio of their surface roughness factors (λ_w/λ_f). The diagonal line indicates conditions where micropore "walls" in naturally weathered grains are non-reactive, and where the remaining area of naturally weathered grains dissolves equally fast as its freshly created counterpart under similar hydrogeochemical conditions (see text). Error bars hold for values that are accurate within a factor 2. \square (top to bottom): Perth Perthite, Grass Valley Anorthite, Evje Albite, Bancroft Microcline, Mitchell Co. Oligoclase and Hybla Alkali Feldspar; Δ (top to bottom): Keystone Microcline run 2 and run 1, indicating the variation between duplos; \diamond (inaccurate data; top to bottom): Crystal Bay Bytownite and Saranac Lake Andesine; \circ (top to bottom): Nova Scotia feldspar-quartz assemblage at pH 3 and pH 5 HCl, respectively. Values of R_f/R_w and λ_w/λ_f were derived from eqs. (3.11) and (3.12) and from data in Tables 2.1 and 3.5 (feldspars by Holdren and Speyer, 1985, 1987), and from eq. (4.6) and data in Tables 4.2 and 4.4 (Nova Scotia assemblage). Values of R_f/R_w hold for Si dissolution at pH 3 HCl, except Bancroft Microcline (pH 2 HCl) and Nova Scotia pH 5 HCl.

Fig. 7.13 that, apart from Saranac Lake Andesine, $R_f/R_w \geq \lambda_w/\lambda_f$, so $(\lambda_w/\lambda_f - 1)R_m + R_p \leq R_f$. The maximum value of R_m may then be calculated by assuming R_p to be zero, which gives $R_m \leq R_f/(\lambda_w/\lambda_f - 1)$. For instance, for all feldspars by Holdren and Speyer (1985, 1987) $\lambda_w/\lambda_f \geq 50$ (Fig. 7.13). This means that the dissolution rate from the micropore walls in the samples by Holdren and Speyer (1985, 1987) was at most some 2 % of the dissolution rate of the freshly created surfaces (see also chapter 3).

It follows from Fig. 7.13 that, for Perth Perthite and Keystone Microcline, run 2: $R_f/R_w \approx 10 \lambda_w/\lambda_f$ (the estimate of 10 may be inaccurate; see, for instance, the variation between duplos for Keystone Microcline). Provided that the value of 10 is correct, substitution in eq. (7.23) gives $(\lambda_w/\lambda_f - 1)R_m + R_p = 0.1 R_f$. Under these conditions, the maximum value of the dissolution rate of the naturally weathered BET surfaces parallel to the geometric surface (which holds if the dissolution rate of the micropore walls is zero) is some 10 % of the dissolution rate of freshly created surfaces. This means that, during the natural weathering of these two feldspars, apart from the formation of non-reactive micropore walls, the remaining BET area has lost most of its initial reactivity too. However, for most feldspars in Fig. 7.13 the data indicate that, apart from the formation of non-reactive micropore walls, the reactivity of the remaining BET area did not change during natural weathering. With respect to dissolution rates, the most essential change in the surface characteristics of feldspar during natural weathering thus seems to be the formation of the non-reactive micropore walls.

7.5. Conclusions

The development of micropores from enhanced dissolution at dislocations was investigated for quartz and sanidine. Thermodynamic principles indicate that: (1) micropores with radii up to 5 nm develop at common dislocations in sanidine if the solution is not too highly undersaturated; and (2) micropores do not form at common dislocations in quartz, regardless of solution composition. Whereas previous work (see chapters 2 and 5) indicates that micropores are very common in naturally weathered feldspar, the saturation state of most actual soil solutions seems too low to explain their formation. It appears from Monte Carlo simulations that this contradiction is resolved by considering diffusion of aqueous reactants and products inside the dissolution holes. As the depth of dissolution holes increases with time, diffusion causes the free energy change of the dissolution reaction at the bottom of the hole (where most dissolution takes place) to increase with increasing depth. For sanidine in contact with typical soil solutions, this causes conditions at the bottom of dissolution holes to shift from those which favor the formation of etch pits to those which favor the formation of

micropores and, finally, to those which favor closed dislocations (no further dissolution). In fact, this mechanism seems so effective that one may wonder why etch pits form at all under natural conditions at common dislocations in sanidine (i.e. Burgers vectors larger than approximately 0.8 nm). The Monte Carlo simulations for dislocations under natural conditions indicate that, below a critical limit, a high value of the surface free energy causes low dissolution rates at the bottom of holes, favoring the formation of deep micropores. Above this critical limit, micropores do not form at all, such as in quartz. Additional Monte Carlo simulations indicate that, both for quartz and for sanidine, the increase in free energy change at the bottom of dissolution holes, due to diffusion, is insufficient to prevent etch pitting at common dislocations in many laboratory experiments.

The thermodynamic considerations and the Monte Carlo simulations showed that the surface area of the micropore "walls" is essentially non-reactive if the composition of the bulk solution is constant with time. A kinetic model is developed to account for the non-reactivity of micropore walls in naturally weathered sample material. Applying the model to experimental data for feldspar indicates that the dissolution rates of naturally weathered surfaces, corrected for the non-reactivity of the micropore walls, are up to two or three orders of magnitude higher than the uncorrected dissolution rates. According to the model, the corrected dissolution rates of the naturally weathered feldspar surfaces are approximately similar to those of freshly created feldspar surfaces under similar hydrogeochemical conditions. This means that the reactivity of feldspar surfaces other than micropore walls remains essentially unchanged during natural weathering. Thus, the formation of non-reactive micropore walls at dislocations probably represents the most essential change in surface character during the natural weathering of feldspar.

Acknowledgements

We are greatly indebted to Nico van Breemen and Leendert van der Plas, Department of Soil Science and Geology, Agricultural University of Wageningen, The Netherlands, for their critical comments during this research. Alex E. Blum of the U.S. Geological Survey, Menlo Park, CA, kindly provided the Monte Carlo program SCSV.FOR. Part of this study was supported by the Netherlands Foundation for Earth Sciences (AWON) with financial aid from the Netherlands Organization for Scientific Research (NWO).

This chapter has been submitted to *Geochimica et Cosmochimica Acta*.

References

- AAGAARD P. and HELGESON H.C. (1982) Thermodynamic and kinetic constraints on reaction rates among minerals and aqueous solutions. I. Theoretical considerations. *Amer. J. Sci.* **282**, 237-285.
- ÅBERG G. and JACKS G. (1985) Estimation of weathering rate by $^{87}\text{Sr}/^{86}\text{Sr}$ ratios. *Geologiska Föreningens i Stockholms Förhandlingar* **107**, 289-290.
- ALTHAUS E. and TIRTADINATA E. (1989) Dissolution of feldspar: The first step. In *Water-Rock Interaction 6* (ed. D.L. MILES), pp. 15-17. A.A. Balkema, Rotterdam.
- AMRHEIN C. and SUAREZ D.L. (1988) The use of a surface complexation model to describe the kinetics of ligand-promoted dissolution of anorthite. *Geochim. Cosmochim. Acta* **52**, 2785-2793.
- AMRHEIN C. and SUAREZ D.L. (1992) Some factors affecting the dissolution kinetics of anorthite at 25 °C. *Geochim. Cosmochim. Acta* **56**, 1815-1826.
- APRIL R. and NEWTON R. (1983) Neutralization of acid deposition in sensitive bedrock terrains: Control of surficial geology on lake acidification. *Sci. Geol. Mem.* **73**, 19-30.
- ARRHENIUS O. (1954) Den kemiska denudationen i Sverige. *Socker* **8**, 147-166.
- AVNIR D., FARIN D. and PFEIFER P. (1985) Surface geometric irregularity of particulate materials: The fractal approach. *J. Colloid Interface Sci.* **103**, 112-123.
- BAKER J.P. and SCHOFIELD C.L. (1980) Aluminum toxicity to fish as related to acid precipitation and Adirondack surface water quality. *Proc. Int. Conf. on Ecological Impact of Acid Precipitation*, 292-293.
- BALEK J., MOLDAN B., PAČES T. and SKOREPA J. (1978) Hydrological and geochemical mass balances in small forested and agricultural basins. *Proc. of the Baden Symp. on Modelling the Water Quality of the Hydrological Cycle*, IAHS-AISH Publ. No. 125, 50-58.
- BAMBAUER H.U. and BERNOTAT W.H. (1982) The microcline/sanidine transformation isograd in metamorphic regions. I. Composition and structural state of alkali feldspars from granitoid rocks of two N-S traverses across the Aar Massif and Gotthard "Massif", Swiss Alps. *Schweiz. Miner. Petrogr. Mitt.* **62**, 185-230.
- BENNEMA P. and VAN ENCKEVORT W.J.P. (1979) On the occurrence of a critical driving force for dissolution: theory and experimental observation on KDP and other crystals. *Ann. Chim. Fr.* **4**, 451-459.
- BERNER R.A. (1976) The solubility of calcite and aragonite in seawater at atmospheric pressure and 34.5 ‰ salinity. *Amer. J. Sci.* **276**, 713-730.
- BERNER R.A. (1978) Rate control of mineral dissolution under earth surface conditions. *Amer. J. Sci.* **278**, 1235-1252.

- BERNER R.A. (1981) Kinetics of weathering and diagenesis. In *Kinetics of Geochemical processes* (eds. A.C. LASAGA and R.J. KIRKPATRICK), Reviews in Mineralogy 8, Chap. 3, pp. 111-134. Miner. Soc. Amer.
- BERNER R.A. and HOLDREN G.R., Jr. (1977) Mechanism of feldspar weathering: some observational evidence. *Geol.* 5, 369-372.
- BERNER R.A. and HOLDREN G.R., Jr. (1979) Mechanism of feldspar weathering. II. Observations of feldspars from soils. *Geochim. Cosmochim. Acta* 43, 1173-1186.
- BERNOTAT W.H. and BAMBAUER H.U. (1982) The microcline/sanidine transformation isograd in metamorphic regions. II. The region of Lepontine metamorphism, Central Swiss Alps. *Schweiz. Miner. Petrogr. Mitt.* 62, 231-244.
- BLUM A.E. (in press) Feldspars in weathering. In *Feldspars and their Reactions* (ed. I. PARSONS). Kluwer, Netherlands.
- BLUM A.E. and LASAGA A.C. (1987) Monte Carlo simulations of surface reaction rate laws. In *Aquatic Surface Chemistry* (ed. W. STUMM), Chap. 10, pp. 255-292. John Wiley and Sons, New York.
- BLUM A.E., YUND R.A. and LASAGA A.C. (1990) The effect of dislocation density on the dissolution rate of quartz. *Geochim. Cosmochim. Acta* 54, 283-297.
- BOLDYREV V.V. (1979) Control of the reactivity of solids. In *Annual Review of Materials Science* (ed. R.A. HUGGINS), vol. 9, pp. 455-469. Palo Alto, CA, Annual Reviews, Inc.
- BRACE W.F. and WALSH J.B. (1962) Some direct measurements of the surface energy of quartz and orthoclase. *Amer. Miner.* 47, 1111-1122.
- BRACE W.F., SILVER E., HADLEY K. and GOETZE C. (1972) Cracks and pores: a closer look. *Science* 178, 162-164.
- BRADY P.V. and WALTHER J.V. (1989) Controls on silicate dissolution rates in neutral and basic pH solutions at 25 °C. *Geochim. Cosmochim. Acta* 53, 2823-2830.
- BRANTLEY S.L., CRANE S.R., CRERAR D.A., HELLMANN R. and STALLARD R. (1986) Dissolution at dislocation etch pits in quartz. *Geochim. Cosmochim. Acta* 50, 2349-2361.
- BRICKER O.P., GODFREY A.E. and CLEAVES E.T. (1968) Mineral-water interaction during the chemical weathering of silicates. In *Trace Inorganics in Water* (ed. R.F. GOULD), Advances in Chemistry Series, Vol. 73, Chap. 6, pp. 128-142. Amer. Chem. Soc.
- BROWN T.H. and SKINNER B.J. (1974) Theoretical prediction of equilibrium phase assemblages in multicomponent systems. *Amer. J. Sci.* 274, 961-986.
- BRUNAUER S., EMMETT P.H. and TELLER E. (1938) Adsorption of gases in multimolecular layers. *J. Amer. Chem. Soc.* 60, 309-319.
- BRUTON C.J. (1986) Predicting mineral dissolution and precipitation during buried synthetic diagenetic sequences. *Proc. Workshop Geochem. Modeling. Lawrence Livermore Natl. Lab. CONF 8609134*, 111-119.

- BUNKER B.C., TALLANT D.R., HEADLEY T.J., TURNER G.L. and KIRKPATRICK R.J. (1988) The structure of leached sodium borosilicate glass. *Phys. Chem. Glasses* **29**, 106-120.
- BUSENBERG E. and CLEMENCY C.V. (1976) The dissolution kinetics of feldspars at 25 °C and 1 atm. CO₂ partial pressure. *Geochim. Cosmochim. Acta* **40**, 41-49.
- CABRERA N. and LEVINE M.M. (1956) On the dislocation theory of evaporation of crystals. *Phil. Mag.* **1**, 450-458.
- CABRERA N., LEVINE M.M. and PLASKETT J.S. (1954) Hollow dislocations and etch pits. *Phys. Rev.* **96**, 1153.
- CARTWRIGHT J. (1962) Particle shape factors. *Ann. Occup. Hyg.* **5**, 163-171.
- CASEY W.H. and BUNKER B.C. (1990) Leaching of mineral and glass surfaces during dissolution. In *Mineral-Water Interface Geochemistry* (eds. M.F. HOCELLA, Jr. and A.F. WHITE), Reviews in Mineralogy, Vol. 23, Chap. 10, pp. 397-426. Miner Soc. Amer.
- CASEY W.H., CARR M.J. and GRAHAM R.A. (1988a) Crystal defects and the dissolution kinetics of rutile. *Geochim. Cosmochim. Acta* **52**, 1545-1556.
- CASEY W.H., WESTRICH H.R. and ARNOLD G.W. (1988b) Surface chemistry of labradorite feldspar reacted with aqueous solution at pH = 2, 3 and 12. *Geochim. Cosmochim. Acta* **52**, 2795-2807.
- CASEY W.H., WESTRICH H.R., ARNOLD G.W. and BANFIELD J.F. (1989a) The surface chemistry of dissolving labradorite feldspar. *Geochim. Cosmochim. Acta* **53**, 821-832.
- CASEY W.H., WESTRICH H.R., MASSIS T., BANFIELD J.F. and ARNOLD G.W. (1989b) The surface of labradorite feldspar after acid hydrolysis. *Chem. Geol.* **78**, 205-218.
- CASEY W.H., WESTRICH H.R. and HOLDREN G.R., Jr. (1991) Dissolution rates of plagioclases at pH = 2 and 3. *Amer. Miner.* **76**, 211-217.
- CHANG R. (1981) *Physical Chemistry with Applications to Biological Systems*. MacMillan Publ. Co., New York, 659 p.
- CHON M.C., TSURU T. and TAKAHASHI H. (1978) Changes in pore structure of kaolin mineral by sulfuric acid treatment. *Clay Sci.* **5**, 155-162.
- CHOU L. and WOLLAST R. (1984) Study of the weathering of albite at room temperature and pressure with a fluidized bed reactor. *Geochim. Cosmochim. Acta* **48**, 2205-2218.
- CHOU L. and WOLLAST R. (1985) Steady-state kinetics and dissolution mechanisms of albite. *Amer. J. Sci.* **285**, 963-993.
- CHOW K.Y. and GRANT D.J.W. (1988) Surface analysis of griseofulvin powders by krypton adsorption: evaluation of specific surface area, BET constant C and Polanyi Adsorption Potential. *Powder Techn.* **56**, 209-223.
- CHRISTIE J.M. and ARDELL A.J. (1976) Deformation structures in minerals. In *Electron Microscopy in Mineralogy* (ed. H.-R. WENK), Chap. 6.1, pp. 374-403. Springer-Verlag.

- CLAASSEN H.C. and WHITE A.F. (1979) Application of geochemical kinetic data to groundwater systems. In *Chemical Modeling in Aqueous Systems* (ed. E.A. JENNE), Chap. 34, pp. 771-793. ACS Symposium Series No. 93.
- CLAYTON J.L. (1986) An estimate of plagioclase weathering rate in the Idaho batholith based upon geochemical transport rates. In *Rates of Chemical Weathering of Rocks and Minerals* (eds. S.M. COLMAN and D.P. DETHIER), Chap. 19, pp. 453-467. Academic Press.
- CLEAVES E.T., GODFREY A.E. and BRICKER O.P. (1970) Geochemical balance of a small watershed and its geomorphic implications. *Geol. Soc. Amer. Bull.* **81**, 3015-3032.
- CLEAVES E.T., FISCHER D.W. and BRICKER O.P. (1974) Chemical weathering of serpentinite in the eastern Piedmont of Maryland. *Geol. Soc. Amer. Bull.* **85**, 437-444.
- COLMAN S.M. (1986) Levels of time information in weathering measurements, with examples from weathering rinds on volcanic clasts in the western United States. In *Rates of Chemical Weathering of Rocks and Minerals* (eds. S.M. COLMAN and D.P. DETHIER), Chap. 15, pp. 379-393. Academic Press.
- CORRENS C.W. (1963) Experiments on the decomposition of silicates and discussion of chemical weathering. *Clays Clay Miner.* **10**, 443-459.
- CORRENS C.W. and VON ENGELHART W. (1938) Neue Untersuchungen über die Verwitterung des Kalifeldspates. *Chemie der Erde* **12**, 1-22.
- COTTRELL A.H. (1953) *Dislocations and Plastic Flow in Crystals*. Oxford Univ. Press, 223 p.
- COUTURIER Y., MICHARD G. and SARAZIN G. (1984) Constantes de formation des complexes hydroxydés de l'aluminium en solution aqueuse de 20 a 70 °C. *Geochim. Cosmochim. Acta* **48**, 649-659.
- CRANK J. (1976) *The Mathematics of Diffusion*. Oxford Univ. Press, 414 p.
- CREMEENS D.L., DARMODY R.G. and JANSEN I.J. (1987) SEM analysis of weathered grains: Pretreatment effects. *Geol.* **15**, 401-404.
- CRONAN C.S. (1985) Chemical weathering and solution chemistry in acid forest soils: differential influence of soil type, biotic processes and H⁺ deposition. In *The Chemistry of Weathering* (ed. J.I. DREVER), Chap. 11, pp. 175-195. Reidel Publ. Co.
- CRONAN C.S. and SCHOFIELD C.L. (1979) Aluminum leaching response to acid precipitation: Effect on high elevation watersheds in the Northeast. *Science* **204**, 306.
- CUMMINS P.G. and STAPLES E. (1987) Particle size distributions determined by a "multiangle" analysis of photon correlation spectroscopy data. *Langmuir* **3**, 1109-1113.
- DAVIS J.C. (1986) *Statistics and Data Analysis in Geology*. John Wiley and Sons, New York, 646 p.
- DEBERNARDEZ L.S., FERRON J., GOLDBERG E.C. and BUITRAGO R.H. (1984) The effect of surface roughness on XPS and AES. *Surface Sci.* **139**, 541-548.

- DE KANEL J. and MORSE J.W. (1979) A simple technique for surface area determination. *J. Phys. Sci. Instr.* **12**, 272-273.
- DELANY J.M. (1985) *Reaction of Topopah Spring Tuff with J13 Water; A Geochemical Modeling Approach using EQ3/6 Reaction Path Code*. Lawrence Livermore National Laboratory Report 53631, 46 p.
- DELVIGNE J. (1965) *Pédogenèse en Zone Tropicale; la Formation des Minéraux Secondaires en Milieu Ferrallitique*. Dunod, Paris, 178 p.
- DIXON J.B. and WEED S.B. (1977) *Minerals in Soil Environments*. Soil Sci. Soc. Amer., 948 p.
- DOREMUS R.H. (1983) Diffusion-controlled reaction of water with glass. *J. Non Cryst. Solids* **55**, 143-147.
- DOUKHAN J. and TREPIED L. (1979) Plasticity of quartz: crystallographic models and T.E.M. observations. *Bull. Minér.* **102**, 138-147.
- EGGLESTON C.M., HOCELLA M.F., Jr. and PARKS G.A. (1989) Sample preparation and aging effects on the dissolution rate and surface composition of diopside. *Geochim. Cosmochim. Acta* **53**, 797-804.
- EGGLETON R.A. and BUSECK P.R. (1980) High resolution electron microscopy of feldspar weathering. *Clays Clay Miner.* **28**, 173-178.
- ELLISON J. McK. (1954) Errors in particle size determination of settled suspensions. *Nature* **173**, 948.
- EVANS B.W. (1965) Application of a reaction-rate method to the breakdown equilibria of muscovite and muscovite plus quartz. *Amer. J. Sci.* **263**, 647-667.
- FAIR G.M. and HATCH L.P. (1933) Fundamental factors governing the streamline flow of water through sand. *J. Amer. Water Works Assoc.* **25**, 1551-1565.
- FERRY J.M. (1985) Hydrothermal alteration of Tertiary igneous rocks from the Isle of Skye, northwest Scotland. II. Granites. *Contrib. Miner. Petrol.* **91**, 283-304.
- FLEER V.N. (1982) The dissolution kinetics of anorthite and synthetic strontium feldspar in aqueous solutions at temperatures below 100 °C: With applications to the geological disposal of radioactive nuclear wastes. Ph.D. dissertation, Penn. State Univ.
- FÖLSTER H. (1985) Proton consumption rates in holocene and present-day weathering of acid forest soils. In *The Chemistry of Weathering* (ed. J.I. DREVER), Chap. 12, pp. 197-209. Reidel Publ. Co.
- FRANK F.C. (1949) The influence of dislocations on crystal growth. *Disc. Faraday Soc.* **5**, 48-54.
- FURRER G. and STUMM W. (1986) The coordination chemistry of weathering: I. Dissolution kinetics of β - Al_2O_3 and BeO. *Geochim. Cosmochim. Acta* **50**, 1847-1860.
- GARRELS R.M. (1967) Genesis of some groundwaters from igneous rocks. In *Researches in*

- Geochemistry* (ed. P.H. ABELSON), Vol. 2, Chap. 15, pp. 405-420. John Wiley and Sons, New York.
- GARRELS R.M. and CHRIST C.L. (1965) *Solutions, Minerals and Equilibria*. Freeman Cooper, San Francisco, 450 p.
- GARRELS R.M. and MACKENZIE F.T. (1967) Origin of the chemical compositions of some springs and lakes. In *Equilibrium Concepts in Natural Water Systems* (ed. W. STUMM), Advances in Chemistry Series Vol. 67, Chap. 10, pp. 222-242. Amer. Chem. Soc.
- GILLMAN G.P. and SUMNER M.E. (1987) Surface charge characterization and soil solution composition of four soils from the Southern Piedmont in Georgia. *J. Soil Sci. Soc. Amer.* 51, 589-594.
- GILMER G.H. (1976) Growth on imperfect crystal faces. I. Monte Carlo growth rates. *J. Cryst. Growth* 35, 15-28.
- GILMER G.H. (1980) Computer models of crystal growth. *Science* 208, 355-363.
- GISLASON S.R. and EUGSTER H.P. (1987a) Meteoric water-basalt interactions. I: A laboratory study. *Geochim. Cosmochim. Acta* 51, 2827-2840.
- GISLASON S.R. and EUGSTER H.P. (1987b) Meteoric water-basalt interactions. II: A field study in N.E. Iceland. *Geochim. Cosmochim. Acta* 51, 2841-2855.
- GOLDICH S.S. (1938) A study in rock-weathering. *J. Geol.* 46, 17-58.
- GOOSSENS D.A., PHILIPPAERTS J.G., GIJBELS R., PIJERS A.P., VAN TENDELOO S. and ALTHAUS E. (1989) A SIMS, XPS, SEM, TEM and FTIR study of feldspar surfaces after reacting with acid solutions. In *Water-Rock Interaction 6* (ed. D.L. MILES), pp. 271-274. A.A. Balkema, Rotterdam.
- GRANDSTAFF D.E. (1977) Some kinetics of bronzite orthopyroxene dissolution. *Geochim. Cosmochim. Acta* 41, 1097-1103.
- GRANDSTAFF D.E. (1978) Changes in surface area and morphology and the mechanism of forsterite dissolution. *Geochim. Cosmochim. Acta* 42, 1899-1901.
- GRANDSTAFF D.E. (1986) The dissolution rate of forsteritic olivine from Hawaiian beach sand. In *Rates of Chemical Weathering of Rocks and Minerals* (eds. S.M. COLMAN and D.P. DETHIER), Chap. 3, pp. 41-59. Academic Press.
- GREGG S.J. and SING K.S.W. (1982) *Adsorption, Surface Area and Porosity*. Academic Press, 303 p.
- GUTHRIE G.D. and VELEN D.R. (1988) Transmission/Analytical Electron Microscopy of turbid alkali feldspars from the Isle of Skye, Scotland. *EOS* 69, 267.
- HALL P.L., CHURCHMAN G.J. and THENG B.K.G. (1985) Size distribution of allophane unit particles in aqueous suspensions. *Clays Clay Miner.* 33, 345-349.
- HEILMAN M.D., CARTER D.L. and GONZALEZ C.L. (1965) The Ethylene Glycol Monoethyl Ether (EGME) technique for determining soil-surface area. *Soil Sci.* 100, 409-413.

- HEIMANN R.B. (1982) Principles of chemical etching - The art and science of etching crystals. In *Silicon/Chemical Etching* (ed. J. GRABMAIER), Vol. 8 (Crystals), pp. 173-224. Springer-Verlag.
- HEINISCH H.L., Jr., SINES G., GOODMAN J.W. and KIRBY S.H. (1975) Stresses and self-energies of dislocations of arbitrary orientation in anisotropic media: olivine, orthopyroxene, calcite, and quartz. *J. Geophys. Res.* **80**, 1885-1896.
- HELGESON H.C., MURPHY W.M. and AAGAARD P. (1984) Thermodynamic and kinetic constraints on reaction rates among minerals and aqueous solutions. II. Rate constants, effective surface area and the hydrolysis of feldspar. *Geochim. Cosmochim. Acta* **48**, 2405-2432.
- HELLMANN R., EGGLESTON C.M., HOHELLA M.F., Jr. and CRERAR D.A. (1990) The formation of leached layers on albite surfaces during dissolution under hydrothermal conditions. *Geochim. Cosmochim. Acta* **54**, 1267-1281.
- HEYWOOD H. (1938) Measurement of fineness of powders. *Proc. Instr. Mech. Engrs.* **140**, 336-347.
- HOHELLA M.F., Jr., PONADER H.B., TURNER A.M. and HARRIS D.W. (1987) The complexity of mineral dissolution as viewed by high resolution scanning Auger microscopy: Labradorite under hydrothermal conditions. *Geochim. Cosmochim. Acta* **52**, 385-394.
- HOLDREN G.R., Jr. and BERNER R.A. (1979) Mechanism of feldspar weathering. I. Experimental studies. *Geochim. Cosmochim. Acta* **43**, 1161-1171.
- HOLDREN G.R., Jr. and SPEYER P.M. (1985) Reaction rate-surface area relationships during the early stages of weathering. I. Initial observations. *Geochim. Cosmochim. Acta* **49**, 675-681.
- HOLDREN G.R., Jr. and SPEYER P.M. (1987) Reaction rate-surface area relationships during the early stages of weathering. II. Data on eight additional feldspars. *Geochim. Cosmochim. Acta* **51**, 2311-2318.
- HOLDREN G.R., Jr., CASEY W.H., WESTRICH H.R., CARR M.J. and BOSLOUGH M. (1988) Bulk dislocation densities and dissolution rates in a calcic plagioclase. *Chem. Geol.* **70**, 79.
- HOLLAND H.D. (1978) *The Chemistry of the Atmosphere and Oceans*. John Wiley and Sons, New York, 352 p.
- HOLLOWAY P.H. (1978) Quantitative Auger Electron Spectroscopy - Problems and prospects. *Scann. Electr. Microsc.* **1978/1**, 361-374.
- HULTBERG H. (1985) Budgets of base cations, chloride, nitrogen and sulphur in the acid Lake Gårdsjön. *Ecol. Bull.* **37**, 133-157.
- HURD D.C. (1973) Interactions of biogenic opal, sediment and seawater in the Central Equatorial Pacific. *Geochim. Cosmochim. Acta* **37**, 2257-2282.

- IUPAC (1985) Reporting physisorption data for gas/solid systems. *Pure Appl. Chem.* **57**, 603-619.
- JAYCOCK M.J. and PARFITT G.D. (1981) *Chemistry of Interfaces*. Ellis Horwood Publ., 279 p.
- JOSHI M.S. and VAGH A.S. (1968) Application of the selective etch method in the study of structural defects in synthetic quartz. *Sov. Phys. Cryst.* **12**, 573-580.
- JOSHI M.S., KOTRU P.N. and ITTYACHEN M.A. (1970) Studying dislocations in quartz by the hydrothermal-etching method. *Sov. Phys. Cryst.* **15**, 83-89.
- KNAUSS K.G. and WOLERY T.J. (1986) Dependence of albite dissolution kinetics on pH and time at 25 °C and 70 °C. *Geochim. Cosmochim. Acta* **50**, 2481-2497.
- LAGACHE M. (1965) Contribution à l'étude de l'altération des feldspaths, dans l'eau, entre 100 et 200 °C, sous diverses pressions de CO₂, et application à la synthèse des minéraux argileux. *Bull. Soc. Fr. Minér. Crist.* **88**, 223-253.
- LASAGA A.C. (1981a) Rate laws of chemical reactions. In *Kinetics of Geochemical Processes* (eds. A.C. LASAGA and R.J. KIRKPATRICK), Reviews in Mineralogy 8, Chap. 1, pp. 1-68. Miner. Soc. Amer.
- LASAGA A.C. (1981b) Transition state theory. In *Kinetics of Geochemical Processes* (eds. A.C. LASAGA and R.J. KIRKPATRICK), Reviews in Mineralogy 8, Chap. 4, pp. 135-169. Miner. Soc. Amer.
- LASAGA A.C. (1983) Kinetics of silicate dissolution. In *Fourth International Symposium on Water-Rock Interaction*, pp. 269-274. Misasa, Japan.
- LASAGA A.C. and BLUM A.E. (1986) Surface chemistry, etch pits and mineral-water reactions. *Geochim. Cosmochim. Acta* **50**, 2363-2379.
- LAZORINA E.I. and SOROKA V.V. (1974) Etching of quartz and some features of the surface layer. *Sov. Phys. Cryst.* **18**, 651-653.
- LEAMNISON R.N., THOMAS J. and EHRLINGER H.P. (1969) *A Study of the Surface Areas of Particulate Microcrystalline Silica and Silica Sand*. Ill. State Geol. Survey, Circ. 444, 12 p.
- LEVENSPIEL O. (1972) *Chemical Reaction Engineering*. John Wiley and Sons, New York, 578 p.
- LEVINE S.M. and GAROFALINI S.H. (1987) A structural analysis of the vitreous silica surface via a molecular dynamics computer simulation. *J. Chem. Phys.* **86**, 2997-3002.
- LIDDELL N.A., PHAKEY P.P. and WENK H.-R. (1976) The microstructure of some naturally deformed quartzites. In *Electron Microscopy in Mineralogy* (ed. H.-R. WENK), Chap. 6.4, pp. 419-427. Springer-Verlag.
- LIPPENS B.C. and DE BOER J.H. (1965) Studies on pore systems in catalysts. V. The *t*-method. *J. Catalysis* **4**, 319-323.

- LORING D.H. and NOTA D.J.G. (1973) *Morphology and Sediments of the Gulf of St. Lawrence*. Bull. Fisheries Res. Board of Canada, Vol. 182, 147 p.
- LUCE R.W., BARTLETT R.W. and PARKS G.A. (1972) Dissolution kinetics of magnesium silicates. *Geochim. Cosmochim. Acta* 36, 35-50.
- LUNDSTRÖM I. (1974) Etch Pattern and albite twinning in two plagioclases. *Arkiv Miner. Geologi* 5, 63-91.
- MANDELBROT B.B. (1983) *The Fractal Geometry of Nature*. Freeman, New York, 468 p.
- MATTIGOD S.V. and SPOSITO G. (1978) Chemical modeling of trace metal equilibria in contaminated soil solutions using the computer program GEOCHEM. In *Chemical Modeling in Aqueous Systems* (ed. E.A. JENNE), Chap. 37, pp. 837-856. ACS Symposium Series No. 93.
- MATZNER E. (1987) Rates of Na, K, Ca and Mg release by weathering derived from long term flux monitoring in two forested ecosystems in Germany. *Geochemical Monitoring in Small Representative Catchments; Proc. of the Geomon. Workshop*, 10-12.
- McKIBBEN M.A. and BARNES H.L. (1986) Oxidation of pyrite in low temperature acidic solutions: Rate laws and surface textures. *Geochim. Cosmochim. Acta* 50, 1509-1520.
- MEIKE A. (1990) A micromechanical perspective on the role of dislocations in selective dissolution. *Geochim. Cosmochim. Acta* 54, 3347-3352.
- MOGK D.W. and LOCKE W.W. (1988) Application of Auger Electron Spectroscopy (AES) to naturally weathered hornblende. *Geochim. Cosmochim. Acta* 52, 2537-2542.
- MONTGOMERY C.W. and BRACE W.F. (1975) Micropores in plagioclase. *Contrib. Miner. Petrol.* 52, 17-28.
- MUIR I.J., BANCROFT G.M. and NESBITT H.W. (1989) Characteristics of altered labradorite surfaces by SIMS and XPS. *Geochim. Cosmochim. Acta* 53, 1235-1241.
- MUIR I.J., BANCROFT G.M., SHOTYK W. and NESBITT H.W. (1990) A SIMS and XPS study of dissolving plagioclase. *Geochim. Cosmochim. Acta* 54, 2247-2256.
- MULDER J. (1988) Impact of acid atmospheric deposition on soils: Field monitoring and aluminum chemistry. Ph.D. dissertation, Agric. Univ. of Wageningen, The Netherlands.
- MULLA D.J., LOW P.F. and ROTH C.B. (1985) Measurement of the specific surface area of clays by internal reflectance spectroscopy. *Clays Clay Miner.* 33, 391-396.
- MURPHY W.M. (1988) Dislocations and feldspar dissolution. *Europ. J. Miner.* 1, 315-326.
- MURPHY W.M. (1989) Dislocations and feldspar dissolution: Theory and experimental data. *Chem. Geol.* 70, 163.
- MURPHY W.M. and HELGESON H.C. (1987) Thermodynamic and kinetic constraints on reaction rates among minerals and aqueous solutions. III. Activated complexes and the pH-dependence of the rates of feldspar, pyroxene, wollastonite, and olivine hydrolysis. *Geochim. Cosmochim. Acta* 51, 3137-3153.

- MURR L.E. and HISKEY J.B. (1981) Kinetic effects of particle-size and crystal dislocation density on the dichromate leaching of chalcopyrite. *Metall. Trans.* **12B**, 255-267.
- NAZARENKO V.A. and NEVSKAYA E.M. (1969) Spectrophotometric determination of hydrolysis constants of aluminum ions. *Russ. J. Inorg. Chem.* **14**, 1696 (orig. publ. in russian).
- NESBITT H.W. and MUIR I.J. (1988) SIMS depth profiles of weathered plagioclase, and processes affecting dissolved Al and Si in some acidic soil solutions. *Nature* **334**, 336-338.
- NONAKA A. (1984) Surface area estimation from the adsorption isotherm gradient at the linear portion by benzene and toluene vapors on mica and aluminum foil samples. *J. Colloid Interface Sci.* **99**, 335-340.
- NORDSTROM D.K., PLUMMER L.N., WIGLEY T.M.L., WOLERY T.J., BALL J.W., JENNE E.A., BASSETT R.L., CRERAR D.A., FLORENCE T.M., FRITZ B., HOFFMAN M., HOLDREN G.R., Jr., LAFON G.M., MATTIGOD S.V., McDUFF R.E., MOREL F., REDDY M.M., SPOSITO G. and THRAILKILL J. (1978) A comparison of computerized chemical models for equilibrium calculations in aqueous systems. In *Chemical Modeling in Aqueous Systems* (ed. E.A. JENNE), Chap. 38, pp. 857-892. ACS Symposium Series No. 93.
- OECD (1977) *The O.E.C.D. Programme on Long Range Transport of Air Pollutants: Measurements and Findings*. O.E.C.D., Paris, 123 p.
- OLSSON M. and MELKERUD P.A. (1987) Pedogenetic alterations in sandy till in southern Sweden. *Geochemical Monitoring in Small Representative Catchments; Proc. of the Geomon. Workshop*, 102-104.
- OVALLE A.R.C. (1987) Element fluxes in a tropical premontane wet forest, Rio de Janeiro, Brazil. *Geochemical Monitoring in Small Representative Catchments; Proc. of the Geomon. Workshop*, 16-18.
- PACCO F., VAN CANGH L. and FRIPIAT J.J. (1976) Etude par spectroscopie infrarouge et résonance magnétique nucléaire de la distribution homogène des groupes silanols d'un gel de silice fibreux. *Bull. Soc. Chim. Fr.* **7-8**, 651-653.
- PAČES T. (1973) Steady-state kinetics and equilibrium between groundwaters and granitic rock. *Geochim. Cosmochim. Acta* **37**, 2641-2663.
- PAČES T. (1983) Rate constants of dissolution derived from the measurements of mass balance in hydrological catchments. *Geochim. Cosmochim. Acta* **47**, 1855-1863.
- PAČES T. (1986) Rates of weathering and erosion derived from mass balance in small drainage basins. In *Rates of Chemical Weathering of Rocks and Minerals* (eds. S.M. COLMAN and D.P. DETHIER), Chap. 22, pp. 531-550. Academic Press.
- PARKS G.A. (1984) Surface and interfacial free energies of quartz. *J. Geophys. Res.* **89**, 3997-4008.

- PARSONS I., REX D.C., GUISE P. and HALLIDAY A.N. (1988) Argon-loss by alkali feldspars. *Geochim. Cosmochim. Acta* **52**, 1097-1112.
- PATEL A.R., BAHL O.P. and VAGH A.S. (1965) Etching of rhombohedral cleavages of quartz. *Acta Cryst.* **19**, 757-765.
- PERRY D.L., TSAO L. and GAUGLER K.A. (1983) Surface study of HF- and HF/H₂SO₄-treated feldspar using Auger electron spectroscopy. *Geochim. Cosmochim. Acta* **47**, 1289-1291.
- PETIT J.-C., DELLA MEA G., DRAN J.-C., SCHOTT J. and BERNER R.A. (1987a) Mechanism of diopside dissolution from hydrogen depth profiling. *Nature* **325**, 705-707.
- PETIT J.-C., DRAN J.-C. and DELLA MEA G. (1987b) Effects of ion plantation on the dissolution of minerals. Part II. Selective dissolution. *Bull. Minér.* **110**, 25-42.
- PETIT J.-C., DRAN J.-C., SCHOTT J. and DELLA MEA G. (1989) New evidences on the dissolution mechanism of crystalline silicates by ion beam techniques. *Chem. Geol.* **76**, 365-371.
- PETROVICH R. (1976) Rate control in feldspar dissolution. II. The protective effect of precipitates. *Geochim. Cosmochim. Acta* **40**, 1509-1521.
- PETROVICH R. (1981a) Kinetics of dissolution of mechanically comminuted rockforming oxides and silicates: I. Deformation and dissolution of quartz under laboratory conditions. *Geochim. Cosmochim. Acta* **45**, 1665-1674.
- PETROVICH R. (1981b) Kinetics of dissolution of mechanically comminuted rockforming oxides and silicates: II. Deformation and dissolution of oxides and silicates in the laboratory and at the earth's surface. *Geochim. Cosmochim. Acta* **45**, 1675-1686.
- PETROVICH R., BERNER R.A. and GOLDHABER M.B. (1976) Rate control in dissolution of alkali feldspars: I. Study of residual feldspar grains by X-ray photoelectron spectroscopy. *Geochim. Cosmochim. Acta* **40**, 537-548.
- PLUMMER L.N. and WIGLEY T.M.L. (1976) The dissolution of calcite in CO₂-saturated solutions at 25 °C and 1 atmosphere total pressure. *Geochim. Cosmochim. Acta* **40**, 191-202.
- RIMSTIDT J.D. and BARNES H.L. (1980) The kinetics of silica-water reactions. *Geochim. Cosmochim. Acta* **44**, 1683-1699.
- ROBERT M., VENEAU G. and BERRIER J. (1980) Solubilisation comparée des silicates, carbonates et hydroxides en fonction des conditions du milieu. *Bull. Minér.* **103**, 324-329.
- ROBIE R.A., HEMINGWAY B.S. and FISHER J.R. (1978) Thermodynamic properties of minerals and related substances at 298.15 K and 1 bar (10⁵ pascals) pressure and at higher temperatures. *U.S. Geol. Survey Bull.* **1452**, 456 p.
- ROBINS W.H.M. (1954) The significance and application of shape factors in particle size analysis. *Brit. J. Appl. Phys.* **3**, S.82-S.85.

- SACERDOTI M., LABERNARDIERE H. and GANDAIS M. (1980) Transmission electron microscope (TEM) study of geologically deformed potassic feldspars. *Bull. Minér.* **103**, 148-155.
- SANGWAL K. (1982) Dissolution kinetics of MgO crystals in aqueous acidic salt solutions. *J. Mat. Sci.* **17**, 3598-3610.
- SANGWAL K. (1987) *Etching of Crystals*. North-Holland, Amsterdam, 497 p.
- SCHALTEGGER U. and VON QUADT A. (1990) U-Pb zircon dating of the Central Aar Granite (Aar Massif, Central Alps). *Schweiz. Miner. Petrogr. Mitt.* **70**, 361-371.
- SCHINDLER P.W. (1981) Surface complexes at oxide-water interfaces. In *Adsorption of Inorganics at Solid Solution Interfaces* (eds. M.A. ANDERSON and A.J. RUBIN), Chap. 1, pp. 1-49. Ann Arbor Science.
- SCHINDLER P.W. and STUMM W. (1987) The surface chemistry of oxides, hydroxides, and oxide minerals. In *Aquatic Surface Chemistry* (ed. W. STUMM), Chap. 4, pp. 83-110. John Wiley and Sons, New York.
- SCHNOOR J.L. (1990) Kinetics of chemical weathering: A comparison of laboratory and field weathering rates. In *Aquatic Chemical Kinetics* (ed. W. STUMM), Chap. 14, pp. 475-504. John Wiley and Sons, New York.
- SCHOTT J. and BERNER R.A. (1985) Dissolution mechanisms of pyroxenes and olivines during weathering. In *The Chemistry of Weathering* (ed. J.I. DREVER), Chap. 3, pp. 35-53. Reidel Publ. Co.
- SCHOTT J. and PETIT J.-C. (1987) New evidence for the mechanisms of dissolution of silicate minerals. In *Aquatic Surface Chemistry* (ed. W. STUMM), Chap. 11, pp. 293-315. John Wiley and Sons, New York.
- SCHOTT J., BERNER R.A. and SJÖBERG E.L. (1981) Mechanism of pyroxene and amphibole weathering - I. Experimental studies of iron-free minerals. *Geochim. Cosmochim. Acta* **45**, 2123-2135.
- SCHOTT J., BRANTLEY S.L., CRERAR D.A., GUY C., BORCSIK M. and WILLAIME C. (1989) Dissolution kinetics of strained calcite. *Geochim. Cosmochim. Acta* **53**, 373-382.
- SIEGEL D.I. (1984) The effect of kinetics on the geochemical balance of a small watershed on mafic terrain. *EOS* **65**, 211.
- SIEGEL D.I. and PFANNKUCH H.O. (1984) Silicate mineral dissolution at pH 4 and near standard temperature and pressure. *Geochim. Cosmochim. Acta* **48**, 197-201.
- SILLEN L.G. and MARTELL A.C. (1964) *Stability Constants of Metal-Ion Complexes*. Special Publ. no. 17, The Chemical Society, London, 754 p.
- STECK A. (1976) Albit-Oligoklas-Mineralgesellschaften der Peristeritlücke aus alpin-metamorphen Granitgneisen des Gotthardmassivs. *Schweiz. Miner. Petrogr. Mitt.* **56**, 269-292.

- STUMM W. and FURRER G. (1987) The dissolution of oxides and aluminum silicates; examples of surface-coordination controlled kinetics. In *Aquatic Surface Chemistry* (ed. W. STUMM), Chap. 8, pp. 197-219. John Wiley and Sons, New York.
- SVERDRUP H.U. (1990) *The Kinetics of Base Cation Release due to Chemical Weathering*. Lund Univ. Press, 246 p.
- SVERDRUP H.U. and WARFVINGE P. (1987) *Kinetikken for Produksjonen av Kationer ved Vittringen av Feltspatsminerale*. Lund Inst. Techn., 33 p.
- SVERDRUP H.U. and WARFVINGE P. (1988) Weathering of primary silicate minerals in the natural soil environment in relation to a chemical weathering model. *Water, Air and Soil Poll.* **38**, 387-408.
- SWOBODA-COLBERG N.G. and DREVER J.I. (1993) Mineral dissolution rates in plot-scale field and laboratory experiments. *Chem. Geol.* **105**, 51-69.
- TAMM O. (1930) Experimentelle Studien über die Verwitterung und Tonbildung von Feldspaten. *Chemie der Erde* **4**, 420-430.
- TARDY Y. (1971) Characterization of the principal weathering types by the geochemistry of waters from some European and African crystalline massifs. *Chem. Geol.* **7**, 253-271.
- TCHOUBAR C. (1965) Formation de la kaolinite à partir d'albite altérée par l'eau à 200 °C. Etude en microscopie et diffraction électroniques. *Bull. Soc. Fr. Minér. Crist.* **88**, 483-518.
- TOBI A.C. (1963) Plagioclase determination with the aid of the extinction angles in sections normal to (010). A critical comparison of current albite-Carlsbad charts. *Amer. J. Sci.* **261**, 157-168.
- TOLE M.P., LASAGA A.C., PANTANO C. and WHITE W.B. (1986) The kinetics of dissolution of nepheline (NaAlSi₃O₈). *Geochim. Cosmochim. Acta* **50**, 379-392.
- ULRICH B., MAYER R. and KHANNA P.K. (1979) Die Deposition von Luftverunreinigungen und ihre Auswirkungen in Waldökosystemen im Solling. *Schriften Forstl. Fak. Univ. Göttingen u. Nieders. Forstl. Vers. Anst.* **58**, 1-291.
- VAN BREEMEN N. and BRINKMAN R. (1978) Chemical equilibria and soil formation. In *Soil Chemistry. A. Basic Elements* (eds. G.H. BOLT and M.G.M. BRUGGENWERT), Chap. 8, pp. 141-170. Elsevier Publ. Co., Amsterdam.
- VAN BREEMEN N., BURROUGH P.A., VELTHORST E.J., VAN DOBBEN H.F., DE WIT T., RIDDER T.B. and REIJNDERS H.F.R. (1982) Soil acidification from atmospheric ammonium sulphate in forest canopy throughfall. *Nature* **299**, 548-550.
- VAN BREEMEN N., MULDER J. and DRISCOLL C.T. (1983) Acidification and alkalization of soils. *Plant and Soil* **75**, 283-308.
- VAN BREEMEN N., DRISCOLL C.T. and MULDER J. (1984) Acidic deposition and internal proton sources in acidification of soils and waters. *Nature* **307**, 599-604.
- VAN DER BIEST O. and THOMAS G. (1976) Fundamentals of electron microscopy. In

- Electron Microscopy in Mineralogy* (ed. H.-R. WENK), Chap. 2.1, pp. 18-51. Springer-Verlag.
- VAN DER HOEK B., VAN DER EERDEN J.P. and BENNEMA P. (1982) Thermodynamical stability conditions for the occurrence of hollow cores caused by stress of line and planar defects. *J. Cryst. Growth* **56**, 621-632.
- VAN DER PLAS L. (1966) *The Identification of Detrital Feldspars*. Elsevier Publ. Co., Amsterdam, 305 p.
- VAN GRINSVEN J.J.M. (1988) Impact of acid atmospheric deposition on soils: Quantification of chemical and hydrologic processes. Ph.D. dissertation, Agric. Univ. of Wageningen, The Netherlands.
- VAN GRINSVEN J.J.M. and VAN RIEMSDIJK W.H. (1992) Evaluation of batch and column techniques to measure weathering rates in soils. *Geoderma* **52**, 41-57.
- VELBEL M.A. (1985) Geochemical mass balances and weathering rates in forested watersheds of the southern Blue Ridge. *Amer. J. Sci.* **285**, 904-930.
- VELBEL M.A. (1986) Influence of surface area, surface characteristics, and solution composition on feldspar weathering rates. In *Geochemical Processes at Mineral Surfaces* (eds. J.A. DAVIS and K.F. HAYES), Chap. 30, pp. 615-634. ACS Symposium Series No. 323.
- VIDICK B. (1987) Specific surface area determination by gas adsorption: influence of the adsorbate. *Cement and Concrete Res.* **17**, 845-847.
- VOGELMAN H.W. (1982) Catastrophe on Camels Hump. *Nat. Hist.* **91**, 8-14.
- WALKER F.D.L. (1990) Ion microprobe study of intragrain micropermeability in alkali feldspars. *Contrib. Miner. Petrol.* **106**, 124-128.
- WALTER L.M. and MORSE J.W. (1984) Reactive surface area of skeletal carbonates during dissolution: effect of grain size. *J. Sed. Petrol.* **54/4**, 1081-1090.
- WEED H.C. and JACKSON D.D. (1979) *Design of a Variable Flow-rate, Single Pass Leaching System*. Lawrence Livermore National Laboratory Report 52785, 13 p.
- WEGNER M.W. and CHRISTIE J.M. (1983) Chemical etching of deformation substructures in quartz. *Phys. Chem. Miner.* **9**, 67-78.
- WEHBI D. and ROQUES-CARMES C. (1985) Surface roughness contribution to the Auger electron emission. *Scann. Electr. Microsc.* **1985/1**, 171-177.
- WEHRLI B. (1989a) Surface structure and mineral dissolution kinetics: A Monte Carlo study. In *Water-Rock Interaction 6* (ed. D.L. MILES), pp. 751-753. A.A. Balkema, Rotterdam.
- WEHRLI B. (1989b) Monte Carlo simulations of surface morphologies during mineral dissolution. *J. Colloid Interface Sci.* **132**, 230-242.
- WEHRLI B., WIELAND E. and FURRER G. (1990) Chemical mechanisms in the dissolution kinetics of minerals; the aspect of active sites. *Aq. Sci.* **52/1**, 3-31.

- WHITE A.F. and CLAASSEN H.C. (1979) Dissolution kinetics of silicate rocks - application to solute modeling. In *Chemical Modeling in Aqueous Systems* (ed. E.A. JENNE), Chap. 22, pp. 447-473. ACS Symposium Series No. 93.
- WHITE A.F. and PETERSON M.L. (1990) Role of reactive surface area characterization in geochemical kinetic models. In *Chemical Modeling of Aqueous Systems II* (eds. D.C. MELCHIOR and R.L. BASSETT), Chap. 35, pp. 461-475. ACS Symposium Series No. 416.
- WHITEHOUSE I.E., McSAVENY M.J., KNUEPFER P.L.K. and CHINN T.J.H. (1986) Growth of weathering rinds on Torlesse Sandstone, Southern Alps, New Zealand. In *Rates of Chemical Weathering of Rocks and Minerals* (eds. S.M. COLMAN and D.P. DETHIER), Chap. 17, pp. 419-435. Academic Press.
- WIELAND E., WEHRLI B. and STUMM W. (1988) The coordination chemistry of weathering: III. A generalization on the dissolution rates of minerals. *Geochim. Cosmochim. Acta* **52**, 1969-1981.
- WILLAIME C. and GANDAIS M. (1977) Electron microscope study of plastic defects in experimentally deformed alkali feldspars. *Bull. Soc. Fr. Minér. Crist.* **100**, 263-271.
- WILSON M.J. (1975) Chemical weathering of some primary rock-forming minerals. *Soil Sci.* **119**, 349-355.
- WINTSCH R.P. and DUNNING J. (1985) The effect of dislocation density on the aqueous solubility of quartz and some geologic implications: a theoretical approach. *J. Geophys. Res.* **90**, 3649-3657.
- WOLLAST R. (1967) Kinetics on the alteration of K-feldspars in buffered solutions at low temperature. *Geochim. Cosmochim. Acta* **31**, 635-648.
- WOLLAST R. and CHOU L. (1985) Kinetic study of the dissolution of albite with a continuous flow-through fluidized bed reactor. In *The Chemistry of Weathering* (ed. J.I. DREVER), Chap. 5, pp. 75-96. Reidel Publ. Co.
- WORDEN R.H., WALKER F.D.L., PARSONS I. and BROWN W.L. (1990) Development of microporosity, diffusion channels and deuteric coarsening in perthitic alkali feldspars. *Contrib. Miner. Petrol.* **104**, 507-515.
- WRIGHT R.J., BALIGAR V.C. and WRIGHT S.F. (1987) Estimation of phytotoxic aluminum in soil solution using three spectrophotometric methods. *Soil Sci.* **144**, 224-232.
- ZHANG H., BLOOM P.R. and NATER E.A. (1993) Change in surface area and dissolution rates during hornblende dissolution at pH 4.0. *Geochim. Cosmochim. Acta* **57**, 1681-1689.

Appendix 1. Surface roughness and dissolution site density of hornblende at pH 4.0

(Comments on "Change in surface area and dissolution rates during hornblende dissolution at pH 4.0" by H. Zhang, P.R. Bloom and E.A. Nater)

In the recent paper by Zhang *et al.* (1993) the changes in surface area and dissolution rates with time were discussed for ground hornblende samples, dissolving in an acetic acid buffer at pH 4. Some critical and complementary remarks concerning this article are in order.

In chapter 2, a model was discussed to determine the ratio of freshly created BET to measured (freshly created plus naturally weathered) BET surface area for ground mineral samples, derived from much larger naturally weathered starting fragments. The BET-nitrogen data for the ground unreacted samples by Zhang *et al.* (1993) are well-suited for such an analysis. A plot of the surface roughness factor (λ_g) versus the average grain diameter of their samples (Fig. A1) is approximately linear at larger grain diameters, and may be non-linear at smaller grain diameters. A similar relationship was found in chapter 2 for the ground feldspar samples by Holdren and Speyer (1985, 1987). Unfortunately, the data in Zhang *et al.* (1993) are insufficient to calculate the exact value of the roughness factor of the freshly created hornblende surfaces (λ_f) in the unreacted samples. The data in Fig. A1 indicate that

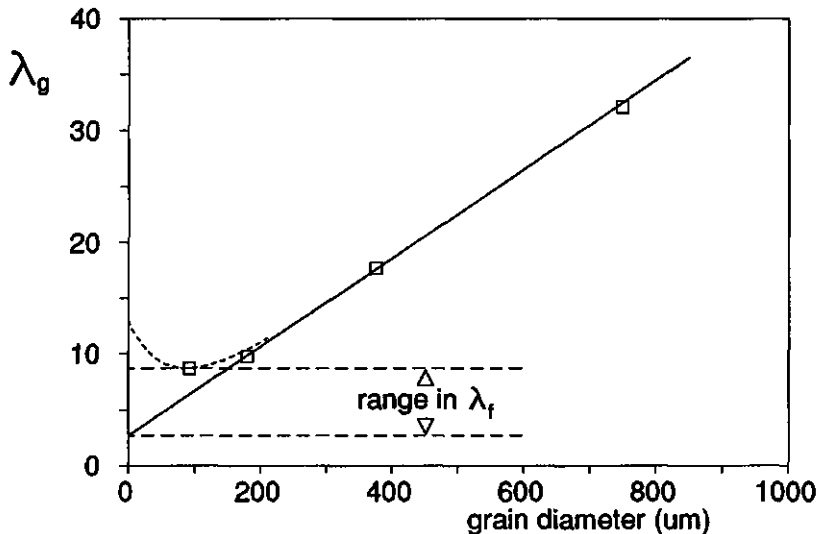


Fig. A1. Plot of the surface roughness factor (λ_g) versus the average grain diameter for the unreacted samples by Zhang *et al.* (1993). The range of possible values of the roughness factor of freshly created hornblende surfaces (λ_f) is indicated by arrows.

λ_f was larger than 2.7 and smaller than 8.7 (see also Fig. 2.1). So, $\lambda_f = 5$ seems a reasonable estimate. Zhang *et al.* (1993) did not report the average diameter of their unfractured starting material, but from their description this should considerably exceed the average diameter of $\approx 750 \mu\text{m}$ in the coarsest ground fraction. The ratio of freshly created to measured BET surface area (F_f) in the unreacted samples may then be estimated from $F_f = \lambda_f/\lambda_g$ (chapter 2), giving $F_f \approx 0.16$ (500-1000 μm), $F_f \approx 0.28$ (250-500 μm), $F_f \approx 0.51$ (110-250 μm), and $F_f \approx 0.57$ (75-110 μm). The remaining fraction of BET area, $1 - F_f$, originates from the very rough naturally weathered starting fragments. For instance, if the average diameter of the starting fragments were 1 cm, their surface roughness factor from extrapolation in Fig. A1 would be approximately 400.

The varying proportions of freshly created BET surface area in the unreacted samples by Zhang *et al.* (1993) question the correctness of their conclusions from bulk dissolution rates ($\text{mol}\cdot\text{g}^{-1}\cdot\text{s}^{-1}$) assuming 100 % fresh surface in all samples. From data on nine different feldspars by Holdren and Speyer (1985, 1987) it was concluded in chapter 3 that: (1) dissolution rates of the freshly created surfaces, normalized to their BET area, were approximately proportional to grain diameter, while dissolution rates of the naturally weathered surfaces, normalized to their BET area, were most likely independent of grain diameter; and (2) dissolution rates, normalized to BET area, of hypothetical fresh-surface grains of similar diameter as the starting fragments were up to several orders of magnitude higher than those of the naturally weathered surfaces. These findings indicate that for freshly created feldspar surfaces, the density of dissolution sites is approximately proportional to grain diameter and may be up to several orders of magnitude higher than the density on surfaces of similarly sized naturally weathered grains (chapters 3 and 5). In that case, intensively ground samples such as those by Holdren and Speyer (1985, 1987) and by Zhang *et al.* (1993) have bulk dissolution rates which are essentially independent of the grain diameter (Appendix 3). In contrast, Zhang *et al.* (1993) concluded that, after 59 days reaction time at pH 4, bulk dissolution rates of their samples were generally smaller for coarser-sized fractions. However, their data indicate that (see Fig. 1 in Zhang *et al.*, 1993): (1) dissolution was not yet at steady state after 59 days; and (2) for most elements analyzed, bulk dissolution rates of the finer-sized fractions at day 59, estimated from the actual data, were smaller than those suggested by the line drawings. This suggests that relationships between dissolution site density and grain diameter for the freshly created and naturally weathered surfaces in the experiments by Zhang *et al.* (1993) were comparable to those in the experiments by Holdren and Speyer (1985, 1987).

Zhang *et al.* (1993) determined the BET-nitrogen surface areas of the ground hornblende samples with increasing reaction time, and found an average increase in BET area of 99 % over the first 30 days, and an additional 12 % over the next 29 days. From

TEM and SEM analysis, and from analysis of hysteresis in adsorption-desorption isotherms, they concluded that: (1) dissolution at pH 4 led to the formation of micropores (diameters 1 to 26 nm) and etch pits; and (2) most increase in BET area during reaction was due to the formation of etch pits. It is interesting to note that their second conclusion is most likely invalid for dissolution of hornblende in the natural environment. This can be seen from the roughness factor of the naturally weathered starting material (≈ 400), which could not result primarily from etch pitting (Helgeson *et al.*, 1984; see also chapter 2). Provided that etch pits and micropores are the only types of surface structures that form during hornblende dissolution, the roughness factor of the starting fragments by Zhang *et al.* (1993) indicates that by far most surface area created during natural weathering is present as micropores. The shift from micropore development under natural conditions to etch pitting in the laboratory can be explained from the difference in free energy change of the dissolution reaction (chapter 7).

Reply to Critical Comments

(P.R. Bloom, E.A. Nater and H. Zhang)

We thank Dr. Anbeek for the interest he has shown in our work but we think that he is making more of our results than the data justify. In our opinion, he is engaging in unwarranted speculation in order to fit our data to his conception of the relationship of surface area to weathering rate.

Anbeek extrapolates from our data to estimate a ratio of freshly ground surface to total surface of 0.57 for the 75-110 μm fraction. According to his estimation, 43 % of the BET surface of these particles is weathered surface from before the sample was taken from the field. This does not correspond with our SEM observations which, although not exhaustive or quantitative, showed only a small fraction of weathered surface before the start of our experiments.

Anbeek goes on to estimate that the initial starting material (which is assumed to be 1 cm cubes) had a roughness factor of 400. Our starting material had particle sizes more in the range of 0.2 to 0.5 cm, but this is not the main problem we have with Anbeek's argument. He assumes that roughness is only a function of weathering features and ignores the contribution of the tremendous irregularity in fractured surfaces that is readily apparent in our SEM photo (Zhang *et al.*, 1993, Fig. 3a). Proper accounting of this would greatly reduce the relative contribution of pitting, due to weathering, in the determination of initial surface roughness. In fact, our approach to the problem of surface roughness assumes that most of the roughness of fractured surfaces is due to roughness created during fracturing. Surface

roughness then becomes a fractal problem. A very simple analysis would suggest that, as the particle size decreases, the relative contribution of the roughness due to fracturing will decrease to a very small value at very small diameters. Thus, a plot of the roughness factor versus diameter is expected to extrapolate to a factor of near unity at zero diameter. As Anbeek shows in Fig. A1, a linear extrapolation of our data yields an intercept of about 3.7 (the data do not justify an attempt to force a curvature as d approaches zero).

We have attempted to answer the question of how weathering might add surface area in addition to the roughness caused by fracturing. This additional surface area must be considered when surface area weathering rates are calculated using an assumption of particle size relationships to roughness.

We do not agree with the conclusion that hornblende dissolution at steady state must be independent of surface area. While we did not attain steady state by day 59, our rate analysis for days 45-55 showed a large dependence on surface area. We believe that a dependence on surface area will continue even at steady state. Following the argument of Holdren and Speyer (1985, 1987), this argument hinges on the question of the defect density relative to the particle size. If the particle size is relatively large, the rate is proportional to surface area. It is not the case that surface area is always unrelated to particle size.

Our conclusion about the size of the pits caused by weathering results from direct interpretation of N_2 adsorption/desorption hysteresis after weathering under conditions far from equilibrium. Hornblende equilibrium cannot be attained in soils and weathering must occur far from equilibrium. Under such conditions, we do not see how the argument of Lasaga and Blum (1986) can be used to reason that our laboratory data are not useful for interpretation of pitting under field conditions.

This appendix is in press for *Geochimica et Cosmochimica Acta*, vol. 58.

Appendix 2. Clustering of dissolution data in the kinetic model from chapter 3

Fig. 3.2d shows that \bar{F}_g and \bar{F}_f may be independent of grain diameter (clustering of data) for the $\gamma=0$ feldspar Bancroft Microcline. For $\gamma=0$ feldspars in general, the relation between λ_g and d_g is linear (chapter 3), so simple geometry shows that eq. (3.3) can be rewritten as:

$$F_f = \lambda_f(d_w - d_g)/(\lambda_g d_w) \quad (\text{A2.1})$$

Combination of eqs. (3.3), (3.18) and (A2.1) leads to:

$$\bar{F}_f = P_f \lambda_f(d_w - d_g)/[P_f \lambda_f(d_w - d_g) + P_w \lambda_w d_g] \quad (\text{A2.2})$$

Since invariably $d_w \gg d_g$ for the samples by Holdren and Speyer (1985, 1987), $d_w - d_g$ is essentially constant. Thus, \bar{F}_f is essentially constant if:

$$P_f = P_w d_g C_5 \quad (\text{A2.3})$$

where (eq. A2.2):

$$C_5 = \lambda_w \bar{F}_f / [\lambda_f (1 - \bar{F}_f) (d_w - d_g)] \quad (\text{A2.4})$$

At a reference grain diameter d_r , eq. (A2.3) gives:

$$C_5 = C_6/d_r \quad (\text{A2.5})$$

where C_6 equals the ratio of P_f to P_w at grain diameter d_r . Combination of eqs. (A2.3) and (A2.5) leads to:

$$P_f = P_w C_6 d_g/d_r \quad (\text{A2.6})$$

which is the condition for \bar{F}_f to be (essentially) constant in the kinetic model for $\gamma=0$ feldspars. Some results for which eq. (A2.6) holds are shown in Fig. A2 for Bancroft Microcline, Hybla Alkali Feldspar and Grass Valley Anorthite. Clustering of data, indicating correctly modeled relations of P_f and P_w with grain diameter, is observed only if $P_f = d_g/d_r$ and $P_w = 1$.

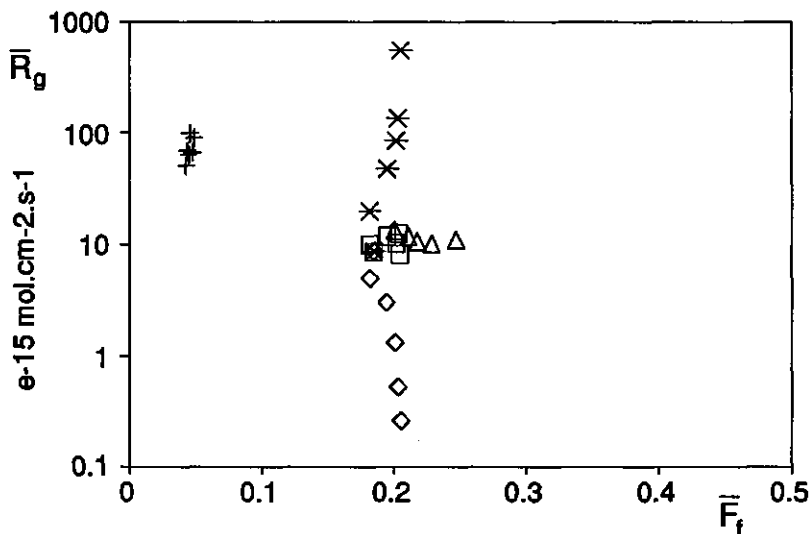


Fig. A2. Examples of the effective dissolution rate (\bar{R}_g) versus the ratio of fresh reactive BET to reactive BET surface area (\bar{F}_f) for the $\gamma=0$ feldspars by Holdren and Speyer (1985, 1987). In all cases: $P_f = P_w C_6 d_g/d_r$ (eq. A2.6). □ : Bancroft Microcline, $P_f = d_g/d_r$ and $P_w = 1$; ◇ : Bancroft Microcline, $P_f = 1$ and $P_w = d_r/d_g$; * : Bancroft Microcline, $P_f = (d_g/d_r)^2$ and $P_w = d_g/d_r$; △ : Hybla Alkali Feldspar, $P_f = d_g/d_r$ and $P_w = 1$; + : Grass Valley Anorthite, $P_f = d_g/d_r$ and $P_w = 1$.

This appendix was published in *Geochimica et Cosmochimica Acta* as part of the paper based on chapter 3.

Appendix 3. Analysis of the kinetic model from chapter 3 in terms of bulk dissolution rates

The kinetic model derived in chapter 3 may also be used to interpret experimental data in terms of the bulk dissolution rate (R^* ; $\text{mol.g}^{-1}.\text{s}^{-1}$). This eliminates all possible effects from surface area measurements. R^* is defined by:

$$R^* \equiv - (1/g) (dn/dt) \quad (\text{A3.1})$$

where g is the sample mass. For a ground sample, combination of eqs. (3.5) and (A3.1) gives:

$$R_g^* = S_g^* R_g \quad (\text{A3.2})$$

where R_g^* is the bulk dissolution rate of the ground sample as a whole, and S_g^* is the specific actual surface area of the sample. It follows from eqs. (3.1), (3.21) and (A3.2) that:

$$R_g^* = R_g \lambda_g \mathfrak{D} / (\rho d_g) \quad (\text{A3.3})$$

where λ_g may be replaced by eq. (3.19). For instance, if the starting material contains only freshly created surface area, then $\lambda_g = \lambda_r$ at all d_g (chapter 2). \mathfrak{D} equals $6 \cdot 10^4$ for smooth spheres if d_g is in μm . Thus, if $P_f = d_g/d_r$, eqs. (3.13) and (A3.3) lead to:

$$R_g^* = \frac{6 \cdot 10^4}{\rho d_r} \lambda_r \bar{R}_f \quad (\text{A3.4})$$

Thus, bulk dissolution rates of ground samples containing only freshly created surface area are independent of the grain diameter if $P_f = d_g/d_r$. For intensively ground samples from $\gamma=0$ feldspars, eq. (3.4) applies and $\beta = \lambda_r$ (chapter 2). If $P_f = d_g/d_r$ and $P_w = 1$, it follows from eqs. (3.4), (3.13), (3.19) and (A3.3) that:

$$R_g^* = \frac{6 \cdot 10^4}{\rho d_r} [\lambda_r \bar{R}_f + (\lambda_r - \lambda_r) \bar{R}_w] \quad (\text{A3.5})$$

where λ_r is the surface roughness factor at grain diameter d_r . Thus, bulk dissolution rates of intensively ground samples from $\gamma=0$ feldspars are essentially independent of the grain diameter if $P_f = d_g/d_r$ and $P_w = 1$. For samples, either containing only freshly created surface

area, or being intensively ground from $\gamma=0$ feldspars, it follows from eqs. (3.4), (3.13), (3.19) and (A3.3) that:

$$R_g^* = \frac{6 \cdot 10^4 \lambda_r \bar{R}_r}{\rho d_r} (P_r d_r / d_g - 1) + R_r^* \quad (\text{A3.6})$$

where R_r^* is the bulk dissolution rate at grain diameter d_r . Thus, R_g^* is independent of grain diameter if $P_r = d_g / d_r$, and R_g^* is strongly dependent of grain diameter if $P_r = 1$. Results that are in general agreement with $P_r = d_g / d_r$ were reached for Vals (Switzerland) Adularia and for Ylijärvi (Finland) Labradorite (Table 3.2).

This appendix was published in *Geochimica et Cosmochimica Acta* as part of the paper based on chapter 3.

Appendix 4. A multivariate linear regression model for the comparison of field- and laboratory dissolution data

Hereafter, a multivariate linear regression model is derived to obtain surface roughness factors of individual minerals in assemblages. Input data for the model are the surface roughness factors of subsamples obtained from density fractionation (Van Der Plas, 1966). Once the surface roughness factors of the individual minerals are known, their relative contributions to the BET surface area of the original assemblage are easily found from their geometric surface areas.

The surface roughness factor of a mineral i in a sample j ($\lambda_{i,j}$) is defined by:

$$\lambda_{i,j} \equiv S_{i,j}/s_{i,j} \quad (\text{A4.1})$$

where $S_{i,j}$ and $s_{i,j}$ are the BET surface area and the geometric surface area of mineral i in sample j , respectively. The BET and the geometric surface area of sample j (S_j and s_j) are defined by:

$$S_j \equiv \sum_i S_{i,j} \quad (\text{A4.2})$$

and:

$$s_j \equiv \sum_i s_{i,j} \quad (\text{A4.3})$$

The fraction of the geometric surface area of sample j that is occupied by the geometric surface area of mineral i ($\xi_{i,j}$) is defined by:

$$\xi_{i,j} \equiv s_{i,j}/s_j \quad (\sum_i \xi_{i,j} \equiv 1) \quad (\text{A4.4})$$

The surface roughness factor of a mineral i primarily depends on the grain diameter, and on the exposure time to and intensity of weathering (chapters 2 and 3). Thus, if a mineral assemblage of given grain diameter, exposure time and intensity of weathering is fractionated into j subsamples of different range of grain density (giving subsamples of varying mineralogical composition), it holds that:

$$\lambda_{i,j=1} = \lambda_{i,j=2} = \dots \equiv \lambda_i \quad (\text{A4.5})$$

Eqs. (A4.1), (A4.2), (A4.4) and (A4.5) can be combined to:

$$\lambda_j = \sum_i (\xi_{ij} \lambda_i) \quad (\text{A4.6})$$

Values of ξ_{ij} can be obtained, for instance, from microscopic observation of individual mineral grains. Alternatively, ξ_{ij} can be estimated from mass fractions as follows. The geometric surface area of a sample j is given by (Cartwright, 1962):

$$s_j = \frac{g_j \mathcal{D}_j}{\rho_j d_j} \quad (\text{A4.7})$$

where g_j is the sample mass, \mathcal{D}_j is a geometry factor related to the shape of the grains (\mathcal{D}_j varies from 6.1 for rounded grains to 7.7 for angular grains; Fair and Hatch, 1933), ρ_j is the density of the sample, and d_j is the average grain diameter. If the mineral volumes of i are homogeneously distributed over the grains in a sample j , eq. (A4.7) holds for all minerals i in j , and from eqs. (A4.4) and (A4.7):

$$\xi_{ij} = \frac{g_{ij} \mathcal{D}_{ij} \rho_j d_j}{g_j \mathcal{D}_j \rho_{ij} d_{ij}} \quad (\text{A4.8})$$

The volume fraction of mineral i in sample j (v_{ij}) is given by:

$$v_{ij} = \frac{g_{ij} \rho_j}{g_j \rho_{ij}} \quad (\text{A4.9})$$

where g_{ij}/g_j is the mass fraction of i in j (which can be obtained, for instance, from X-Ray fluorescence spectrometry and from normative calculations) and where $\rho_{ij} \equiv \rho_i$ (incomplete purification by density fractionation normally results from the presence of minerals i of constant density in rock fragments of varying composition). Eqs. (A4.8) and (A4.9) give:

$$\xi_{ij} = v_{ij} \frac{\mathcal{D}_{ij} d_j}{\mathcal{D}_j d_{ij}} \quad (\text{A4.10})$$

For instance, for a sample j with grains of equal size and shape ($d_j = d_{ij}$; $\mathcal{D}_j = \mathcal{D}_{ij}$), eqs. (A4.6) and (A4.10) combine to:

$$\lambda_j = \sum_i (v_{ij} \lambda_i) \quad (\text{A4.11})$$

Thus, under the mentioned conditions, the surface roughness factor of a mineral assemblage

equals the weighted average of the surface roughness factors of the constituent minerals, and the volume fractions are the weighting factors. In eq. (A4.11), values of λ_i are the unknowns, so the resulting multivariate linear regression model can be solved if $j \geq i$.

Eq. (A4.11) holds both for naturally weathered and for artificially ground samples. However, the relationship between surface roughness factor and grain diameter of minerals i in such samples is often linear (chapters 2 and 5):

$$\lambda_i = \alpha_i d_i + \beta_i \quad (\text{A4.12})$$

where α_i and β_i are the slope and intercept, respectively. Under these conditions, in cases where $d_j = d_{i,j}$, the multivariate linear regression model is found from combination of eqs. (A4.11) and (A4.12):

$$\lambda_j = \sum_i [v_{i,j} (\alpha_i d_j + \beta_i)] \quad (\text{A4.13})$$

where α_i and β_i are the unknowns. In this case, the model can be solved if $j \geq 2i$.

This appendix was published in the July 1993 special issue of *Chemical Geology* on the 3rd International Symposium on Geochemistry of the Earth Surface.

Appendix 5. Introduction of one-dimensional aqueous diffusion in the Monte Carlo program SCSV.FOR

Hereafter, a model is derived to account for diffusion of aqueous reactant and product species inside dissolution holes during Monte Carlo simulations. It is assumed that: (1) solutions are dilute, and activity coefficients are unity; (2) activities of aqueous species i in the bulk solution are constant with time; and (3) concentration profiles of aqueous species inside the dissolution holes are linear functions of depth (Fig. A5). Under these conditions it follows that:

$$a_i = a_{b,i} + \Theta_i L \quad (\text{A5.1})$$

where a_i is the activity of aqueous species i as a function of depth, $a_{b,i}$ is the bulk activity of species i , Θ_i is the concentration gradient of species i , and L is depth inside the hole. Θ_i equals $(a_{m,i} - a_{b,i})/L_m$, where $a_{m,i}$ is the activity of species i at maximum depth L_m . $a_{m,i}$ is found from (Fig. A5):

$$a_{m,i} = 2a_{av,i} - a_{b,i} \quad (\text{A5.2})$$

where $a_{av,i}$ is the average activity inside the dissolution hole, which would hold at all L if the

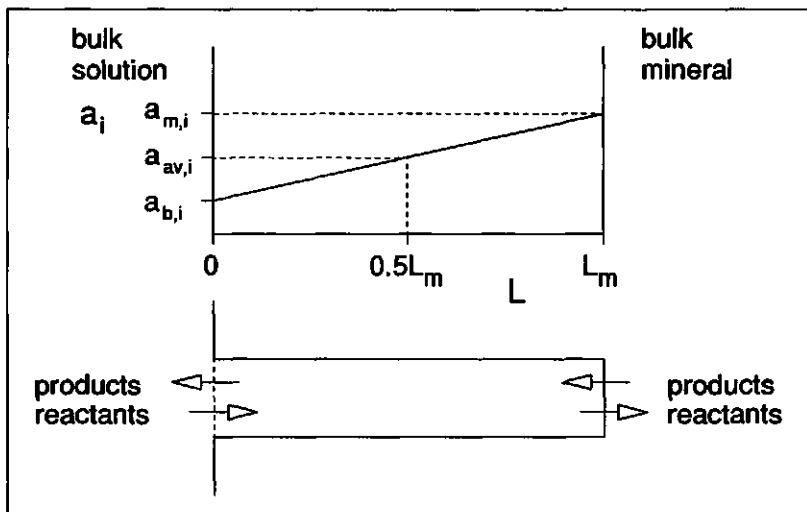


Fig. A5. Schematic representation of the system for which diffusion was introduced in the Monte Carlo program SCSV.FOR.

aqueous solution inside the hole were stirred. For the Monte Carlo simulations in chapter 7, aqueous bulk activities $a_{b,i}$ are part of the program input. Thus, if $a_{av,i}$ at given maximum depth L_m is known, a_i and ΔG can be determined at any depth from eqs. (7.2), (A5.1) and (A5.2).

Values of $a_{av,i}$ at given L_m can be found from iteration as follows. At time $t+\Delta t$, it holds that:

$$(a_{av,i})_{t+\Delta t} = (a_{av,i})_t + (\Xi_{P,i})_{\Delta t} - (\Xi_{R,i})_{\Delta t} \quad (A5.3)$$

where $(a_{av,i})_{t+\Delta t}$ and $(a_{av,i})_t$ are the average activities at $t+\Delta t$ and t , respectively, $\Xi_{P,i}$ (mol.l^{-1}) is a production term over the time interval Δt due to mineral dissolution at the bottom of the hole, and $\Xi_{R,i}$ (mol.l^{-1}) is a removal term over the time interval Δt due to the diffusion flux over the cross-sectional surface area of the hole at zero depth. By definition, $\Xi_{P,i}$ and $\Xi_{R,i}$ are positive for products and negative for reactants. Application of Fick's first law to this type of system gives (Crank, 1976):

$$J_i = D_i(a_{m,i} - a_{b,i})/L_m \quad (A5.4)$$

where J_i (mol.cm^{-2} of cross-sectional surface area. s^{-1}) is the diffusion flux of species i , and D_i ($\text{cm}^2.\text{s}^{-1}$) is the diffusion coefficient of that species. It follows from eqs. (A5.2) and (A5.4) that:

$$(\Xi_{R,i})_{\Delta t} = 2D_i[(a_{av,i})_t - a_{b,i}]\Delta t/L_m^2 \quad (A5.5)$$

$\Xi_{P,i}$ depends on the dissolution reaction under consideration. For quartz it follows that (Table 7.3):

$$(\Xi_{P,H_4SiO_4})_{\Delta t} = (R_{Q,m})_t \Delta t/L_m \quad (A5.6)$$

where $R_{Q,m}$ (mol.cm^{-2} of cross-sectional surface area. s^{-1}) is the dissolution rate of quartz at depth L_m (see below). Thus, diffusion during the dissolution of quartz can be described by combining eqs. (A5.3), (A5.5) and (A5.6) to:

$$(a_{av,H_4SiO_4})_{t+\Delta t} = (a_{av,H_4SiO_4})_t + (R_{Q,m})_t \Delta t/L_m - 2D_{H_4SiO_4} [(a_{av,H_4SiO_4})_t - a_{b,H_4SiO_4}]\Delta t/L_m^2 \quad (A5.7)$$

For sanidine, the stoichiometric coefficient q (Table 7.3) varies with pH, due to the speciation of Al. Taking into consideration the Al complexes in Table 7.3, q is found from:

$$q = \frac{4 + 3K_1 10^{\text{pH}} + 2K_2 10^{2\text{pH}} + K_3 10^{3\text{pH}}}{1 + K_1 10^{\text{pH}} + K_2 10^{2\text{pH}} + K_3 10^{3\text{pH}} + K_4 10^{4\text{pH}}} \quad (\text{A5.8})$$

Thus, according to the dissolution reaction of sanidine (Table 7.3):

$$(\Xi_{\text{P,H}^+})_{\Delta t} = - (q_m R_{\text{S,m}})_t \Delta t / L_m \quad (\text{A5.9})$$

where q_m is q at depth L_m , and $R_{\text{S,m}}$ is the dissolution rate of sanidine at depth L_m (see below). Eqs. (A5.3), (A5.5) and (A5.9) can be combined to:

$$(a_{\text{av,H}^+})_{t+\Delta t} = (a_{\text{av,H}^+})_t - (q_m R_{\text{S,m}})_t \Delta t / L_m - 2D_{\text{H}^+} [(a_{\text{av,H}^+})_t - a_{\text{b,H}^+}] \Delta t / L_m^2 \quad (\text{A5.10})$$

Furthermore, it follows from the sanidine dissolution reaction that: $(\Xi_{\text{P,K}^+})_{\Delta t} = - (\Xi_{\text{P,H}^+})_{\Delta t} / q_m$, and: $(\Xi_{\text{P,H}_4\text{SiO}_4})_{\Delta t} = - 3 (\Xi_{\text{P,H}^+})_{\Delta t} / q_m$. Thus:

$$(a_{\text{av,K}^+})_{t+\Delta t} = (a_{\text{av,K}^+})_t + (R_{\text{S,m}})_t \Delta t / L_m - 2D_{\text{K}^+} [(a_{\text{av,K}^+})_t - a_{\text{b,K}^+}] \Delta t / L_m^2 \quad (\text{A5.11})$$

and:

$$(a_{\text{av,H}_4\text{SiO}_4})_{t+\Delta t} = (a_{\text{av,H}_4\text{SiO}_4})_t + 3(R_{\text{S,m}})_t \Delta t / L_m - 2D_{\text{H}_4\text{SiO}_4} [(a_{\text{av,H}_4\text{SiO}_4})_t - a_{\text{b,H}_4\text{SiO}_4}] \Delta t / L_m^2 \quad (\text{A5.12})$$

For H^+ , K^+ and H_4SiO_4 , eqs. (A5.10), (A5.11) and (A5.12) give $a_{\text{av},i}$ at time $t+\Delta t$ from $a_{\text{av},i}$ at time t . The corresponding activities of H^+ , K^+ and H_4SiO_4 at time $t+\Delta t$ at the bottom of the hole can then be found from eq. (A5.2). Once these are known, the corresponding total activity of the Al complexes at time $t+\Delta t$ at the bottom of the hole follows directly from the principle of electroneutrality:

$$(a_{\text{m,Al(tot)}})_{t+\Delta t} = [a_{\text{b,H}^+} - (a_{\text{m,H}^+})_{t+\Delta t} + a_{\text{b,K}^+} - (a_{\text{m,K}^+})_{t+\Delta t} + 10^{-14} / (a_{\text{m,H}^+})_{t+\Delta t} - 10^{-14} / a_{\text{b,H}^+} + (q_b - 1) a_{\text{b,Al(tot)}}] / [(q_m)_{t+\Delta t} - 1] \quad (\text{A5.13})$$

where Al(tot) refers to the average composition of the Al complexes considered, given by

$Al(OH)_4^{(q-1)+}$ (Table 7.3), and q_b is the aqueous bulk value of q .

Incorporation of this model into the Monte Carlo program requires input of the dissolution rates at the bottom of the hole ($R_{Q,m}$ and $R_{S,m}$), and of the diffusion coefficients (D_i). For a spherical species i in aqueous solution, D_i may be estimated from (Chang, 1981):

$$D_i = \frac{kT}{6\pi\eta_{H_2O}r_i} \quad (A5.14)$$

where k is Boltzmann's constant, T is temperature (K), η is the viscosity, and r_i is the radius of the species. For $\eta_{H_2O} = 1.01 \cdot 10^{-12}$ kJ.s.cm⁻³ (Chang, 1981) and $T = 300$ K, it follows that: $D_{H^+} \approx 0.47 \cdot 10^{-5}$ cm².s⁻¹ ($r_{H^+} \approx 0.45$ nm), $D_{K^+} \approx 1.60 \cdot 10^{-5}$ cm².s⁻¹ ($r_{K^+} \approx 0.133$ nm), and $D_{H_4SiO_4} \approx 1.22 \cdot 10^{-5}$ cm².s⁻¹ ($r_{H_4SiO_4} \approx 0.178$ nm). These values are used throughout the simulations in chapter 7.

For a mineral j , the dissolution rate at the bottom of the hole ($R_{j,m}$) is a function of the aqueous activities at the bottom of the hole, and is given by (see Aagaard and Helgeson, 1982):

$$(R_{j,m})_t = R_{j,b} \frac{K'_{eq} - (\prod_i a_{m,i}^{q_{m,i}})_t}{K'_{eq} - \prod_i a_{b,i}^{q_{b,i}}} \quad (A5.15)$$

where $R_{j,b}$ is the dissolution rate of mineral j at the bottom of the hole if the solution inside the hole were of constant (bulk) composition, and K'_{eq} is the equilibrium constant of the dissolution reaction, corrected for the strain energy. At the dislocation, K'_{eq} is found from K_{eq} (Table 7.3) according to:

$$K'_{eq} = K_{eq} \exp [\Delta H_m / (RT)] \quad (A5.16)$$

Using the data in Table 7.1, $K'_{eq} = 10^{-2.57}$ for quartz, and $K'_{eq} = 10^{+12.07}$ for sanidine. Diffusion inside the dissolution hole can then be modeled once $R_{j,b}$ has been determined from Monte Carlo simulations assuming constant ΔG at all sites and over total computing time (see chapter 7). Periodic re-iteration as the maximum depth L_m increases with increasing computing time allows to keep track of ΔG as a function of depth L inside the hole at all L_m .

This appendix has been submitted to *Geochimica et Cosmochimica Acta* as part of the paper based on chapter 7.

Summary

Introduction

Since the beginning of industrialization in the previous century, the emission and atmospheric deposition of potentially acid chemicals have increased considerably. The increased acid deposition has resulted, among others, in unwanted acidification of many surface waters, groundwaters and soils. The damage caused by acid deposition to the biota in terrestrial and aquatic ecosystems is considerable, and the long-term fate of these systems is a matter of great concern.

Soils can consume protons ("acids") in several ways. In most soils the long-term rate of proton consumption is determined by the dissolution rates of the base cation-bearing minerals (calcite, feldspar, pyroxene, amphibole, etc.). However, the reaction mechanism and dissolution kinetics of these minerals are not yet sufficiently understood to accurately predict their dissolution rates under varying conditions. In this thesis the relationships between crystal structure, grain diameter, surface morphology and dissolution kinetics are investigated for feldspar and quartz under acid leaching conditions. Feldspar was chosen because it is the most abundant base cation-bearing mineral in soils, and quartz was chosen because its dissolution behaviour differs distinctly from that of feldspar. The typical scale of interest here is in the order of nm to μm .

The mineral surface area in laboratory dissolution studies

Large, naturally weathered mineral fragments are often ground and sieved to obtain samples for dissolution studies in the laboratory. If the fragments are ground to much smaller dimensions, the samples are normally assumed to contain only freshly created surface area (i.e. the original, naturally weathered surface area is neglected). To calculate the dissolution rate in $\text{mol}\cdot\text{cm}^{-2}\cdot\text{s}^{-1}$ from experimental dissolution data, the surface area of the ground sample must be known. The most widely used surface area estimate in mineral dissolution studies is obtained from the gas adsorption isotherm (BET method), using nitrogen, argon or krypton as the adsorbate gas. The diameter of these gas molecules (≈ 0.4 nm) is very similar to the effective diameter of a water molecule (≈ 0.3 nm), so the BET surface area is probably a reasonable estimate of the wetted mineral surface.

It is shown in this thesis that, for large, naturally weathered feldspar fragments, by far most surface area at the nm scale of the krypton molecule is not observed at the μm scale of

scanning electron microscopy. This means that by far most BET surface area of naturally weathered feldspar fragments is present as "internal" surface area. In contrast, the fresh feldspar surfaces created by grinding are quite smooth, with essentially similar surface areas revealed at the scale of the krypton molecule and of scanning electron microscopy. Due to the much higher "roughness" of naturally weathered feldspar surfaces than of freshly created feldspar surfaces, grinding is highly ineffective in creating a large proportion of fresh BET surface area. It is shown in this thesis that, even after intensive grinding, samples from large naturally weathered mineral fragments can still contain substantial proportions of naturally weathered, "internal" BET surface area. This means that previous dissolution studies on ground samples that failed to recognize the simultaneous presence of these two types of surface morphology need reinterpretation.

The dissolution site density on mineral surfaces

Experimental dissolution rates of ground samples, normalized to the BET surface area, are often independent of the grain diameter after grinding. Based on the idea that essentially all BET surface area of ground samples is freshly created, this led to the hypothesis that the dissolution site density (expressed as the number of identical dissolution sites per cm^2 of BET surface area) is independent of the grain diameter after grinding. In this thesis, a kinetic model is derived to test the validity of this hypothesis by explaining experimental dissolution data from the simultaneous presence of freshly created and naturally weathered BET surfaces in samples. Applying the model to literature data for nine different feldspars shows that, in fact, grinding has two (partly) counteracting effects on dissolution rates. These are: (1) increase of the proportion of the measured BET surface area which is freshly created; and (2) decrease of the proportion of the freshly created BET surface area which is dissolution reactive. Thus, by taking into account the "internal" surface area of naturally weathered feldspars, we find that, within the range of grain diameters investigated ($< 1000 \mu\text{m}$), the dissolution site density of freshly created feldspar surfaces is approximately proportional to, and not independent of, the grain diameter. This can be explained if preferential fracture planes have relatively high densities of potentially dissolution reactive sites. In that case, continued grinding exposes fresh surfaces with decreasing dissolution site densities, which would lower the average dissolution site density at all grain diameters. So, the fresh reactive surface area is "diluted", rather than "destroyed" by grinding. According to the kinetic model, the dissolution site density of naturally weathered surfaces in ground samples is independent of the grain diameter. This can be explained if fracturing of naturally weathered surfaces in smaller pieces does not change the "internal" surface structure itself.

In that case, naturally weathered surface area on fractured grains originates from the unfractured starting fragments at all grain diameters after grinding. It follows from the kinetic model that, for fresh-surface feldspar grains, dissolution rates ($\text{mol}\cdot\text{cm}^{-2}$ of BET surface $\cdot\text{s}^{-1}$) are up to several orders of magnitude higher than those of similarly sized naturally weathered feldspar grains. In terms of identical dissolution sites, this would mean that, for feldspar, the density on freshly created BET surfaces is up to several orders of magnitude higher than the density on naturally weathered BET surfaces.

The formation of micropores during natural weathering

The nature and reactivity of the "internal" BET surface area are investigated for a naturally weathered feldspar-quartz assemblage. It is concluded that: (1) the internal surface area is largely present as micropores of approximately 2 nm diameter; (2) during natural weathering, micropores form in feldspar but not in quartz grains; (3) the micropore "walls" (perpendicular to the grain surface) are essentially non-reactive; (4) the micropore "bottoms" (parallel to the grain surface) are highly reactive; and (5) between 200 and 800 μm , the density of micropores in feldspar is essentially proportional to the grain diameter.

From the preceding, both the dissolution site density on fresh-surface feldspar grains as well as the micropore density on naturally weathered feldspar grains are proportional to grain diameter. This suggests that, during natural weathering, micropores develop at dissolution reactive sites. The development of micropores from enhanced dissolution at dislocations (crystal line defects) is evaluated using thermodynamic principles and Monte Carlo simulations. The thermodynamic considerations show that micropore development in feldspar but not in quartz during natural weathering can be explained from the properties of dislocations in these two minerals as follows. In moderately undersaturated solutions, micropores form in feldspar and etch pits form in quartz. In highly undersaturated solutions, etch pits form in both feldspar and quartz. Although the internal surface area of naturally weathered feldspar grains is largely present as micropores (thus indicating moderate undersaturation), most natural soil solutions seem sufficiently undersaturated with respect to feldspar to explain the formation of etch pits, and not of micropores. This apparent contradiction is resolved by considering the effect of aqueous diffusion of reactants and products on the degree of solution saturation at the "bottom" of the hole (where most dissolution takes place). By introducing one-dimensional diffusion into an existing Monte Carlo program it is concluded that: (1) under natural conditions, aqueous diffusion over the length of the dissolution hole gives a saturation state at the bottom of the hole which is sufficiently high to favor micropore development; and (2) under normal laboratory conditions

(very highly undersaturated solutions), aqueous diffusion gives a saturation state at the bottom of the hole which is still sufficiently low to favor etch pitting. In conclusion, conditions during the natural weathering of feldspar favor the formation of micropores, while conditions during many laboratory experiments on feldspar favor the formation of etch pits.

The effect of micropores on dissolution rates

The thermodynamic theory and the Monte Carlo simulations confirmed the earlier findings that micropore "walls" are non-reactive and that micropore "bottoms" are highly reactive. A kinetic model is developed to account for the non-reactivity of the micropore walls. The model was applied to experimental dissolution data for similarly sized fresh-surface and naturally weathered feldspar grains. The results show that, if the non-reactivity of the micropore "walls" is accounted for, dissolution rates of the remaining naturally weathered BET surface areas are approximately similar to those of the freshly created BET surface areas under similar hydrogeochemical conditions. So, the formation of non-reactive micropore "walls" at dislocations probably represents the most essential change in surface character during the natural weathering of feldspar.

Dissolution rates of freshly created feldspar surfaces in the laboratory are frequently several orders of magnitude higher than those of naturally weathered feldspar surfaces in actual field situations. At grain diameters often used in laboratory experiments, approximately one order of magnitude in this rate discrepancy can be explained from the non-reactivity of micropore "walls" under field conditions. Other factors, such as imperfect contact between solution and solids in the field, the presence of organic ligands, etc., should be considered to explain the remaining part of the discrepancy in dissolution rates.

Samenvatting

Inleiding

Sinds het begin van de industrialisatie in de vorige eeuw is de emissie en atmosferische depositie van potentieel zure stoffen aanzienlijk toegenomen. Deze toename heeft, onder andere, geresulteerd in ongewenste verzuring van oppervlaktewater, bodem en grondwater. De schade, toegebracht door zure depositie, aan organismen in terrestrische en aquatische ecosystemen is aanzienlijk en het lot van deze systemen op lange termijn geeft reden tot bezorgdheid.

Protonen ("zuren") kunnen in de bodem op diverse manieren worden geneutraliseerd. In de meeste bodems wordt de snelheid waarmee protonen worden geneutraliseerd op lange termijn bepaald door de verwerkingssnelheid van mineralen met basische kationen in het rooster (calciet, veldspaat, pyroxeen, amphibool, etc.). Echter, het reactiemechanisme en de oplossingskinetiek van deze mineralen zijn onvoldoende bekend om hun verwerkingssnelheid onder diverse omstandigheden nauwkeurig te voorspellen. In dit proefschrift wordt voor veldspaat en kwarts het verband onderzocht tussen kristalstructuur, korrelgrootte, oppervlaktemorfologie en oplossingskinetiek onder zure omstandigheden. Veldspaat werd gekozen omdat het een der mineralen is met basische kationen in het rooster en omdat het een algemeen voorkomend mineraal is in vele bodems. Kwarts werd gekozen omdat het oplossingsgedrag van dit mineraal sterk afwijkt van dat van veldspaat. De karakteristieke afstandsschaal waarop het onderzoek zich concentreerde ligt in de orde van nm tot μm .

Het minerale oppervlak in laboratoriumverweringsproeven

Grote, natuurlijk verweerde minerale fragmenten worden vaak gemalen en gezeefd om monsters voor verweringsproeven in het laboratorium te krijgen. Als de fragmenten tot veel kleinere afmetingen worden gemalen, wordt normaliter aangenomen dat alle oppervlak vers gecreëerd is (d.w.z. het oorspronkelijk aanwezige, natuurlijk verweerde oppervlak wordt verwaarloosd). Om de verwerkingssnelheid in $\text{mol}\cdot\text{cm}^{-2}\cdot\text{s}^{-1}$ te berekenen uit experimentele oplossingsgegevens dient de hoeveelheid oppervlak in het gemalen monster bekend te zijn. De meest gebruikte schatting van het minerale oppervlak in oplossingsexperimenten wordt verkregen uit de gasadsorptie-isotherm (BET methode), met behulp van stikstof, argon of krypton als het adsorberende gas. De diameter van deze gasmoleculen ($\approx 0,4$ nm) is vrijwel gelijk aan de effectieve diameter van het moleculair water ($\approx 0,3$ nm), zodat het BET oppervlak waarschijnlijk een redelijke schatting is van het bevochtigde minerale oppervlak.

In dit proefschrift wordt aangetoond dat, voor grote, natuurlijk verweerde veldspaatfragmenten, verreweg het meeste oppervlak op de nm schaal van het krypton molecuul niet waarneembaar is op de μm schaal van scanning electronen-microscopie. Dit betekent dat verreweg het meeste BET oppervlak van natuurlijk verweerde veldspaatfragmenten aanwezig is als "intern" oppervlak. In tegenstelling hiermee is vers gecreëerd veldspaatoppervlak tamelijk glad, met ongeveer dezelfde hoeveelheden oppervlak waarneembaar op de schaal van het krypton molecuul en die van scanning electronen-microscopie. Ten gevolge van de hoge "ruwheid" van natuurlijk verweerde veldspaatoppervlaktes, in vergelijking met vers gecreëerde veldspaatoppervlaktes, is malen een uiterst ongeschikte methode om een grote fractie vers BET oppervlak te krijgen. In dit proefschrift wordt aangetoond dat monsters, verkregen uit grote, natuurlijk verweerde minerale fragmenten, zelfs na intensief malen nog voor een groot gedeelte kunnen bestaan uit natuurlijk verweerd, "intern" BET oppervlak. Dit betekent dat eerdere verweringsstudies aan gemalen monsters waarin het gelijktijdig voorkomen van deze twee typen oppervlaktemorfologie niet werd onderkend opnieuw dienen te worden geïnterpreteerd.

De dichtheid van oplossingsreactieve plaatsen op minerale oppervlaktes

Experimentele verwerkingssnelheden van gemalen monsters, genormaliseerd naar het BET oppervlak, zijn veelal onafhankelijk van de korrelgrootte. Uitgaande van het idee dat vrijwel alle BET oppervlak van gemalen monsters vers gecreëerd is, leidde dit tot de hypothese dat de dichtheid van oplossingsreactieve plaatsen (uitgedrukt als het aantal identieke reactieve plaatsen per cm^2 BET oppervlak) onafhankelijk is van de korrelgrootte. In dit proefschrift wordt een kinetisch model beschreven waarmee deze hypothese werd getoetst. Hiertoe worden experimentele oplossingsdata verklaard uit het gelijktijdig voorkomen van vers gecreëerd en natuurlijk verweerd BET oppervlak in één monster. Toepassing van het model op literatuurdata voor negen verschillende veldspaten laat zien dat, tijdens het malen, in feite sprake is van twee, elkaar (gedeeltelijk) tegenwerkende effecten op de verwerkingssnelheid. Deze zijn: (1) toename van de fractie van het gemeten BET oppervlak dat vers gecreëerd is; en (2) afname van de fractie van het vers gecreëerde BET oppervlak dat oplossingsreactief is. Aldus vinden we, door rekening te houden met het "interne" oppervlak van natuurlijk verweerde veldspaten, dat voor de onderzochte korrelgroottes ($< 1000 \mu\text{m}$) de dichtheid van oplossingsreactieve plaatsen op vers gecreëerde veldspaatoppervlaktes ongeveer evenredig is met, en niet onafhankelijk is van, de korrelgrootte. Dit kan worden verklaard indien preferente breukvlakken een relatief hoge dichtheid aan potentiële oplossingsreactieve plaatsen bezitten. In dat geval worden door malen verse

oppervlaktes blootgelegd met een steeds kleinere dichtheid aan oplossingsreactieve plaatsen, waardoor de gemiddelde dichtheid afneemt met kleiner wordende korrelgrootte. Dientengevolge vindt tijdens malen eerder "verdunning" plaats van vers, reactief oppervlak, dan "vernietiging". Volgens het kinetisch model is de dichtheid van oplossingsreactieve plaatsen op natuurlijk verweerde oppervlaktes in gemalen monsters onafhankelijk van de korrelgrootte. Dit kan worden verklaard indien het breken van natuurlijk verweerde oppervlaktes in kleinere delen geen gevolgen heeft voor de "interne" structuur van het oppervlak zelf. In dat geval stammen de natuurlijk verweerde oppervlaktes op gebroken korrels, ongeacht de diameter, rechtstreeks af van het ongebroken beginmateriaal. Uit het kinetisch model blijkt dat, bij gelijke diameters, de verwerkingssnelheid ($\text{mol.cm}^{-2} \text{ BET oppervlak.s}^{-1}$) van veldspaatkorrels bestaande uit louter vers gecreëerd oppervlak tot verscheidene ordegroottes hoger is dan de verwerkingssnelheid van natuurlijk verweerde veldspaatkorrels. In termen van identieke oplossingsreactieve plaatsen zou dit betekenen dat, voor veldspaat, de dichtheid op vers gecreëerde BET oppervlaktes tot verscheidende ordegroottes hoger is dan de dichtheid op natuurlijk verweerde BET oppervlaktes.

De vorming van microporiën tijdens natuurlijke verwerking

De aard en reaktiviteit van het "interne" BET oppervlak zijn onderzocht voor een natuurlijk verweerd veldspaat-kwarts monster. De conclusies luiden: (1) het interne oppervlak is voornamelijk aanwezig als microporiën van ongeveer 2 nm diameter; (2) microporiën vormen zich tijdens de natuurlijke verwerking wel in veldspaat- maar niet in kwartskorrels; (3) de "wanden" van de microporiën (loodrecht op het korreloppervlak) zijn in essentie niet-reactief; (4) de "bodems" van de microporiën (parallel aan het korreloppervlak) zijn uiterst reactief; en (5) tussen 200 en 800 μm is de dichtheid van de microporiën ongeveer evenredig met de korrelgrootte.

Uit het voorgaande blijkt dat, voor veldspaat, zowel de dichtheid van oplossingsreactieve plaatsen op vers gecreëerde oppervlaktes als de dichtheid van microporiën op natuurlijk verweerde oppervlaktes evenredig is met de korrelgrootte. Dit suggereert dat, tijdens de natuurlijke verwerking, microporiën zich vormen op de oplossingsreactieve plaatsen. De vorming van microporiën door het selectief oplossen van dislokaties (kristal-lijnfouten) is geëvalueerd met behulp van thermodynamische principes en Monte Carlo simulaties. Het thermodynamische model laat zien dat de vorming van microporiën in veldspaat- maar niet in kwartskorrels tijdens de natuurlijke verwerking als volgt beschreven kan worden met behulp van de eigenschappen van dislokaties in deze twee mineralen. In matig onderverzadigde oplossingen vormen zich microporiën in veldspaat en etch pits in kwarts. In sterk onderverzadigde oplossingen vormen zich etch pits in zowel veldspaat als kwarts. Ondanks

dat het interne oppervlak van natuurlijk verweerde veldspaatkorrels grotendeels aanwezig is als microporiën (duidend op matige onderverzadiging), zijn de meeste bodemoplossingen in de praktijk voldoende onderverzadigd voor veldspaat om de vorming van etch pits te verklaren in plaats van microporiën. Deze schijnbare tegenstelling verdwijnt indien mede het effect wordt beschouwd van diffusie in de oplossing op de verzadigingsgraad onderin de opgeloste holte (waar de meeste oplossing van mineraal materiaal plaatsvindt). Introductie van een-dimensionale diffusie in een bestaand Monte Carlo programma leidde tot de volgende conclusies: (1) onder natuurlijke omstandigheden is het effect van diffusie zodanig dat de verzadigingsgraad van de oplossing in de holte voldoende hoog wordt voor de vorming van microporiën; en (2) onder normale laboratoriumomstandigheden (zeer sterk onderverzadigde oplossingen) is het effect van diffusie zodanig dat de verzadigingsgraad van de oplossing in de holte voldoende laag blijft voor de vorming van etch pits. Concluderend: tijdens de natuurlijke verwerking van veldspaat vormen zich normaliter microporiën en tijdens laboratoriumexperimenten vormen zich normaliter etch pits.

Het effect van microporiën op de verwerkingssnelheid

Het thermodynamische model en de Monte Carlo simulaties bevestigden de eerdere bevindingen dat de "wanden" van microporiën niet-reaktief zijn en dat de "bodems" van microporiën zeer reaktief zijn. Een kinetisch model is ontwikkeld om verwerkingssnelheden te corrigeren voor het niet-reaktieve karakter van de "wanden" van microporiën. Het model is toegepast op experimentele oplossingsdata voor verse en natuurlijk verweerde veldspaatkorrels van gelijke diameter. Voor veldspaatkorrels van gelijke grootte laten de resultaten zien dat, na correctie voor het niet-reaktieve karakter van de "wanden" van microporiën, de verwerkingssnelheid van het overige natuurlijk verweerde BET oppervlak in essentie gelijk is aan die van vers gecreëerd BET oppervlak. Dit houdt in dat de vorming van niet-reaktieve "wanden" van microporiën, ten gevolge van het selectief oplossen van dislokaties, waarschijnlijk de meest essentiële verandering is in de aard van het veldspaatoppervlak tijdens de natuurlijke verwerking.

De verwerkingssnelheid van vers gecreëerd veldspaatoppervlak in het laboratorium is veelal enkele ordegroottes hoger dan die van natuurlijk verweerde veldspaatoppervlaktes onder veldomstandigheden. Voor korrelgroottes zoals vaak gehanteerd in laboratoriumexperimenten kan ongeveer één ordegrootte in dit verschil worden verklaard doordat onder veldomstandigheden niet-reaktieve "wanden" van microporiën aanwezig zijn. Andere factoren, zoals onvolledig contact tussen de oplossing en de mineraalkorrels, de aanwezigheid van organische liganden, etc., dienen beschouwd te worden om het resterende deel van het verschil in verwerkingssnelheid te verklaren.

Curriculum Vitae



Chris Anbeek is geboren op 10 augustus 1954 te Ede. In 1972 behaalde hij het eindexamen h.b.s. B aan het Christelijk Lyceum te Veenendaal. In 1980 studeerde hij af in de Bodemkunde en Bemestingsleer, specialisatie Regionale Bodemkunde, aan de Landbouwniversiteit te Wageningen. Het afstudeeronderzoek bij prof. L. Pons (Regionale Bodemkunde), prof. L. van der Plas (Bodemmineralogie) en prof. G.H. Bolt (Bodemscheikunde) betrof alpiene bodemvorming op dolomiet. Na het vervullen van zijn militaire dienstplicht werd hij in 1982 werkzaam als bodemkundig medewerker bij de afdeling Milieu, Provinciale

Waterstaat in Overijssel te Zwolle. Daar richtte hij in 1984, samen met zijn vrienden Romke Boskma, Jan Brand en Harry Verheesen, de zwolse afdeling van het R.D.D.T. op, waarmee enige furore in het buitenland werd gemaakt.

Gedurende de periode 1988 tot 1993 was hij verbonden aan de Vakgroep Bodemkunde en Geologie van de Landbouwniversiteit, alwaar dit proefschrift tot stand kwam. Het promotie-onderzoek is bedoeld om fundamenteel inzicht te verschaffen in de relaties tussen kristalstructuur, korrelgrootte, oppervlaktetopografie en de verwerkingssnelheid van mineralen. Een dergelijk inzicht blijkt vrijwel onmisbaar voor het modelmatig inschatten van verwerkingssnelheden in geochemische, bodemkundige en milieukundige studies.

In 1990 trouwde hij met Gerrie Kuipers, en in 1993 werd hun zoon Daan geboren. Sinds 1 september 1993 is hij hoofd Bodemsanering en Beschermingstechnieken bij TAUW Milieu bv te Deventer.